The Pennsylvania State University

The Graduate School

College of Earth and Mineral Sciences

{0 0 1} TEXTURED GROWTH OF DOPED, GRADIENT FREE, LEAD ZIRCONATE TITANATE THIN FILMS BY CHEMICAL SOLUTION DEPOSITION

A Thesis in

Materials Science and Engineering

by

Trent M. Borman

Submitted in Partial Fulfillment
of the Requirements
for the Degree of

Master of Science

December 2016

The thesis of Trent M. Borman was reviewed and approved* by the following:

Susan E. Trolier-McKinstry
Professor of Materials Science and Engineering and Electrical Engineering
Thesis Advisor

Clive A. Randall
Professor of Materials Science and Engineering

Srinivas A. Tadigadapa
Professor of Electrical Engineering

Suzanne Mohney
Professor of Materials Science and Engineering and Electrical Engineering
Chair, Intercollege Graduate Degree Program in Materials Science and Engineering

*Signatures are on file in the Graduate School.

Abstract

This work studied means of enhancing the performance of $PbZr_xTi_{1-x}O_3$ (PZT) thin films via {0 0 1} textured growth, doping, and reduction of Zr/Ti compositional gradients. Factors which control the microstructure and crystallographic quality of polycrystalline {111} Pt thin films on silicon substrates were investigated. Platinum deposited at high temperature (500 – 600 °C) on TiO_2 adhesion layers exhibited a narrower Pt {111} rocking curve peak width and a larger grain size than platinum sputtered at room temperature on Ti adhesion layers. Variations in the final grain size and rocking curve peak width of high temperature were demonstrated to depend predominately on the platinum deposition conditions with minimal influence from variations in the underlying TiO_2 layer.

The direct seeding of {0 0 1} PZT on platinized silicon substrates was studied in relation to the platinum characteristics, doping, solution Pb stoichiometry and layer thickness. High temperature platinum was observed to enhance PZT grain size and reduce surface coverage of the pyrochlore secondary phase when compared to room temperature platinum, indicating a higher Pt density and a lower propensity for lead absorption. Generally, no significant crystallographic difference was observed between seed layers deposited on high temperature or room temperature platinum, nor was any microstructural difference observed in seed layers on different sources of high temperature platinum. Increases in solution lead excess reduced surface pyrochlore significantly. Niobium doping was found to increase grain size and pyrochlore coverage while Mn doping exhibited a rosette microstructure with poor crystallization on High Temperature (HT) Pt (via XRD), attributed to possible dopant segregation. A thickness regime of 30 – 70 nm was found to yield strongly {0 0 1} oriented PZT seed layers.

Degradation of {0 0 1} orientation as a function of film thickness was attributed to surface pyrochlore converting to misoriented perovskite grains. Lead oxide capping layers could convert only small amounts of pyrochlore to {0 0 1} perovskite. In cases of thick layers of pyrochlore coverage, misoriented perovskite grain formation was unavoidable. Use of lead rich solutions (particularly at the top surface of each crystallization) provided a means of preventing pyrochlore formation. Niobium doped films with Lotgering factors in excess of 0.99 were attainable with solutions ranging from 10-20 at.% Pb excess in various stacking sequences. In addition to films with low, medium and high lead contents, a film with thin layers of manganese doping was deposited.

No significant trend was observed in the dielectric or piezoelectric properties as a consequence of lead content. The film with Mn doped layers exhibited reduced dielectric properties (including Rayleigh coefficients) and small signal piezoelectric properties while exhibiting similar large signal piezoelectric performance ($d_{33,f}$ of ∼120 pm/V). Films with high lead content exhibited a higher leakage contribution to the polarization in hysteresis measurements. Films with higher lead contents were found to undergo dielectric breakdown in a tighter distribution at lower electric fields than films with a low lead content, which exhibited a larger spread of failures at a higher average field. All films tended to microcrack prior to dielectric breakdown events and material ejection occurring. Microcracks were found to propagate predominately in a straight line with no preference for following grain boundaries. Cracks were found to propagate throughout the entire film thickness ∼1.4 µm.

Table of Contents

List of Figures

List of Tables

Acknowledgments

First, and foremost, I would like to thank my advisor, Professor Susan Trolier-McKinstry, for the broad wealth of guidance and support she has provided over my two years at Penn State. She finds time to provide detailed guidance to each of her numerous students even in the midst of her many teaching and administrative obligations. While being an incredible source of pertinent knowledge and experience in conducting and reporting research, her mentorship stretched beyond this. She takes care to foster the personal and professional development of her students, including making sure students find the career path that is right for them and that which they also enjoy.

This work would not have been possible, in more ways than one, without the generous help of Xaar plc and their creative, talented staff of scientists and engineers. Peter Mardilovich helped catalyze communications and productivity between Penn State, Xaar, and suppliers. Song Won Ko's position in an office outside of the cleanroom was immensely helpful by allowing us to coordinate efforts towards numerous common goals pertaining to our respective projects. The entire bi-weekly teleconference team at Xaar (Murray Allen, Carlos Fragkiadakis, Michael Hook, Garfay Liu, Silvia Marson, Mani Sivaramakrishnan, and Anja Wehrum in addition to Peter and Song Won) provided valuable insight.

The highly talented technical staffs in the Materials Characterization Laboratory and the Nanofabrication Facility are a resource all users are privileged to have. Whether a problem with equipment (minor or major), a process question, or coming to them with something entirely new, they were always happy to provide their input and help. In particular I would like to thank Bill Drawl, Beth Jones, Mike Labella, Jeff Long, Joe Stitt, Gino Tambourine, and Nichole Wonderling for their frequent assistance.

An added benefit of Dr. Trolier-McKinstry's large research team is the fostering of collaboration and mutual discussion of results (similar or different). My fellow group members were instrumental in training on procedures, sharing process parameters, and troubleshooting unexpected results. To that end I would like to thank Betul Akkopru-Akgun, Jon Bock, Jason Chan, Lyndsey Denis, Lauren Garten, Raegan Johnson, Ryan Keech, Song Won Ko, Sun Young Lee, Tianning Liu, Lizz Michael-Sapia, Carl Morandi, Adarsh Rajashekhar, Smitha Shetty, Julian Walker, Margeaux Wallace, Dixiong Wang, Aaron Welsh, Derek Wilke, Jung In Yang, Charley Yeager, Hong Goo Yeo, and Wanlin Zhu. Special thanks go to Wanlin Zhu and Song Won Ko, the postdoctoral scholar and Xaar employee respectively, who worked on this project with me. Song Won was particularly helpful with the fabrication and characterization of platinized silicon wafers, in addition to his work with optimizing the PZT seed layer process. I would also like to thank Michelle Lieu and Bo Truong, REU students for the summer of 2016, for their assistance with the poling study.

I cannot thank Wanlin enough for all the help she gave me in the deposition and characterization of the thick films in the latter chapters of this work. She saved me countless trips in and out of the cleanroom, taking my samples to the XRD to check orientation quality on the first few crystallization steps for each film. She participated in marathon cleanroom sessions, making films one day and having them ready for electrical measurements the next. When I fell ill, she deposited films for me so I would not contaminate them or the rest of the nanofab. We worked in conjunction to thoroughly and reproducibly characterize the four thick film samples in order to ensure our measurement accuracy, whether the measurements took seconds or hours to complete.

Finally, I would like to thank my family for their support from halfway across the country. They have encouraged my drive for furthering my education and support me whenever I stumble. Above anyone else, they believe my potential success is limitless and do everything they can to ensure it. Special thanks to my older sister Brittany for providing competition when I was young which helped me excel from a young age. Additionally, I would like to thank my friends, from one desk over to around the world, for their support both intellectually and mentally. They kept me on my feet and encouraged optimism, even in the face of difficult research problems and provided breaks from the monotony of lab work and writing.

Chapter 1

Introduction and Motivation

1.1 Ferroelectric Materials

Ferroelectrics are a set of materials which exhibit a spontaneous electrical polarization. Furthermore, this polarization is limited to specific crystallographic axes within the material and can be reoriented with the application of an electric field. By nature of being polar, all ferroelectrics are also pyroelectric (a first rank tensor property) and piezoelectric (a third rank tensor property). The spontaneous electrical polarization in a ferroelectric can be altered by an applied electric field, stress, strain, or change in temperature. The primary piezoelectric coefficients utilized in this work are the d and e coefficients (in particular $d_{33,f}$ and $e_{31,f}$) as defined (for the bulk form) within Equation (1.1); where D is dielectric displacement, E is electric field, X is stress, x is strain, i is a direction, and j denotes an element of the stress or strain tensor in Voigt notation.[1,2]

$$d_{ij} = \left(\frac{\partial D_i}{\partial X_j}\right)_E = \left(\frac{\partial x_j}{\partial E_i}\right)_X \qquad e_{ij} = \left(\frac{\partial D_i}{\partial x_j}\right)_E = -\left(\frac{\partial X_j}{\partial E_i}\right)_x \tag{1.1}$$

In thin films, the piezoelectric coefficients are measured under mixed boundary conditions and hence are not identical to the coefficients typically reported for bulk materials. This is a consequence of mechanical clamping from the substrate coupling the longitudinal or transverse effects, and inhibiting their direct measurement. Thus, measured film piezoelectric coefficients are denoted the *effective* coefficient (subscript f). Lefki & Dormans developed a model which considers the elastic properties of the film's underlying substrate, relating the measured coefficient ($d_{33,f}$) of clamped piezoelectric thin films to the material piezoelectric coefficient (d_{33}).[3] If the substrate is considered to be perfectly rigid, as in [3–5], the piezoelectric film is clamped from straining in the in-plane directions. In this case the $d_{33,f,Rigid}$ and $e_{31,f,Rigid}$ coefficients are given by Equation (1.2)[5]; d_{33} and d_{31} are the material piezoelectric coefficients, ν_{PE} is the Poisson's ratio of the piezoelectric film (PE), and Y_{PE} is the of elastic modulus of the PE. A second model considers that the substrate is not perfectly rigid, (i.e. strains can develop in the substrate and in-plane in the film) as in the case of a silicon substrate. The resultant effective piezoelectric coefficients defined as in Equation (1.3).[5] κ_{Si} is defined in Equation (1.4), where Y_{Si} is the elastic modulus of Si, ν_{Si} is the Poisson's ratio of Si, and l_{PZT} and l_{Si} are the thicknesses of the PZT film and silicon substrate respectively.

$$d_{33,f,Rigid} = 2d_{31}\frac{\nu_{PE}}{1+\nu_{PE}} + d_{33} \qquad e_{31,f,Rigid} = d_{31}\frac{Y_{PE}}{1-\nu_{PE}} \tag{1.2}$$

$$d_{33,f,Elastic} = \frac{d_{33,f,Rigid} + d_{33}\kappa_{Si}}{1+\kappa_{Si}} \qquad e_{31,f,Elastic} = \frac{e_{31,f,Rigid}}{1+\kappa_{Si}} \tag{1.3}$$

$$\kappa_{Si} = \frac{Y_{PE}}{1-\nu_{PE}} \frac{1-\nu_{Si}}{Y_{Si}} \frac{l_{PEF}}{l_{Si}} \tag{1.4}$$

An important, early ferroelectric oxide ceramic was the perovskite $BaTiO_3$, which remains a model system. $BaTiO_3$ adopts the cubic perovskite structure as well as tetragonal (as depicted for $Pb(Zr,Ti)O_3$ in Figure 1.2), orthorhombic and rhombohedral distortions (Figure 1.1). The structure is defined by barium atoms at the corners, oxygen atoms near the face centers and titanium at approximately the center of the unit cell. In the cubic prototype phase, the titanium atom is centered, and the material behaves as a nonlinear dielectric[6–9]; with no spontaneous polarization and thus no piezoelectricity, ferroelectricity, or pyroelectricity. Upon cooling, the material first distorts tetragonally, displacing the titanium from the center of the unit cell along the $\langle 0\,0\,1 \rangle$. This displacement creates a separation of the centers of positive and negative charge, resulting in a dipole polarization along the $\langle 0\,0\,1 \rangle$. Further cooling is followed by orthorhombic and rhombohedral distortions with polarizations along the pseudocubic $\langle 1\,1\,0 \rangle$ and $\langle 1\,1\,1 \rangle$ directions respectively. All distorted $BaTiO_3$ phases exhibit ferroelectricity and, by extension, piezoelectricity and pyroelectricity.[1]

Development of a spontaneous polarization, which is aligned throughout the entire material, would require charge to develop at the surfaces, forming a depolarization field (Figure 1.3 (a)). In order to lower the overall energy of the system, a domain structure forms in the ferroelectric material (Figure 1.3 (b)). Domains are regions within the material in which unit cells are polarized in the same direction (or nearly so).[13,14] The domain walls separate regions with different polarization directions. Polarization in the perovskite structure requires a lattice distortion; as a result, domain structures also interact with strain. The driving force for domain structure formation is the reduction in energy contributions from strain and electrostatic sources (depolarization fields).[1,10]

Domain walls are often denoted by the angle between the polarization directions in the two domains that the wall separates. In the case of a tetragonal perovskite, there are 6 polarization directions available with angles of 90° or 180° between them, yielding domain walls categorized by the same angles. Rhombohedral phases, with polarization along the $\langle 1\,1\,1 \rangle$, have 71°, 109°, and 180° domain walls. Upon application of an electric field, domains with polarizations (or components of the polarization) which are aligned (most nearly) parallel to the electric field will grow in size while those with other orientations will decrease in size. This process is called poling the material, and allows development of a net polarization in a polycrystalline material. In the case of low electric fields, the displacement of domain walls will be small and reversible due to pinning centers, at higher electric fields it will become irreversible as described in Section 1.4.1, and above the coercive field (E_C) it will become strongly hysteretic.[10]

1.2 Lead Zirconate Titanate

Lead zirconate titanate ($Pb(Zr_{1-x}Ti_x)O_3$) is a solid solution (see Figure 1.4 for the phase diagram) of the ferroelectric, tetragonal perovskite $PbTiO_3$ and the antiferroelectric, orthorhombic perovskite $PbZrO_3$.

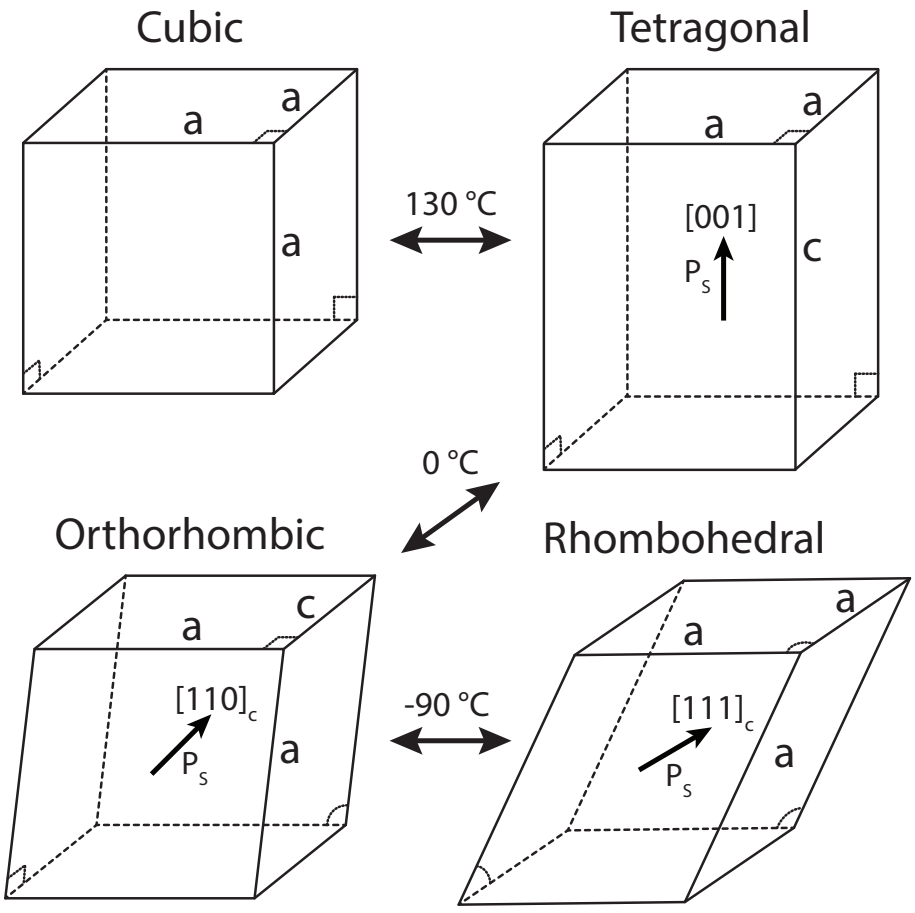

Figure 1.1: Distortions of the $BaTiO_3$ unit cell. The magnitudes of the distortions are exaggerated for clarity. Figure adapted from Moulson & Herbert.[10]

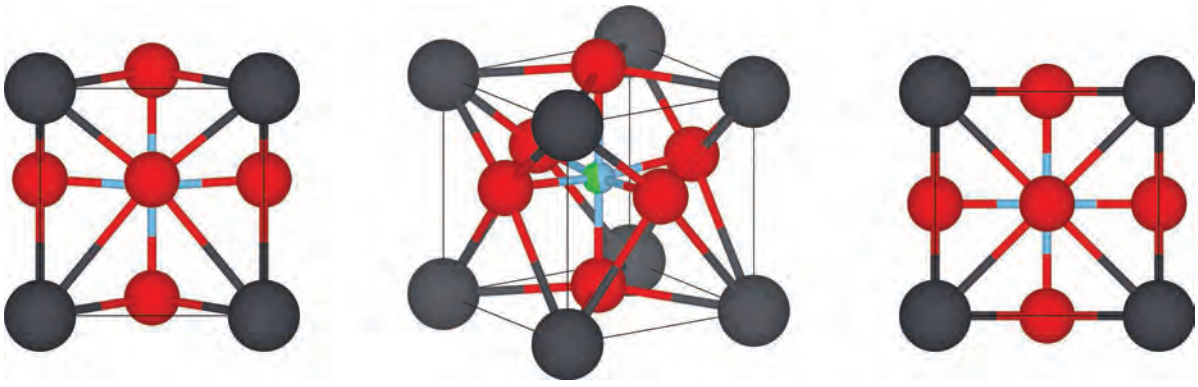

Figure 1.2: Tetragonal unit cell of PZT with atomic positions from Frantti *et al.*[11] Corners, face centers and the approximate body center represent Pb, O, and Zr/Ti, respectively. Views are along [1 0 0], [2 3 1], and [0 0 1] from left to right, respectively.[12]

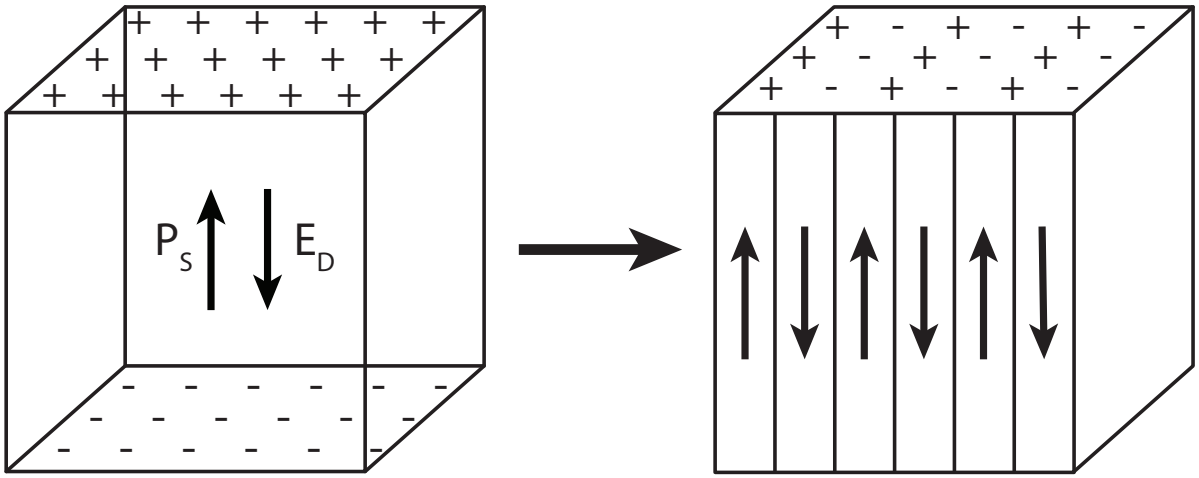

Figure 1.3: (a) Charge development at surfaces as a result of spontaneous polarization (P_S), forming a depolarization field (E_D) in the opposite direction. (b) 180° domain structure which minimizes electrostatic energy associated with charge at the surfaces. Adapted from Moulson & Herbert.[10]

As zirconium is substituted for titanium in the $PbTiO_3$ structure, the material progressively becomes less tetragonal until it reaches the morphotropic phase boundary near a Zr:Ti ratio of 52:48. The morphotropic phase boundary (MPB) is an abrupt phase transition between the ferroelectric tetragonal and rhombohedral[1,15] or monoclinic[11,16] phases which is controlled by composition. Additionally, the MPB's position is relatively independent of temperature. This provides phase stability over a broad temperature range, even for compositions directly adjacent to the morphotropic phase boundary.[1,17,18]

The morphotropic phase boundary is particularly advantageous for the high electromechanical and dielectric properties observed its vicinity. Jaffe *et al.* demonstrated maxima in the piezoelectric d coefficients near the morphotropic phase boundary (Figure 1.5), with rapidly diminishing values to either side of the boundary.[15] Berlincourt *et al.* later demonstrated maxima in the piezoelectric coupling, piezoelectric d and g coefficients, and dielectric permittivity, all of which occurred at a composition of 52 at.% Zr (the morphotropic phase boundary).[24]

In thin film applications, the maxima of piezoelectric and dielectric properties have been reported to occur at different compositions. While most researchers report that the MPB composition is unchanged in relaxed films, Hiboux *et al.* noted that the maxima in the d_{33} piezoelectric response was found at a composition 5 at.% higher in titanium than the dielectric maxima. Additionally, in contrast with the sharp MPB found in bulk ceramics, a more diffuse transition in the region of 40 to 50 at.% Zr was noted for piezoelectric films. The divergence in the compositions for maxima in the electronic and piezoelectric properties was attributed to the strains induced from clamping by the electrode and substrate.[25] Alternatively, it is possible that the shift in the piezoelectric properties maxima was an

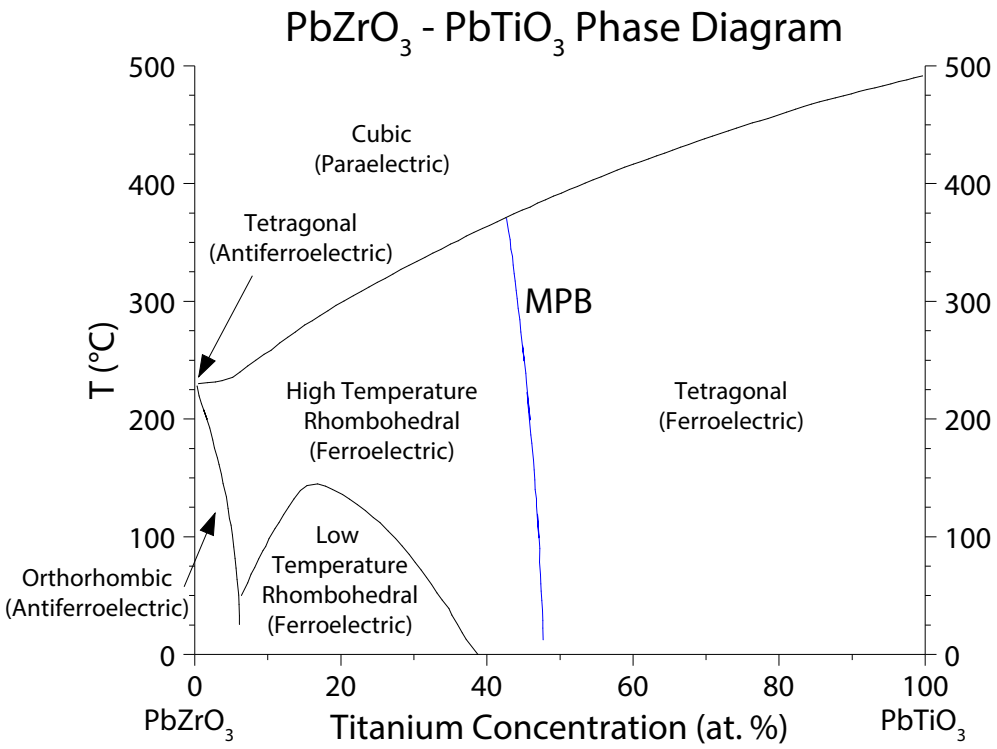

Figure 1.4: Jaffe *et al.*'s phase diagram of the lead zirconate – lead titanate solid solution. The morphotropic phase boundary is indicated in blue. Replotted with data from Jaffe *et al.*[1,19] Modified phase diagrams have been proposed by Noheda *et al.*,[16] Ragini *et al.*,[20] Woodward *et al.*,[21] and Zhang *et al.*[22,23] among others.

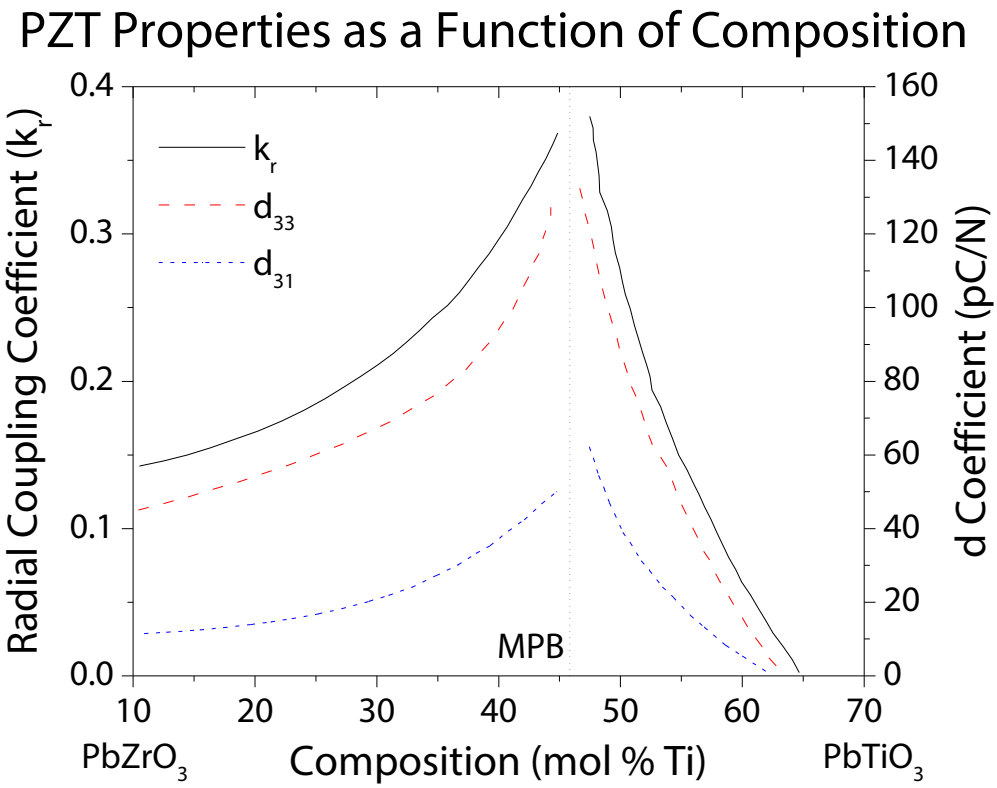

Figure 1.5: Electromechanical properties of the lead zirconate – lead titanate solid solution as a function of composition. Data replotted from Jaffe *et al.*[15,19]

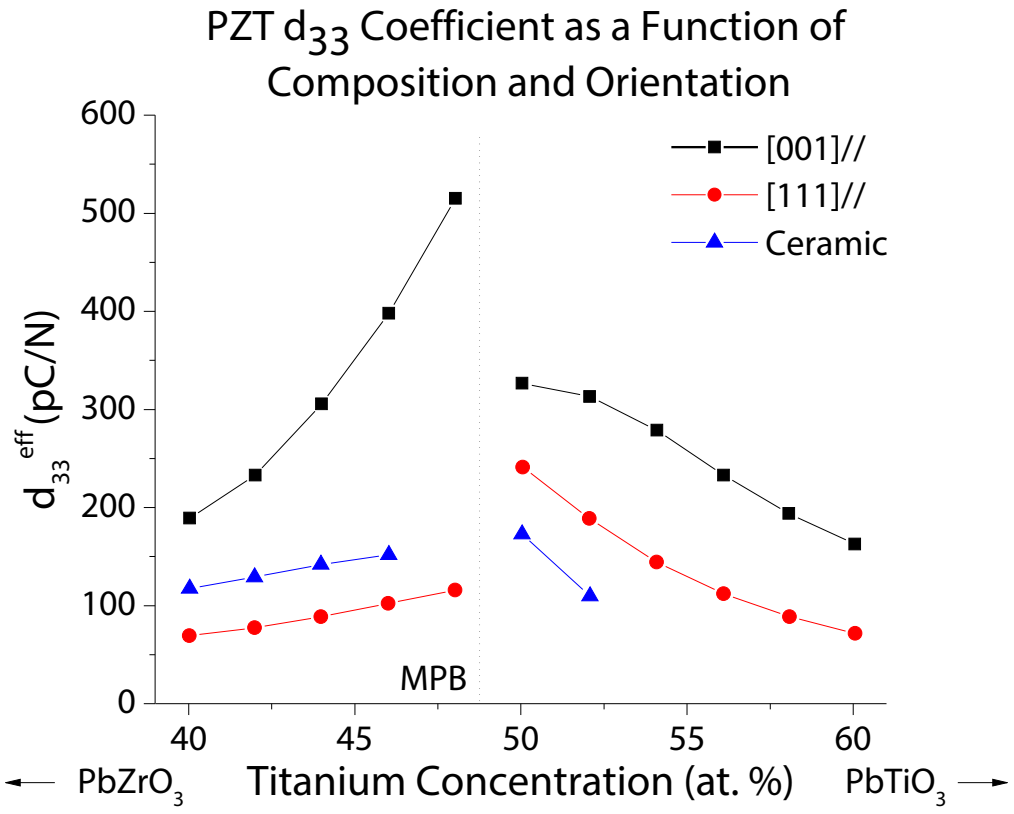

Figure 1.6: Calculated values of d_{33} as a function of composition for oriented single crystals as compared to experimental data from ceramics. Data replotted from Du *et al.*[19,26]

artifact of compositional gradients within the films or improved poling in the more tetragonal nominal composition.

Phenomenological calculations by Du *et al.* demonstrate the piezoelectric coefficients maximize near the morphotropic phase boundary for both rhombohedral and tetragonal phases with the [0 0 1] direction exhibiting the highest piezoelectric d_{33}^{eff} coefficient (Figure 1.6).[26,28] Ledermann *et al.* demonstrated that the maximum in the transverse piezoelectric coefficient ($e_{31,f}$) for {0 0 1} textured thin films was obtained at compositions of approximately 53% Zr (the MPB).[29,30]

While demonstrating a maximum in $e_{31,f}$ at the morphotropic phase boundary, Ledermann *et al.* found substantial compositional variation within each crystallization step for sol-gel derived PZT. Despite deposition of a nominally Zr:Ti 53:47 film, the film composition was a Ti rich 44:56 at the crystallization interface (bottom of the layer). Throughout the thickness of each crystallized layer, the composition gradually changed to a Zr rich 65:35 near the top surface, giving a compositional variability near ±10 at.% throughout each layer's thickness. At a later date, Calame & Muralt demonstrated growth of 'gradient-free' PZT thick films which reduced compositional variation to ±2.5 at.%, as shown in Figure 1.7. This was accomplished by depositing four layers per crystallization with compositions of 63,

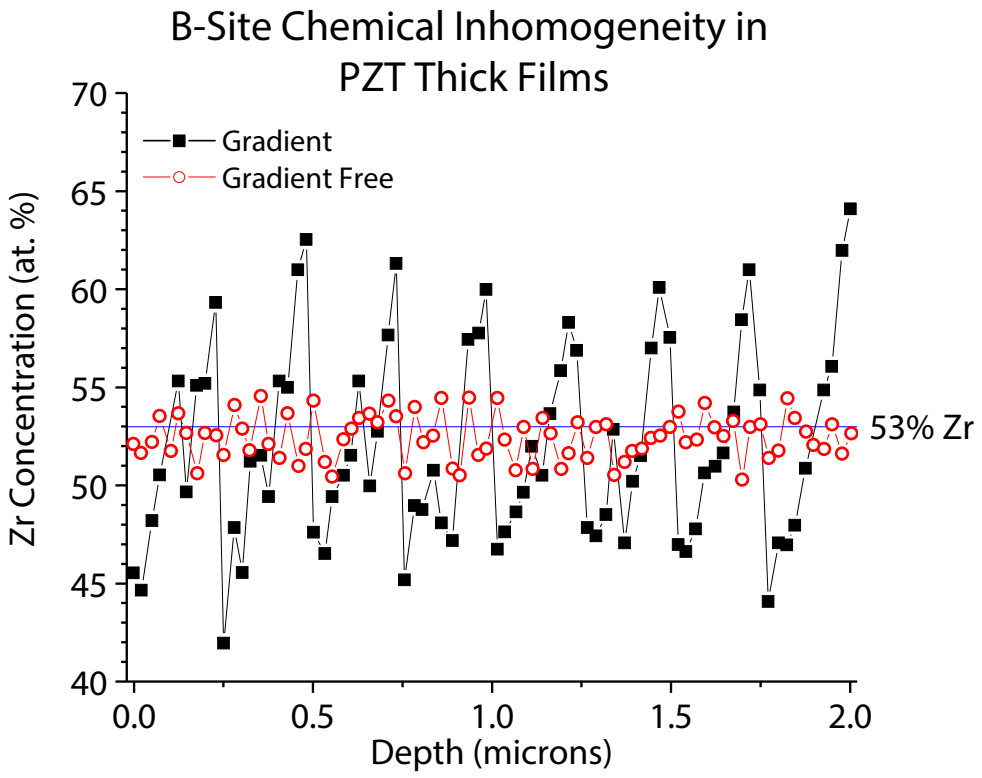

Figure 1.7: Zr/(Zr+Ti) ratio as measured by EDS across a 2 μm thick film of nominal composition 53:47 (blue horizontal line). Data replotted from Calame & Muralt.[19,27]

58, 48, and 43 at.% zirconium, in order, from bottom to top. This built a gradient into the amorphous film which opposed that which forms in the crystallized film, allowing the two gradients to offset each other, and reduce the overall composition gradient. The reduced compositional gradients resulted in increases of the $e_{31,f}$ coefficient and dielectric constant by 20% as compared to films with large compositional gradients.[27]

Presently, there is not a consensus on the impact that compositional gradients have on the properties of PZT thin films. In contrast to Calame & Muralt, Bastani & Bassiri-Gharb found little improvement in the dielectric properties, Rayleigh parameters and $d_{33,f}$ coefficient when transitioning from multi layer annealed films (4 spins per crystallization) to gradient free films. Furthermore, they demonstrated frequent and steep compositional gradients, induced by 1 spin per crystallization, enhanced dielectric and piezoelectric properties.[31] Similarly, Pelloquin *et al.* observed enhanced breakdown strength in thin, gradient-free films relative to standard films with gradients. As thickness increased, the breakdown strength of gradient free films rapidly declined while that of standard films increased, crossing over at 420 nm. The authors theorized that gradient free films may form more electrically robust interfaces with electrodes while forming weaker interfaces between PZT layers. Thus, as the thickness (number of PZT interfaces) increases, the breakdown strength would reduce.[32] Furthermore, gradient free growth techniques have yet to be widely applied to doped thin films.

1.3 Doped Lead Zirconate Titanate

Aliovalent substitution of the A or B site cations in the perovskite lattice can strongly influence the properties of lead zirconate titanate. Dopant cations can be classified as donor or acceptor dopants in the cases where they have a higher or lower charge than the cation being replaced respectively. In principle, donor dopants (D) can lead to the formation of either conduction electrons or cation vacancies (typically lead due to its high volatility), while acceptor dopants (A) can lead to formation of conduction holes or oxygen vacancies as demonstrated in Table 1.1.[1,10] In practice, it is difficult to make PZT strongly conducting, so ionic compensation often dominates.[1,33]

Bulk ceramic PZT has been donor doped with a broad range of cations, including Nb^{5+}, Ta^{5+}, W^{6+}, Th^{4+}, Bi^{3+}, and rare earths such as La^{3+}. Similarly a variety of acceptor dopants have also been utilized such as Mn^{2+}, Mn^{3+}, Sc^{3+}, Mg^{2+}, K^{+}, and Fe^{3+}. In general, donor dopants are associated with "softening" PZT, allowing increased domain wall motion. This, in turn, increases the dielectric constant, the dielectric loss, the elastic compliance, and piezoelectric coupling while reducing the mechanical quality factor and the coercive field. Because PZT often has a finite p-type conductivity due to charge compensation associated with the finite volatility of lead, donor doping (with partial electronic compensation) also tends to increase the electrical resistivity (see Figure 1.8).[1,33] Conversely, acceptor dopants "harden" PZT, reducing domain wall motion and subsequently increasing the mechanical

quality factor, the coercive field, and the resistance to changes in poling while lowering the dielectric constant and loss.[1,10]

Aliovalent substituents can form dipoles with the corresponding vacancy defect such as $D^{\bullet}_{Zr/Ti}-V''_{Pb}$ or $A'_{Zr/Ti}-V^{\bullet\bullet}_{O}$.[34–38] Each defect dipole will be accompanied by a corresponding strain field and local electric field in the material. In the case of donor doping, cation vacancies are relatively immobile, resulting in a random distribution of local electric and strain fields throughout the material. In contrast, the oxygen vacancies induced by acceptor doping are mobile at temperatures $<200\,^{\circ}C$.[36,39] This allows reorientation of the dipoles under an applied electric field, yielding a built in internal field in the material which resists changes to the domain structure.[10]

Similarly to bulk PZT, thin films of PZT have been doped with a broad range of cationic species, including Nd^{3+} [40], Fe^{3+} [40], La^{3+} [38,41,42], Zn^{2+} [43], and most commonly Nb^{5+} [38,44–46] and Mn^{3+} [37,47–49]. The primary goal of this thesis is to understand the implications graded doping and composition have on the performance and reliability of $\{0\,0\,1\}$ PZT thin films used in piezoelectric applications. The envisioned graded doping involves regions of soft PZT (donor doping) for enhanced piezoelectric properties and reduced leakage current, and regions of hard PZT (acceptor doping) to retain the poled domain structure via defect dipole alignment. Donor and acceptor dopants were chosen from the broad range of available options based on the available literature.

1.3.1 Donor Doped Lead Zirconate Titanate

Lanthanum and niobium are both commonly utilized donor dopants in PZT thin films. Haccart *et al.* studied PZT thin films deposited via sputter deposition with a doping level of 1 to 7 at.% Nb. The dielectric constant and remanent polarization increased from 800 to 1100 and from 15 to 21 $\mu C/cm^2$ respectively upon doping with 2 at.% Nb, followed by a gradual decline with further increases in dopant concentration.[44,46,50] Klissurska *et al.* found a maxima of the P_r and ε_r at 1 at.% niobium, attributing the decline in properties at high doping levels to an increase in pyrochlore concentration associated with

Table 1.1: Kroger-Vink reactions for donor (D^{5+}) and acceptor (A^{3+}) doping on the B site in lead zirconate titanate

Donor doping with electronic compensation	$2\,PbO + D_2O_5 \xrightarrow{PZT} 2\,Pb^{\times}_{Pb} + 2\,D^{\bullet}_{Zr/Ti} + 6\,O^{\times}_{O} + 2\,e^{-} + \frac{1}{2}\,O_2(g)$
Donor doping with ionic compensation	$2\,PbO + D_2O_5 \xrightarrow{PZT} Pb^{\times}_{Pb} + V''_{Pb} + 2\,D^{\bullet}_{Zr/Ti} + 6\,O^{\times}_{O} + PbO(g)$
Acceptor doping with electronic compensation	$2\,PbO + A_2O_3 + \frac{1}{2}\,O_2(g) \xrightarrow{PZT} 2\,Pb^{\times}_{Pb} + 2\,A'_{Zr/Ti} + 6\,O^{\times}_{O} + 2\,h^{\bullet}$
Acceptor doping with ionic compensation	$2\,PbO + A_2O_3 \xrightarrow{PZT} 2\,Pb^{\times}_{Pb} + 2\,A'_{Zr/Ti} + 5\,O^{\times}_{O} + V^{\bullet\bullet}_{O}$

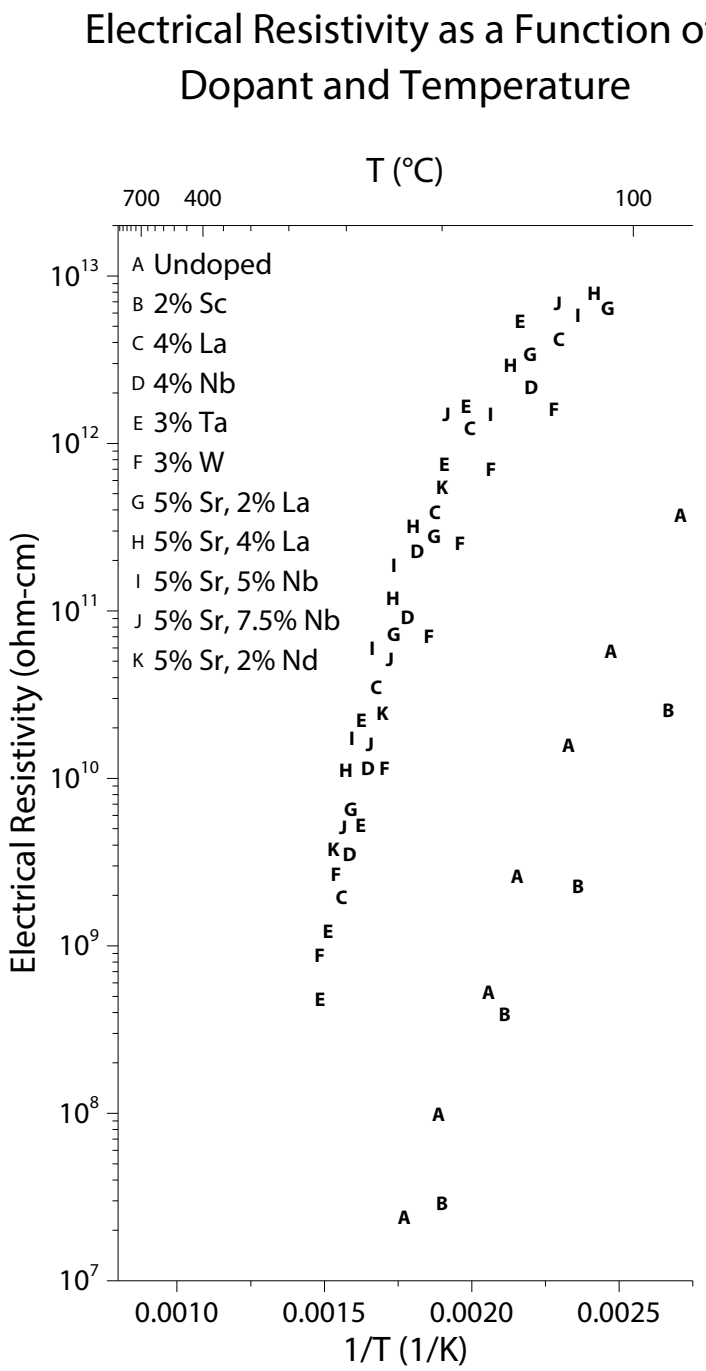

Figure 1.8: Temperature dependence of electrical resistivity of PZT ceramics as a function of dopant species and concentration replotted from Jaffe *et al.*[1,19] A is undoped PZT, B is acceptor doped, and C–K are donor doped. Furthermore, G-K have an isovalent substitution of 5% Sr on the A-site, in addition to donor doping.

increasing niobium content.[51,52] Additionally, Haccart *et al.* found an increase in fatigue resistance (by two orders of magnitude), the piezoelectric $d_{33,eff}$ and $e_{31,eff}$ coefficients, and the grain size, coupled with a decrease in conductivity as observed in bulk ceramics.[46] These results are corroborated by the work of Zhu *et al.* which demonstrated a maximum in the remanent polarization, and irreversible component of the Rayleigh behavior at 2 at.% Nb doping with a maxima in dielectric constant and reversible Raleigh component at 4 at.% Nb.[38] Haccart *et al.* and Al-Shareef *et al.* found increases in lifetime under DC electric fields of 2 orders of magnitude and a factor of 3, respectively, upon niobium doping.[46,53] Finally, Al-Shareef *et al.* demonstrated a reduction in leakage current density by three orders of magnitude with 3 at.% Nb doping.[53] Similarly to other authors, Akkopru-Akgun reported mean time to failure increased 14 fold upon increasing Nb doping from 0.5 at.% to 4 at.%. as well as a peak in $d_{33,eff}$ at 2 at.%. Additionally, aging rates were reported to decrease with increasing niobium doping.[54]

Despite the agreement of many authors, contradictory findings do exist within the literature. Ryder & Raman found no significant improvement in the fatigue resistance, and Aoki & Fukuda reported decreased fatigue resistance in niobium doped films as compared to undoped films.[55,56] Es-Souni *et al.* deposited films with high niobium doping levels (5-12 at.%) and found, that even in the case of 5 at.% doping, the remanent polarization was suppressed relative to an undoped film.[57] Comparatively, Haccart *et al.* found the remanent polarization in the 5 at.% doped films to be similar to that of the undoped film.[46] Additionally, Es-Souni *et al.* found the dielectric constant to be highest in films with 8 at.% Nb doping, while Haccart *et al.* found 2 at.% to yield a maximum. It is worth noting that Pereira *et al.* reported that the solubility limit of Nb within PZT is 7 at.%.[58] As niobium concentration was further increased, a pyrochlore or fluorite phase was detected via x-ray diffraction, in agreement with the findings of Klissurska *et al.*[51,52,58] However, phase pure, perovskite films with niobium doping levels as high as 13 at.%, produced via RF sputtering have been reported.[59,60]

Lanthanum doping has been demonstrated to increase properties in PZT thin films in a similar manner to niobium doping, while simultaneously dropping the Curie temperature. As a result, Zhu *et al.* found that different properties tended to peak at different doping concentrations, with dielectric permittivity, and remanent polarization, and the irreversible Rayleigh component α' peaking at 1 at. %, $e_{31,f}$ at 2 at.% and the reversible Rayleigh coefficient ε_{init} at 4 at.%.[38] Zhu *et al.* demonstrated a decrease in the temperature at which the maximum permittivity ($\varepsilon_{r,max}$) occurs in La doped PZT by −20 K/mol% from 0 – 2 mol% and −38 K/mol% from 2 – 4 mol%.[38] Comparatively, niobium doping decreases T_C by −5 – 9 K/mol%.[1,61] As a result of this, niobium doping was chosen in this work for the marked improvement in piezoelectric and dielectric properties and a reduction in current leakage while maintaining a high Curie temperature. The literature summary presented in Table 1.2 shows that, despite the disparity in reported results, 2 at.% Nb doping has been reported by a range of authors to maximize the dielectric constant, remanent and saturation polarization, and piezoelectric coefficients, while also increasing the lifetime under DC electric fields. Consequently, the niobium doped films in this work

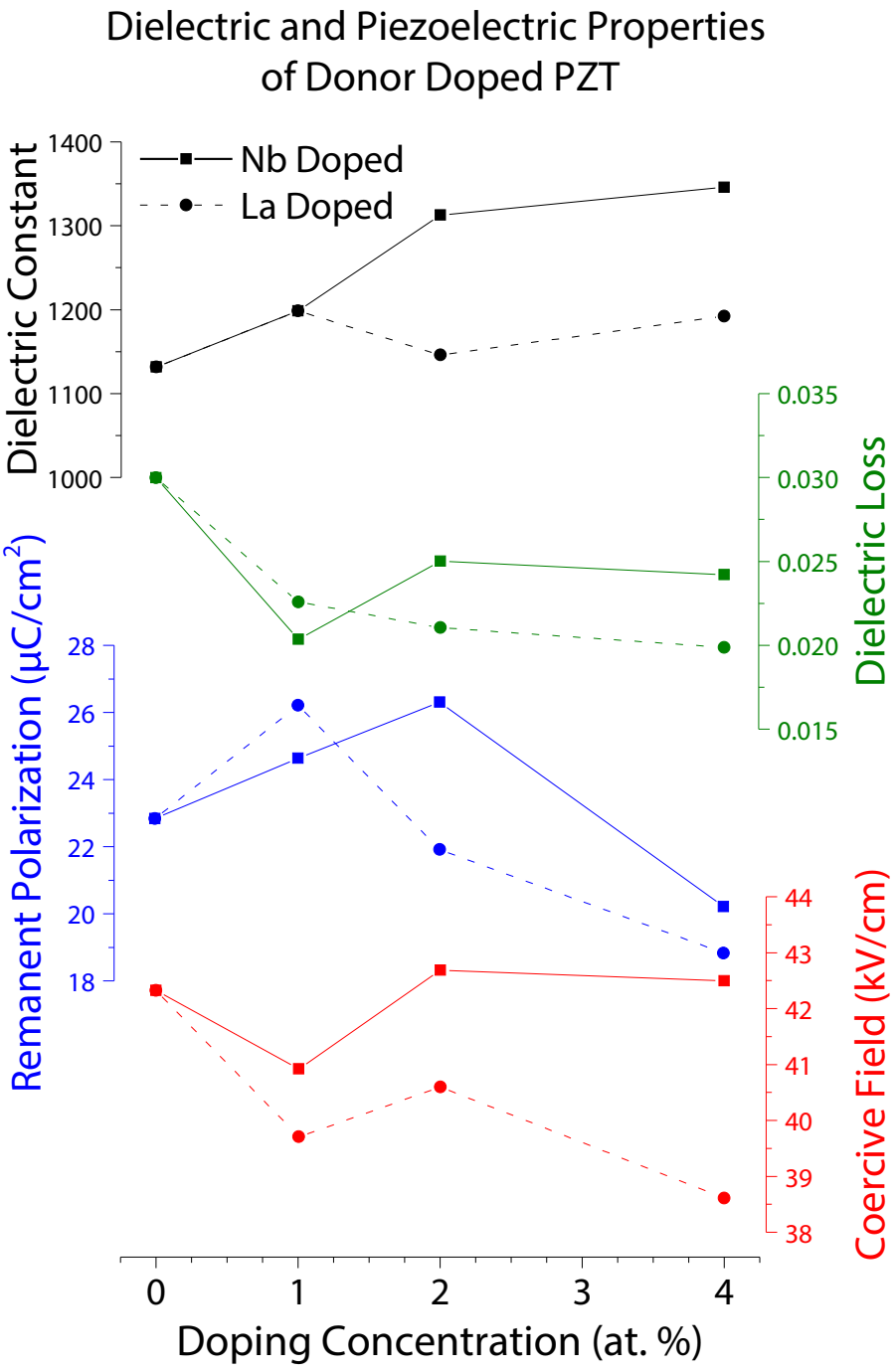

Figure 1.9: Dependence of dielectric permittivity, dielectric loss, remanent polarization and coercive field on the concentration of La or Nb dopant. Replotted data from Zhu *et al.*[19,38]

Table 1.2: Summary of literature findings on niobium doping of PZT thin films organized by property, observed change, and doping level.

Property	Observation
Dielectric Constant	Maxima: 1 at.%,[52] 2 at.%,[46] 4 at.%,[38] 8 at.%,[57] 13 at.%[60]
Loss Tangent (tan δ)	Maxima: 8 at.%,[57]
	Minima: 1 at.%[38], >12 at.%[57]
	Unchanged[46]
Remanent Polarization (P_r)	Maxima: 1 at.%,[51] 2 at.%[38,46,52]
	Decreased from 5 - 12 at.% with minima at 12 at.%[57]
Saturation Polarization (P_S)	Maxima: 2 at.%[46]
	Decreased from 5 - 12 at.% with minima at 12 at.%[57]
Coercive Field (E_c)	Maxima: <1 at.%,[55] 2 at.%[52]
	Minima: 4 at.%,[55] 8 at.%[57]
	Unchanged[38,50]
$d_{33,f}$	Maxima: 2 at.%[46,54]
$e_{31,f}$	Maxima: 2 at.%,[38] 7 at.%[46]
Lifetime	Increase 100 fold: 2 at.%,[46] 3 at.%[53]
	Increased by 14 fold: 4 at.%,[54]
	Unchanged[55]
Resistivity	Increase 1000 fold: 3 at.%,[53] >5 at.%[55]

used doping level of 2 at.%. Moreover, a doping level of 2 at.% is close the level utilized in PZT-5 soft ceramics (2.4 at.%).[1,62]

1.3.2 Acceptor Doped Lead Zirconate Titanate

Manganese is frequently used to acceptor dope lead zirconate titanate in order to reduce domain wall motion, increase retention of poling state, and reduce dielectric loss.[1] Zhang & Whatmore observed a −28.5 kV/cm internal bias field in poled 1 at.% Mn doped PZT 30/70, an increase over the −11.5 kV//cm internal bias field observed in poled undoped PZT 30/70. In separate work, they reported an internal bias field as large as −49 kV/cm in poled 1 at.% Mn doped PZT films.[64] Akkopru-Akgun reported internal fields of 25 kV/cm in 1% Mn doped PZT films, finding an activation energy for failure of 0.5 – 0.8 eV, similar to that of oxygen vacancy migration. Aging rates of 4.4% per decade at 180 °C were also reported, half of that observed in 2 at.% niobium doped PZT under the same conditions.[54]

Fatigue testing of Au/PZT/Pt capacitors with undoped and Mn doped PZT exhibited a reduction of the switching polarization after 10^4 cycles for undoped PZT, reaching 70% of the initial value by 10^8 cycles. Conversely, PZT with 1 at.% manganese doping did not exhibit fatigue until 10^8 cycles, with a 7% reduction in switching polarization by 10^{10} cycles.[63] In another work, Zhang *et al.* doped 30/70 PZT with 0, 0.2, 0.5, 1, 2, and 4 at.% manganese, finding increased fatigue resistance in the 0.2, 0.5, and 1 at. % doped samples, with undoped, 2, and 4% samples yielding similar fatigue levels.[65] Similarly, Akkopru-Akgun reported enhanced lifetime in 1 at.% Mn doped samples relative to 0.5 at.% Mn or 0.5-1 at.% Nb doped samples; 1% Mn and 2% Nb doping exhibited comparable lifetimes.[54]

These findings are in contrast to the expected defect reactions upon Mn doping (increase in $[V_O^{\bullet\bullet}]$), and the mechanisms for fatigue in perovskite oxides (postulated by some to be electromigration of $V_O^{\bullet\bullet}$, and pinning of domain walls by $V_O^{\bullet\bullet}$).[66–68] Variable-energy positron beam measurements indicated a decrease in the concentration of oxygen vacancy defects for low levels of manganese doping. Zhang & Whatmore attributed this to a change in the oxidation state of manganese compensating for a change of the Ti oxidation state from 4+ to 3+, which would typically result in the formation of oxygen vacancies.[65] Manganese has been verified to have oxidation states of 2+, 3+, and 4+ in PZT via electron spin resonance, with could allow for, in principle, charge compensation for defects via changes in oxidiation state.[69]

However, the explanation of Zhang & Whatmore does leave some ambiguity when the Gibbs free energies of formation (Figure B.2 and [70]) for the oxides of Mn and Ti are considered near 500 °C (the crystallization temperature used by Zhang & Whatmore).[63] Titanium should be fully oxidized in the 4+ state except at extremely low partial pressures of oxygen ($<10^{-50}$ atm) where some Ti ions may reduce to the 3+ state. However, at such low partial pressures of oxygen, any Mn in the system should be reduced to the metallic state (the equilibrium p_{O_2} for Mn^{2+} is $<10^{-42}$ atm).[70] Furthermore the films were crystallized on a hotplate in air where the p_{O_2} is 0.21 atm. While the carbon content in the amorphous

films can create a reducing environment upon crystallization,[71] it is unclear how Mn would change oxidation state to compensate for Ti^{3+} as all Ti ions should be in the 4+ state before Mn can change from the 2+ to 3+ or 4+ state.

One possible explanation is as follows: Ti^{3+} may exist in the undoped film creating oxygen vacancies. Upon manganese doping with a 3+ manganese precursor, the Mn^{3+} ions could reduce while the Ti^{3+} oxidizes, resulting in Mn^{2+} and Ti^{4+} (such ions could coexist at the same oxygen partial pressure according to the Ellingham diagram)[70]. If the Mn^{2+} proceeded to occupy the A-site, no charge imbalance would exist, requiring no compensating oxygen vacancies. While reports of Mn ions on the A-site do exist (as described in the next paragraph), it remains unclear if this explanation is any closer to that which Zhang & Whatmore meant to convey.

He & Li suggested that at low doping concentrations, Mn substitutes on the A-site rather than the B-site. In this case manganese would serve as a donor dopant in the 3+ state or an isovalent substitution in the 2+ state.[72] Similarly, Hennings & Pomplun found that at low p_{O_2} and p_{PbO} Mn^{2+} will occupy the A site while Mn^{3+} will occupy the A or B-sites in $PbTiO_3$. At higher p_{PbO}, Mn^{4+} will incorporate on the B-site of the $PbTiO_3$.[73] The ceramics produced by He & Li had no excess lead and were not embedded in any lead bearing powder during sintering. Futhermore, $MnCO_3$ was added directly to stoichiometric PZT powders, with no calcination prior to sintering.[72] It can be speculated that He & Li processed under low p_{PbO} with a possibility of low p_{O_2} as well, leading to the observed A-site occupancy of Mn. Expanding upon this, Xin *et al.* reported that the binding energy of Pb 4*f* XPS spectra shifted to higher binding energies for low doping levels (attributed to an increase in lead vacancies), and lower binding energies for high doping levels (attributed to an increase in oxygen vacancies) relative to an undoped film. Similarly they attributed an increase in the O 1*s* binding energy at low manganese doping levels to a change in the lattice volume as a consequence of Mn occupying the A-site.[49]

Zhu *et al.* characterized the dielectric nonlinearity of PZT doped with 1 or 2% manganese using Rayleigh analyses (see Section 1.4.1) finding decreases in the reversible and irreversible Rayleigh coefficients upon manganese doping. This indicates increased resistance to domain wall motion, attributed to substrate clamping and defects formed upon doping.[37]

1.4 Characterizing Dielectric Nonlinearity

Ferroelectric materials exhibit a nonlinear dielectric and piezoelectric response. In linear dielectrics or piezoelectrics, there is a linear relationship between polarization or strain and electric field. A perfect linear dielectric or piezoelectric without loss will have a straight line, while those with loss (via electronic, piezoelectric or elastic mechanisms)[74] will form an ellipsoidal loop. Ferroelectrics exhibit a lossy, non-linear dielectric response, which is represented by hysteresis loops.[1] A means of characterizing and quantifying nonlinearity allows for attribution of any changes to factors such as

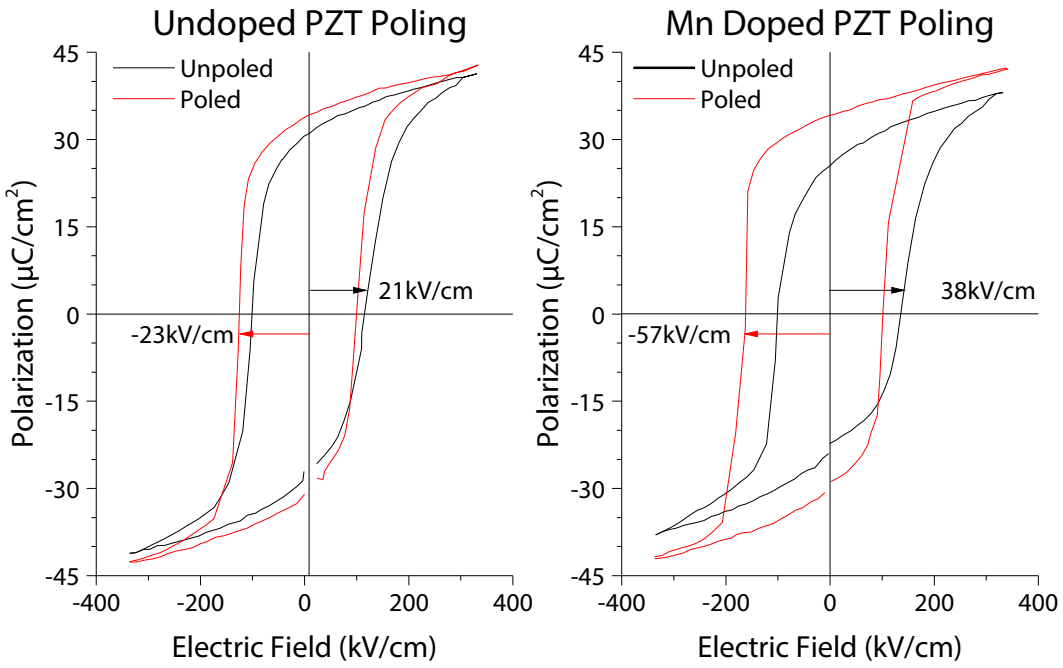

Figure 1.10: Hysteresis loops of unpoled and poled PZT thin films with and without manganese doping. Data replotted from Zhang & Whatmore.[19,63] In both cases the poled hysteresis loops are shifted relative to the unpoled hysteresis loops. The magnitude and direction of the hysteresis loop shift ($|E_{C+}| - |E_{C-}|$) in unpoled and poled states are represented by the arrows and accompanying electric field labels (arrows not to scale).

doping or thickness.[37,38,75] Methods for the characterization of nonlinearity include the Rayleigh Law and Preisach Analysis.

1.4.1 Rayleigh Analysis

Lord Rayleigh empirically demonstrated a quadratic relationship, later coined the Rayleigh Law, between the magnetization M and the magnetizing field H for ferromagnetic materials. The H-field was cycled between $-H_0$ and positive H_0 while remaining below the coercive field of the material. This took the form of Equation (1.5) for H decreasing from H_0 to $-H_0$ and Equation (1.6) for H increasing from $-H_0$ to H_0.[76]

$$M = \alpha H \pm \beta H_0^2 \left(1 - \frac{1}{2}\left(1 - \frac{H}{H_0}\right)^2\right) \tag{1.5}$$

$$M = \alpha H \pm \beta H_0^2 \left(-1 + \frac{1}{2}\left(1 + \frac{H}{H_0}\right)^2\right) \tag{1.6}$$

The Rayleigh Law was first applied for the analysis of domain wall contributions in piezoelectric ceramics by Damjanovic & Demartin, providing a means for quantification of domain wall motion.[77] The Rayleigh law for the piezoelectric d coefficient and the dielectric permittivity (ε) take the forms shown in Equations (1.7) and (1.8)

$$d = d_{init} + \alpha'_d E_0 \tag{1.7}$$

$$\varepsilon = \varepsilon_{init} + \alpha'_\varepsilon E_0 \tag{1.8}$$

The functional property measured at a given field (d or ε) is related to a reversible component (d_{init} or ε_{init}) and an irreversible component (α'_d or α'_ε) multiplied by the amplitude of an AC electric field (E_0). The reversible component is attributed to the intrinsic response of the lattice, as well as reversible domain wall motion. The irreversible component refers to irreversible domain wall motion. Additionally, in the case of lead zirconate titanate at the morphotropic phase boundary (of particular interest in this work) tetragonal and rhombohedral phases are present. The domain walls and rhombohedral/tetragonal (R/T) phase boundary interfaces are also capable of moving under an applied electric field.[77,78]

The physical basis of Rayleigh law and the values of the reversible and irreversible components are based on the spatial dependence of potential energy experienced by the moving boundaries. The potential energy of domain and R/T phase boundaries depends on, among other factors, local electric or elastic fields. As a consequence of the strain and electronic dependencies, any modifications to the local strain or electric fields in the material can interact with these interfaces. Features such as defects, dopants (or impurities), and grain boundaries will interact with domain walls and phase boundaries, creating spatial variation in the potential energy of the interfaces.[77]

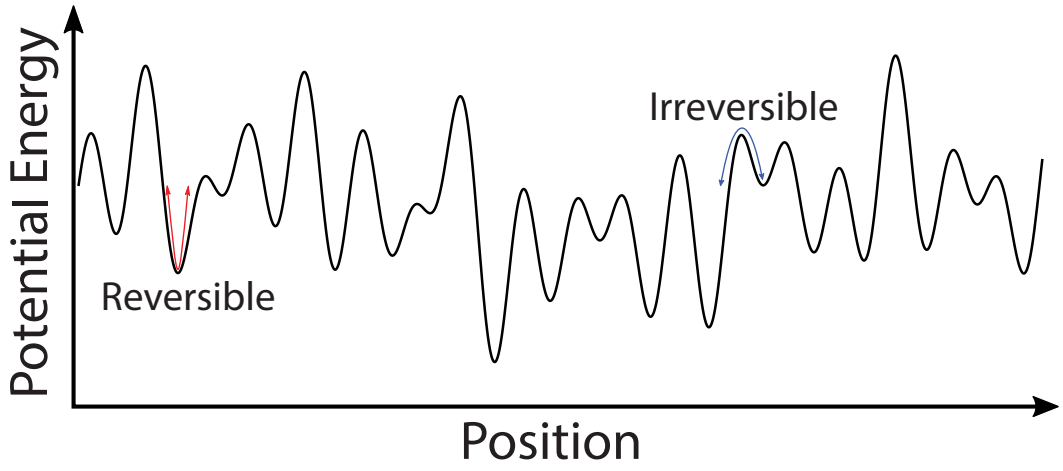

Figure 1.11: Spatial variation of potential energy allows for reversible motion (left) and irreversible motion (right) of phase boundaries with application of an electric field.

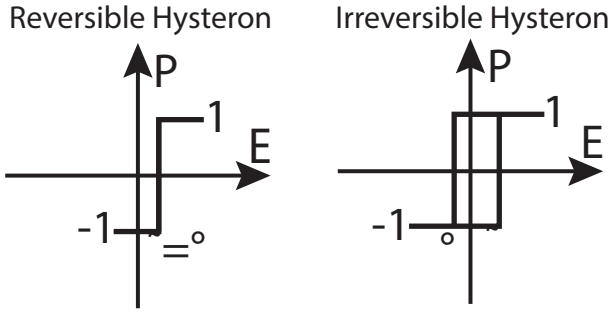

Figure 1.12: Schematic representation of reversible and irreversible hysterons.

Application of an electric field across the material can alter the potential energy landscape which interacts with the domain walls or phase boundaries (Figure 1.11). In the case of low electric fields, boundaries will reversibly oscillate within one potential well (red curve on left), returning to the local minimum when the electric field is removed. As the electric field increases, oscillations can become large enough that boundaries shift from one well to another irreversibly (blue curve on right). Further increases in the electric field allow for a larger fraction of boundaries to move irreversibly, increasing the total response of the material. The rate at which the response increases with electric field is quantified with α'.

1.4.2 Preisach Analysis Using First Order Reversal Curves (FORC)

Applicability of the Rayleigh law requires the assumption that sources of domain wall pinning are randomly distributed throughout the material with random pinning strengths. Additionally, it is assumed that domain structure retains a constant number of walls, precluding application of fields

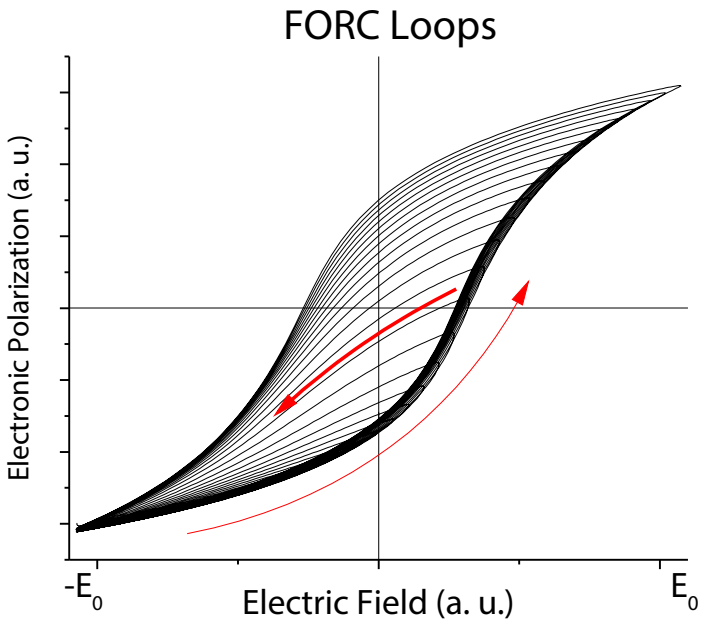

Figure 1.13: Example set of 40 FORCs measured in even spacings from $-E_0$ to E_0.

above the coercive field.[79] In the case of acceptor doped (hard) PZT, the dopants can serve as pinning centers. Often the dopants, or dopant-defect dipoles such as $Mn'_{(Ti,Zr)} - V_O^{\bullet\bullet}$, form internal bias fields in the material. As a consequence of internal bias fields within the material, the spatial dependence of the potential energy can deviate from a random distribution, as in Figure 1.11, to deep potential wells which heavily pin domain walls.[80] Consequently, relationships between the nonlinearity, quantified by the Rayleigh law, and the hysteretic response of the system are no longer valid as the assumption of randomness is no longer valid.[79,81]

The Preisach model, like the Rayleigh law, was originally developed for ferromagnetic materials but has subsequently been applied to piezoelectric and dielectric materials.[82–84] It serves as a valuable technique for examining nonlinearity induced by defect dipoles in hard ferroelectrics, as well as allowing analysis above the coercive field of the material.[37,38,78]

The basis of the model is the assumption that the net hysteresis loop of a ferroelectric (such as a P-E loop) can be modeled by the summation of rectangular hysteresis loops denoted as hysterons. Hysterons are characterized by switching fields α (different from α' in Rayleigh law) and β where there is an instantaneous and complete switching (due to the rectangular shape) from the current state to the up or down states respectively; thus $\alpha \geq \beta$. Hysterons can additionally be classified as reversible ($\alpha = \beta$) or irreversible ($\alpha > \beta$) as demonstrated in Figure 1.12. The Preisach distribution is the distribution of hysterons in electric field space (in terms of switching fields α and β). Plotted on a contour plot, the

reversible hysterons form a diagonal line along $\alpha = \beta$ while irreversible hysterons fill the area where $\alpha > \beta$. Contour values represent the density of hysterons of a particular α and β value.

One means of acquiring the necessary data to calculate the Preisach distribution of the material is by measuring a set of first order reversal curves (FORCs); a set of 40 evenly spaced curves is in Figure 1.13.[85] This method is advantageous as it allows for direct numerical measurement of the Preisach function rather than developing a mathematical function which describes the behavior of the particular ferroelectric being studied.[78] A large-signal hysteresis loop measures the aggregate properties of the material, providing no separation of different contributions to the polarization. The FORC technique has been successfully utilized in magnetic and electronic applications as a means of discerning the different contributions to the polarization including mixed phases or defect dipole-induced peak splitting for ferroelectrics.[37,38,78,86]

By analyzing the paths the material follows in polarization and electric field space, beginning from a state of polarization saturation, a distribution of hysterons can be calculated numerically. The precision of the distribution in electric field space will be limited by the dE and, by extension, the number of FORCs and their spacing. This can be demonstrated visually utilizing the set of four FORC curves presented in Figure 1.14 and the related Preisach distribution plots in Figure 1.15.

The four FORC loops sweep from $-E_0$ to E_0 in increasing intervals of $E_0/2$. All curves start at point A, where all switchable elements with $\beta > -E_0$ are polarized downward (gray). All curves then move to point B, where all elements remain polarized down except for those where $\alpha < -E_0/2$ (Region 1 of the bottom right schematic in Figure 1.15). In the case of the first loop, the system is then swept back to point A. The change in polarization associated with sweeping A to B and B to A is equivalent to the density of hysterons within region 1 having the condition $-E_0 < \beta \leq \alpha < -E_0/2$.

The second curve initally follows the same path as the first, moving from point A to point B, polarizing region 1 upwards. It then sweeps to point C, switching regions 2 and 5 upwards as well. The change in polarization associated with sweeping from point B to C is linked to the hysteron density in regions 2 and 5. Upon sweeping to point D, region 5 switches back to the down state, thus the polarization change from C to D is related to the hysteron density of 5. Finally, the sweep from D to A will switch both 1 and 2 downward. The hysteron density in region 1 is already known, thus the remainder of the polarization change associated with sweeping from D to A can be associated with region 2. A similar process can be followed for the remaining regions and FORC curves. In practice, the Preisach distributions (reversible and irreversible) are calculated. A rigorous derivation and demonstration of the necessary calculations can be found in Mayergoyz with application to ferroelectrics in Fujii.[78,85]

In the case of lead zirconate titanate, the primary contribution to the polarization originates from dipoles produced by ionic displacements. These displacements can be switched at electric fields similar in magnitude to that of the coercive field. The coercive field of the material represented in Figure 1.14 is

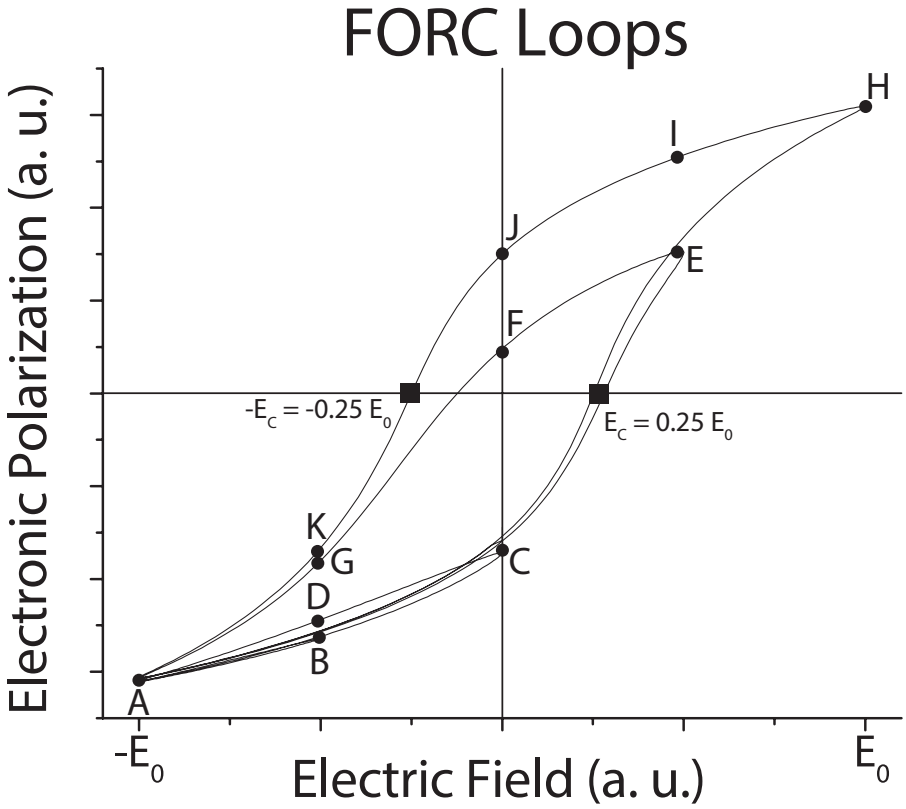

Figure 1.14: Four first order reversal curves collected from a ferroelectric specimen in intervals of $E_0/2$. The state of the Preisach distribution for each point denoted by a letter is depicted in Figure 1.15

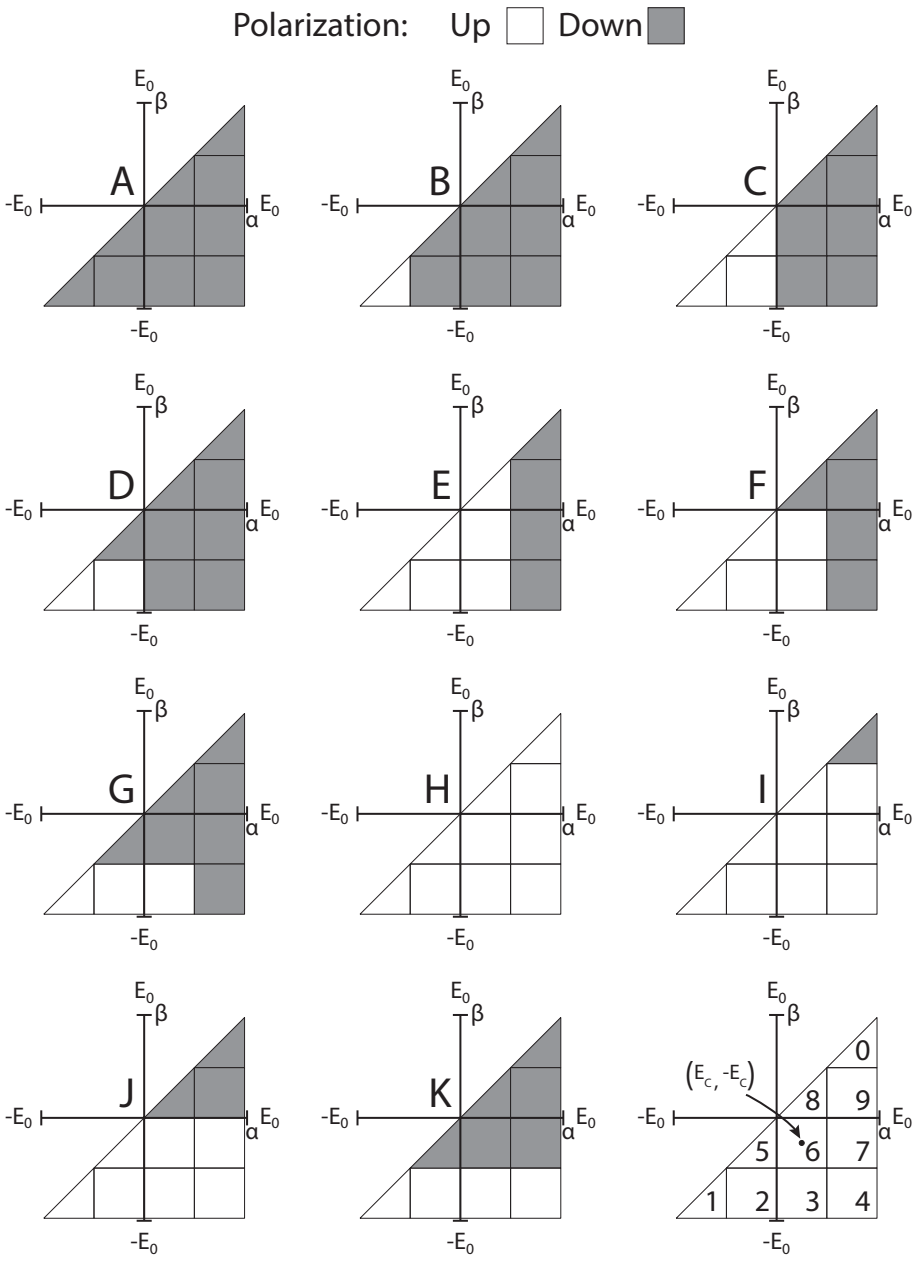

Figure 1.15: Switching state of the Preisach distribution at 11 points of interest, A-K. The letters represent points on the four FORC curves depicted in Figure 1.14. The numbers in the bottom right figure indicate the smallest, distinguishable, hysteron population regions (in electric field space) which can be calculated from 4 FORC loops. These region numbers are used in the text to describe how the first two FORC loops can calculate the hysteron populations in regions: 1, 2, and 5.

approximately $\pm 0.25E_0$, thus one would expect a peak in the Preisach distribution in region 6 where α is near the positive coercive field and β is near the negative coercive field.

In a material with numerous, aligned defect dipoles, local electric fields are present in regions of the material. If these local electric fields were oriented anti-parallel to an applied global field, some regions would require a higher global field in order to switch the polarization. This would result in the hysteron population splitting into two separate populations. For instance, if the local electric fields resisted the application of a positive global field, one might find that the distribution shifts towards region 9 in Figure 1.15. In practice, the number of FORC loops collected and the spacing between them (in electric field) will dictate what behaviors can be observed. In the case of Figures 1.14 and 1.15, the hysteron distribution is defined by regions which are $\sim 2E_c$ in breadth. As such, a shift on the order of $\sim E_c$ would be necessary in order to observe the hysteron distribtuion peak moving from one region to another (assuming it starts centered in the first region.)

1.5 Motivation, Thesis Organization, and Statement of Goals

An improved understanding of the link between the processing and properties in PZT thin film piezoelectric actuators is sought in this research project. Previous research has demonstrated that the properties of a PZT thin film are strongly influenced by composition, compositional uniformity, and crystallographic orientation. As discussed in this chapter, the maxima in piezoelectric and dielectric properties occurs at the morphotropic phase boundary (MPB), a compositional ratio near 52:48 Zr:Ti.[1] Integration of PZT thin films on platinized silicon substrates enables a broad range of microelectromechanical systems (MEMS). Developing preferential $\{0\,0\,1\}$ crystallographic texture in thin films on platinized silicon substrates, doping, and improving compositional uniformity all enhance the piezoelectric properties, and so is of interest for many devices.[26,28] However, an improved understanding of the way in which these factors affect the nucleation and growth of PZT thin films is needed.[87,88]

The literature on doping and compositional uniformity reveals data which range from strong agreement to divergence of results. Some strategies for property improvement have been combined in the literature, such as doped or gradient-free films which are also preferentially $\{0\,0\,1\}$ oriented. However, other areas, such as doped gradient-free films, are not widely discussed in the literature. Similarly, while doping with more than one element has been reported ([43, 89] among others), this prior work studied spatially uniform doping. This work serves as a means of understanding the effects preferential orientation, Zr/Ti compositional control (gradients), and spatially varying doping when combined within a single PZT thin film. The process of achieving preferentially oriented thin films with controlled Zr/Ti and doping gradients are outlined in the following chapters.

Of particular interest in this work is examining whether using separate regions of acceptor doped and donor doped PZT throughout the film thickness (graded doping) can serve as a means of combining the desirable characteristics of Mn and Nb doping within a single film. While Mn doped films suppress

the piezoelectric response of the film, the large, temporally stable internal field which can be developed is desirable for poling retention. Additionally, an enhancement in the lifetime of PZT films upon Mn is desirable for device longevity. Niobium doping can similarly enhance the longevity of PZT thin films, however it trades a large, temporally stable internal field for higher peak piezoelectric properties which age more rapidly with time.[54] By fabricating a PZT film with Mn doped and Nb doped layers, it may be possible to create a stable internal field by harnessing the re-orientable $Mn'_{Zr/Ti}-V_O^{\bullet\bullet}$ defect dipole and an increase in lifetime while benefiting from the enhanced piezoelectric response of Nb doped PZT.

Chapter 2 outlines the materials and methods utilized to deposit $\{0\,0\,1\}$ textured PZT seed layers and thin films via chemical solution deposition and the characterization of the resulting films. Chapter 3 demonstrates the effects of platinum microstructure, solution concentration, dopants, and solution lead excess content on the nucleation of highly $(1\,0\,0)$ textured PZT seed layers. With the understanding established within Chapter 3, the deposition of highly $(1\,0\,0)$ textured, niobium doped, gradient-free, PZT thick films is detailed in Chapter 4. The films described within Chapter 4 are electromechanically characterized in Chapter 5 with an emphasis on the piezoelectric response, poling behavior, and failure of films.

Chapter 2

Experimental Materials and Methodology

2.1 Chemical Solution Deposition (CSD) Materials

Commercial sol-gel solutions produced by Mitsubishi Materials Corporation (MMC) were utilized to prepare PZT seed layers with varying dopants, lead excess contents and solution concentrations. These solutions are less prone to gelation or precipitation relative to 2-methoxyethanol–based solutions, allowing for reproducible deposition conditions across a broad timespan.[55,90,91] This enabled a study of the role of dopants, solution concentration, solution lead content, and Pt microstructure on the resulting PZT properties, with fewer confounding variables.

The processing and chemistry of the 'E1' sol-gel solutions produced by MMC is described in the safety data sheets, patents, and limited journal publications. The 'E1' solutions are propylene glycol-based with 1-butanol as a diluent to control viscosity. Undoped, niobium doped (2 at.%), and manganese doped (1 at.%) PZT as well as undoped lead titanate were utilized. Within each of these categories, solution concentration (12-15 wt.% PZT, 1-10 wt.% PT), lead excess (10-17 at.% in PZT, 25-40 at.% in PT) and Zr/Ti ratio (from 60/40 to 44/56) were varied. These modifications allowed for increased control over thickness, adjustment of lead stoichiometry for phase purity, and control of compositional gradients in resultant films, respectively.[90,92–95]

In order to produce gradient free PZT films, multiple solutions with different Zr/Ti ratios must be utilized. Naturally, PZT thin films form a gradient which is titanium rich at the bottom and zirconium rich at the top of each crystallized layer. This gradient can be countered by imposing a gradient in the opposite direction in the amorphous film. In this work, three solutions were utilized per gradient free layer set with Zr/Ti ratios of 60/40, 52/48, and 44/56, in order, from bottom to top.

When needed to correct for a lead-deficient surface layer, a dilute lead oxide solution was applied to the top of a lead zirconate titanate thin films in order to convert surface pyrochlore or fluorite structures to the perovskite structure. This lead oxide solution was synthesized at a concentration 0.08 M using a 2-methoxyethanol solvent route described in Appendix A.[96]

2.2 CSD Deposition Process

Platinized silicon wafers were cleaned with acetone and isopropyl alcohol, dried with nitrogen, and finally heated on a hotplate at 100 °C in order to evaporate any residual solvent. Solutions were cast onto substrates using a spin coater (Brewer Science Cee 200X) following the generalized spin coating recipe outlined in Table 2.1; spin speeds of 1500 – 6000 rpm were used in this work to control the thickness of the layers. Upon completion of spinning, films were dried and pyrolyzed on hot plates followed by crystallization in a rapid thermal annealer. Hot plates with spatially varying temperatures (±15 °C across

Table 2.1: Typical spin coating process recipe

Step #	Speed	Acceleration to Step	Time
1	500 rpm	1500 rpm/s	5 s
2	1500 rpm	15000 rpm/s	2 s
3	Desired speed	15000 rpm/s	45 s
4	900 rpm	1500 rpm/s	1 s
5	0 rpm	1500 rpm/s	N/A

Table 2.2: Pyrolysis conditions for PZT

Parameter	Condition
Temperature 1 (°C)	100
Time 1 (s)	60
Temperature 2 (°C)	300
Time 2 (s)	240

Table 2.3: Crystallization conditions for PZT

Parameter	Condition
Ramp Rate (°C/s)	10
Temperature (°C)	700
Hold Time (s)	60
Atmosphere	O_2
Gas Flow (slpm)	2

the surface) were covered with a 3/8" carbon steel plate in order to reduce this variation to ±3 °C across the surface, enabling uniform pyrolysis of large (wafer scale) samples. A consequence of the increased thermal mass and heat loss resultant from adding the steel plate required setting hotplates as high as 100 °C above the desired temperature. In order to verify the surface temperature, a digital thermometer and surface thermocouple probe (HH11B & 88006 respectively – OMEGA Engineering) were used to measure the temperature at multiple points across the surface.

The thermal processing parameters for deposition of seed layers were primarily adapted from reported parameters in Doi *et al.*[97] Typical values for this work are shown in Table 2.2. While Doi *et al.* reports use of a single pyrolysis temperature (e.g. 300 °C for 5 min), in this work, a 100 °C drying step for 1 min was added to prevent porosity development induced by rapid evaporation of solvent, as shown in Table 2.2. Large (6") wafers bowed upwards when placed on hotplates. In order to ensure spatially uniform pyrolysis, the edges of wafers were pushed downward with tweezers until the wafer remained flat without any applied force; at this point the timer for pyrolysis was started.

Finally, pyrolyzed films were crystallized in a rapid thermal processor/annealer (RTP/RTA) (Allwin21 Corp AW 810 RTP) with a silicon carrier wafer utilized for piece parts. Temperatures in the RTP were measured via a thermocouple in contact with the bottom of the wafer. A summary of common thermal processing parameters utilized in this work can be seen in Tables 2.2 and 2.3. These parameters were utilized for all deposition steps unless otherwise specified.

2.3 Structural Characterization

The crystallographic texture of the Pt and PZT films was assessed with x-ray diffraction using the Bragg-Brentano geometry (X'pert Pro MPD or Empyrean, utilizing PIXcel detectors in 1D strip mode – PANalytical). Copper K_α radiation generated at 45 kV and 40 mA was utilized with divergence slit set to 1/4° and anti-scatter slits set to 1/2°. Scans were in the range of 10 – 90 °(2θ) with a step size of 0.0263° and collection times of 100 s or 15 s per step for collection of quantitative and qualitative data, respectively. Orientation quality was semi-quantified using the Lotgering factor (f) as defined in Equation (2.1):[98]

$$f = \frac{\frac{\sum I_{HKL,film}}{\sum I_{hkl,film}} - \frac{\sum I_{HKL,PDF}}{\sum I_{hkl,PDF}}}{1 - \frac{\sum I_{HKL,PDF}}{\sum I_{hkl,PDF}}} \tag{2.1}$$

where $\sum I_{HKL}$ represents the summation of the integrated intensity of peaks associated with a desired $\{HKL\}$ orientation and $\sum I_{hkl}$ represents the summed integrated intensities of all peaks present. 'Film' refers to peaks from the film while 'PDF' represents values taken from the powder diffraction file (PDF)# 01-070-4060 in the International Center for Diffraction Data PDF 4+ 2014 database.[99] Data from the PDF file serves to normalize the textured film data against a randomly textured sample. The XRD pattern from the PDF file can be found in Figure B.1.

The out of plane orientation distribution of highly textured thin films was measured via rocking curves. Samples were irradiated with monochromatic Cu K_α x-rays in on a 4-circle diffractometer with 1/4° divergence slits (X'pert Pro MRD with a 4 bounce Ge(2 2 0) monochromator and Xe proportional detector – PANalytical). Films with low x-ray scattering intensities (such as 30 nm Ti or 50 nm TiO_2) were scanned with a step size of 0.02° in ω and a counting time of 1 s, while samples with high x-ray scattering intensities (such as Pt or PZT) were scanned with steps of 0.005 °ω and counting times of 0.2 s. Increased counting times for samples with low x-ray scattering enhanced signal to noise ratio, while smaller step sizes yielded no improvement to data quality. The full-width at half-max (FWHM) of rocking curve peaks were measured utilizing a Gaussian fit within Data Collector (PANalytical) or Origin (OriginLab).

Micrographs were acquired by field emission scanning electron microscopy (FESEM) (Merlin, Leo, and Sigma – ZEISS Microscopy) operating at accelerating voltages of 5 kV using in-lens secondary electron detectors and working distances near 2.5 mm. Compositional analysis was collected with energy dispersive spectroscopy (EDS) (X-Max^N 80 mm^2 – Oxford Instruments) on the ZEISS Sigma. A working distance of (8 ± 1) mm was utilized to maximize EDS signal strength with an accelerating voltage of 10 kV in order to capture spectra of all elements of interest. Grain size was quantified by drawing lines across the micrograph (as in the line intercept method) and measuring the diameter of each grain intersected by the lines via ImageJ. Films were presumed to be columnar, so no multiplication factor was employed.

Nanoscale surface topography was measured via atomic force microscopy (Dimension Icon with Scanasyst-Air tips – Bruker Corporation). Data were collected in PeakForce Tapping mode with 1 nN of tapping force, a scan rate of 0.977 Hz, and a scan size of 2 µm × 2 µm measured across 512 lines. Due to the smoothness of many samples, the height range (z-range within software) was reduced from over 10 µm to 1 µm in order to reduce noise associated with the resolution of the analog to digital converter.

Film thickness was measured via contact profilometry (KLA-Tencor P16+) across an etched step in the film and confirmed with cross sectional micrographs. To pattern the etch steps, Microposit S1800 series photoresists (Dow Electronic Materials) were applied via cotton swab to the surface of the film, leaving an approximately 1 cm × 1 cm region of the film exposed. The photoresist was cured at 100 °C until dry. PZT was etched with a combination of 10:1 ([40% w/w NH_4F] : [49% w/w HF]) buffered oxide etch, and hydrochloric acid (36% w/w HCl).[100] BOE was applied until a droplet covered the entire exposed region. The droplet was immediately wiped off with an HCl coated swab followed by rinsing the sample in deionized (DI) water. The process was repeated until the reflective platinum electrode was observed. After the bottom electrode was exposed, the photoresist was removed with acetone and isopropyl alcohol. The exposed region allowed thickness measurements and provided access to the bottom electrode for electrical measurements.

2.4 Electrical Characterization

Platinum top electrodes were patterned via a photolitographic lift-off process. LOR-5A (Microchem) photoresist was dynamically dispensed on a sample spinning at 900 rpm, followed by spinning at 4000 rpm for 45 s and baking at 180 °C for 2 min. A layer of SPR3012 (Dow Electronic Materials) was spun with the same conditions and baked at 95 °C for 1 min on top of the LOR-5A layer. The pattern was exposed on a contact mask aligner (MA/BA6 – Süss Microteec) for 7 s at a power density of 8 mW/cm². The exposed photoresist was developed in MF CD-26 developer (1-5% Tetramethylammonium hydroxide (TMAH) in water – Dow Electronic Materials) for 2 min, followed by rinsing with DI water.

Any remaining photoresist or residue within the patterned features was removed via an oxygen plasma ash (M4L – PVA TePla America). Gas flows of 50 sccm He and 150 sccm O_2, a pressure of 550 mTorr, and an RF power of 200 W for 1 min were used for the ashing process. Immediately after the oxygen plasma ash, the sample was loaded into a sputter system (CMS-18 – Kurt Lesker), and platinum was deposited with DC magnetron sputtering, following the parameters outlined in Table 2.4. The platinum-coated, patterned photoresist was lifted off by submersion in acetone and gentle agitation, leaving behind platinum in the patterned features. After the lift-off process, isopropyl alcohol was used to remove any remaining residue. The top electrodes were finally annealed at 500 °C for 1 min in an RTA with no gas flow (ambient chamber conditions).

Table 2.4: Platinum deposition parameters for lift-off top electrodes

Parameter	Condition
Pt target size	75 mm
Pt target purity	99.99%
Target-to-substrate distance	150 mm
Temperature	∼25 °C
Power	200 W
Pressure	2.5 mTorr
Gas flow	11 – 12 sccm Ar
Growth Rate	2.4 Å/s
Thickness	100 nm

All measurements, unless otherwise specified, were collected on 500 µm diameter top electrodes driven from the bottom electrode.[(I)] Dielectric properties were measured with an LCR (4284A – Hewlett Packard or E4980A – Agilent Technologies / Keysight). Dielectric constant frequency sweeps, and verification of good contact for other measurements were conducted with a 1 kV/cm excitation signal. Rayleigh measurements were taken on the E4980A as the greater excitation signal precision allowed for 1 kV/cm electric field steps regardless of sample thickness. Three electric field sweeps 1 – 30 kV/cm were taken at each frequency. Linear regressions of the Rayleigh data were generated with Python scripting under the following conditions: 6-20 data points were included in the fit, and the starting point of the fit was constrained to fall in the range of 2 – 4 kV/cm.[(II)] The second and third sweeps were fit under the same conditions and the R^2 value's were averaged; where the "best" fit maximized this value.

Ferroelectric hysteresis loops were measured at 500 kV/cm on a multipurpose ferroelectric test system (Precision Premier II – Radiant Technologies, Inc.) with a frequency of 100 Hz. A preset pulse with the same conditions was performed prior to the measurement pulse, with 10 ms of separation between the pulses.

A picoamp meter (4140B - Hewlett Packard) was used to measure leakage currents in steps of 0.5 V with a hold for 60 s at each voltage, allowing the current reading to stabilize. Breakdown strength was defined as the point at which the measured current increased 100-fold. Failure strengths were measured

[(I)] The standard deviation in thickness measurements across all thick film samples were ∼1% of the thickness. All measurements were performed in the same colored region near the center of the film. The standard deviation of the electrode sizes was ∼0.5% of the electrode area. Thus, the summation of errors associated with electrode area and thickness uncertainty is ∼1.5%.

[(II)] The combination of the number of data points in the fit and the starting field limited fits to the field range of 2 – 24 kV/cm. The Rayleigh behavior was found to exist up to ∼23 kV/cm in all thick film samples. No significant variation in the maximum field (relative to electrode to electrode variation of ±1 kV/cm) was observed as a function of lead content or the presence of thin Mn doped layers.

with a picoamp meter. The applied voltage was increased by 0.5 V every 1 s while watching the top electrode for evidence of failure (cracking and/or burning of the film), at which point the current voltage was recorded. Probe stations with a hot stage (Micromanipulator, Cascade) were used in conjunction with the picoamp meter (4140B) to pole top electrodes. The sample was heated to 150 °C and the field applied for the specified amount of time. At this point the sample was cooled, under field, until the stage reached $\leq$40 °C, at which point the field was removed.

The piezoelectric $d_{33,f}$ coefficient was measured with a double beam laser interferometer (aixDBLI – aixACCT Systems). All measurements on the aixDBLI are measured by driving the top electrode and measuring the bottom electrode. The small signal piezoelectric response was measured with a 1 kHz 500 mV excitation signal and DC bias steps of 2 kV/cm up to 100 kV/cm. The large signal piezoelectric response was measured with unipolar 100 kV/cm triangle waves at 100 Hz. Measurements consisted of 1 prepolarization pulse followed by 100 averaged measurement pulses with a 1 second delay between all pulses.

2.5 Platinized Silicon Substrates

Platinized silicon wafers for this work were either fabricated at Penn State or sourced from the U.S. Army Research Laboratory (ARL) or XP. Substrates for which the platinum was deposited at elevated temperature 500 – 600 °C will be referred to as HT. XP also deposited platinum at room temperature; these samples are labeled XP RT. Wafers metallized at PSU were prepared following the work of Fox *et al.* with 30 nm of titanium, as described in detail below.[101] ARL platinized Si wafers were processed according to methods outlined in Potrepka *et al.*[102]

For Pt bottom electrodes prepared at Penn State, polished (1 0 0) silicon wafers served as the starting substrates. In most cases, 0.5 – 1 µm of SiO_2 was grown thermally via wet oxidation, creating a smooth, amorphous surface which favors deposition of hexagonal close-packed (HCP) titanium with strong (0 0 0 1) texture.[101] Some XP HT platinized silicon substrates had 80 nm of alumina serving as a buffer layer between the SiO_2 and TiO_2 layers. Titanium serves as an adhesion layer, increasing the bonding of the platinum electrode on the substrate. XP, ARL, and Penn State deposited titanium via sputter deposition in thicknesses from 21 – 30 nm. The parameters for each deposition are outlined within Table 2.5. Oxidation of the (0 0 0 1) titanium adhesion layer has been demonstrated to convert the metal to rutile with (1 0 0) texture.[101,102] Titanium was oxidized in an rapid thermal annealer by both Penn State and XP, while the U.S. Army Research Lab oxidized in a tube furnace. In both cases, the (0 0 0 1) Ti was converted to strongly (1 0 0) textured rutile (TiO_2). The oxidation processing parameters are outlined within Table 2.6. The resulting strongly-oriented TiO_2 serves as a templating layer favoring the deposition of highly {111} textured platinum.[88,101,103]

In order to assess similarities and differences between different bottom electrodes, studies of each layer in each process were conducted. It was found that titanium adhesion layers, as deposited by ARL,

Table 2.5: Titanium deposition parameters for platinized silicon wafers

Substrate	PSU	ARL	XP RT & HT
Deposition tool	Kurt J. Lesker CMS-18	Unaxis (Oerlikon) Clusterline 200	
Ti target size	75 mm	270 mm	314 mm
Ti target purity	99.99%	99.99%	99.995%
Target-to-substrate distance	150 mm	50 mm	65 mm
Power	200 W	500 W	1500 W
Pressure	2 mTorr	3.8 mTorr	
Gas flow	8-9 sccm Ar	30 sccm Ar	
Thickness of Ti	30 nm	21 nm	23 nm

have a uniform spherical grain morphology, with grains 20 nm in diameter (See Figure 2.1 (a)). Titanium deposited at Penn State and by XP exhibit no clear morphology to the detection limits of FESEM analysis. Upon oxidation, TiO_2 microstructures are visible via FESEM for all suppliers (Figure 2.1). The grain structure of titanium sourced from ARL coarsens a small amount upon oxidation in the tube furnace, yielding grain sizes from 25 – 35 nm. While no Ti microstructure could be resolved for XP's or PSU's samples, upon oxidation a coarse TiO_2 microstructure develops with grain sizes of 40 – 60 nm. The difference in TiO_2 grain size was suspected to be induced either by the starting titanium grain structure, or the difference in oxidation treatment (tube furnace vs RTA) between ARL and the other sources. To determine which of these factors was dominant, ARL Ti was oxidized at PSU following PSU's oxidation process (Table 2.6). The resulting TiO_2 microstructure was similar to that of ARL Ti oxidized at ARL. This suggested that the microstructure of the Ti layer prior to oxidation controlled the microstructure of the resulting TiO_2 film.

Table 2.6: Titanium oxidation conditions for platinized silicon wafers

Substrate	PSU	ARL	XP HT
Oxidation tool	Rapid thermal annealer	Tube furnace	Rapid thermal annealer
Temperature	700 °C	750 °C	730 °C
Gas flow rate	10 slpm O_2	10 slpm O_2	10 slpm O_2
Heating rate	20 °C/s	10 min insertion / removal from hot zone	30 °C/s
Time	15 min	30 min	5 min

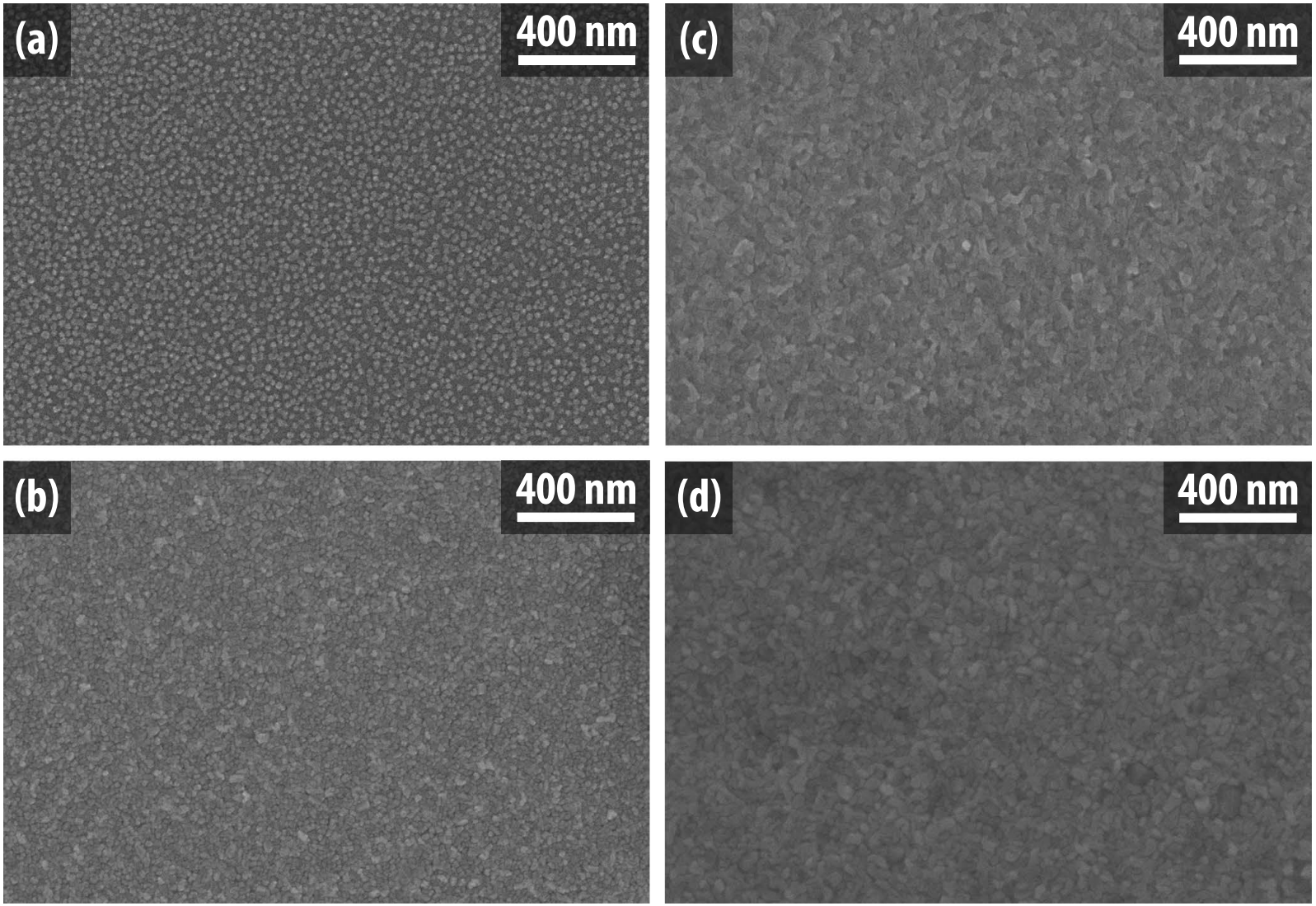

Figure 2.1: Micrographs of titanium and titanium dioxide adhesion layers prior to platinization. (a) ARL Ti, (b) ARL TiO_2, (c) PSU TiO_2, (d) XP TiO_2

Table 2.7: Rocking curve FWHM and surface roughness of Ti and TiO_2 adhesion layers. RMS is the root mean square roughness while "range" is the height range in the AFM scans.

Source	FWHM (°ω)		Surface Roughness (nm)			
	Ti (0 0 0 2)	TiO_2 (2 0 0)	Ti RMS	Ti Range	TiO_2 RMS	TiO_2 Range
PSU	∼5.8	∼3.7	0.2 ± 0.03	2.5 ± 0.5	1.52 ± 0.03	13.5 ± 0.8
ARL	∼5.3	∼3.4	0.25 ± 0.01	2.4 ± 0.4	1.35 ± 0.01	12.3 ± 0.1
XP	∼5.1	∼3.1	0.26 ± 0.01	2.5 ± 0.1	1.35 ± 0.05	12.7 ± 0.3

All Ti and TiO_2 films show phase pure XRD patterns (Figures B.4 and B.7) with strong (0 0 0 1) or (1 0 0) texturing respectively. The rocking curve FWHM decreases in all cases by almost 2° upon oxidation from Ti to TiO_2 (Figures B.5 and B.8), in agreement with the work of Fox *et al.*[101] Topography measurements via AFM (Figures B.6 and B.9) show an increase in roughness upon oxidation from circa 0.25 nm to 1.3 nm, as summarized in Table 2.7.

Finally, highly (111) textured platinum was DC sputtered either at room temperature onto Ti, or at elevated temperature (500 – 600 °C) onto TiO_2 adhesion layers. Thicknesses of the sputtered platinum films range from 100 – 200 nm, dependent on the source. Detailed process parameters are outlined in Table 2.8.

X-ray diffraction scans of the as-received platinum-coated Si substrates deposited are presented in Figure 2.2. In all cases strongly {111} oriented platinum was deposited. Platinum peak widths and intensities are similar for all HT Pt wafers; those deposited at reduced temperature exhibit a lower, broader peak. The peak position of the {111} Pt is shifted to lower 2θ angles for room temperature platinum relative to high temperature platinum, indicating a larger out of plane d-spacing. At elevated temperatures, Pt has a higher lattice parameter than at room temperature due to thermal expansion ($8.8 \times 10^{-6}\,K^{-1}$ at room temperature and $10.4 \times 10^{-6}\,K^{-1}$ at 500 – 600 °C).[104] Upon cooling, the platinum will attempt to contract but this is mechanically resisted by the low thermal expansion silicon substrate ($2.6 \times 10^{-6}\,K^{-1}$ at room temperature and $4.2 \times 10^{-6}\,K^{-1}$ at 500 – 600 °C),[105] placing the film under in-plane tensile strain. Poisson's ratio states that a lateral elongation (in-plane) will be countered by a transverse contraction (out-of-plane). As a result, it is expected that the out-of-plane interplanar spacing (d_{111}) would be smaller for platinum deposited at elevated temperature, thus diffracting at larger 2θ values.

Rocking curve measurements of the Pt {111} peaks were also collected; FWHMs are presented in Table 2.9. A decrease in FWHM was observed from room temperature platinum to ARL platinum, and finally to XP and PSU HT Pt, which were similar in value. This suggests that high temperature deposition allows for better control of the out of plane texture. Further refinement of the orientation quality is

Table 2.8: Platinum deposition parameters for platinized silicon wafers

Substrate	PSU	ARL	XP HT	XP RT
Deposition tool	Kurt J. Lesker CMS-18	Unaxis (Oerlikon) Clusterline 200		
Pt target size	75 mm	270 mm	300 mm	300 mm
Pt target purity	99.99%	99.99%	99.99%	99.99%
Target-to-substrate distance	150 mm	50 mm	57 mm	57 mm
Power	200 W	500 W	500 W	500 W
Pressure	2.5 mTorr	3.8 mTorr	1.3 mTorr	
Gas flow	11 – 12 sccm Ar	50 sccm Ar	30 sccm	
Growth rate	2.4 Å/s	16.4 Å/s	11.8 Å/s	11.8 Å/s
Substrate temperature	600 °C setting ∼525 – 550 °C actual	500 °C setting	500 °C actual	∼25 °C
Pt deposition thickness	100 nm	100 nm	165 nm	200 nm

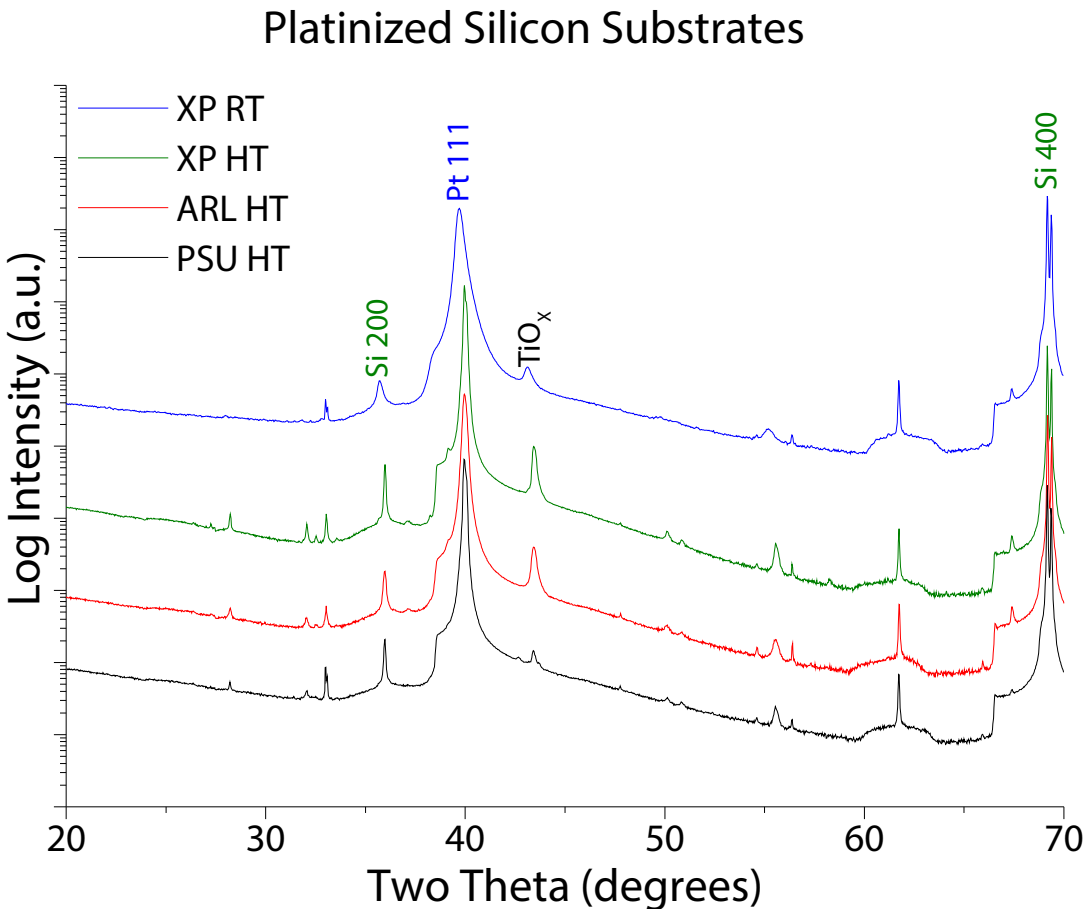

Figure 2.2: XRD scans of platinized silicon wafers as deposited by PSU, ARL, and XP. Unlabeled peaks are additional substrate peaks, arising from secondary wavelengths or phases in the adhesion layers, which are present in all substrates.

Table 2.9: Summary of structural characteristics of platinized silicon wafers

Pt Wafer	Roughness (nm)	Z Range (nm)	Pt {111} FWHM (°)	Grain Size (nm)
ARL	1.7 ± 0.1	12 ± 1	2.5 ± 0.3	80 ± 20
XP HT	1.2 ± 0.1	11 ± 0.5	1.6 ± 0.2	180 ± 50
XP RT	1.0 ± 0.1	11 ± 2	4.7 ± 0.5	25 ± 5
PSU	1.7 ± 0.3	17 ± 2.5	1.9 ± 0.3	160 ± 50

observed in XP and PSU HT Pt. Potrepka *et al.* observed a positive correlation when comparing TiO_2 (2 0 0) FWHM and the Pt {111} FWHM. Based on the observed TiO_2 (2 0 0) FWHM's of 3.7, 3.4, and 3.1 for PSU, ARL and XP respectively, one would expect Pt {111} peak widths to follow the same order. This is not the observed case, indicating that both the underlying TiO_2 layer (as observed by Potrepka *et al.*), and Pt sputtering conditions may be influencing the Pt {111} FWHM.

FESEM micrographs of all Pt bottom electrodes are presented in Figure 2.3. Grains of platinum deposited at elevated temperature (80 – 180 nm in lateral scale) are significantly larger than those deposited at room temperature (25 nm grain sizes). Additionally, the grain size of ARL HT Pt (c) is smaller than PSU or XP's HT Pt. The change in grain size from RT to HT platinum was attributed to the elevated temperature, allowing for grain coarsening during deposition due to increased thermal energy. This is in agreement with the structure zone model, which states that an increase in deposition temperature from a T_{dep}/T_{melt} of ∼0.1 to ∼0.4 will be accompanied by a densification of grain boundaries and some grain coarsening due to increased adatom mobility.[106] Additionally, HT Pt was deposited on larger grained TiO_2 adhesion layers rather than Ti adhesion layers, which could, in principle alter the nucleation kinetics. The underlying TiO_2 adhesion layers also exhibited a change in grain size between suppliers, which could lead to a change in nucleation and thus grain size. HT Pt electrodes which were deposited by ARL showed smaller grain sizes (by a factor of 2-3) to XP and PSU samples. It is unknown what the actual substrate temperature is at ARL. Following the trend observed at PSU and XP it is suspected that ARL's actual deposition temperature may be below the 500 °C setting, however other deposition parameters could also be responsible for the difference in grain size. AFM topography measurements (Figure B.11) found XP's wafers to be the smoothest while PSU and ARL were rougher, as summarized in Table 2.9. Similarly, PSU's HT Pt had an increased z-range.

Simultaneous sputtering on multiple substrate pieces was investigated in order to determine if the TiO_2 layer or sputtering conditions governed the grain size and orientation quality of the resulting Pt film. High temperature platinum was simultaneously deposited on pieces of TiO_2 films from PSU, XP, and ARL as well as pieces of Ti films from XP and ARL which were oxidized at PSU. Micrographs of the resulting films all exhibited the same grain structure as is pictured in Figure 2.3 (d). This indicated

that the Pt grain structure was controlled by the specific process parameters of the high temperature Pt deposition, rather than the underlying adhesion layers. Rocking curve measurements of the Pt {111} peak on all TiO_2 samples with HT Pt deposited at PSU were the same, within the margin of error. This suggests that the particular sputtering process is the dominating factor in the FWHM of the Pt {111} peak.

2.5.1 Conclusions on Platinum Metallization of Silicon Wafers

Deposition of platinum at elevated temperature yielded an increase in the grain size and a narrowing of the orientation distribution of Pt {111} planes in the Pt bottom electrodes. The orientation quality of the underlying Ti/TiO_2 adhesion layer impacts the FWHM of the {111} peak in the resultant Pt film. As the orientation distribution of grains in the adhesion layer becomes narrower, the FWHM of the Pt which templates from it also decreases. It was demonstrated that the resultant Pt grain microstructure is dependent on the HT Pt deposition process, with negligible influence from the adhesion layer. The exact cause of the difference in grain size between ARL and XP or PSU HT Pt has yet to be determined. Parameters such as actual deposition temperature, deposition rate, and sputtering pressure may play a role in the microstructural development and warrant further investigation (see Proposed Future Work).

As will be shown in subsequent sections: stable, reproducible processing conditions have a strong impact on the quality of the final PZT film. Films deposited by XP exhibited the most stable microstructural and crystallographic properties from sample to sample. ARL's samples, deposited in a dedicated tool at a government lab, had a stable microstructure and roughness but exhibited an increased orientation distribution as indicated by the Pt {111} FWHM. Films deposited in PSU's user facilities (on tools which are not dedicated to one particular process) show the largest variations of all the HT platinum varieties. As a result, XP's or ARL's Pt was used in the remainder of this work to minimize electrode-induced variations in the processing of PZT layers.

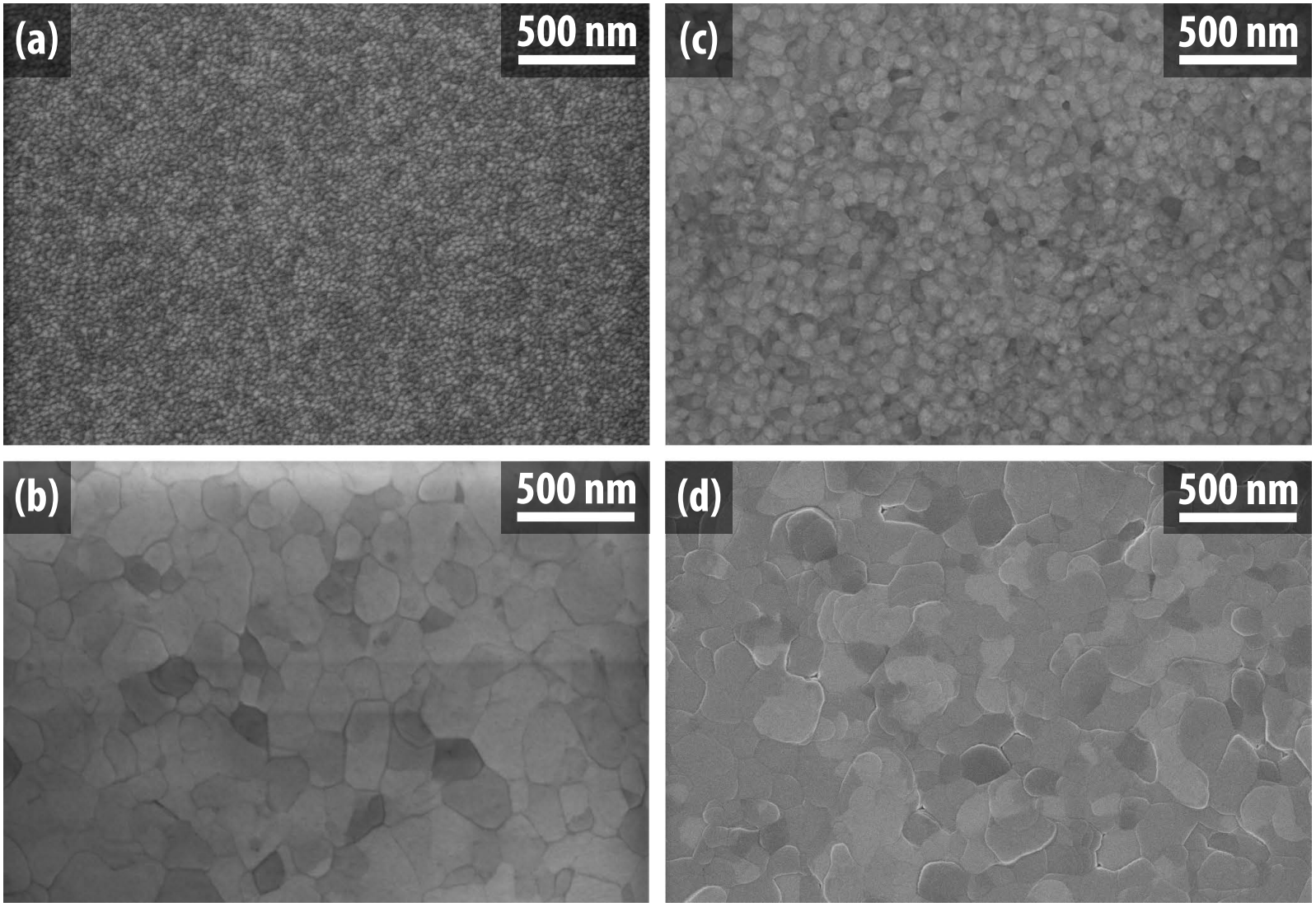

Figure 2.3: SEM micrographs of platinized silicon wafers as deposited by PSU, ARL, and XP. (a) XP RT, (b) XP HT, (c) ARL HT, (d) PSU HT

Chapter 3

Textured Seeding of Doped Lead Zirconate Titanate Thin Films via Chemical Solution Deposition

3.1 Introduction

$PbTiO_3$ seed layers can be used to impart strong crystallographic texture to PZT thin films[107]; the use of lead rich $PbTiO_3$ has been widely adopted for deposition of highly {0 0 1} textured PZT thin films.[29,97,107–111] Fewer reports have been made on the seeding of {0 0 1} textured PZT thick films directly on platinized silicon, with no intermediary layer of another material. Sanchez *et al.* demonstrated enhanced preferential {1 1 1} orientation of PZT on platinum-coated silicon substrates, for which the Pt was deposited at 500 °C as described by Potrepka *et al.*[102,112] Doi *et al.* demonstrated a method for preferential {0 0 1} orientation with an approximately 60 nm thick PZT seed layer on platinum deposited at room temperature.[97] Finally, Chen & Chen and Kalpat & Uchino demonstrated control of PZT texture through thermal processing conditions as summarized within Table 3.1.[113,114]

The available literature has not clarified the influence of the Pt deposition conditions on the quality of the resulting orientation for PZT films grown without a $PbTiO_3$ seed layer. Fox *et al.* demonstrated that the density, roughness, and orientation distribution of the Pt underlayer has a profound influence on the orientation of resulting {1 1 1} PZT layers deposited directly on platinum.[101] Similarly, Sanchez *et al.* found improved {0 0 1} texture in $PbTiO_3$-seeded PZT on Pt surfaces with narrow orientation distributions (e.g. Pt {1 1 1} FWHM less than 3° in ω)). In contrast, PZT deposited without a $PbTiO_3$ orienting layer had enhanced {0 0 1} texture on substrates with a wider orientation distribution.[112] The findings of Sanchez *et al.* and Fox *et al.* suggest that the suitability of Pt surfaces with narrow orientation distributions for preferential texturing of PZT depends on both the PZT composition and the desired orientation. In both studies, a single PZT deposition solution of MPB composition, with 10 at.% excess lead, was utilized. Hence, it is interesting to explore whether comparable effects are observed in different

Table 3.1: Summarized findings of Chen & Chen and Kalpat & Uchino on the impacts of thermal processing conditions on preferential orientation development

Chen & Chen[113]	Kalpat & Uchino[114]
Heating rates of 10 – 30 °C/s favor {1 1 1} PZT, lower rates favor {1 1 0} PZT	Slowest heating rate (40 °C/s) favors {0 0 1} PZT, higher rates favor {1 1 1} PZT
Pyrolysis at 400 – 550 °C favors {0 0 1} oriented PZT	Crystallization profiles which pause at 550 °C for 30 s favor {0 0 1} while those without a pause for nucleation favor {1 1 1}

Table 3.2: PZT seed deposition parameters used for platinum microstructure and deposition temperature study

Parameter	Specifications
Substrates	XP (RT & HT), ARL (HT)
Solution	12 wt.% PZT 52/48 with 10 at.% excess Pb
Spin Speed (rpm)	3500
Thermal Processing	Tables 2.2 and 2.3

compositions of PZT nucleated directly on Pt electrodes with a broad range of deposition conditions. Thus, one goal of this research was to determine whether the Pt deposition conditions and the resultant orientation distributions affect the nucleation and growth of {0 0 1} PZT seed layers with variations in doping, lead stoichiometry, and layer thickness.

In this chapter, the effects of platinum deposition temperature and grain size on the orientation and structure of PZT seed layers was studied as a function of the solution doping, lead excess content, and seed layer thickness. After an understanding of the factors which control nucleation was established, these principles were applied to the growth of thick films in Chapter 4.

3.2 Platinized Substrate Microstructure and Deposition Temperature

As discussed, dense, highly {1 1 1} textured Pt thin films, sputter deposited at elevated temperature (500 – 600 °C) have been reported to improve the orientation of PZT films.[101,112,115] However, many reports on high temperature platinum, including those by Potrepka *et al.,* Sanchez *et al.,* Ea Kim *et al.*, and Fox *et al.*, are limited to discussing platinum deposited at one temperature, from one sputter tool.[101,102,112,115] In many cases, the primary analysis reported is x-ray diffraction.[101,102,112] The data summarized in Table 2.9 show substantial differences in the microstructure of platinum deposited at different temperatures or by different sources. The impact of these changes to the platinum surface on the nucleation of {0 0 1} textured PZT thin films, deposited under the same conditions, has yet to be demonstrated.

The range of platinized silicon substrates available for this work enabled two primary areas of study to increase the understanding of how the platinum bottom electrode affects the nucleation of {0 0 1} PZT. First, significant changes in the density, grain size and orientation distribution of platinum surfaces can be investigated by comparing XP RT Pt to the range of HT Pt bottom electrodes. The role of grain size of the high temperature platinum surface can be understood by comparing nucleation on ARL's HT Pt against HT Pt from XP. The two factors were investigated following the parameters outlined in Table 3.2.

X-ray diffraction patterns of PZT seed layers on each type of platinized silicon wafer are shown in Figure 3.1. For these processing conditions, the XRD patterns show predominantly perovskite peaks; the

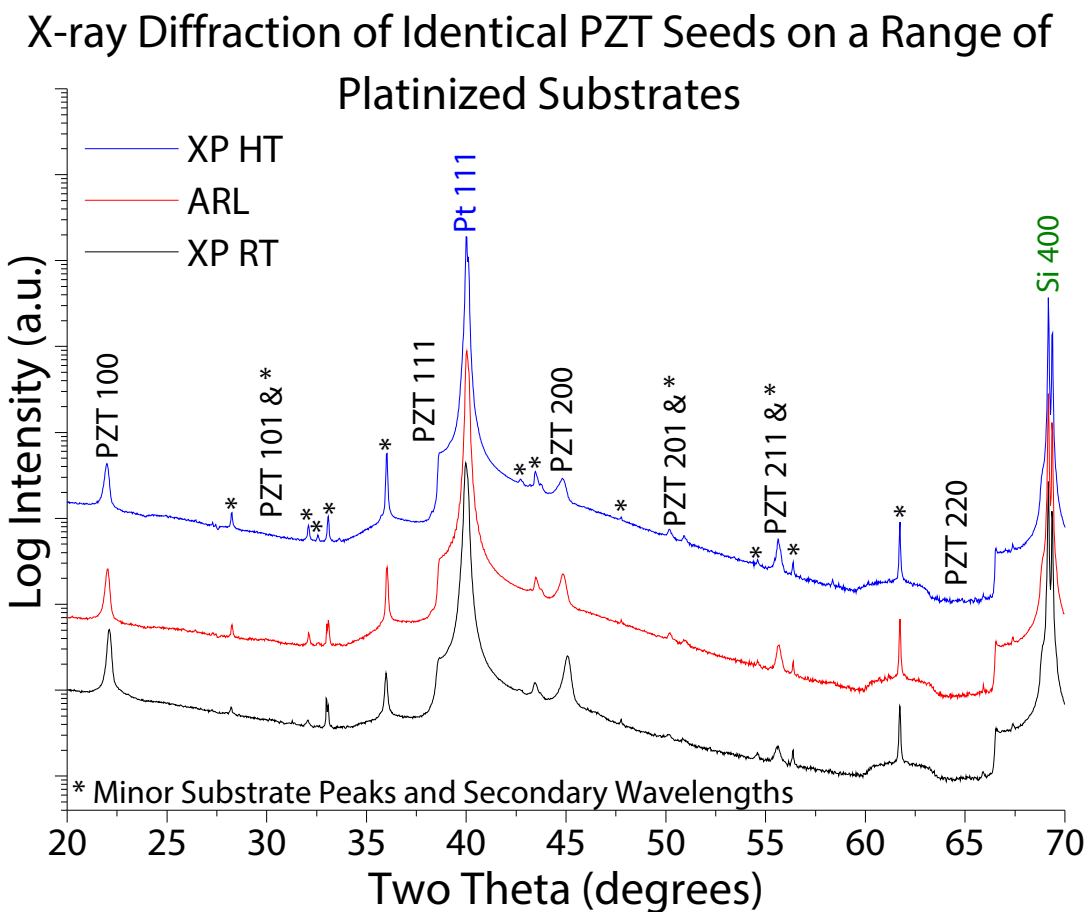

Figure 3.1: X-ray diffraction patterns collected from PZT seed layers of equal thickness (∼55 nm), composition (52Zr/48Ti) and lead excess (10 at.%) deposited on three sources of platinized wafers.

resulting films are similar in orientation quality. The apparent perovskite peaks for the {2 0 1} and {2 1 1} planes are from the substrate (Figure 3.2). In all seed layers depicted in Figure 3.1, the intensity of these peaks did not change by more than the intensity variations present within multiple patterns collected on the same sample. As such, the only perovskite PZT peaks present in this sample are {0 0 1} or {0 0 2}, yielding a Lotgering factor near or equal to 1. This same method of comparison will be utilized for all future samples even though figures such as Figure 3.2 may not be presented. In future plots, only PZT peaks which are actually present within the film will be labeled, rather than all peaks.

A comparison of the peak intensities of the {1 0 0} and {2 0 0} PZT peaks, relative to the background, shows that the XP RT wafer has a slightly higher intensity than either of the high temperature Pt wafers. This agrees with the findings of Sanchez *et al.*, who found that {0 0 1} orientation was enhanced on Pt surfaces with wider orientation distributions. Rocking curve measurements of the {0 0 2} peak

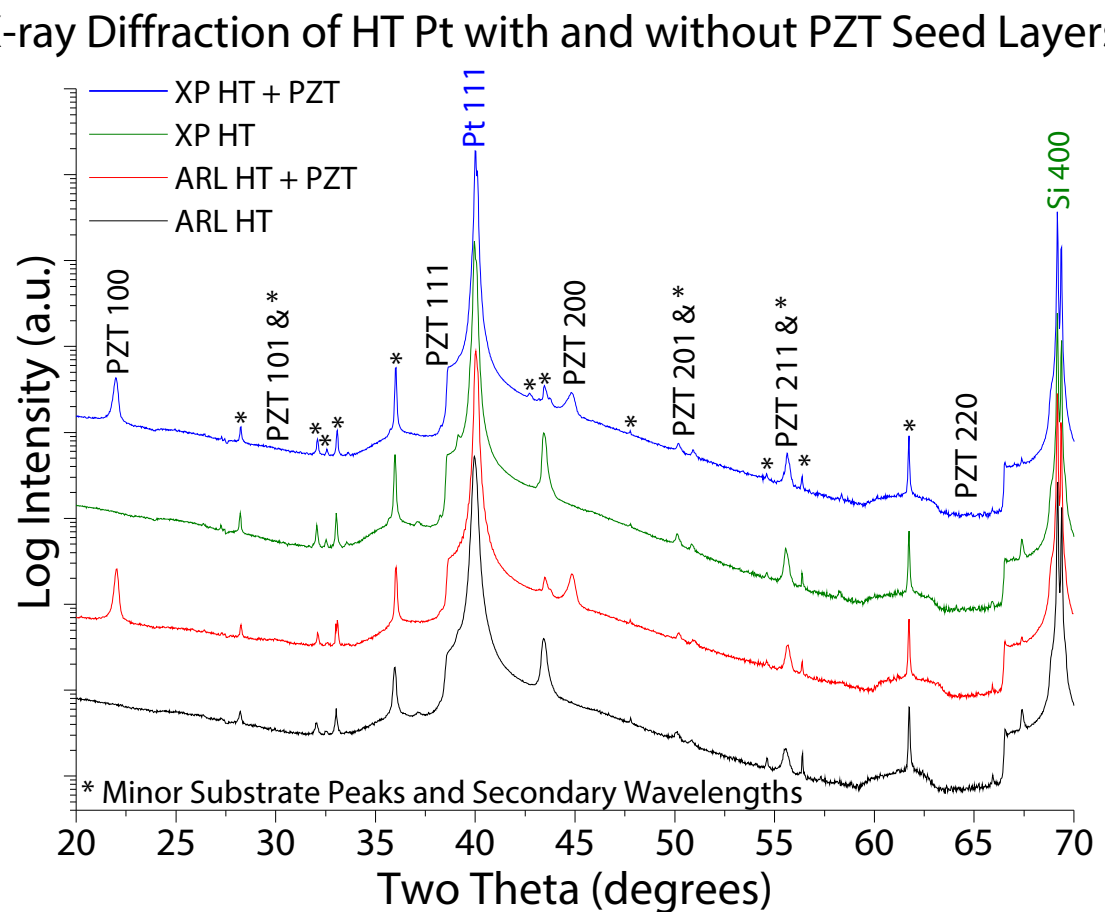

Figure 3.2: X-ray diffraction patterns collected from PZT seed layers (Figure 3.1) and patterns collected from the underlying platinized silicon substrates (Figure 2.2). Peaks located at the PZT {2 0 1} and {2 1 1} positions do not change in intensity upon deposition of PZT, indicating that the peaks originate from the substrate.

(Figure B.12) indicate that the differences in peak intensity are not a function of sample misalignment during the Bragg-Brentano scan.

Micrographs (Figure 3.3) show multiple structural differences between the films deposited on room temperature and high temperature platinum bottom electrodes. First, the grain size increased substantially between RT and HT platinum, from PZT grains averaging (100 $\pm$ 25) nm in diameter to grains averaging (300 $\pm$ 100) nm in diameter. Additionally, it is apparent that there are pockets of very

fine-grained material which corresponds to a pyrochlore[(I)] phase. The area fraction of pyrochlore was much smaller (from ∼50% to ∼7%) when platinum deposited at elevated temperature is utilized.

In comparing HT Pt from different sources, there is a small increase in the maximum grain size observed in PZT deposited on ARL relative to XP HT Pt. Furthermore, some pyrochlore regions on ARL HT substrates had lateral dimensions in excess of 1 µm while regions on XP HT were generally limited to the order of 500 nm.

While the quality of PZT orientation does not appear to change significantly (as quantified with Lotgering factor) between room temperature and high temperature platinum; there are substantial microstructural differences between seed layers on platinum deposited at different temperatures. The PZT seed layer grain sizes varied by a factor of three despite the grain size of the underlying platinum bottom electrode varying by a factor of seven with changes in deposition condition.

One reported motivation for the use of high temperature platinum is that the increased density can reduce lead diffusion from the amorphous PZT film into the platinum electrode and layers beneath it.[101] Lead rich conditions are favorable for the nucleation of PZT on {111} oriented Pt as evidenced by the use of lead rich $PbTiO_3$ or PbO seeding layers.[75,87,109] While high concentrations of lead at the Pt – amorphous PZT interface are desirable for nucleation, the concentration gradient at the interface can cause lead diffusion into the substrate layers, often along Pt grain boundaries.[118,119] Small levels of diffusion and reducing conditions can lead to the formation of transient Pt_3Pb phases, while substantial levels can lead to formation of a lead deficient secondary phase (pyrochlore).[88,120]

In the case of XP's RT platinum, the small grain size (25 ± 5) nm leads to a high density of grain boundaries. Additionally, Ti from metallic adhesion layers is reported to diffuse into the Pt and oxidize, widening the grain boundaries.[103] The small resultant perovskite grain size suggests a high nucleation density while significant amounts of pyrochlore indicates that substantial lead loss is occurring in PZT seeds deposited on room temperature platinum with titanium adhesion layers, in agreement with the literature.[103] While, lead deficient conditions are less favorable for nucleation of perovskite PZT[87], the small grain size of the underlying platinum deposited at RT can provide a high density of nucleation sites. Inability to convert lead deficient pyrochlore to the perovskite phase may also limit the growth (and final size) of grains, further reducing the grain size; this is investigated further in Section 3.3.

High temperature platinum from ARL and XP have grain sizes which vary by a factor of two to three. Deposition at elevated temperatures will allow for grain growth and increased densification of the Pt film relative to room temperature platinum. The larger grains of XP HT combined with the slower, post-Pt-deposition cooling rate may hinder the diffusion of lead into the platinum relative to substrates from ARL. The average perovskite grain size is relatively similar on both ARL platinum and XP HT (within ∼20%)

[(I)] Lead deficient PZT can take on a disordered fluorite structure or the pyrochlore structure, a 2 x 2 x 2 fluorite structure which is both oxygen vacancy and cation site ordered.[116,117] While crystallographically distinct, both forms are lead deficient phases convertible to perovskite when adequate additional lead oxide is supplied. Within the context of this work, both phases will be referred to as pyrochlore.

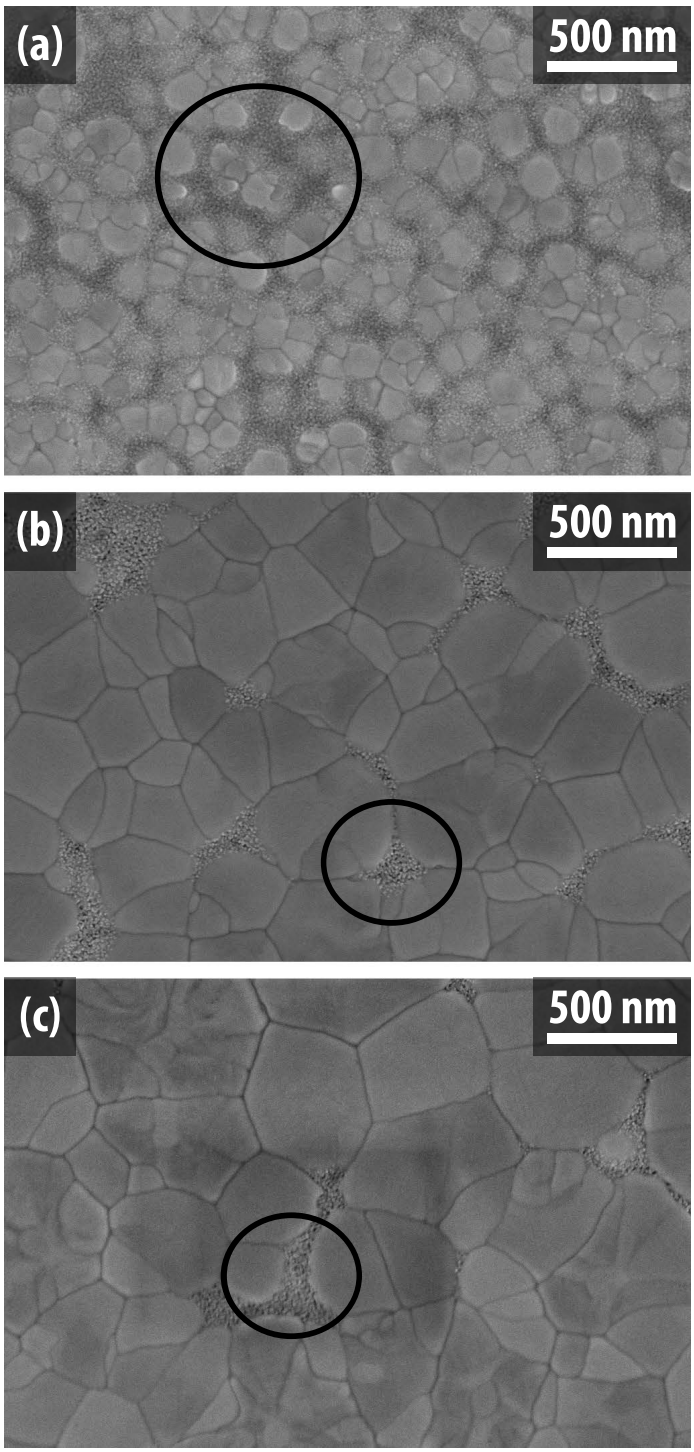

Figure 3.3: Micrographs from PZT seed layers of equal thickness (∼55 nm), composition (52Zr/48Ti) and lead excess (10 at.%) deposited on three sources of platinized wafers. (a): XP RT, (b): XP HT, (c): ARL HT. Circled regions contain pyrochlore with a very fine microstructure.

Table 3.3: Parameters used for lead excess content study

Parameter	Specifications
Substrates	XP (RT), ARL (HT)
Solutions	12 wt.% PZT 52/48 with 10, 12, 14, or 16% excess Pb
Spin Speed (rpm)	3500
Thermal Processing	Tables 2.2 and 2.3

when compared to PZT deposited on RT Pt. This observation suggests that any increased lead diffusion into the ARL substrate does significantly impede nucleation or enhance growth of perovskite grains relative to that of the XP HT substrate. Lower lead diffusion rates in HT Pt relative to XP RT reduces stabilization of lead deficient pyrochlore, and is consistent with the better perovskite phase purity in the PZT seed layer. This is consistent with the volume fraction of pyrochlore observed, which, in the case of HT Pt, is lower ($\sim$5% compared to $\sim$40%) and clustered together rather than spread more uniformly across the surface.

Changes in the platinum deposition temperature result in large changes in grain size and pyrochlore content of resultant PZT films. Platinum bottom electrodes deposited at RT allows for more lead diffusion into the bottom electrode and thus exhibit increased pyrochlore content. Furthermore, a decreased perovskite grain size is observed which may result from an increased nucleation density, grain growth inhibition by pyrochlore or a combination of both factors. In contrast, there does not appear to be any difference as a consequence of HT Pt grain size (changed by a factor of 2) or Pt 111 FWHM (changed from $\sim$1.6° to $\sim$2.5° in ω).

3.3 Lead Excess in Solution

Lead rich conditions have been demonstrated to enhance the nucleation of perovskite grains from {111} Pt.[87,109,119,121] As such, many techniques involve the use of lead rich conditions to seed highly {0 0 1} textured perovskite materials, including use of lead oxide,[109,122,123] lead rich $PbTiO_3$[97,108], and simultaneous use of lead oxide and lead titanate.[109] Studies on CSD film growth on platinum bottom electrodes sputtered at high temperatures by Fox *et al.* and Sanchez *et al.* were limited to a single solution composition, containing 10 at.% excess lead. In order to achieve lead rich nucleation conditions, the solution lead excess content is typically increased by 15 – 30 at % when utilizing a $PbTiO_3$ seed layer[97,108]. The amount of lead enrichment is more difficult to quantify in the case of PbO undercoats.[109,122,123] In this work, the impact that small increases in lead concentration (6 at.%, rather than the 15 – 30 at % increases commonly used in $PbTiO_3$[97,108]) will be assessed.

Table 3.4: Pyrochlore content (area fraction in percent) as a function of lead excess

Lead Excess	Platinized Substrate	
(at.%)	ARL HT	XP RT
10	5.6	42
12	6.5	39
14	5.2	33
16	4.9	30

Table 3.5: PZT grain size as a function of lead excess

Lead Excess	Platinized Substrate	
(at.%)	ARL HT	XP RT
10	(620 ± 230) nm	(140 ± 30) nm
16	(640 ± 190) nm	(130 ± 40) nm

In Section 3.2, the dominant factor in the microstructural development of PZT seed layers was demonstrated to be the deposition temperature of the platinum electrode. Changes in pyrochlore concentration indicate significant differences in the kinetics of lead loss between RT and HT Pt. Seed layers deposited on RT and HT Pt were both well $\{0\,0\,1\}$ oriented despite differences in grain size and surface pyrochlore concentration on by factors of $\sim$ 4 and $\sim$ 6 respectively. The small grain size of PZT deposited on XP's RT Pt may occur due to either a higher nucleation density, pyrochlore inhibiting grain growth, or a combination of both. Thus, it is of interest to examine if small additions of lead to the solution chemistry can alter the grain size and pyrochlore concentration of PZT seed layers on RT Pt. Similarly, the low pyrochlore content of films on HT Pt was attributed to the dense bottom electrode inhibiting lead diffusion. Small increases of lead in solution may reduce the presence of pyrochlore regions. With these theories in mind, the role of lead content in the texture and microstructural development of PZT seed layers deposited on XP's RT Pt and ARL's HT Pt was examined (Table 3.3)

X-ray diffraction data (Figures 3.4 and 3.5) yield similar results to those in Section 3.2; the PZT diffraction peaks from XP RT wafers are more intense than those from ARL wafers and all seed layers are highly $\{0\,0\,1\}$ textured. No apparent change is observed in the patterns collected from seed layers on XP RT Pt with changes in lead content. Conversely, in seed layers deposited on ARL HT Pt, those utilizing solutions with 10 or 12 at.% lead excess have a small pyrochlore peak while those with 14 or 16 at.% have more intense $\{0\,0\,1\}$ PZT peaks. The presence of a pyrochlore peak in two of the eight films within this section may be attributable to changes in the coherent scattering length of the fine grained material.[124]

The microstructures of the films (Figure 3.6) with varying lead content on various substrates also yield similar results to Section 3.2; room temperature platinum yields a smaller grain size with a higher concentration of surface pyrochlore compared to HT Pt. On RT Pt substrates, the area fraction of pyrochlore in PZT seed layers decreases substantially with increases in lead excess (Table 3.4). This

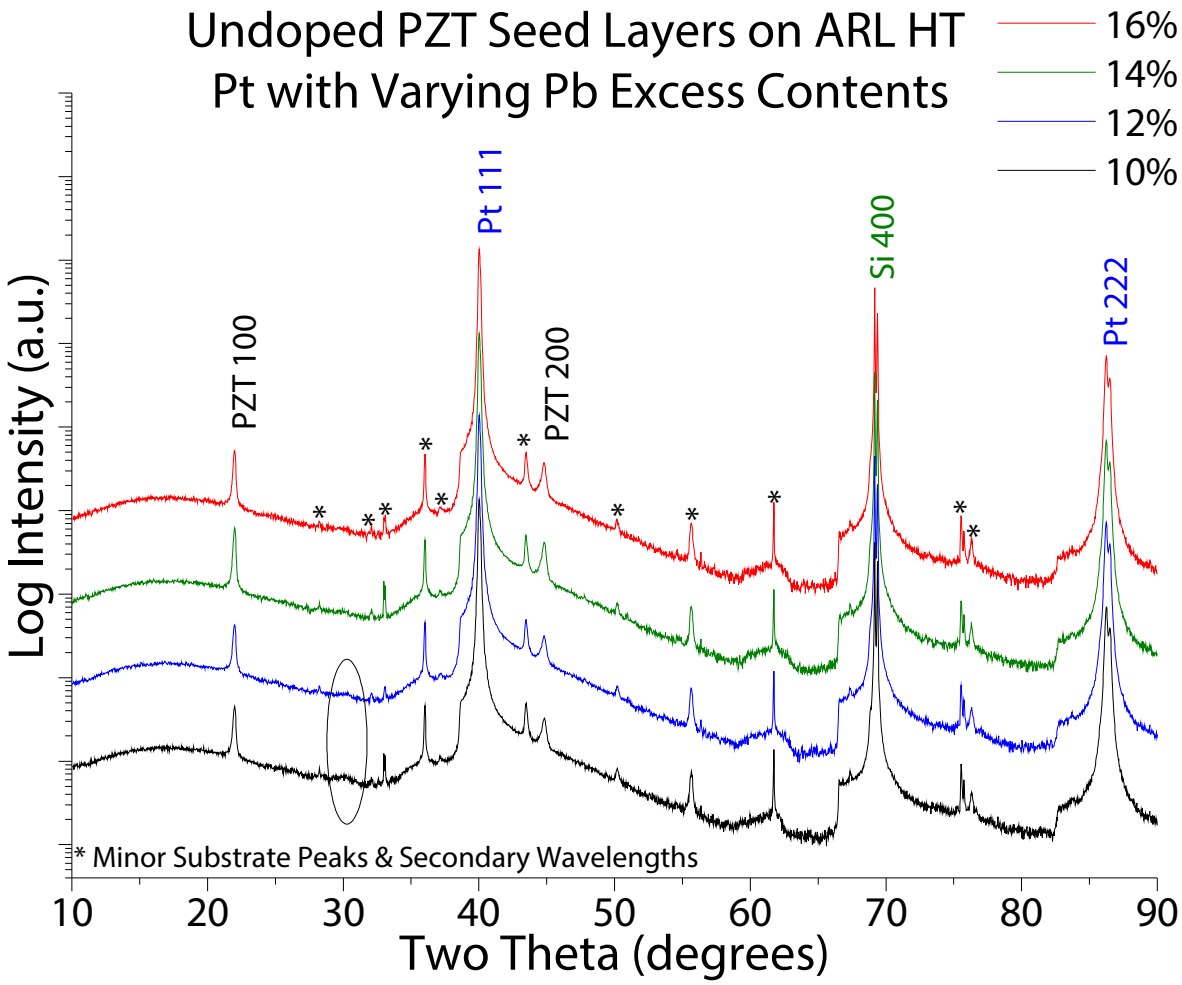

Figure 3.4: X-ray diffraction patterns collected from samples of equal thickness (55 nm), and Zr/Ti (52Zr/48Ti) stoichiometry deposited with varying lead excess (10, 12, 14, and 16%) on wafers platinized at high temperature (500 °C) by the U.S. Army Research Laboratory. A diffuse pyrochlore peak falls within the circled region.

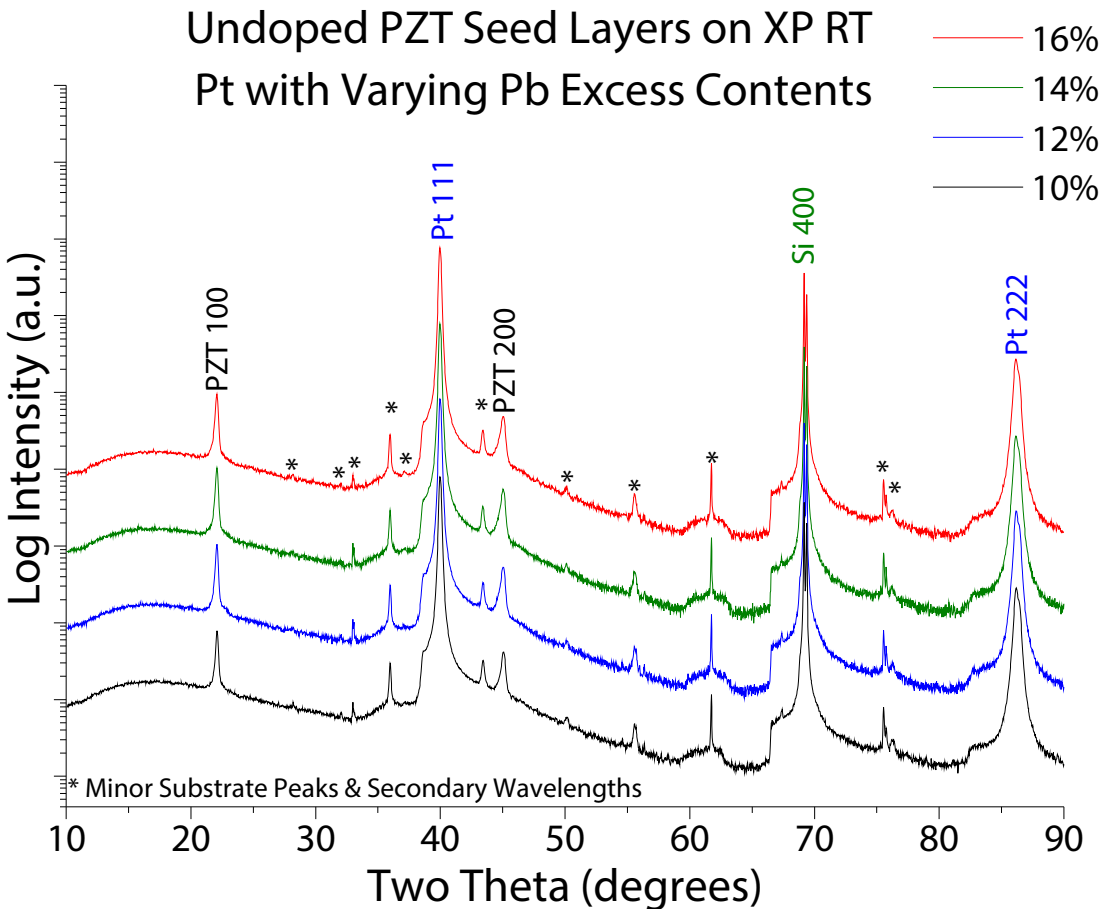

Figure 3.5: X-ray diffraction patterns collected from samples of equal thickness (55 nm), and Zr/Ti (52Zr/48Ti) stoichiometry deposited with varying lead excess (10, 12, 14, and 16%) on wafers platinized at room temperature by XP.

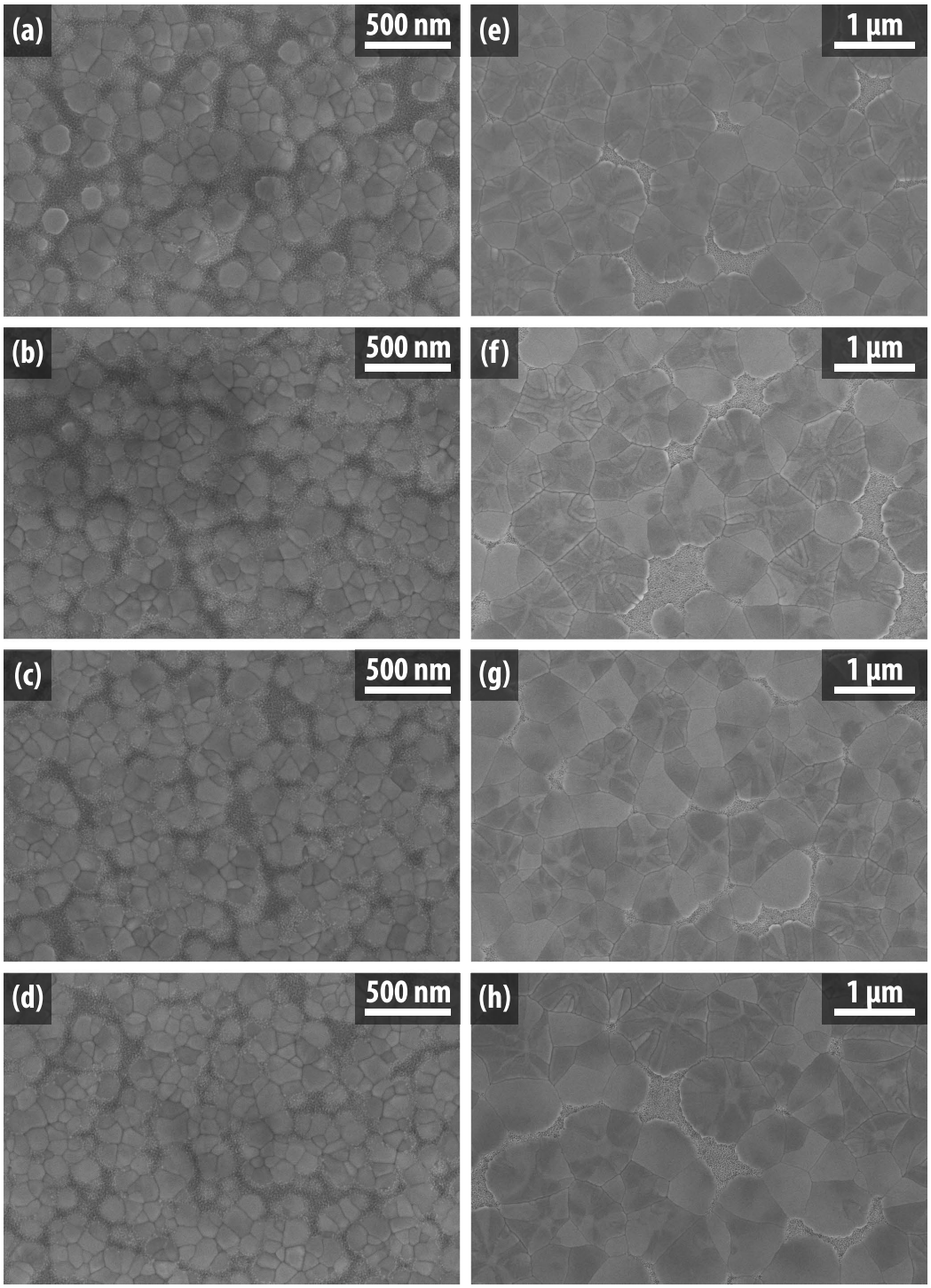

Figure 3.6: Micrographs collected from samples of equal thickness (∼55 nm), and Zr/Ti stoichiometry (52/48) deposited with varying lead excess (10, 12, 14, or 16%) on wafers platinized at room temperature (XP RT) or high temperature (ARL HT). Left and right columns are samples on XP's RT and ARL's HT Pt respectively. Rows are 10, 12, 14, and 16% Pb excess from top to bottom.

suggests that the additional excess lead helps compensate for lead diffusion into the platinum electrode, preventing the pyrochlore regions from growing (or persisting) to the same spatial extent.

In the case of HT Pt substrates, the change with an increase in lead content is far more subtle. Pyrochlore regions remain scattered and large in size (as in Section 3.2), marginally decreasing in area fraction with increases in lead excess levels (Table 3.4). It appears that increased lead content has a smaller effect on the pyrochlore content of PZT seed layers on high temperature platinum where the electrode is more resistant to lead diffusion. Conversely, changes in average grain size were well within the standard deviations in both cases (Table 3.5). This indicates that the PZT grain size is dominated by the nucleation density rather the presence of lead deficient pyrochlore restricting grain growth.

3.4 Doped PZT Seed Layers

Lead zirconate titanate is frequently utilized in its doped form in order to tailor properties in a way that best suits the application, as discussed in Chapter 1. In addition to changes in the functional properties, dopants can also change the microstructure of the PZT. Niobium is often cited for its role in increasing the grain size of PZT thin films[46,52,125]. However, reports that it decreases grain size in bulk ceramics and films are also present.[58,126–128] Similarly, manganese has been reported to increase[72,129] or decrease[48,130,131] grain size in both PZT films and ceramics.

In thin films, crystallization of PZT has been demonstrated to be nucleation limited as a consequence of the 4:1 ratio of nucleation to growth activation energies (441 kJ/mol and 112 kJ/mol respectively).[132] As a result, changes in grain size upon doping might be expected to be controlled by changes in nucleation behavior. It is therefore prudent to examine the combined effects of different platinum electrodes (which were demonstrated to alter PZT grain size and phase formation) and dopants on the nucleation behavior of {0 0 1} oriented PZT, as outlined in Table 3.6.

Diffraction patterns collected from doped and undoped seed layers on XP's RT platinized silicon wafers are similar (Figure 3.8). All seed layers, regardless of doping, are highly {0 0 1} textured, yielding

Table 3.6: Parameters used for dopant nucleation study

Parameter	Specifications
Substrates	XP (RT), ARL (HT)
Undoped Solution	12 wt.% PZT 52/48 with 12% excess Pb
Mn Doped Solution	12 wt.% PZT 52/48 with 12% excess Pb and 1% manganese
Nb Doped Solution	12 wt.% PZT 52/48 with 14% excess Pb and 2% niobium
Spin Speed (rpm)	3500
Thermal Processing	Tables 2.2 and 2.3

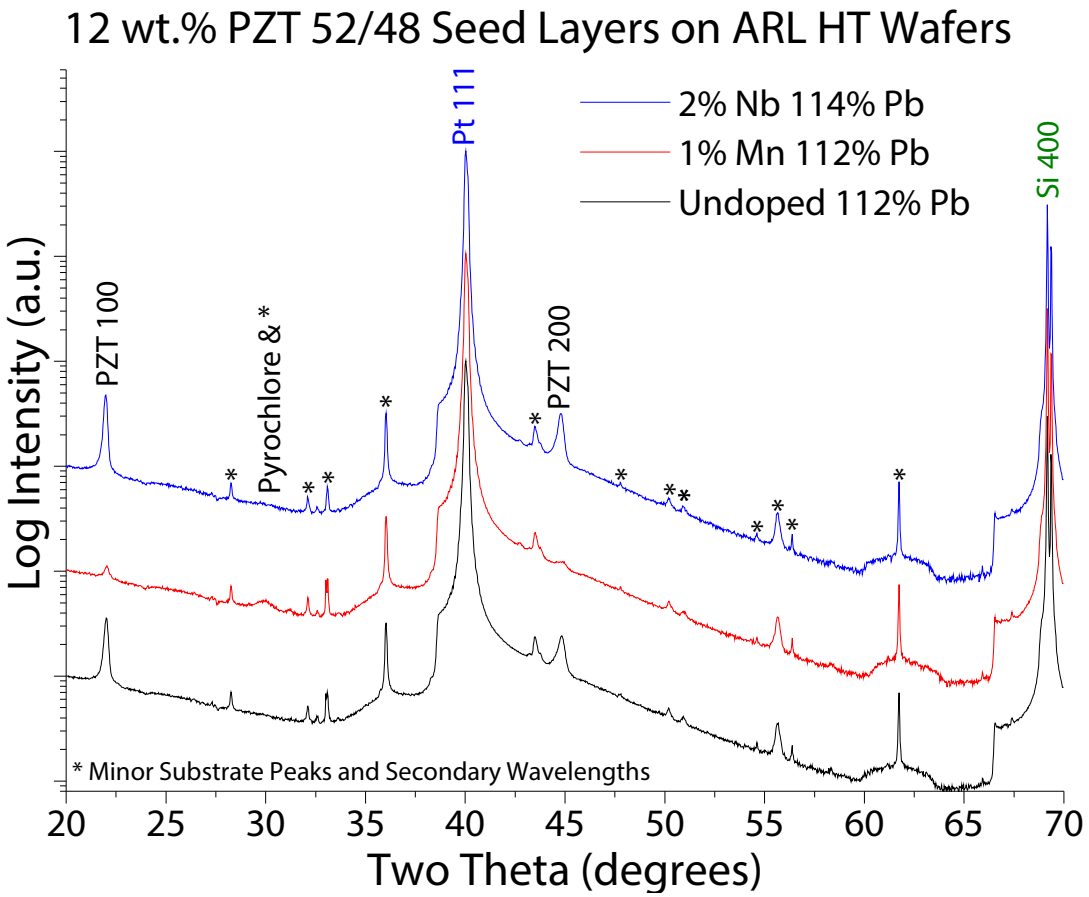

Figure 3.7: X-ray diffraction patterns collected from undoped and doped PZT seed layers deposited on ARL HT platinized silicon wafers.

Lotgering factors near 1. In contrast, phase-pure highly {0 0 1} textured PZT seed layers grown on ARL's HT platinized silicon (Figure 3.7), were achieved only from niobium doped and undoped solutions. Compared to the other seed layers, the diffraction pattern collected from a manganese doped seed layer on ARL HT Pt has {1 0 0} and {2 0 0} peaks of low intensity. Additionally, at 30° in 2θ a rather broad, low intensity peak is observed. This peak represents pyrochlore, indicating that manganese doping may be either stabilizing the pyrochlore phase or suppressing perovskite nucleation in the film. This diffraction pattern was reproducible across multiple Mn doped seed layers, including those on XP's HT Pt, indicating that the platinum deposition temperature plays a role in the anomalous crystallization. The intensity of the apparent perovskite {2 0 1} and {2 1 1} peaks remains constant, despite significant changes in the {0 0 1} and {0 0 2} peak intensities; further indicating that these apparent perovskite peaks originate from the substrate.

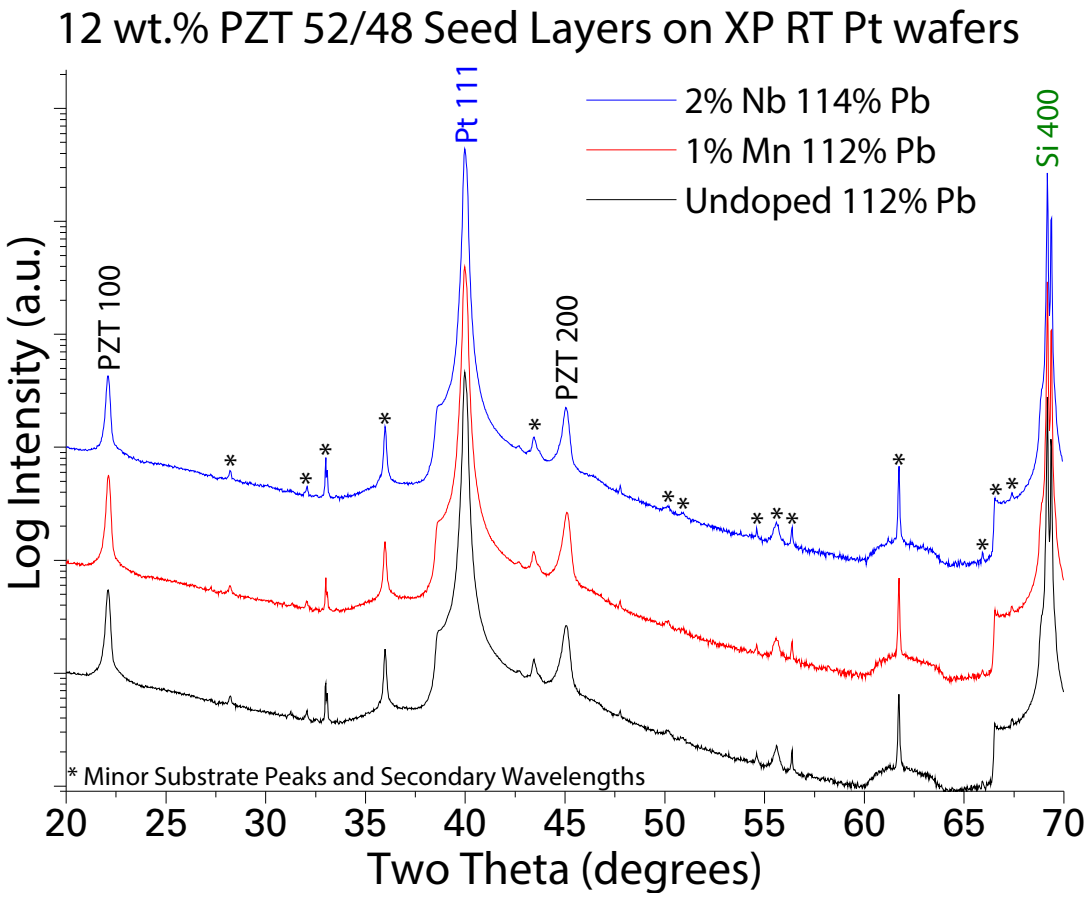

Figure 3.8: X-ray diffraction patterns collected from undoped and doped PZT seed layers deposited on XP RT platinized silicon wafers.

Table 3.7: Grain size distributions of doped and undoped PZT seed layers. Note that the overall diameters of rosettes were measured rather than the size of the individual features within the rosettes for Mn doped seed layers on ARL HT Pt.

Dopant	Platinized Si Substrate	
	XP RT	ARL HT
Undoped	(100 ± 30) nm	(360 ± 130) nm
1% Manganese	(110 ± 30) nm	(2200 ± 800) nm
2% Niobium	(140 ± 40) nm	(430 ± 250) nm

Micrographs collected from the seed layers deposited on XP RT platinum are presented on the left half of Figure 3.9 with grain sizes tabulated in Table 3.7. 1% manganese doped films in this work have a

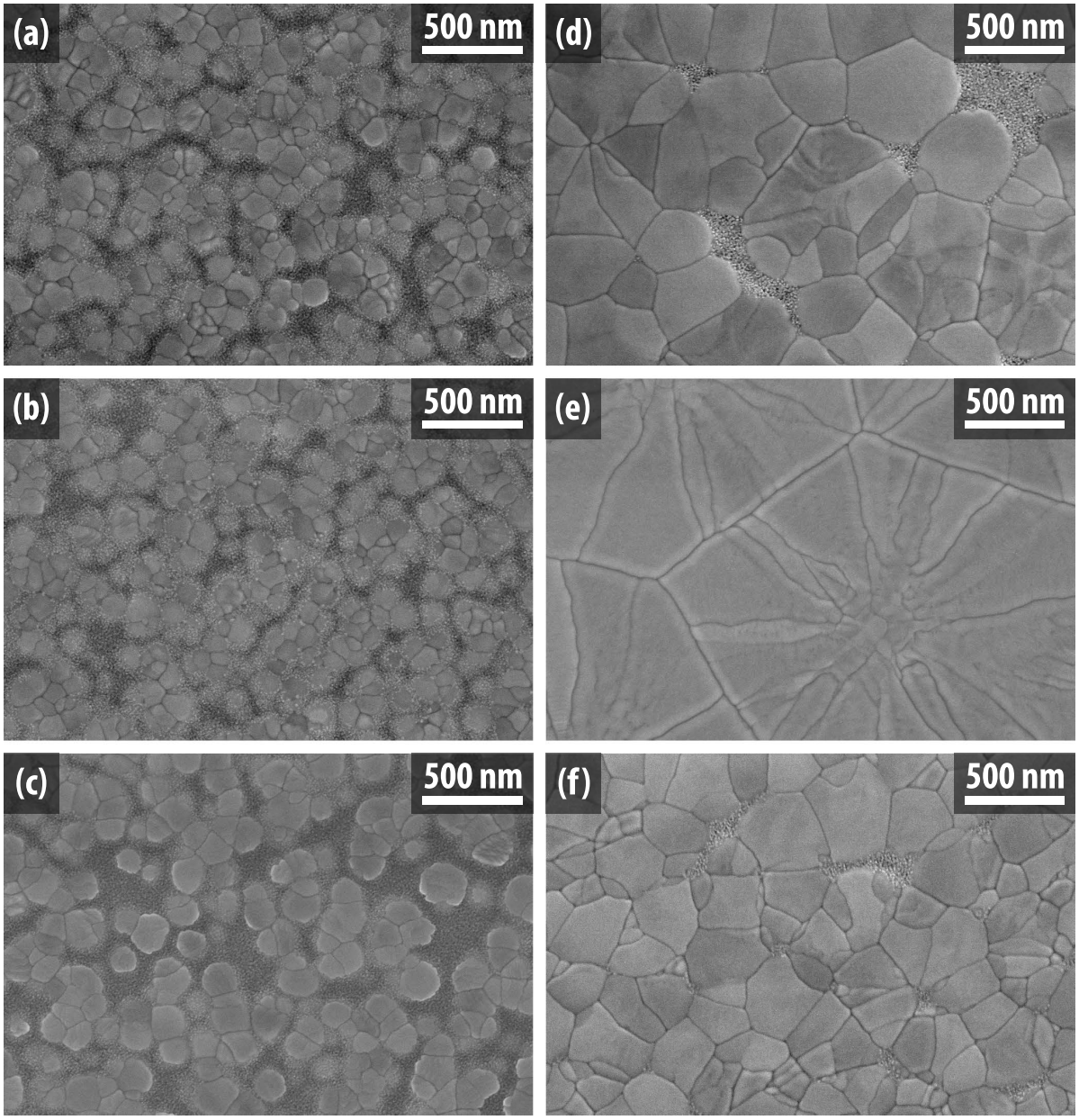

Figure 3.9: Micrographs from ∼55 nm thickness PZT 52/48 seed layers deposited with varying dopants and lead excess concentrations. (a) XP RT undoped, (b) XP RT Mn doped, (c) XP RT Nb doped, (d) ARL HT undoped, (e) ARL HT Mn doped, (f) ARL HT Nb doped.

similar average grain size to the undoped film (∼110 and 100 nm respectively). Wersing reported that manganese accumulated at grain boundaries with increases in doping concentration.[131] Similarly, He & Li reported that low Mn doping levels (under 1.5 at.%) would be fully incorporated entirely on the perovskite B-site.[72] The absence of any grain size change at low Mn doping concentrations (1% in this work) is in agreement with the results of multiple publications.[37,49,130]

As in the work of Haccart *et al.* among others, in this work the average perovskite grain size increased from ∼ 100 to 140 nm upon niobium doping.[46,52] However, this is in contrast to the works of Zhu *et al.* and Sun *et al.* who observed no change and a decrease in grain size respectively upon niobium doping.[38,128] Another point of note is the higher concentration of pyrochlore present in the niobium doped films compared to the undoped or manganese doped films. The pyrochlore concentration was higher despite a 2 at.% increase in lead content relative to the other solutions. The pyrochlore structure is characterized by the chemical formula $A_2B_2O_7$ (or $A_2B_2O_6O'$ to distinguish the two crystallographically distinct oxygen sites) and allows a broad range of elemental substitutions and vacancy concentrations relative to the perovskite structure.[117] In $Pb(Zr,Ti)O_3$ in order to form $Pb_2(Zr,Ti)_2O_6\square'$, oxygen vacancies must form.[117]

As described by Subramanian *et al.*, the stability of the pyrochlore is dependent on the size of the 4+ B-site cation. As the B-site cation size increases, the 48f Oxygen x parameter is also lengthened. When the x parameter exceeds 0.33 the pyrochlore structure is more favorable than the perovskite structure; the x parameter is 0.375 for Zr^{4+}.[52,117] Pyrochlore regions were observed to be Zr-rich by Klissurska *et al.*, an indication of the role of Zr in pyrochlore stabilization.

Similarly, lead deficient pyrochlores can form via PbO evaporation during annealing, taking on the chemical composition $Pb_{2-x}(Zr,Ti)_2O_{6-x}$. While A:B site stoichiometry is important for perovskite phase formation, the A site ions are not "very essential" for pyrochlore stabilization.[52,117] This leads to lead deficient pyrochlores which cannot form a stable perovskite structure for higher temperature heat treatments.[52] When Nb^{5+} is added to the perovskite structure, it is compensated by A-site vacancies (as described by nil $\longrightarrow$ $2\,Nb^{\bullet}_{Zr/Ti} + V''_{Pb}$). In the pyrochlore structure Nb doping can result in the formation of A-site vacancies or oxygen vacancies, altering the pyrochlore phase stability.

Micrographs from seed layers deposited on ARL high temperature platinized substrates yield different phenomena. The niobium doped and undoped seed layers have similar grain sizes and pyrochlore contents in some regions (see Figure 3.9). However, in other regions of the niobium doped films (see Figure 3.10), grain sizes are substantially larger, consistent with the findings of Haccart *et al.*[46] This indicates that niobium doping may be hindering the nucleation process, allowing fewer nuclei to form and existing nuclei to grow larger. Niobium doped samples had higher pyrochlore concentrations than undoped seed layers deposited on the same substrate, as seen by comparing Figure 3.9 (a) and (c) or (d) and (f). Similarly to what was observed in Figure 3.6 and tabulated in Table 3.4, the change in pyrochlore concentration between undoped and Nb doped seed layers is less significant on ARL's HT

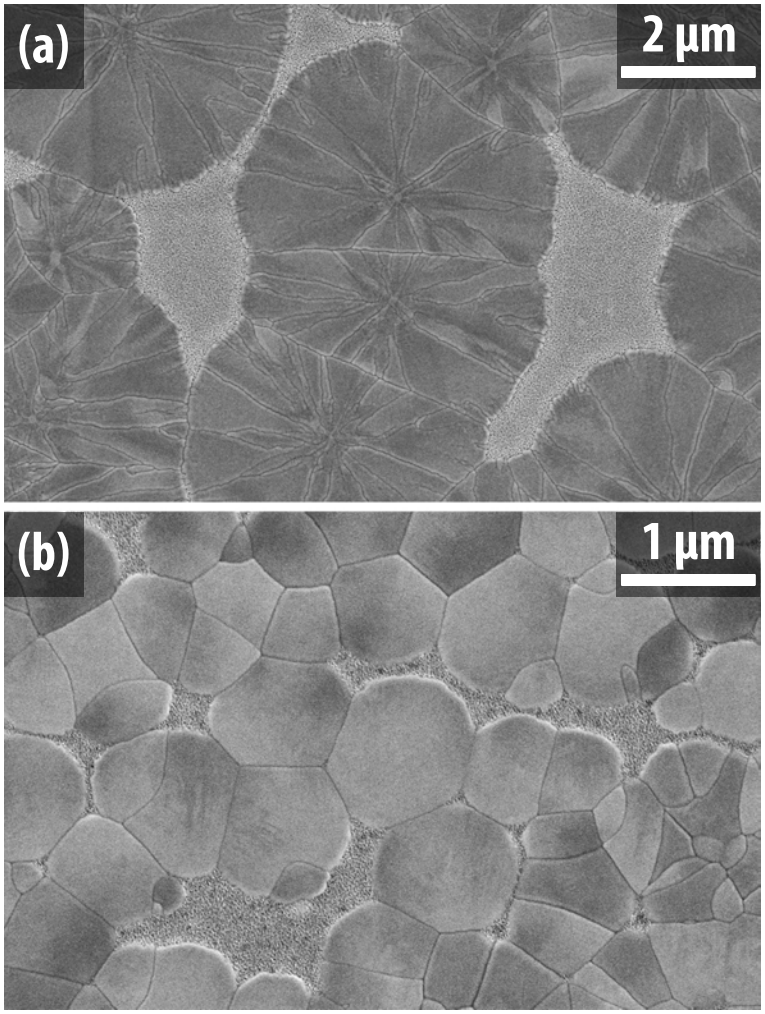

Figure 3.10: Additional micrographs from ∼55 nm thickness PZT 52/48 seed layers deposited with varying dopants and lead excess concentrations on ARL HT Pt substrates. (a) Mn doped, (b) Nb doped

Pt than on XP's RT Pt. This suggests that, despite the fact that Nb^{5+} can stabilize the pyrochlore phase, pyrochlore phase retention is predominantly a consequence of the lead loss kinetics associated with the substrate, rather than stabilization by Nb.

Manganese doped films deposited on high temperature platinum have very large grain clusters due to a rosette growth mechanism. At the center of each rosette is a nuclei from which the rosette grows, often into numerous slender grains arranged radially around the central nuclei.[133] Micrographs covering a larger spatial extent (Figure 3.10) show rosettes on the order of 5 µm in diameter with large area pyrochlore regions in between. This demonstrates that manganese doping is hindering nucleation of perovskite PZT on substrates platinized at elevated temperatures. Similar results were seen on XP's high temperature platinum.

Rosettes are described by both Myers & Chapin and Spierings *et al.* as forming in instances of low nucleation density and unfavorable conditions (e.g. Zr rich PZT films).[133,134] Nucleation is most favorable when there is a high density of nucleation sites such as a solid-solid interface at the bottom electrode.[88] In order for a rosette structure to form, nucleation must be significantly stymied such that few nuclei form (rosette center) and additional nucleation events occur on the original nuclei (slender grains radiating from the rosette center). The large size of the rosettes suggests a significantly diminished nucleation density, providing ample room for rosettes to grow to 5 μm. Rosettes do not form in Mn doped seed layers deposited on RT Pt, but do form on HT Pt; this indicates that the film-platinum interface and Mn doping both contribute to the observed rosette formation.

The origin of the reduced nucleation in the Mn-doped films on HT Pt substrates is unknown. It is speculated, however, that it could be due to some degree of segregation of Mn to the bottom electrode interface. Zirconium-titanium concentration gradients are reported to form in PZT films upon crystallization.[27] Similarly, manganese may preferentially diffuse to the bottom electrode interface. Several reports of manganese inhibiting grain growth by segregating to grain boundaries have been made for bulk PZT ceramics.[131,135] If manganese segregates to the boundaries, including the electrode-film interface, it may inhibit nucleation of the perovskite phase. This would result in a sparse population of nucleation sites from which the perovskite phase could nucleate, forming rosettes as a consequence. Similar behavior was observed on both ARL and XP HT Pt despite differing bottom electrode grain sizes. It is furthermore speculated that the significantly increased nucleation density of Mn-doped PZT on room temperature deposited platinum bottom electrodes may be due to the high density of grain boundaries in such electrodes. This is an area that warrants further investigation and will be discussed in more detail in Proposed Future Work (Section 6.2).

3.5 Seed Layer Thickness

Another common research focus for controlling crystallographic texture of PZT films is thickness, as in the work of Cattan *et al.* and Doi *et al.*[97,110] Cattan *et al.* characterized the growth mechanism and texture of sputter deposited $PbTiO_3$ films, every 2.5 – 5 nm up to 20 nm. They found that 5 nm or 7.5 – 15 nm of $PbTiO_3$ imparted strong (0 0 1) texture to PZT layers deposited on the thin PT seed layers.[110] Recent work on the textured seeding of {0 0 1} PZT via PZT based seed layers, has been reported by Doi *et al.* of Mitsubishi Materials Corporation, utilizing MMC's PZT-E1 sol-gel solutions. While Doi *et al.* did not directly specify thickness, a separate solution was used solely for seed layers. This seed layer solution had a concentration between those of the other solutions, which provided 45 nm and 80 nm thicknesses per layer under their processing conditions. However, in a patent application,[95] the same authors state that "an orientation controlling layer … has a layer thickness in which a crystal orientation is controlled in a (1 0 0) plane preferentially in a range of 45 nm to 150 nm".[95] A comparison of these

Table 3.8: Parameters used for thickness study

Parameter	Specifications
Substrate	ARL (HT) & XP RT
Solution	12 wt.% PZT 52/48 with 10% excess Pb
Spin Speeds (rpm)	2000, 2500, 3000, 3500, 4000, 4500, 5000, 5500, 6000
Thermal Processing	Tables 2.2 and 2.3

two reports suggests that the processing "sweet spot" for a {0 0 1} oriented PZT seed layer is between 45 nm and 80 nm.[95,97]

These reports suggest that deviations from the single nanometer scale (as in Cattan *et al.*[110]) to 10s of nanometers (as in Doi *et al.*[95,97]) in thickness can influence orientation control. It is speculated that thickness-dependent changes in average film lead concentration or nucleation processes (such as increased surface nucleation) may be responsible for the reported sensitivity of orientation to thickness. Given the disparities of the optimum conditions reported elsewhere, in this work a broad range of seed layer thicknesses (30 – 75 nm) were deposited via variations in spin speed (Table 3.8) to assess the effect on the orientation quality. Analysis via XRD and SEM further demonstrated the role of thickness in microstructural and texture development of PZT.

As shown in Figures 3.11 and 3.12, X-ray diffraction plots are similar across the majority of the chosen spin speed range. It is noted that 3500 rpm yields a film 55 nm thick and the minimum and maximum speeds, 2000 rpm and 6000 rpm, yield films 75 nm thick and 37 nm thick respectively. Films deposited from 2500 – 5500 rpm have strong {0 0 1} texturing, while films deposited at the slowest speed, 2000 rpm, yield {1 1 1} preferential orientation; those deposited at 6000 rpm have minimal if any crystallization detected by XRD. Furthermore, no difference in the spin speed processing window is observed with changes in the platinum deposition temperature.

Micrographs (Figure 3.13) of the strongly {0 0 1} oriented films yielded dense microstructures similar to those seen in Figure 3.9 (a) & (d). Films with {1 1 1} preferential orientation had a finer grain size than films spun at faster speeds, suggesting an increase in nucleation density for thick films. The thinnest films, with limited evidence of PZT crystallization, had the largest grain sizes for both varieties of platinized substrates. In the case of ARL HT (f), large rosettes on the order of 2 – 4 μm formed on the surface with pyrochlore between grains. XP RT (c) formed triangular grains surrounded by a pyrochlore layer. Thinner, yet well crystallized, films also exhibited larger grain sizes, suggesting diminished nucleation densities when compared to thicker films. The increasing surface area to volume ratio in thin films, may leave the material more lead deficient (as evidenced by pyrochlore concentrations). Lead deficiency in the amorphous film hinders nucleation mechanisms[97,109,111,119,136,137], leading to larger grain sizes.

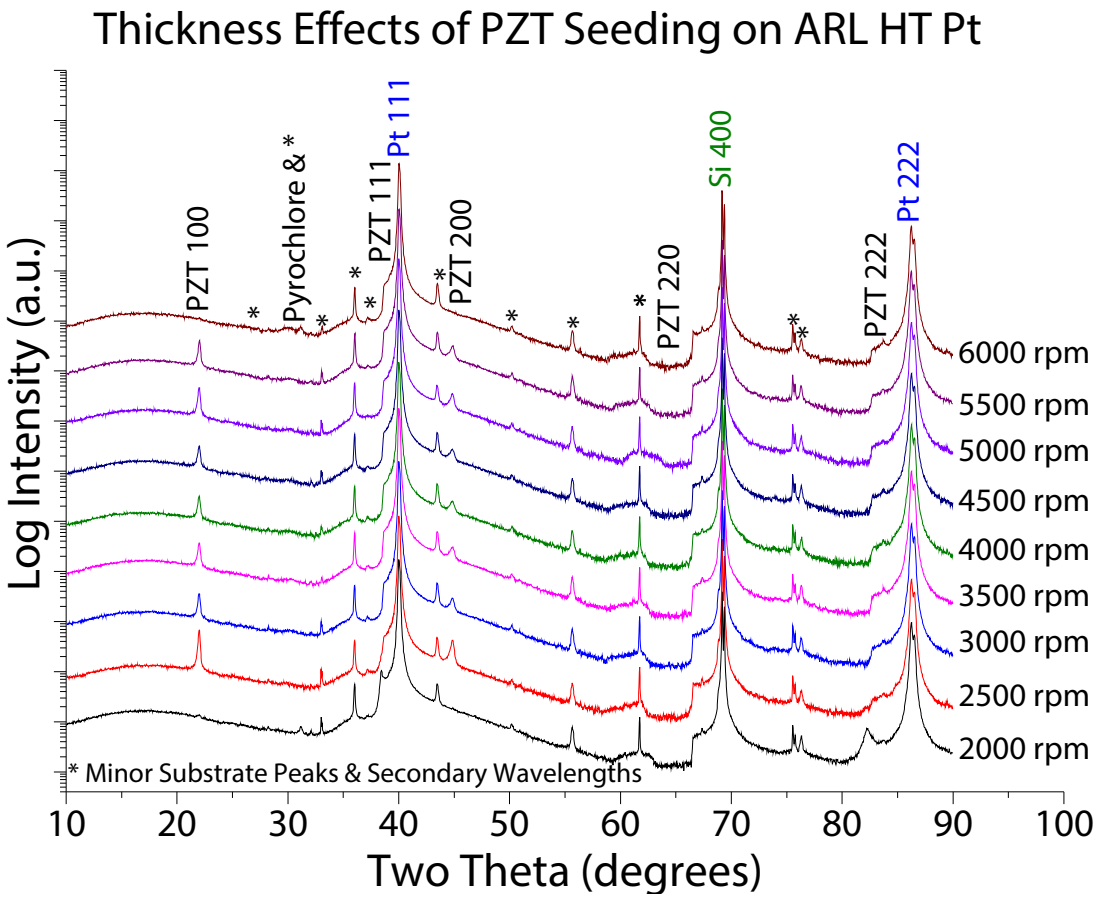

Figure 3.11: X-ray diffraction of undoped 12 wt.% PZT seed layers on ARL HT platinum as a function of thickness (spin speed). A window of 2500 – 5500 rpm yields strongly {0 0 1} textured films. Some pyrochlore (Py) is present in most films.

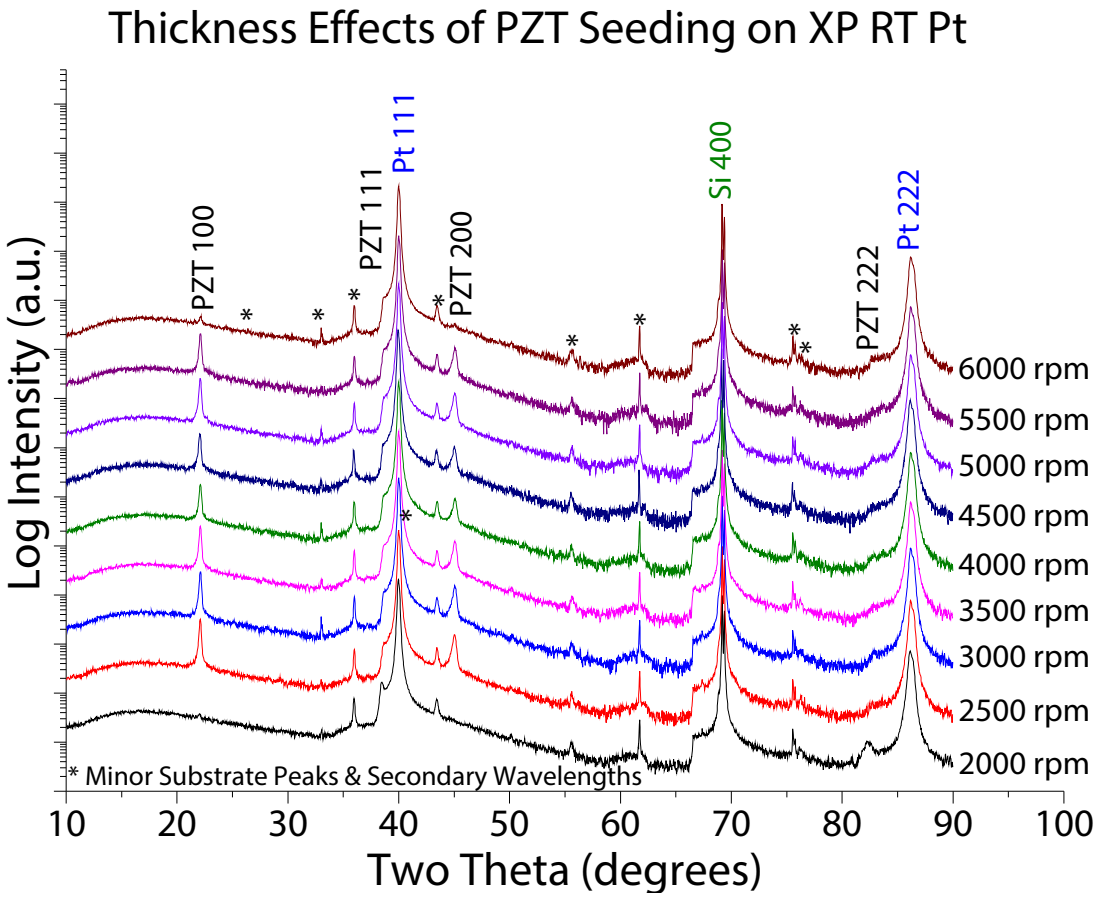

Figure 3.12: X-ray diffraction of undoped 12 wt.% PZT seed layers on XP RT platinum as a function of thickness (spin speed). A window of 2500 – 5500 rpm yields strongly {0 0 1} textured films.

.

Crystallized films spun at 6000 rpm were found to be approximately 7 nm thicker than films spun at 5500 rpm as measured by contact profilometry with a stylus tip radius of several microns, converse to the anticipated trend. However, measurements of the amorphous film thicknesses via ellipsometry disagreed with the profilometry data; the film thickness was found to be 70 nm and 60 nm respectively, for films spun at 5500 rpm and 6000 rpm.

To understand the origin of this discrepancy, the crystalline films were examined by FESEM and atomic force microscopy. Micrographs of crystalline films spun at 6000 rpm exhibit two distinct regions which appear to have different heights; a thicker region of perovskite rosettes, and thinner residual pyrochlore. Due to the size of these regions, the tip of a contact profilometer would be expected to glide over any concavities in the microstructure. Atomic force microscopy, with a tip radius on the order of 2 nm, was used to accurately measure any concave regions in the microstructure (Figure 3.14). The observed height difference between perovskite grains and porous pyrochlore regions was similar in

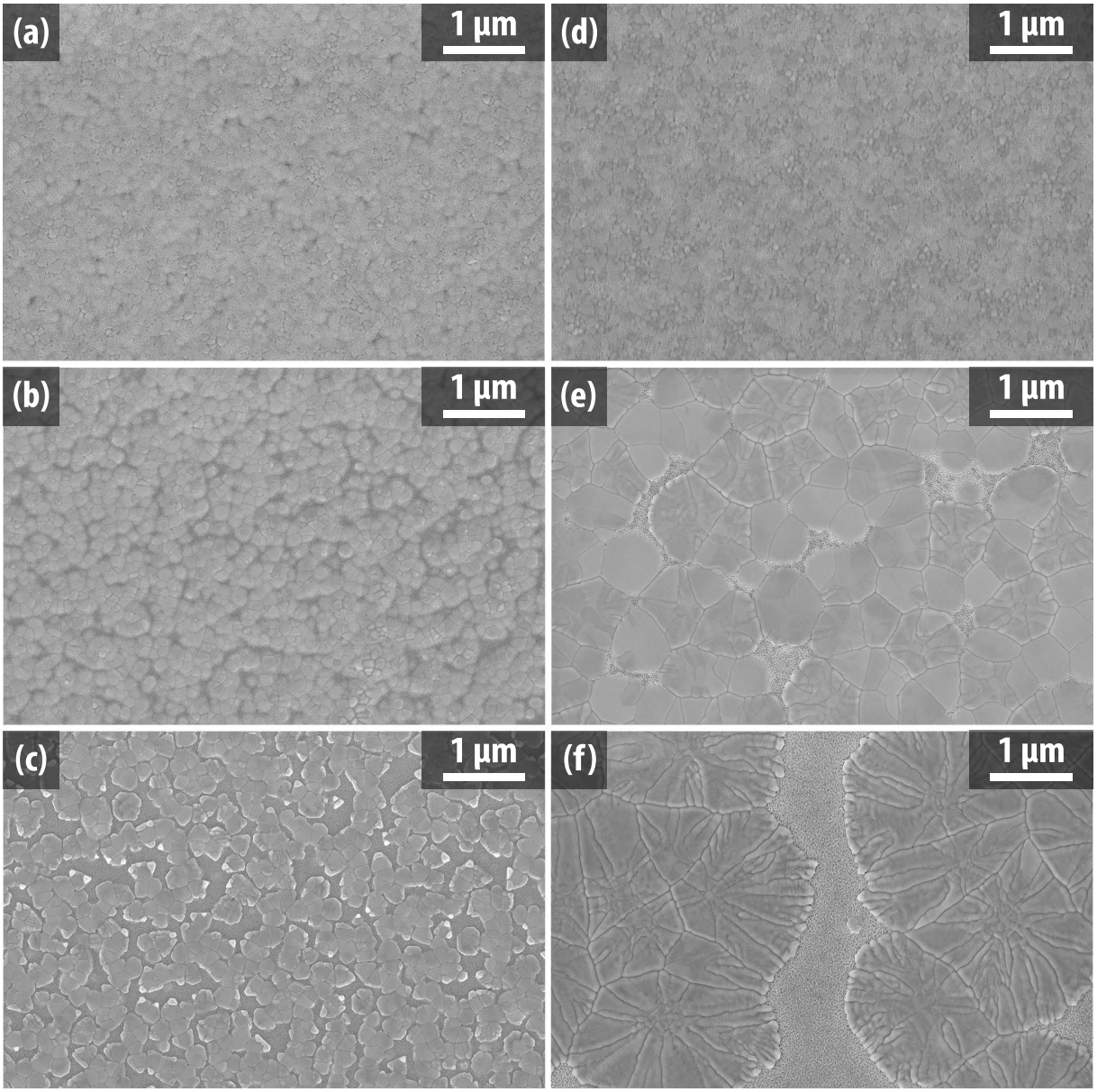

Figure 3.13: Micrographs collected from samples of varying thickness deposited with 12 wt.% solution on ARL HT and XP RT platinum. (a) XP RT 2000 rpm, (b) XP RT 3500 rpm, (c) XP RT 6000 rpm, (d) ARL HT 2000 rpm, (e) ARL HT 3500 rpm, and (f) ARL HT 6000 rpm

magnitude to the anomalous thickness increase (10 ± 2) nm. This indicates that, upon crystallization, perovskite grains may draw material (presumably PbO) from pyrochlore regions, leaving perovskite grains thicker and pyrochlore regions thinner than the average film thickness. Similar behavior was observed by Muralt, generating 1 micron wide Pb depletion regions surrounding lithographically

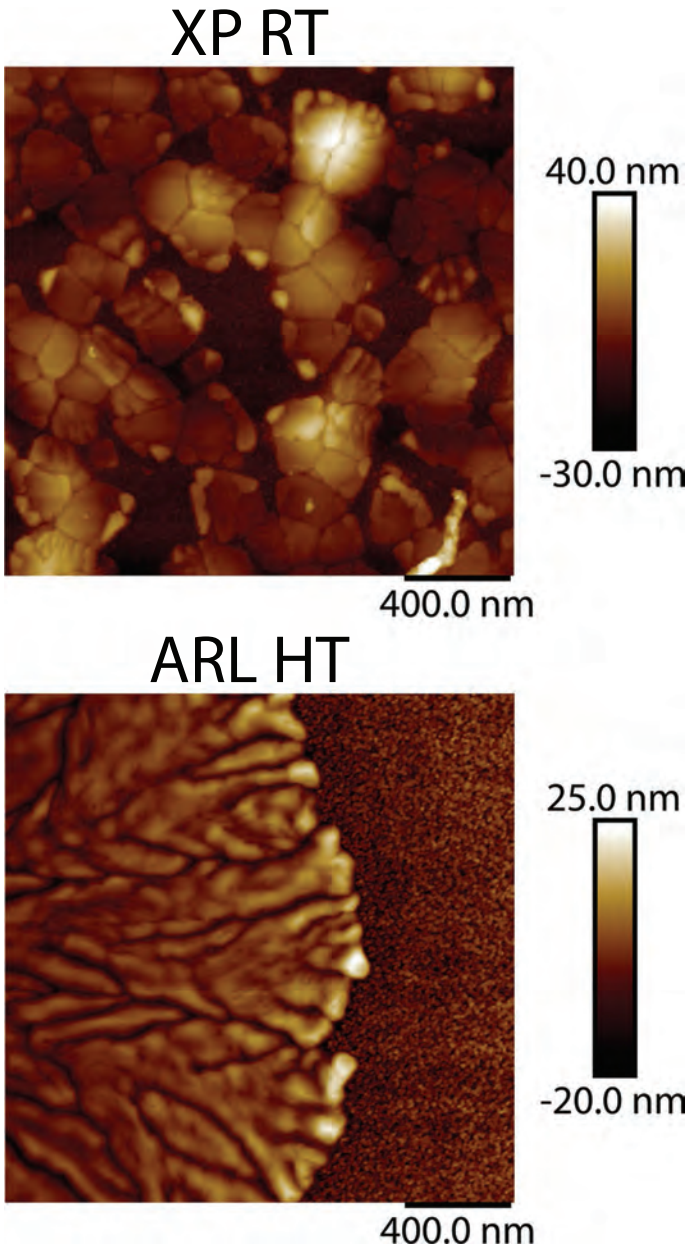

Figure 3.14: AFM scans of seed layers spun at 6000 rpm using 12 wt.% solution. The step height between the large perovskite grains and the porous pyrochlore regions is (10 $\pm$ 2) nm, in-line with the anomalous increase in thickness.

patterned TiO_2 seed features. This indicates that regions with favorable perovskite growth conditions could procure extra material from surrounding regions with less favorable growth conditions.[138]

Highly {0 0 1} textured PZT seed layers have been demonstrated in crystallized layers 30 – 70 nm thick for the processing conditions used in this thesis. However, at high spin speeds (6000 rpm in this

case) the apparent thickness can fall within the range where {0 0 1} texture is anticipated. This is due to a change in nucleation behavior and subsequent roughening of the crystalline film surface on a scale too small for contact profilometry to detect. While thickness does correlate with {0 0 1} orientation in a rather large range, it is important to ensure that the measured thickness is representative of the entire film's average thickness.

3.6 Conclusions on Textured Seeding of PZT

The influences of a broad range of parameters on the seeding and growth of highly {0 0 1} textured PZT thin films were investigated utilizing Mitsubishi Materials Corporation sol-gel solutions. In particular, focus was placed on physical and chemical factors that could alter the nucleation mechanisms active in seed layers. Room temperature platinum leads to a smaller PZT grain size, suggesting restriction of the grain growth mechanism by lead deficient pyrochlore. The higher concentration of surface pyrochlore on room temperature platinum indicates lead absorption by the substrate. However, these differences in nucleation behavior had little impact on orientation quality. Despite large changes in Pt grain size, the grain size of PZT deposited on high temperature platinum is relatively similar. This yields a seed layer with larger PZT grains than similar seed layers deposited on room temperature platinum. From this, it can be inferred that the platinum deposition temperature is the primary variable which controls differences in nucleation on platinized silicon.

Dopants were demonstrated to have a limited effect on the orientation quality of seed layers deposited on room temperature platinum, besides minor changes in grain size. Manganese doping greatly affects nucleation behavior on high temperature platinum, leading to a rosette microstructure of large grain clusters with a large volume of pyrochlore as evidenced by XRD. Niobium doping can lead to a substantial increase in grain size of PZT deposited on high temperature platinum, yielding grains over 1 μm in diameter.

Seed layer thickness can affect orientation quality: thick layers decrease grain size and preferentially {1 1 1} orient while thin layers have large, weakly diffracting grains with significant amounts of pyrochlore and increased surface roughness. The processing window for strong {0 0 1} orientation requires an average film thickness in the range of 30 – 70 nm. No change was observed in the thickness processing window for {0 0 1} orientation upon changes in platinum deposition temperature.

It is noted that since the appearance of residual pyrochlore regions can degrade nucleation, that differences in process equipment may change the relative degree of lead volatility during the heat treatment steps. Likewise, differences in lead loss to the underlying Pt bottom electrodes could also affect the nucleation, and hence the orientation of the films, even from the same precursor under ostensibly the same process conditions.

Chapter 4

Deposition of Highly {001} Textured, Niobium Doped, Gradient-Free Lead Zirconate Titanate Thick Films Using Lead Zirconate Titanate Seed Layers

4.1 Lead Optimization for Growth of Thick Films

The preceding chapter investigated the deposition of the first layer of PZT on a platinized silicon substrate; focusing on the factors which resulted in preferential {1 0 0} rather than {111} orientation or random texture. By optimization of the growth conditions, highly textured seed layers were developed, as described in Chapter 3. Depositions of thick films (7 – 10 layers) were met with degrading orientation as thickness increased. An example of this degradation is seen in an undoped thin film processed under the parameters outlined in Table 4.1.

As evidenced by x-ray diffraction data (Figure 4.1), orientation degraded from the seed layer with a Lotgering factor near 1 (as discussed in prior sections), to a value of 0.85 at 800 nm thick (approximately half of the desired final thickness). Degradation of orientation with thickness indicates that there is a poor transfer of the preferential orientation from the crystalline layers to the crystallizing amorphous film. In the seed layers shown in Figures 3.6, 3.9, and 3.10, pyrochlore was always present at the surface; it was also often present at the interfaces of thicker films (Figure B.13).

The pyrochlore concentration on the surface of films was found to be a function of the amount of lead oxide which is built up in the RTA in addition to solution stoichiometry. The rapid thermal annealer used for crystallization in this work is part of a user facility, and is used for processing a wide variety of materials under different conditions. Many users clean the RTA before use by heating to 800 °C for 5 min with high gas flows. This lowers the lead partial pressure present by evaporating PbO built up on the RTA chamber walls. Additionally, the rapid thermal annealer is periodically disassembled and the chamber

Table 4.1: Parameters used for thick film orientation degradation

Parameter	Specifications
Substrate	XP (RT)
MPB Solution	15 wt.% PZT 52/48 with 10% excess Pb
Spin Speeds (rpm)	6000 (seed layer) 4000 (bulk layers)
All Pyrolysis	Table 2.2 sans 100 °C drying step
Crystallization	Table 2.3
Layers	1 seed, 10 bulk layers, crystallized individually

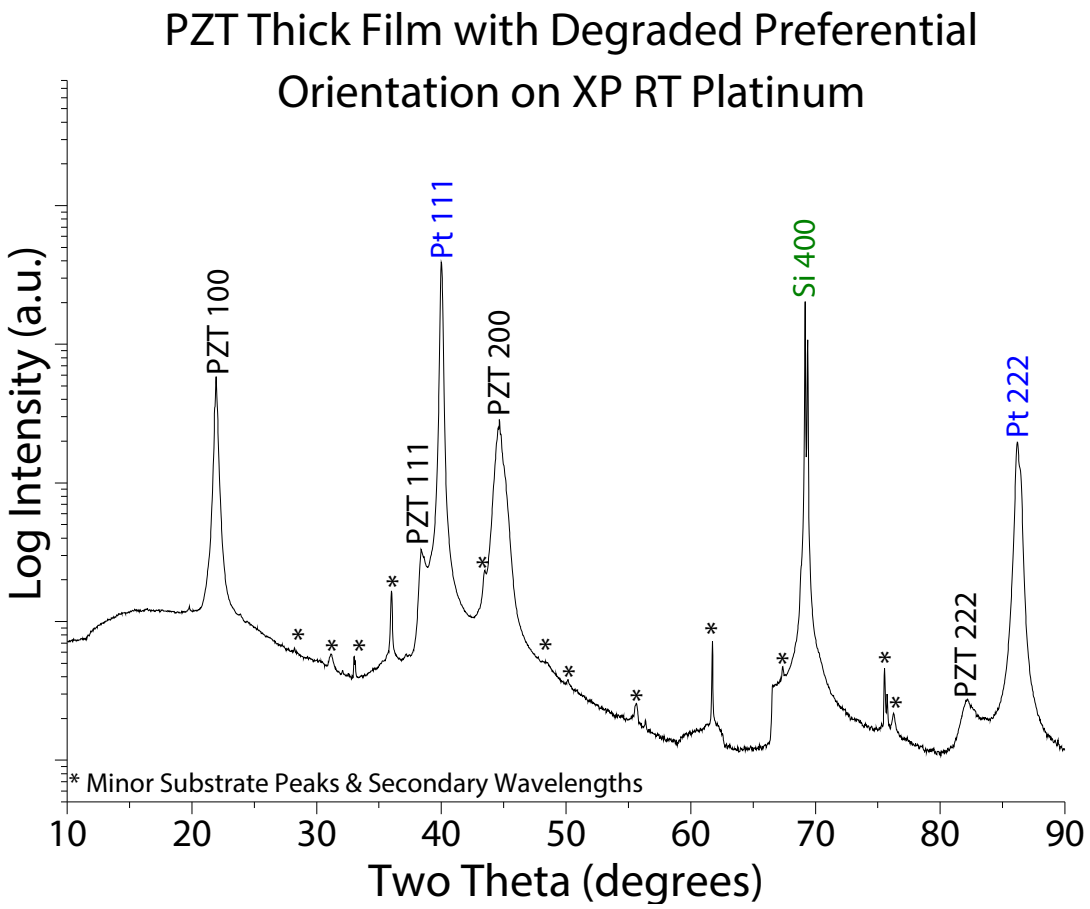

Figure 4.1: X-ray diffraction pattern of a 10 layer undoped PZT 52/48 film deposited on XP RT platinized silicon.

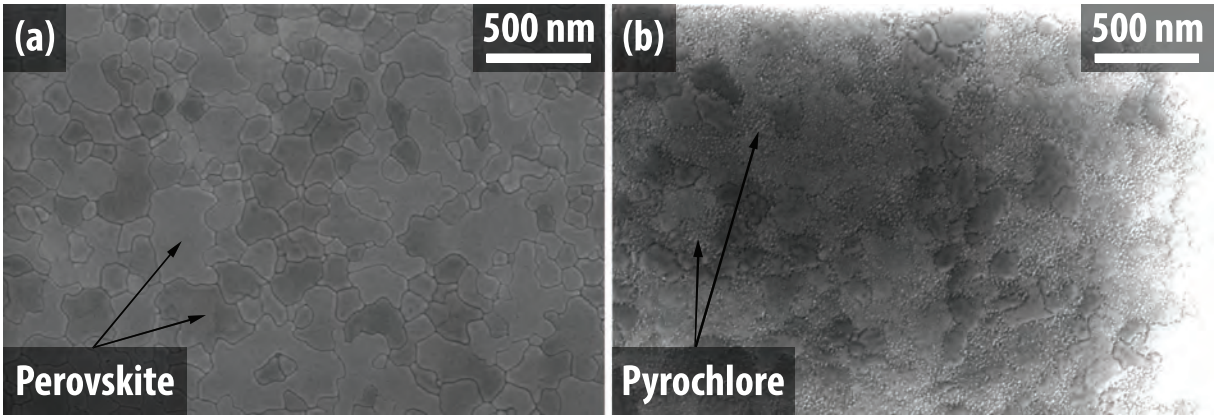

Figure 4.2: Micrographs depicting the range of pyrochlore concentrations which can be obtained depending on furnace conditions. Both samples used 10% Pb excess solutions on PSU HT Pt. (a) is an example of crystallization in a lead-rich furnace with little or no surface pyrochlore present. (b) is an example of a crystallization in a lead-depleted furnace with high levels of surface pyrochlore.

is etched in acid, removing additional PbO. As a consequence of the large variation in the lead content of the furnace, a wide range of surface pyrochlore concentrations can be achieved as is demonstrated in Figure 4.2. Films with higher pyrochlore concentrations were found to degrade in orientation quality more rapidly than those with low pyrochlore concentrations.

In principle, there are two primary ways which *residual* (lead deficient) pyrochlore[(I)] at the surface of a PZT layer could misorient layers deposited over it. First, perovskite grains could nucleate directly off of randomly oriented residual pyrochlore crystallites. Alternatively, the residual pyrochlore could first convert to the perovskite phase in any variety of orientations depending on energetic favorability. Following this, these new perovskite grains could continue growing into the amorphous PZT film, increasing the volume fraction of material with the same orientation as the converted pyrochlore.

Voigt *et al.* suggested that perovskite nucleation does not occur on sites originating from the residual pyrochlore phase; rather the perovskite structure nucleates in the amorphous film from the underlying oriented perovskite. The new perovskite grains consume the residual pyrochlore, converting it to oriented perovskite as the perovskite grains continue to grow.[139] Carim *et al.* reported that the fastest growth condition for the perovskite structure, growing from a pyrochlore matrix, is when the {2 2 2} in pyrochlore are aligned with the {1 0 1} in the perovskite structure. They further suggested that less energetically favorable pyrochlore orientations (as a consequence of the random orientation) could experience delayed conversion to perovskite. If nucleation from oriented perovskite is sufficiently

[(I)] Pyrochlore can form as an intermediary structure in the transition to the perovskite structure or as a sign of imbalanced stoichiometry (often lead depletion). In this case the focus is on pyrochlore which is formed and stabilized as a consequence of lead depletion, denoted here as *residual* pyrochlore as it is pyrochlore which did not complete the conversion to perovskite.

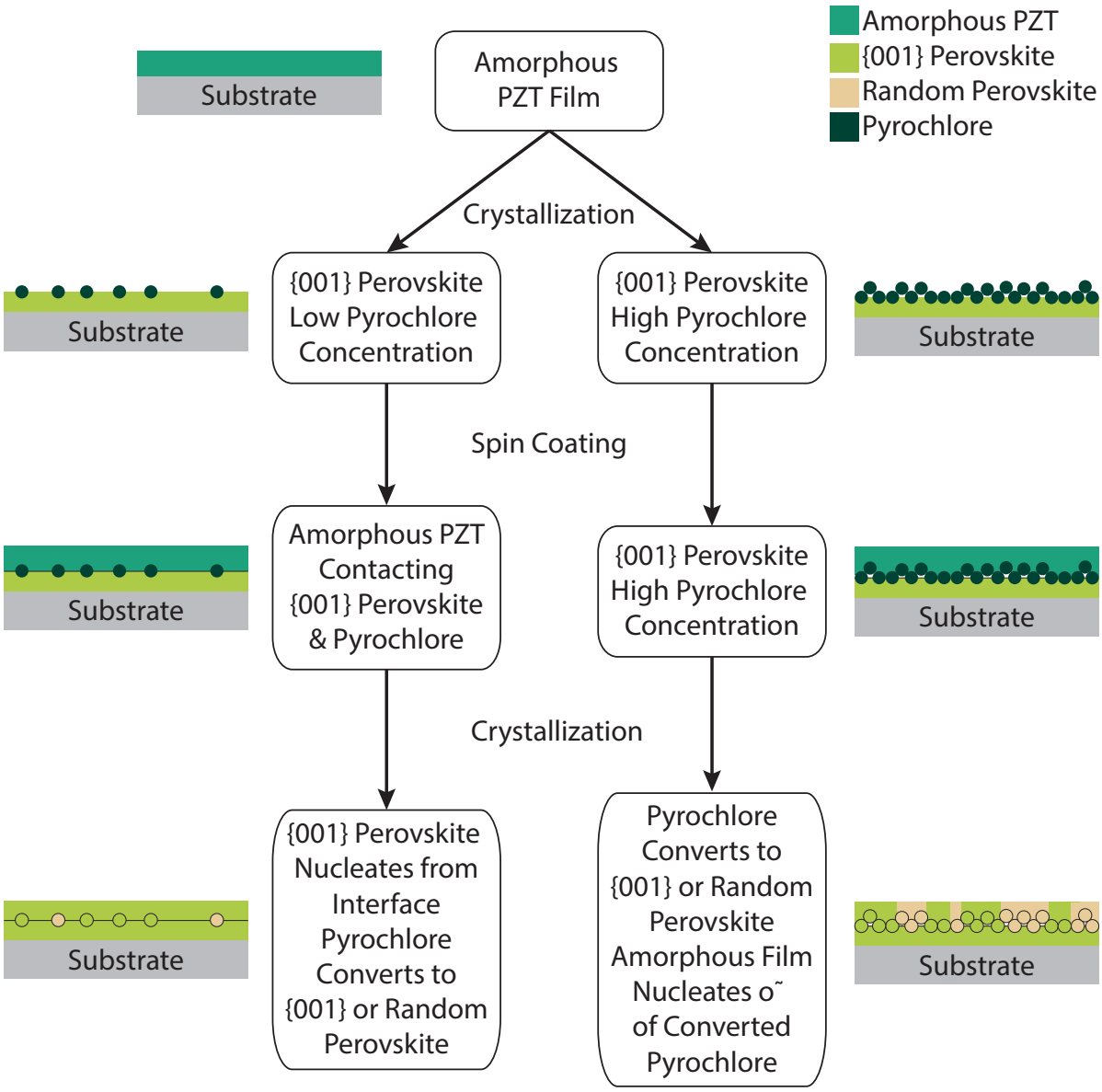

Figure 4.3: Flow chart depicting the crystallization of amorphous PZT on a {0 0 1} oriented PZT layer with low (left) or high (right) concentrations of pyrochlore.

unfavorable, nucleation of small, misoriented perovskite grains within the oriented perovskite matrix may occur.[125]

For the perovskite grains to nucleate in the amorphous layer from the underlying {0 0 1} PZT, contact must be made. Therefore, in cases of low pyrochlore concentrations (left half of Figure 4.3), one might expect that the film will maintain strong {0 0 1} texturing. However, as suggested by Carim *et al.*, some misoriented perovskite grains may form when converting pyrochlore with non-ideal orientations for conversion to perovskite. These misoriented grains may continue to grow if amorphous material remains surrounding the grains, leading to small amounts of misoriented material. Conversely, if the pyrochlore layer is thick and continuous (as in the right half of Figure 4.3), the amorphous PZT film will only be in contact with pyrochlore, not with the underlying {0 0 1} PZT. As a result, the amorphous PZT film must nucleate either from the pyrochlore layer, perovskite grains formed from converted pyrochlore, or other nucleation sites such as the surface. These other nucleation sites are likely to produce misoriented material.

While it is understood that low pyrochlore concentrations should be beneficial to maintaining strong {0 0 1} orientation, the point at which the pyrochlore concentration becomes substantial enough to inhibit orientation is unknown. This will, in part, depend on the fraction of pyrochlore which converts to {0 0 1} perovskite, as opposed to random perovskite upon conversion via additions of lead oxide. If the pyrochlore can be fully converted to {0 0 1} perovskite (using PbO cover-coats), then the converted pyrochlore should not affect the orientation of the overall film. However, if the surface pyrochlore is too thick, degradation of the orientation is expected. In this chapter, the use of lead oxide overcoats and alterations to solution lead excess levels were investigated as means of maintaining strong {0 0 1} texture in thick films.

4.2 Lead Oxide Coatings and Temperature Alterations to Remove Residual Surface Pyrochlore

First, the use of lead oxide overcoats was investigated as a means of converting surface pyrochlore on the films to the perovskite structure between crystallization steps. In principle, this method should help maintain strong {0 0 1} orientation. Concurrently, crystallization temperatures were lowered from 700 °C to 650 °C for some films in order to reduce lead volatilization and pyrochlore formation. Processing parameters are outlined in Table 4.2 with the following exceptions. PbO processing followed the same conditions as PZT, except for a reduced pyrolysis time of 2 min. Samples which were crystallized at 650 °C followed the same parameters except for the change in hold temperature for the crystallization step.

Layers of lead oxide were applied to each of the crystallization layer sets (either a single seed layer, or the set of 3 layers necessary for a gradient free film – 60/40, 52/48, and 44/56 Zr/Ti ratios). PbO overcoats were applied either before or after the crystallization of a set of layers. The former, in principle,

Table 4.2: Parameters used for PbO coating study

Parameter	Specifications
Substrate	PSU (HT)
Zr-Rich Solution	15 wt.% PZT 60/40 with 10% excess Pb
MPB Solution	15 wt.% PZT 52/48 with 10% excess Pb
Ti-Rich Solution	15wt. % PZT 44/56 with 10% excess Pb
PbO Solution	0.08 M PbO (2-methoxyethanol)
Spin Speeds (rpm)	6000 (seed layer) 4000 (bulk layers)
PZT Layers	1 seed and 2 x (3 - Gradient Free)
Thermal Processing	Tables 2.2 and 2.3 without drying step, PbO pyrolyzed for 2 min only

would prevent surface pyrochlore formation, while the latter would convert existing residual surface pyrochlore to perovskite. Finally, the crystallization temperature was also decreased without use of a PbO capping layer in order to reduce lead volatilization and subsequently the preponderance of lead-deficient pyrochlore formation. The three processing conditions are referred to in Figure 4.4 as PbO Before, PbO After and No PbO with the crystallization temperatures respectively.

X-ray diffraction patterns (Figure 4.4) show that application of additional lead oxide coatings before PZT crystallization results in orientation primarily along the {2 1 1} plane, rather than the desired {1 0 0} planes, regardless of crystallization temperature. This indicates that lead rich conditions at the top surface of the amorphous PZT film facilitate heterogeneous surface nucleation in a random orientation. If this is the case, a new grain structure would be expected with each layer. As seen in Figure 4.5 (a) and (b), additions of PbO prior to the crystallization step result in a new grain structure forming at each crystallization step, leading to a rough surface morphology. This phenomenon persisted, as shown in (a) and (b), independent of the crystallization temperature.

Films with PbO added after the PZT crystallization showed strong {1 0 0} orientation with Lotgering factors near or equal to 1. This indicates that residual pyrochlore may be successfully converted to oriented perovskite, or prevented from forming, reducing the impact on orientation quality. However, the films had a total of 3 crystallization steps, or two opportunities (two layer interfaces) for pyrochlore to degrade the orientation; thicker films may be necessary to determine the true success. Moreover, when lead oxide is added after crystallization, followed by recrystallization at 700 °C, the film is significantly smoother (Figure 4.5 (c)) and the cross section shows continuous grain structures between the layers (d). However, lead oxide applied after crystallization resulted in lead oxide precipitation on the surface of the film when combined with reduced crystallization temperatures (see Figure 4.5 (e)). The excess lead oxide is easily removable with the use of dilute acetic acid etching.

Finally, while processing at 650 °C with PbO capping layers produced reasonably clean XRD patterns, it is not enough to prevent surface pyrochlore formation in solutions with 10% excess lead (Figure 4.5 (f)).

Films 1.5 – 1.8 µm thick could be grown with Lotgering factors up to 0.97, using a PbO capping layer after crystallizing each layer set (i.e. 3 layers per crystallization for a gradient free film). However, the technique of PbO overcoats also resulted in films with Lotgering factors as low as 0.75. This range in variability suggests that the process of using capping layers is not robust. While the film is pure perovskite after the addition of a PbO overcoat, pyrochlore which converts to misoriented perovskite may exist in volume fractions below the detection limit of XRD, resulting in an apparently clean XRD pattern for thin films (Figure 4.4). As demonstrated in Figure 4.2, there are a broad range of pyrochlore surface

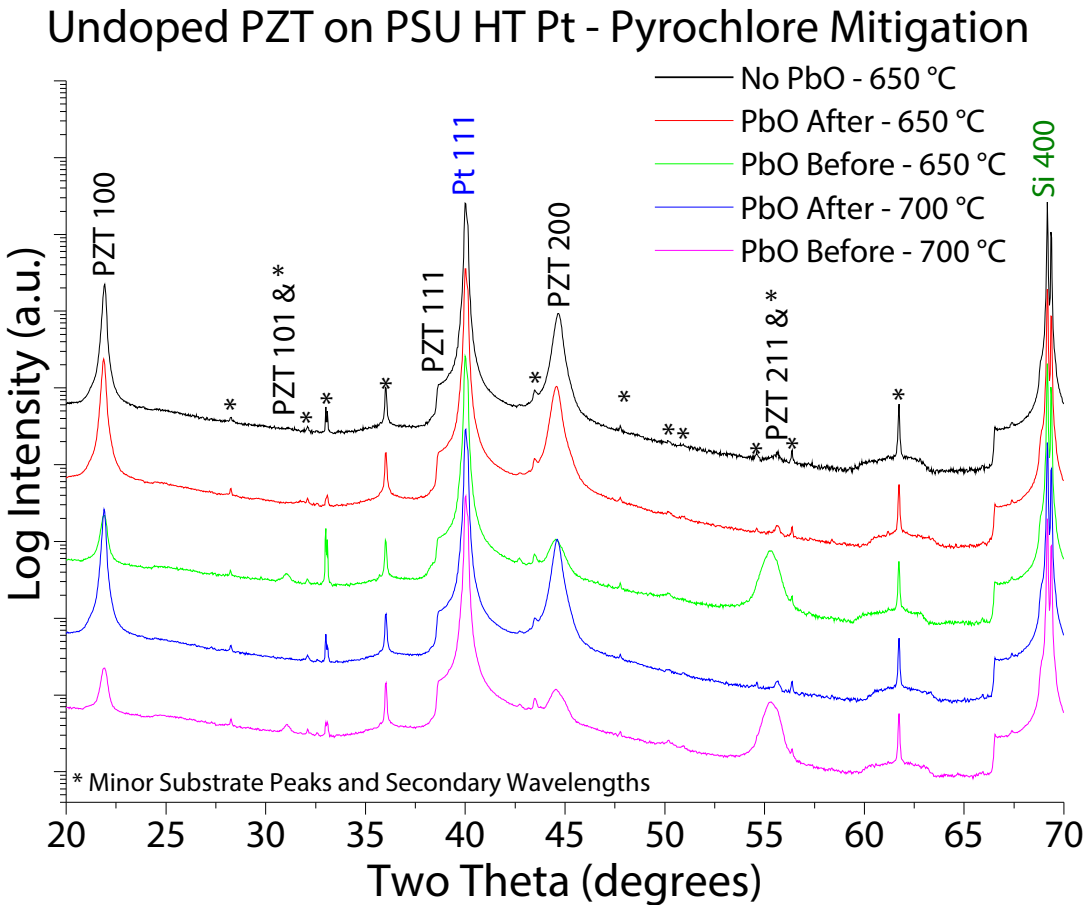

Figure 4.4: X-ray diffraction patterns of gradient free PZT thin films crystallized on high temperature platinum processed at PSU. Films were crystallized at either 700 °C or 650 °C and had additional lead oxide applied before or after PZT crystallization. One sample crystallized at 650 °C had no PbO applied

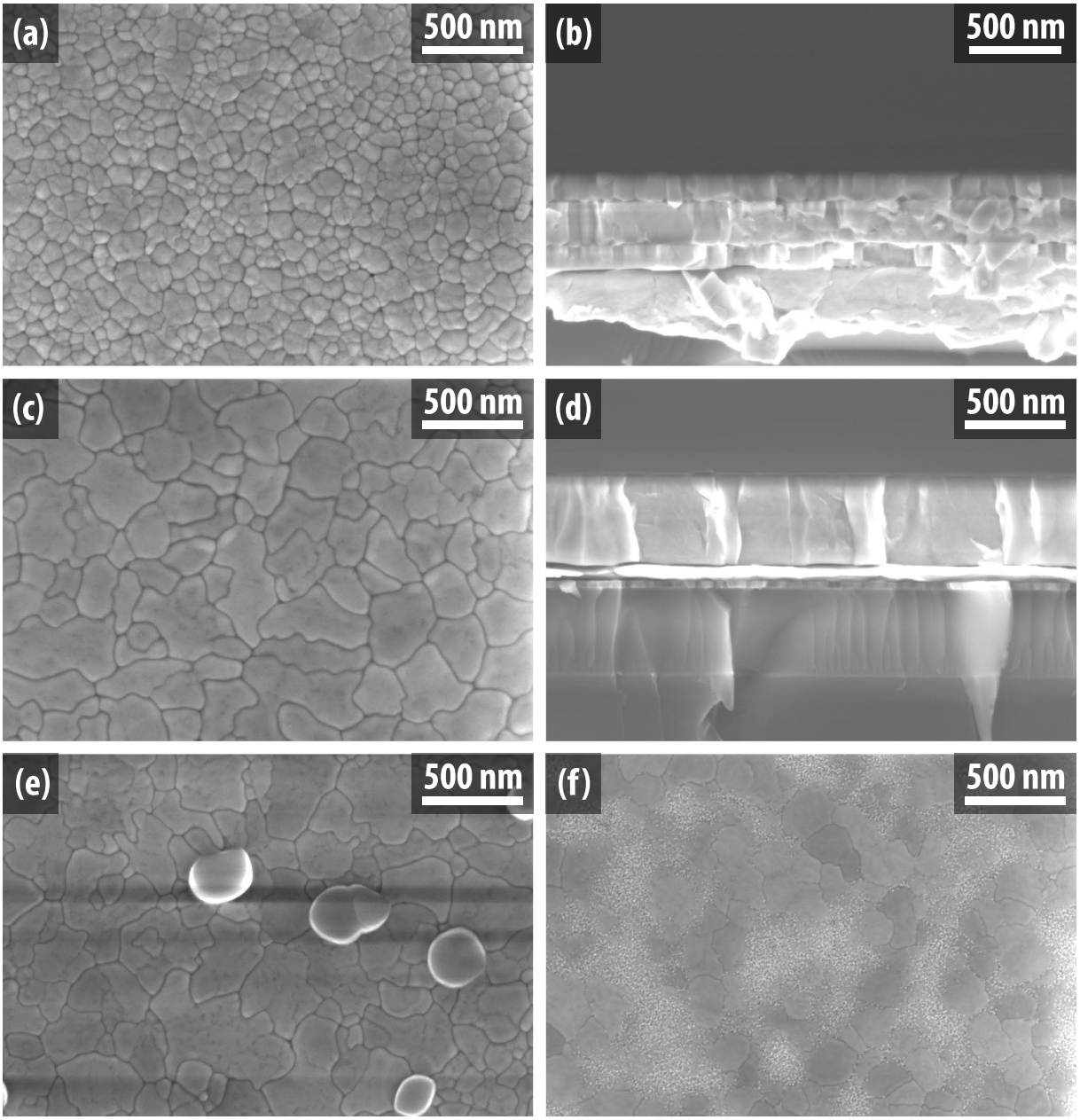

Figure 4.5: Micrographs collected of gradient free PZT thin films crystallized on PSU high temperature platinum. Films had the following crystallization temperatures and PbO treatments: (a) & (b) 700 °C with PbO before crystallization, (c) & (d) 700 °C with PbO after crystallization, (e) 650 °C with PbO after crystallization, and (f) 650 °C with no PbO

coverages on uncapped films, from pyrochlore-free to near complete surface coverage. This is likely to be what produces erratic orientation results.

4.3 Lead Excess in Solutions for Pyrochlore Mitigation

The use of lead oxide coatings increases processing time and complexity. Alternatively, misorientation could, in principle, be reduced by preventing formation of surface pyrochlore. Surface pyrochlore could be mitigated by the addition of excess lead to the solution. However, high levels of lead can result in films with high leakage currents, due to segregation of excess PbO to grain boundaries in the PZT.[140] The electrical resistivity of PbO is inferior to that of PZT.[1,141] Thus, the correct amount of excess lead content in solutions was investigated as a means of controlling the delicate balance between low lead content leading to high pyrochlore concentrations against high lead contents leading to degraded electrical properties.[142–145] This balance was further influenced by the variation in the lead partial pressure of the RTA.

In this study, XP HT platinized substrates were utilized. High temperature platinized silicon partially alleviates lead loss into the substrate. As discussed in Section 3.2, the differences between ARL and XP HT Pt wafers have a minor effect on the grain size of the seed layer. Fabricated films were niobium doped and gradient free in order to enhance the resultant piezoelectric properties, as discussed in Chapter 1. Additionally, one film was made with Mn doped layers near the electrode interfaces in order to test the hypothesis that thin layers of manganese doped PZT may enhance imprint and poling retention.(II)

Maximizing orientation of the first layer of thick films is critical, as degraded orientation in the seed will propagate through the film thickness. Niobium doped seed layers did not always enable strong $\{0\,0\,1\}$ preferential orientation on Pt, so a lead titanate seed layer was utilized to achieve a well oriented seed layer. A reduced seed layer pyrolysis temperature (Table 4.4) was also used due to the enhanced orientation quality observed. The lead titanate process utilized a composite procedure combining elements of Bintachitt & Doi *et al.*, all process parameters are outlined in Table 4.3.[97,108] Films were deposited using the layer sequences shown schematically in Figure 4.6.

Films 1.34 – 1.45 µm thick, grown with lead rich solutions, had Lotgering factors in excess of 0.99. This provides evidence that use an average of 14-17 at.% excess lead, with the thermal budget utilized by the RTA processes, is adequate to maintain highly $\{0\,0\,1\}$ oriented PZT throughout the film thickness. This result is in agreement with the results from Section 4.2; 10 at.% excess lead is not adequate for the thermal processing conditions utilized in this work, and that additional lead must be added to compensate for lead loss. Of further note, while a 6 at.% variation in lead excess resulted in only minor

(II) The rationale for the graded doping is described in more detail in Section 1.5. The use of a titanium-rich niobium doped layer at the top of the film was to maintain doping symmetry throughout the film thickness relative to the electrodes. In principle, Mn doped PZT at one electrode and Nb doped PZT at another electrode could lead to properties which are asymmetric with electric field direction.

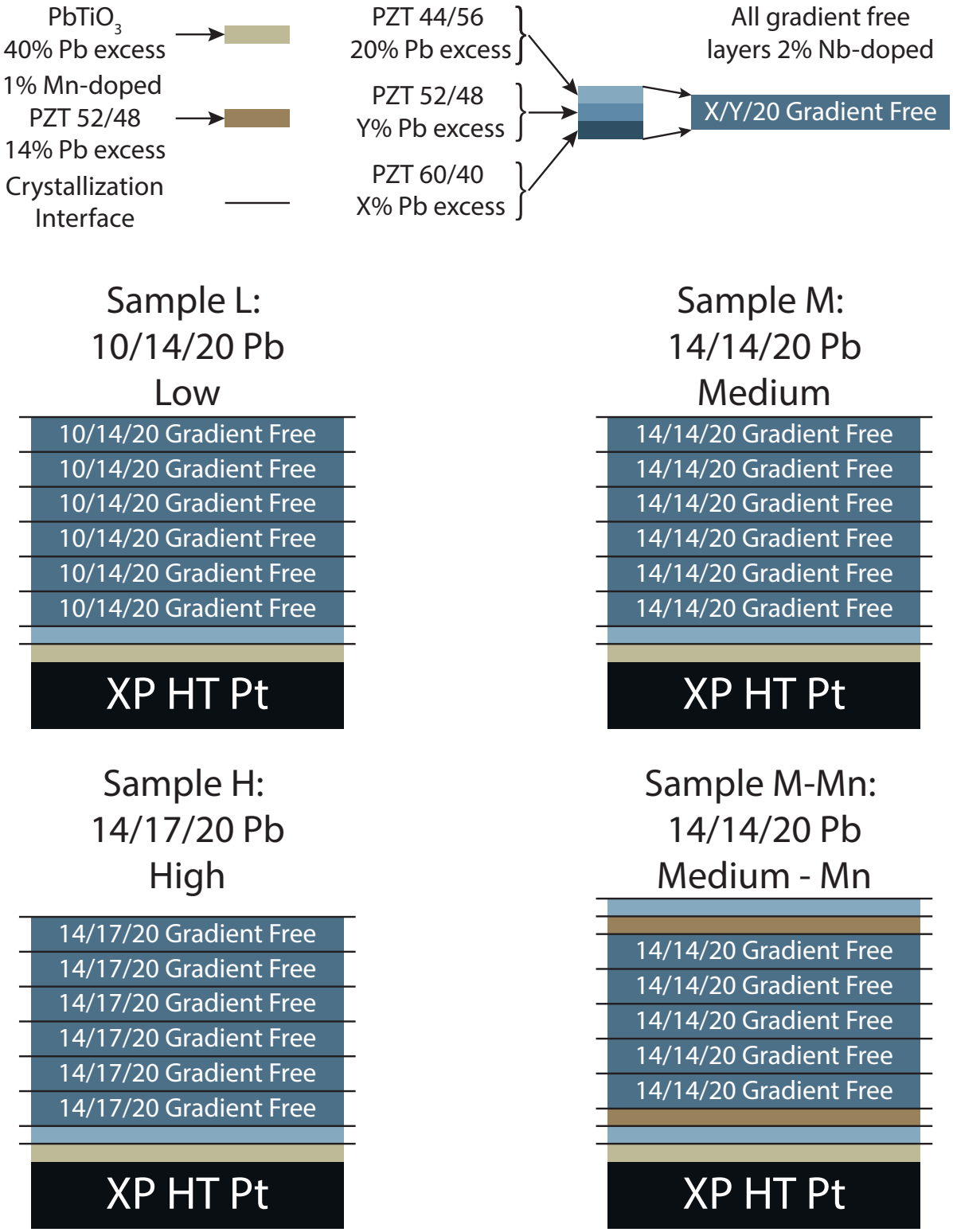

Figure 4.6: Schematics of the layer sequences utilized to deposit niobium doped gradient free thick films.

Table 4.3: Parameters used for lead excess study

Parameter	Specifications
Substrate	XP HT Pt
Nb-doped Zr-rich Solution	15 wt.% PZT 60/40 with 10 or 14% excess Pb & 2% Nb
Nb-doped MPB Solution	15 wt.% PZT 52/48 with 14 or 17% excess Pb & 2% Nb
Nb-doped Ti-Rich Solution	15wt.% PZT 44/56 with 20% excess Pb & 2% Nb
Mn-doped MPB Solution	15wt.% PZT 52/48 with 14% excess Pb & 1% Mn
$PbTiO_3$ (PT) Solution	3 wt.% PT with 40% excess Pb
Spin Speeds (rpm)	3000 (PT seed layer), 6000 (PZT seed layer), and 4000 (bulk layers)
Seed Layers	1 PT seed and 1 PZT 44/56 Seed
Bulk Layers	Figure 4.6
$PbTiO_3$ Seed Thermal Processing	Tables 4.4 and 4.5
PZT Seed Thermal Processing	Tables 2.3 and 4.4
PZT Bulk Thermal Processing	Tables 2.2 and 2.3

Table 4.4: Pyrolysis conditions for PT & PZT seed layers

Parameter	Condition
Temperature (°C)	200
Time (s)	150

Table 4.5: Lead titanate seed crystallization conditions used for thick film growth

Parameter	Condition
Ramp Rate 1 (°C/s)	10
Hold Temperature 1 (°C)	500
Hold Time 1 (s)	10
Ramp Rate 2 (°C/s)	1
Hold Temperature 2 (°C/s)	550
Hold Time 2 (s)	60
Atmosphere	O_2
Gas Flow (slpm)	2

changes to the microstructure and x-ray diffraction of PZT seed layers on high temperature platinum (Figures 3.4 to 3.6), a 6 at.% increase (from 10 at.% in Section 4.2 to an average of ∼16 at.% in this section) has a substantial influence on the quality and reproducibility of orientation which can be maintained to high film thicknesses. All films processed in this section have grains in the 50 – 400 nm range, with some pyrochlore present along grain boundaries. A ∼20% reduction in the grain size was observed in the film with Mn doped regions (M-Mn), as reported in the literature[37,49,72,130,131], however the average

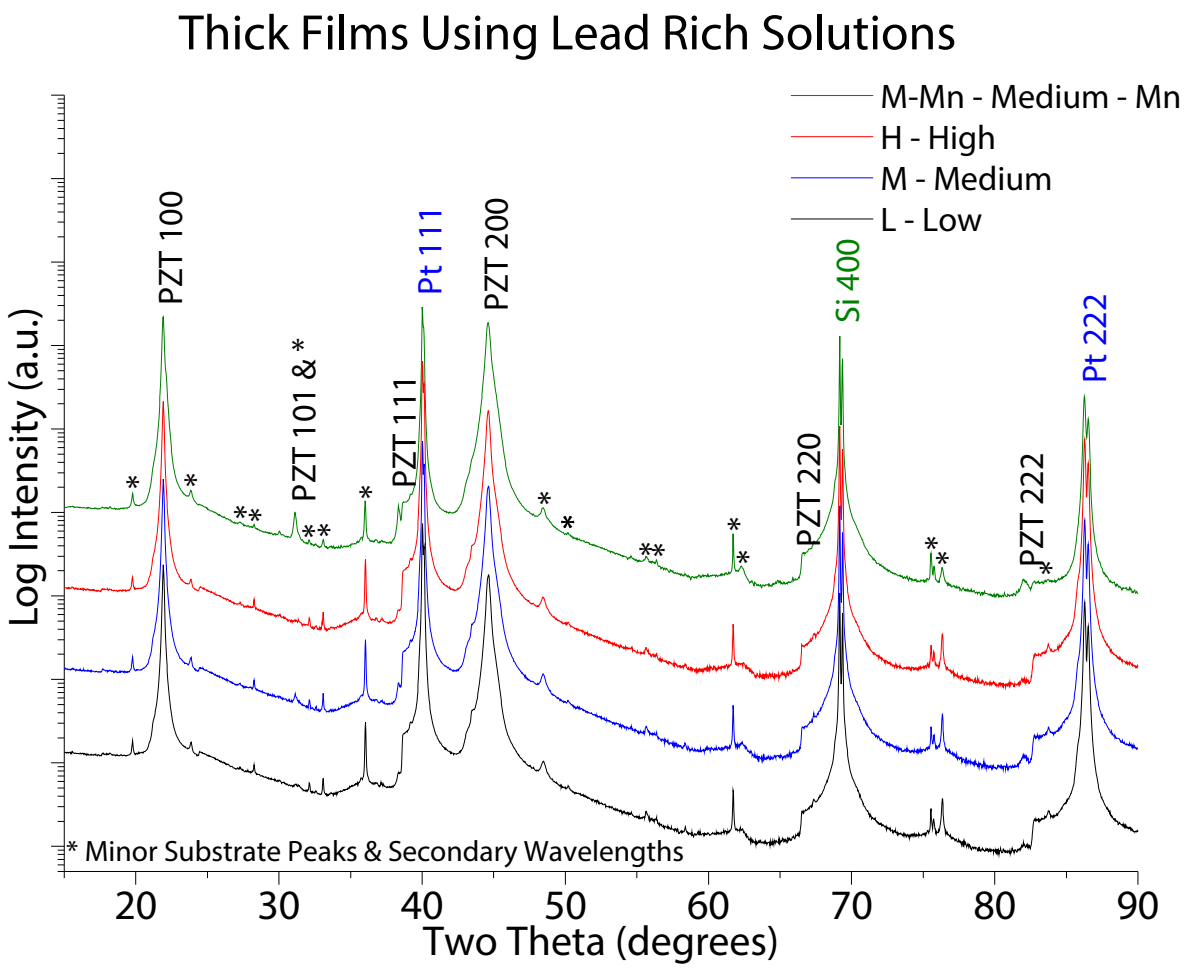

Figure 4.7: X-ray diffraction pattern of the gradient free PZT thick films (schematically represented in Figure 4.6) deposited on XP HT platinized silicon substrates. All films have Lotgering factors in excess of 0.99.

grain sizes of all films fall within the standard deviation of grain size in all other films. The cross sections of the films shows a highly dense, columnar structure with subtle crystallization interfaces visible.

Table 4.6: Average and standard deviation of grain size in PZT thick films processed with lead rich solutions.

Sample	Grain Size
L (Lowest Pb)	(190 ± 80) nm
M (Medium Pb)	(190 ± 90) nm
H (Highest Pb)	(200 ± 90) nm
M-Mn (Medium Pb with Mn Doped Regions)	(150 ± 70) nm

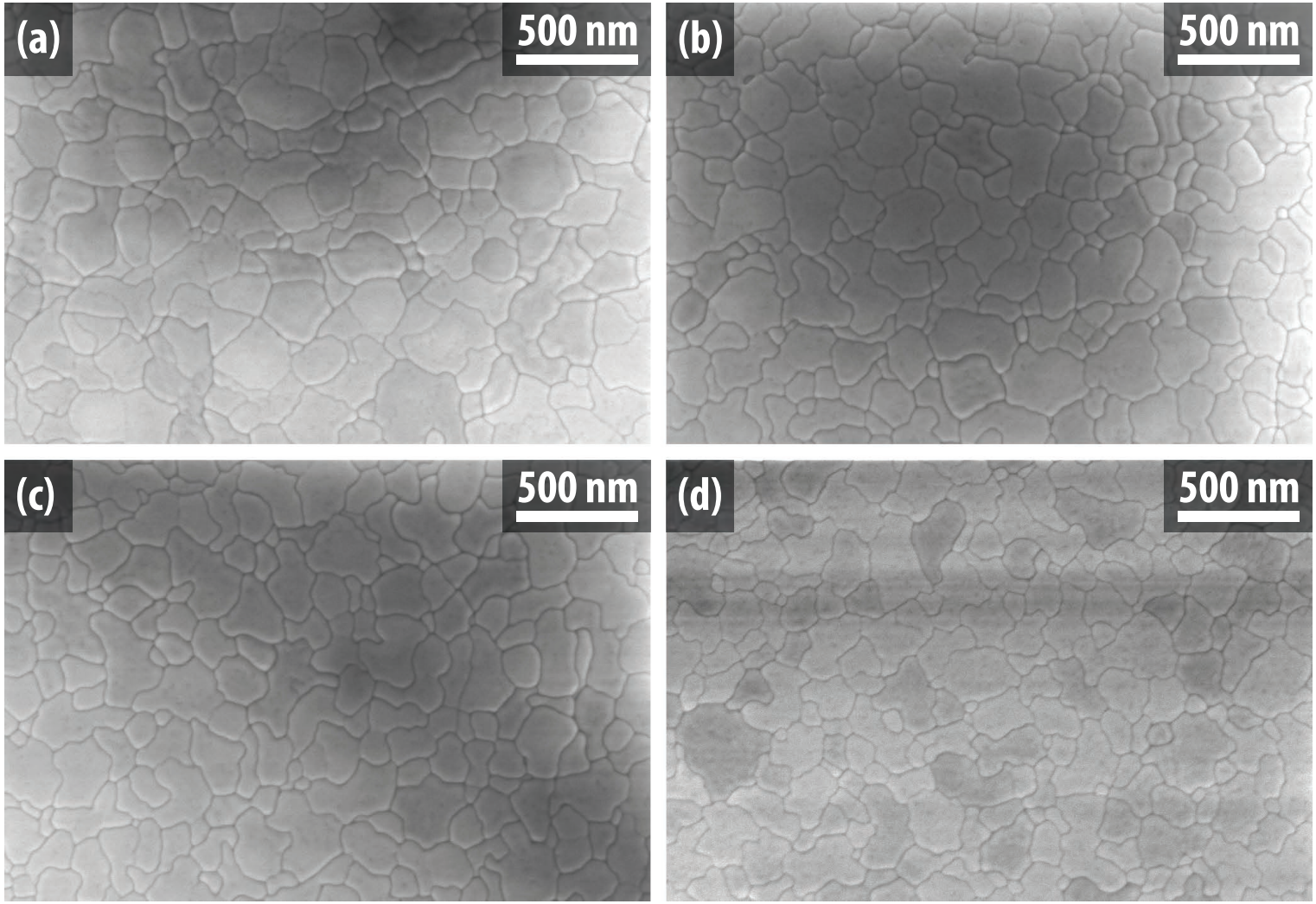

Figure 4.8: Surface micrographs of thick films grown on XP HT Pt. (a) Sample L - 10/14/20 at.% lead excess (low), (b) Sample M - 14/14/20 at.% lead excess (medium), (c) Sample H - 14/17/20 at.% lead excess (high), (d) Sample M-Mn - 14/14/20 at.% lead excess with Mn doping near the electrode interfaces (medium-Mn).

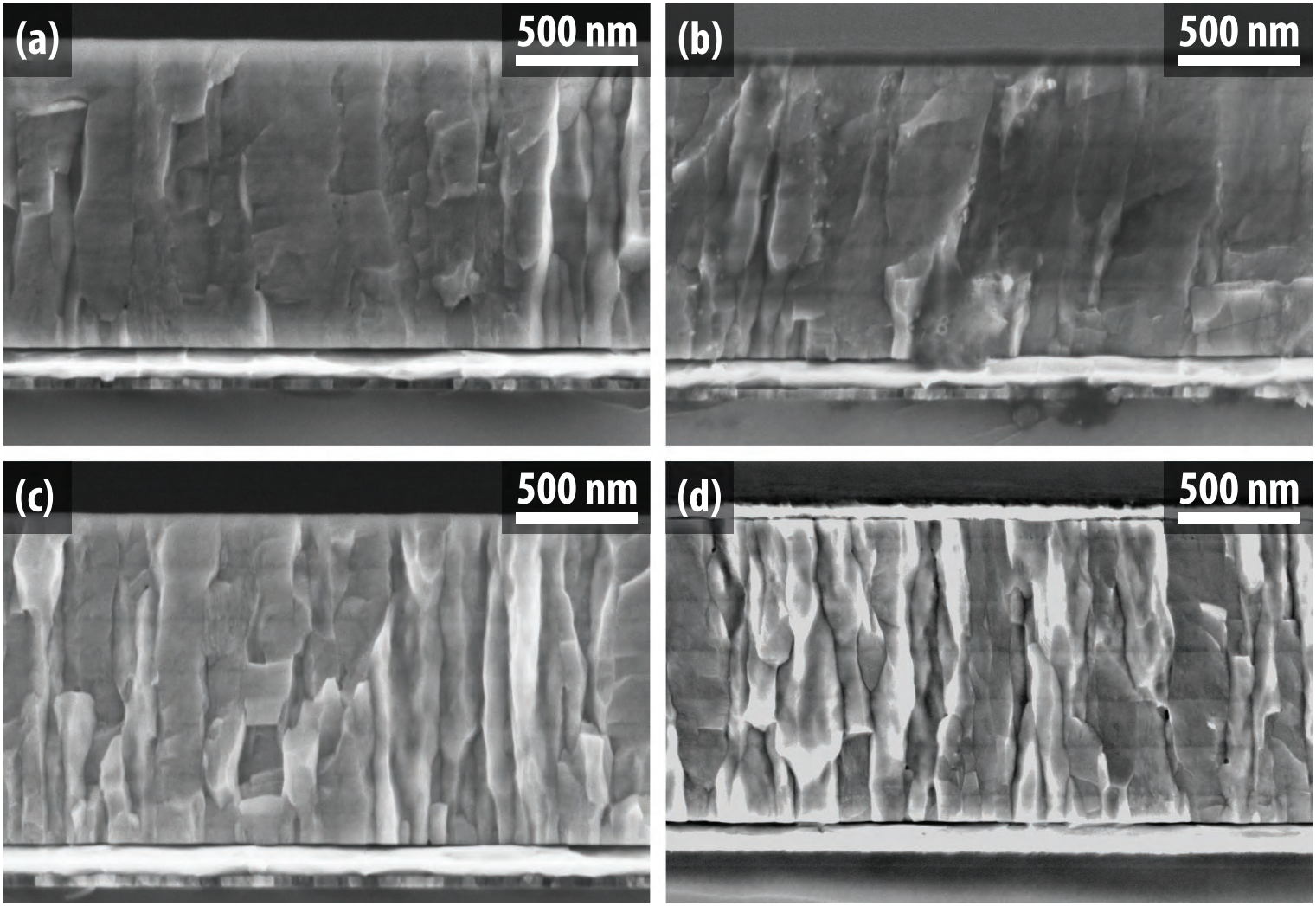

Figure 4.9: Cross sectional micrographs of thick films grown on XP HT Pt. (a) Sample L - 10/14/20 at.% lead excess (low), (b) Sample M - 14/14/20 at.% lead excess (medium), (c) Sample H - 14/17/20 at.% lead excess (high), (d) Sample M-Mn - 14/14/20 at.% lead excess with Mn doping near the electrode interfaces (medium-Mn). Cross sections were taken of cleaved specimens near the sample edges. Apparent sample thicknesses are not necessarily indicative of the sample as a whole.

4.4 Conclusions on Growth of Doped Thick Films

While lead content does not appear to make substantial differences in formation of well oriented seed layers on high temperature platinum, it was demonstrated to have a substantial role in maintaining strong $\{0\,0\,1\}$ orientation in thick films. For the thermal processing conditions used in this work, lead excess on the order of 16 at. % allowed growth of 1.34 – 1.46 μm thick films with Lotgering factors ≥ 0.99 in the equipment and processing environment of this work. If this study were repeated on room temperature platinum, it is suspected that higher lead contents than those necessary for HT Pt would be required for the first few layers while diffusion into the substrate is still kinetically favorable. As the film becomes thicker, the diffusion of lead, from the new surface layers of the film into the substrate, will become less favorable in the short time frames utilized for crystallization.

Chapter 5

Electrical and Piezoelectric Characterization of Strongly {0 0 1} Oriented PZT Thick Films

The films deposited in Section 4.3 were used to study the impacts of two compositional factors on the properties of the resulting PZT thick films.[(I)] Using samples L (lowest lead), M (medium), and H (highest lead), the effects of solution lead excess on the properties of phase pure (to the detection limits of XRD) strongly oriented films can be ascertained. More lead rich solutions were explored to alleviate concerns with pyrochlore formation and grain misorientation, but there should be an optimum lead concentration above which excess PbO segregates to the grain boundaries, producing leakage pathways.[129,146,147] Thus, it is of interest to see if there are any enhancements or reductions in properties as a consequence of adding more lead than necessary to produce highly oriented films.

Similarly, using samples M and M-Mn, the effects of a small amount of Mn doped PZT (∼10 vol.%) on the peak electrical and piezoelectric properties, as well as lifetime and poling retention can be studied. Of particular interest was whether a small amount of Mn can be used to either stabilize the remanent polarization direction or modulate Schottky barrier heights at the electrodes without degrading the induced strain response. Due to the layer sequence in sample M-Mn (a total of 5 gradient free layer sets, 2 44/56 PNbZT layers, 2 52/48 PMnZT layers and a $PbTiO_3$ layer) as compared to sample M (a total of 6 gradient free layer sets, 1 44/56 PNbZT layer and a $PbTiO_3$ layer) a small decline in properties may be expected as a consequence of the increased Zr/Ti compositional inhomogeneity in sample M-Mn.[27] In applications where a specific thickness (and by extension total number of layers) and graded doping are desired, removing one gradient free layer set (i.e. decreasing the volume fraction of gradient free material) and substituting with multiple, individually crystallized, gradient-bearing, layers may be necessary to maintain the desired thickness.

5.1 Dielectric and Ferroelectric Properties

5.1.1 Frequency Dependence of Dielectric Response

The dielectric constant and loss as a function of frequency (10^2 – 10^5 Hz)[(II)] are presented in Figure 5.1. Sample M-Mn exhibits a reduced dielectric constant (approximately 7%) and the marginally lowest

[(I)] The high, similar Lotgering factors (0.99+) for this film set, enable attributing the majority of the differences in properties to compositional differences between samples, rather than a mix of composition and texture quality. The large range of Lotgering factors for the films in Section 4.2 hindered the ability to draw any meaningful conclusions on compositional differences.

[(II)] While the LCRs used in this work are capable of 1 – 2 MHz (depending on the model), the RC time constant of the measurement setup and sample capacitor are on the order of 10^{-6} s. This results in an artificially high tan δ at such frequencies. As such, all frequency dependent data are truncated to 10^5 Hz.

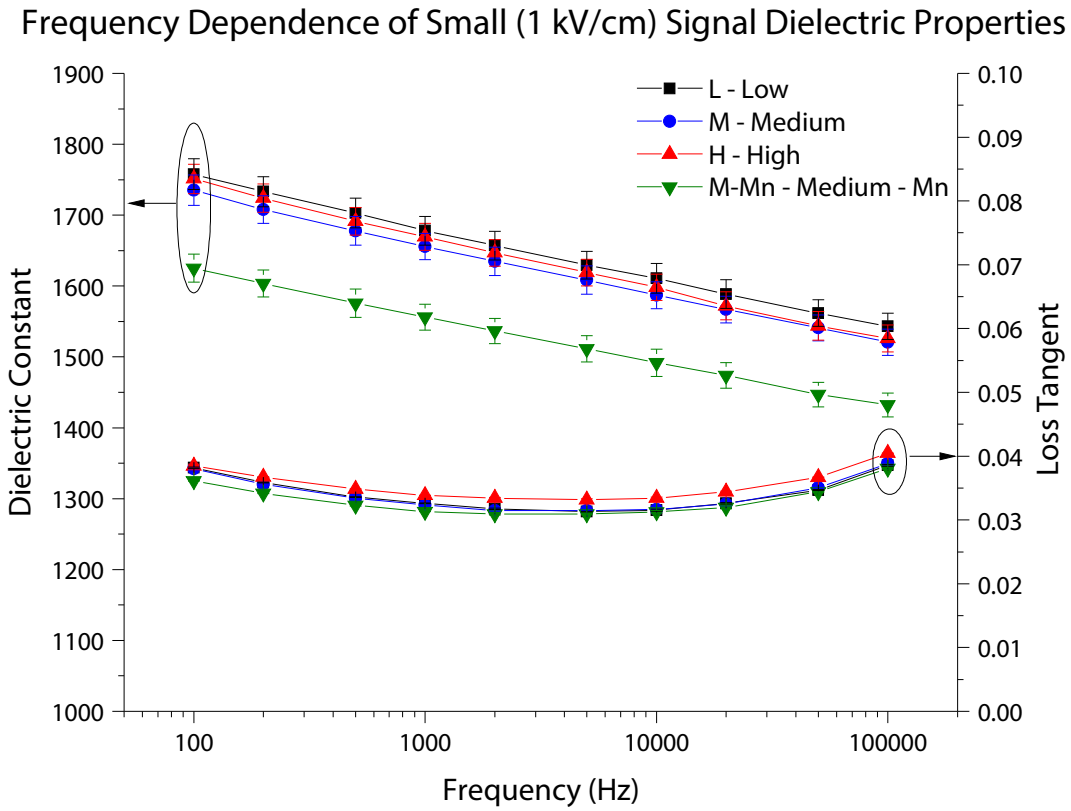

Figure 5.1: Dielectric constant and loss tangent of all samples as a function of frequency. All datapoints were collected with a 1 kV/cm excitation signal. Error bars represent the standard deviation across multiple electrodes plus 1.5% error from film thickness and electrode diameter.

loss of any of the samples. The small reduction in dielectric loss is comparable to the observations by Zhu *et al.* on acceptor doped PZT films.[37] The large reduction in dielectric constant is believed to be a consequence of a combination of the manganese doping (with associated reductions in extrinsic contributions to ε_r) and the layer sequence used to deposit the film (with the associated increase in Zr/Ti gradients). Calame & Muralt observed a ∼30% increase in the dielectric constant for gradient free films when compared to gradient-containing counterparts.[27] In the case of sample M-Mn, ∼ 80 vol.% of the film is gradient free whereas approximately ∼ 94 vol.% of the film is gradient free in L, M, and H. Furthermore, Zhu *et al.* observed a ∼ 20% decrease in the dielectric constant upon 1% Mn doping relative to an undoped film, and a ∼ 15% increase of the dielectric constant upon 2% Nb doping.[37,38]. In sample M-Mn, approximately 10 vol.% of the material is Mn doped instead of Nb doped.

If γ is defined as the ratio of dielectric constants (of a given layer composition compared to undoped, gradient-bearing, MPB PZT), then γ for the layers used in each film are defined in Equation (5.1).[27,37,38,148] Each film can be modeled as a series of capacitors (Equation (5.2)) representing the different layers where v is the thickness fraction of each layer ($v_{L,M,H}$ and v_{M-Mn} represent the entire

film and are, by definition, equal to 1). From this series capacitor model, the γ for each film can be calculated (Equations (5.3) and (5.4)).[III]

$$\gamma_{GF} \approx 1.3 \quad \gamma_{2\%\ Nb} \approx 1.15 \quad \gamma_{1\%\ Mn} \approx 0.8 \quad \gamma_{44/56} \approx 0.77 \quad \gamma_{PbTiO_3} \approx 0.076 \tag{5.1}$$

$$\frac{1}{C_{L,M,H}} = \frac{1}{C_{PbTiO_3}} + \frac{1}{C_{44/56,\ 2\%\ Nb}} + \frac{1}{C_{GF,\ 2\%\ Nb}} \tag{5.2}$$

$$\frac{\nu_{L,M,H}}{\gamma_{L,M,H}} = \frac{\nu_{PbTiO_3}}{\gamma_{PbTiO_3}} + \frac{\nu_{44/56,\ 2\%\ Nb}}{\gamma_{44/56,\ 2\%\ Nb}} + \frac{\nu_{GF,\ 2\%\ Nb}}{\gamma_{GF,\ 2\%\ Nb}} = \frac{0.013}{0.076} + \frac{0.052}{0.77 \times 1.15} + \frac{0.935}{1.3 \times 1.15} = \frac{1}{1.17} \tag{5.3}$$

$$\begin{aligned}\frac{\nu_{M-Mn}}{\gamma_{M-Mn}} &= \frac{\nu_{PbTiO_3}}{\gamma_{PbTiO_3}} + \frac{\nu_{44/56,\ 2\%\ Nb}}{\gamma_{44/56,\ 2\%\ Nb}} + \frac{\nu_{GF,\ 2\%\ Nb}}{\gamma_{GF,\ 2\%\ Nb}} + \frac{\nu_{1\%\ Mn}}{\gamma_{1\%\ Mn}} \\ &= \frac{0.013}{0.076} + \frac{0.104}{0.77 \times 1.15} + \frac{0.779}{1.3 \times 1.15} + \frac{0.104}{0.8} = \frac{1}{1.06}\end{aligned} \tag{5.4}$$

By definition, the ratio of the dielectric constants should be equivalent to the ratio of the γ values for each film. The range of the ratio of the dielectric constants of L, M, or H (uniform doping) to M-Mn (graded doping) was calculated at 100 Hz from Figure 5.1, while the ratio of $\gamma_{L,M,H}$ to γ_{M-Mn} was calculated from Equations (5.3) and (5.4). The values are close at the upper bound (sample L vs M-Mn, yielding a ratio of 1.08) and are within 4% at the lower bound (sample L vs M-Mn, yielding a ratio of 1.065), indicating that the reduction in dielectric constant observed in sample M-Mn is close to the expected value.

$$\frac{\varepsilon_{L,M,H}}{\varepsilon_{M-Mn}} = \frac{\gamma_L}{\gamma_{M-Mn}} \qquad \frac{\varepsilon_{L,M,H}}{\varepsilon_{M-Mn}} = \frac{1655 \text{ to } 1680}{1555} = 1.065 \text{ to } 1.08 \qquad \frac{\gamma_{L,M,H}}{\gamma_{M-Mn}} = \frac{1.17}{1.06} = 1.10 \tag{5.5}$$

In principle, the only difference between samples L, M, and H is the lead stoichiometry of the solution, and subsequently of the film. Marincel *et al.* examined the role of controlled lead oxide content on the dielectric and piezoelectric properties of PZT 52/48 and 30/70 thin films. They observed that the dielectric constant increased with lead content from low lead conditions (pyrochlore formation) to high partial pressures of lead (near the PbO(g)−PbO(s) equilibrium). The total reported change in the dielectric constant was a transition from 1100 in the low lead case to 1150 in the high lead case for films with a fixed microstructure.[144] As in the work of Marincel *et al.*, no statistically significant difference in grain size is observed between films with the exception of M-Mn, which has a smaller grain size yet still remains within a standard deviation of the average values (Table 4.6). All uniformly niobium doped films in this work have very similar dielectric constants (within error bars associated with film thickness and electrode area uncertainty) and no statistically significant trend as a function of lead content. While Marincel *et al.* did have overlapping error bars, the data reported were spread further apart such that error

[III] The effects of solution lead stoichiometry are ignored in this calculation. Additionally, the $PbTiO_3$ layer is assumed to be 20 nm thick and all PZT layers are assumed to be 80 nm thick, (i.e. a gradient free set is 240 nm thick).

bars did not completely overlap all other data points (i.e. the error bars for the sample with the highest dielectric constant did not capture the data point for the sample with the lowest dielectric constant). This increased spread of data might be anticipated due to the wider range of lead stoichiometry examined by Marincel *et al.*[144]

5.1.2 Rayleigh Law - Electric Field Dependence of the Dielectric Constant

The electric field dependence of dielectric constant was measured as a function of frequency.[(IV)] Linear fits were calculated to determine the Rayleigh Law coefficients for each sweep. A sweep at 1 kHz and the accompanying linear Rayleigh Law fit is presented for each sample in Figure B.14. The dielectric constant exhibited a linear dependence on electric field (i.e. Rayleigh behavior) from ∼5 – 25 kV/cm, in relative agreement with the results of Bintachitt (up to approximately half of the coercive field)[108] and Bassiri-Gharb (∼12 – 36 kV/cm).[149] The Rayleigh Law coefficients ε_{init} and α'_{ε} and the ratio of the coefficients are plotted as a function of frequency in Figure 5.2.

The reversible coefficient, ε_{init} (representing the intrinsic lattice response and reversible domain wall motion) exhibits a similar trend to that of the small signal dielectric response (i.e. no statistically significant trend as a function of lead content). This is expected as the reversible coefficient is the extrapolation of the permittivity to 0 field. As observed by Zhu *et al.*, Mn doping should reduce ε_{init} relative to undoped and Nb doped films as a consequence of domain wall pinning attributed to $V_O^{\bullet\bullet}-Mn'_{Ti/Zr}$ (or $Mn''_{Zr/Ti}-V_O^{\bullet\bullet}$) defect dipoles.[37] However, Bastani & Bassiri-Gharb reported an increase in the ε_{init} when transitioning from gradient free films to single layer crystallizations (as used in the Mn and additional Ti-rich layers).[31] In the case of sample M-Mn, either no enhancement is observed from the gradient single layer crystallizations, or the reduction associated with Mn doping is greater than any enhancement from the gradient layers.

Although the variations between undoped polycrystalline PZT 52/48 samples with different lead contents were modest in Marincel *et al.*, the variations in the Nb doped films of this work were half of those observed by Marincel *et al.* at frequencies above 1 kHz (Figure 5.3) and statistically insignificant relative to error bars. No difference in phase purity was observed between samples L, M, and H; only perovskite grains were observed in the SEM, with no PbO or pyrochlore secondary phases. Conversely, Marincel *et al.* equilibrated the low and high lead films in partial pressures of lead oxide just short of the bounds for secondary phase formation (pyrochlore and PbO respectively).[144] As such, the lead content range in samples L, M, and H should, in principle, be smaller than that in Marincel *et al.*; subsequently the properties of L, M, and H may also be expected to vary by a smaller amount than in the work of Marincel *et al.*[144]

[(IV)] Samples were heated at 500 °C to reset the domain structure, followed by aging of the unpoled domain structure for 12 h at 150 °C in order to ensure the domain structure in each film had the same thermal history prior to measurement.

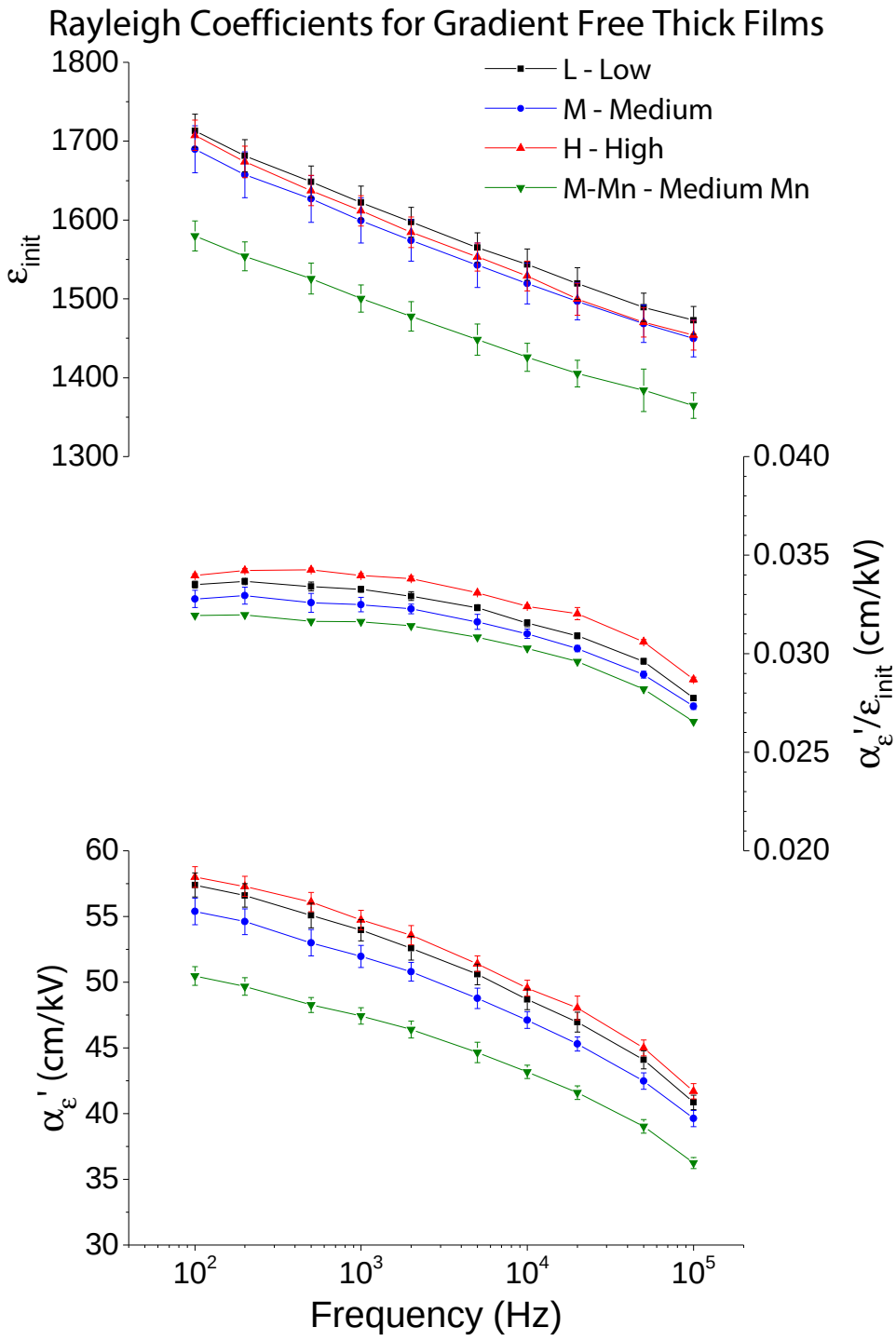

Figure 5.2: Frequency dependence of the reversible (ε_{init}), irreversible (α'_ε) Rayleigh coefficients and the ratio of the irreversible to reversible coefficients. Error bars represent the standard deviation across multiple electrodes plus 1.5% error from film thickness and electrode diameter.

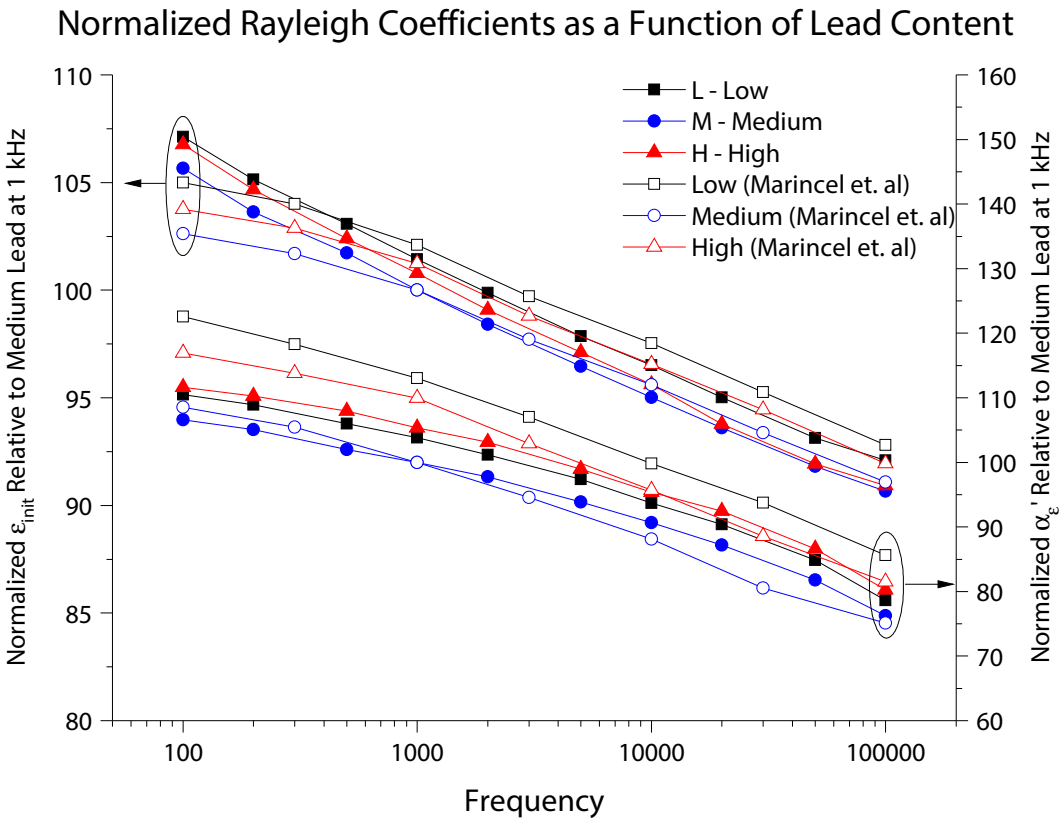

Figure 5.3: Normalized irreversible and reversible Rayleigh Law coefficients from Figure 5.2 (closed symbols) and Marincel *et al.* (open symbols).[144] Both datasets were normalized such that the value for the medium lead content sample at 1 kHz was set to be 100 for each coefficient and data source (this work and [144]). For example, Marincel *et al.*'s 1 kHz, medium lead ε_{init} data point was normalized to 100 and all remaining ε_{init} data points (across all of Marincel *et al.*'s samples) were normalized by the same normalization factor. This process was repeated for α_{ε} in Marincel *et al.* and both coefficients in this work. Variations in ε_{init} as a function of lead content fall within error bars for Marincel *et al.*, all other variations as a function of lead content and frequency fall outside of error bars.

The irreversible Rayleigh Law coefficient, α'_ε measures irreversible domain wall motion contributions to the dielectric constant below the switching field. The manganese doped film exhibited a reduced irreversible coefficient relative to the uniformly doped films (by ∼12% in the range of 10^2 – 10^5 Hz; yielding values of ∼52 – 55 cm/kV and 47 cm/kV at 1 kHz for uniformly (Nb) doped and graded doped (regions of Mn doping) films). This is likely a consequence of $Mn'_{Zr/Ti}-V_O^{\bullet\bullet}$ (or $Mn''_{Zr/Ti}-V_O^{\bullet\bullet}$) defect dipoles which can serve as pinning sites for domain walls, restricting their motion.[37,144] Similar behavior was observed by Zhu *et al.* in uniformly doped films, with α'_ε of 50 cm/kV and 36 cm/kV for 2% Nb and 1% Mn doped films respectively.[37,38] Similarly to the ε_{init} coefficient, Bastani & Bassiri-Gharb also reported an enhancement of the α'_ε in films with layers crystallized individually (with a Ti/Zr gradient).[31] If such an enhancement is present (from a Ti/Zr gradient) in the Mn doped and Ti-rich layers, it does not appear to counteract the properties reduction associated with Mn doping and the Ti-rich (44/56) layer.

Of the uniformly Nb doped thin films, samples H and L exhibit similar α'_ε values (nearly within error bars) while M falls closely to M-Mn. Based on the theory that point defects (including lead vacancies) can pin domain walls, one might anticipate that the α'_ε of H would be higher than that of M as domain walls would move more freely as a consequence of fewer lead vacancies and compensating oxygen vacancies.[144] However, the theory of domain wall pinning by lead vacancies does not adequately explain the high irreversible Rayleigh coefficient observed in the low lead film (L) relative to the medium lead film (M). Marincel *et al.* noted that if domains were pinned by lead vacancies (or defect dipoles with a lead vacancy), the pinning strength may be intermediate as differences most clearly manifested themselves in minor loops. As was the case for the reversible Rayleigh coefficient, the variations in the irreversible Rayleigh coefficient were observed to be half as large as those observed by Marincel *et al.*[144,150] Given the narrower window of lead stoichiometry used in this work, sample L should, in principle, have fewer lead vacancies than the lead-poor sample from Marincel *et al.*, making it subject to less pinning from lead vacancies (or associated defect complexes). However it remains unclear why the irreversible coefficient of sample M is significantly lower than those of samples L and H. It is noted, though, that the same trend was observed by Marincel *et al.* in undoped 52/48 PZT thin films.[144]

$$A(\omega) = a_0 + a \ln\left(\frac{1}{\omega}\right) \tag{5.6}$$

The frequency dependencies of the reversible and irreversible Rayleigh coefficients are presented in Table 5.1. A larger value of the slope indicates a greater sensitivity of the Rayleigh coefficients to frequency in the range of the fit (100 – 5000 Hz) while a larger value of the intercept indicates a higher base value of the Rayleigh coefficient at low frequencies.[(V)] When comparing the intercept values for ε_{init} and α'_ε between the samples of this work and those in the work of Bassiri-Gharb, it is immediately apparent that

[(V)] By definition, from Equation (5.6), the intercept is the Rayleigh coefficient extrapolated to $1/2\pi$ Hz or ∼0.159 Hz

Table 5.1: The logarithmic frequency dependence of the Rayleigh coefficients in Figure 5.2. Fitted with Equation (5.6) where A is either the irreversible or reversible Rayleigh coefficient, a_0 and a are the fitting coefficients, and $\omega = 2\pi f$. Values from this work are compared to the work of Bassiri-Gharb on $PbYb_{0.5}Nb_{0.5}O_3-PbTiO_3$ films.[149] Data on samples L, M, H, and M-Mn were fit from 100 – 5000 Hz to avoid including any bridge artifacts. All gt fits had R^2 values in excess of 0.98. Error is the standard error of the fit with a 95% confidence intervals

Sample	Frequency Dependence of ε_{init}	Frequency Dependence of α'_ε (cm/kV)
Sample L - Low	$(1950 \pm 20) + (37.5 \pm 2.1)\ln(1/\omega)$	$(68.9 \pm 2.0) + (1.74 \pm 0.08)\ln(1/\omega)$
Sample M - Medium	$(1930 \pm 20) + (37.3 \pm 2.3)\ln(1/\omega)$	$(66.5 \pm 1.8) + (1.68 \pm 0.21)\ln(1/\omega)$
Sample H - High	$(1960 \pm 25) + (39.2 \pm 2.8)\ln(1/\omega)$	$(69.2 \pm 2.8) + (1.68 \pm 0.33)\ln(1/\omega)$
Sample M-Mn - Medium - Mn	$(1795 \pm 10) + (33.5 \pm 1.1)\ln(1/\omega)$	$(60.1 \pm 1.4) + (1.47 \pm 0.17)\ln(1/\omega)$
{1 0 0} Textured $PbYb_{0.5}Nb_{0.5}O_3-PbTiO_3$[149]	$1452 + 33\ln(1/\omega)$	$34.2 + 1.64\ln(1/\omega)$
{1 1 1} Textured $PbYb_{0.5}Nb_{0.5}O_3-PbTiO_3$[149]	$1264 + 29\ln(1/\omega)$	$33.8 + 2.16\ln(1/\omega)$

PZT (particularly {0 0 1} textured, gradient free, niobium doped, MPB PZT) has significantly enhanced irreversible and reversible dielectric responses when compared with $PbYb_{0.5}Nb_{0.5}O_3-PbTiO_3$ in the low frequency / kinetically slow limit. Similarly, it is apparent that, even with low frequency excitation signals, films with manganese doping exhibit a reduced irreversible and reversible response relative to niobium doped PZT.[VI] It is worth noting that the films in this thesis are over twice the thickness of those studied by Bassiri-Gharb (1.37 – 1.46 μm vs 0.6 μm respectively), as such an increased extrinsic contribution may be expected in the films of this work.[149,151–153]

Moreover, the relative frequency dependencies (a in Equation (5.6)) of these PZT is approximately double those of $PbYb_{0.5}Nb_{0.5}O_3-PbTiO_3$ in the measured frequency regime. The higher slope (frequency sensitivity) suggests that more of the pinning events have characteristic relaxation times in this frequency range, so that they are gradually lost from the response. Thus a small change in frequency can have a significant impact on the response as some of the contributing population may no longer be able respond in time. A lower slope (frequency insensitivity) could indicate either that some of the domain walls are already kinetically limited from contributing at the frequency of interest or that all of the domain walls are significantly faster kinetically than the frequency of interest. However, it is worth noting that if a decrease in the slope and intercept of the fit are both observed, this may be a consequence of a lower overall response.[149]

The niobium doped films within this work (L, M, and H) exhibit a modest enhancement in the frequency sensitivity of the reversible Rayleigh coefficient (ε_{init}) relative to the undoped PYbN-PT films of Bassiri-Gharb.[149] Causes of this increase would manifest from differences in the reversible domain wall motion between PZT and PYbN-PT (as the intrinsic lattice response should not be affected in this frequency range). While niobium has been demonstrated to soften the Rayleigh response, increasing both the irreversible and reversible coefficients,[38] such a difference could also be a result of relative densities and frequency dependencies of reversibly mobile domain walls in Nb-doped PZT and PYbN-PT and the higher extrinsic contribution in the thicker PZT films.[149,152] When comparing the PZT films within this work, the films with variations in lead content all exhibit similar (within error bars) frequency dependencies of ε_{init}. Conversely, the Mn doped sample exhibits a ∼12% reduction in the frequency dependence of ε_{init}. This can be attributed to domain wall pinning by $Mn'_{Ti/Zr}-V_O^{\bullet\bullet}$ or $Mn''_{Ti/Zr}-V_O^{\bullet\bullet}$ defect dipoles, decreasing the population of domain walls which can move reversibly and thus the magnitude of the frequency dependence. The ratio of the intercept and slope fitting parameters is approximately constant for all films, further indicating that the Mn doped film isn't necessarily less frequency dependent but rather exhibits a reduced overall response (a consequence of pinning which may be relatively immobile regardless of frequency).

[VI] It is worth noting that the intercept is extrapolating 2 orders of magnitude beyond the 4 orders of magnitude measured by Bassiri-Gharb (20 – 200 000 Hz)[149] and 3 orders of magnitude beyond the 3 orders of magnitude measured (1.7 linearly fit) in this work. As such, extrapolation of the trend observed in the range of the linear regression may not accurately represent data at 0.159 Hz.

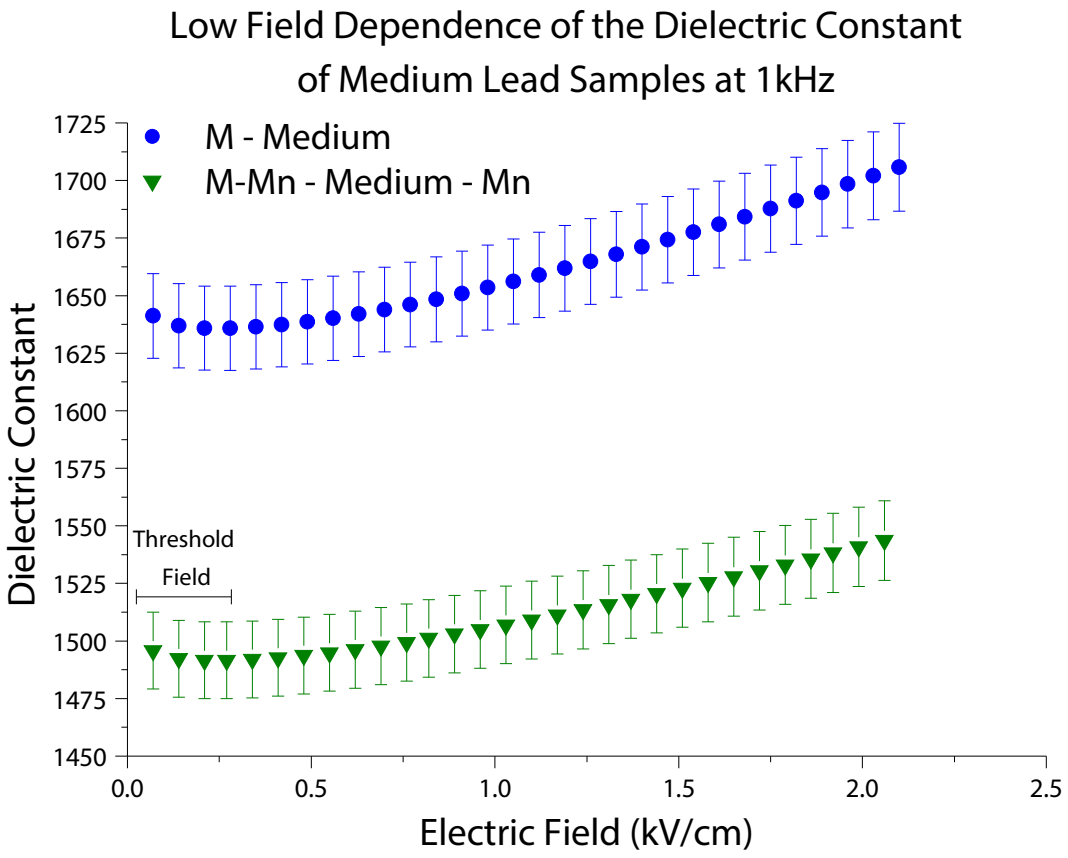

Figure 5.4: Low-field electric field dependence of the dielectric constant of sample D - Medium-Mn at 1 kHz. A small threshold field (∼0.25 kV/cm) is labeled. Error bars are derived from uncertainty in film thickness and electrode area and only apply when comparing different samples. That is, differences in dielectric constant as a function of field within a given sample are still significant.

The frequency dependencies of the α'_ε (i.e. the slope) are all within $\pm 20\%$ of the average value. As with the reversible coefficient, no significant difference in the frequency dependence of the irreversible coefficient is observed as a function of lead content in the niobium doped thin films. Furthermore, Mn doped regions lower both the low frequency extrapolation and the frequency dependency of the irreversible Rayleigh coefficient relative to films with only niobium doping. When normalizing the frequency dependence to the low frequency extrapolation, all films within this work have an approximately constant ratio. The fixed slope over intercept across all films is a further indication that the Mn doped film doesn't necessarily change the frequency dependency[(VII)] of reversible domain wall motion in the film, but rather decreases the film properties overall.

As a consequence of the electrical field formed by the $Mn'_{Zr/Ti}-V^{\bullet\bullet}_O$ defect dipole, a threshold field develops, as observed by Zhu *et al.*[37] The field dependence of dielectric constant at low fields. ($<$2.5 kV/cm) exhibits a small threshold field in sample M-Mn, on the order of 0.25 kV/cm (Figure 5.4). This is approximately an order of magnitude lower than what is typically observed in hard PZT ceramics.[154] Damjanovic reported that the length and coefficients of the Rayleigh regime were sensitive to aging.[155] Therefore prior to Rayleigh measurements, samples were heated to 500 °C (cubic structure) for 30 minutes and rapidly cooled to room temperature on a metal plate. Samples were then heated to 150 °C for 12 h allowing the "as-quenched" domain structure to age. For the thin film (M-Mn), only 10 vol.% of the sample is Mn doped: an order of magnitude lower than uniformly doped, hard PZT. A combination of this and aging of the as-quenched domain structure are believed to be the origin, at least in part, of the smaller threshold field. However, a threshold field of similar magnitude is also observed in sample M, despite having only niobium doping. This suggests that the level of Mn doping in M-Mn may not be sufficient to influence the low field response of the entire film.

5.1.3 Polarization - Electric Field Hysteresis

Polarization-electric field loops were measured at maximum fields ranging from 25 kV/cm to 600 kV/cm in 25 kV/cm steps on all samples (Figures B.15 to B.18). In loops at 500 kV/cm (Figure 5.5), it is observed that the tip of the PE loop is widest in the case of sample M-Mn, followed by H and M, with L forming the narrowest loop. This is an indication that leakage or space charge may be contributing to the measured charge (and calculated polarization) in samples H and M-Mn, with a decreased contribution in M, and the lower contribution (if any) in L and is further investigated with Positive Up Negative Down (PUND) measurements.[140,156]

While all samples share approximately the same coercive field (circa 50 kV/cm), another large increase in maximum and remanent polarization is observed above 350 kV/cm in all films. In the case

(VII) It is possible that a change in the frequency dependency of the dielectric response of PZT films may occur with Nb or Mn doping. As discussed prior, the kinetics of processes (such as pinning and depinning of domain walls or defect migration) may occur at time scales outside the investigated frequency range. Relaxation of domain wall and intrinsic contributions should occur at much higher frequencies.

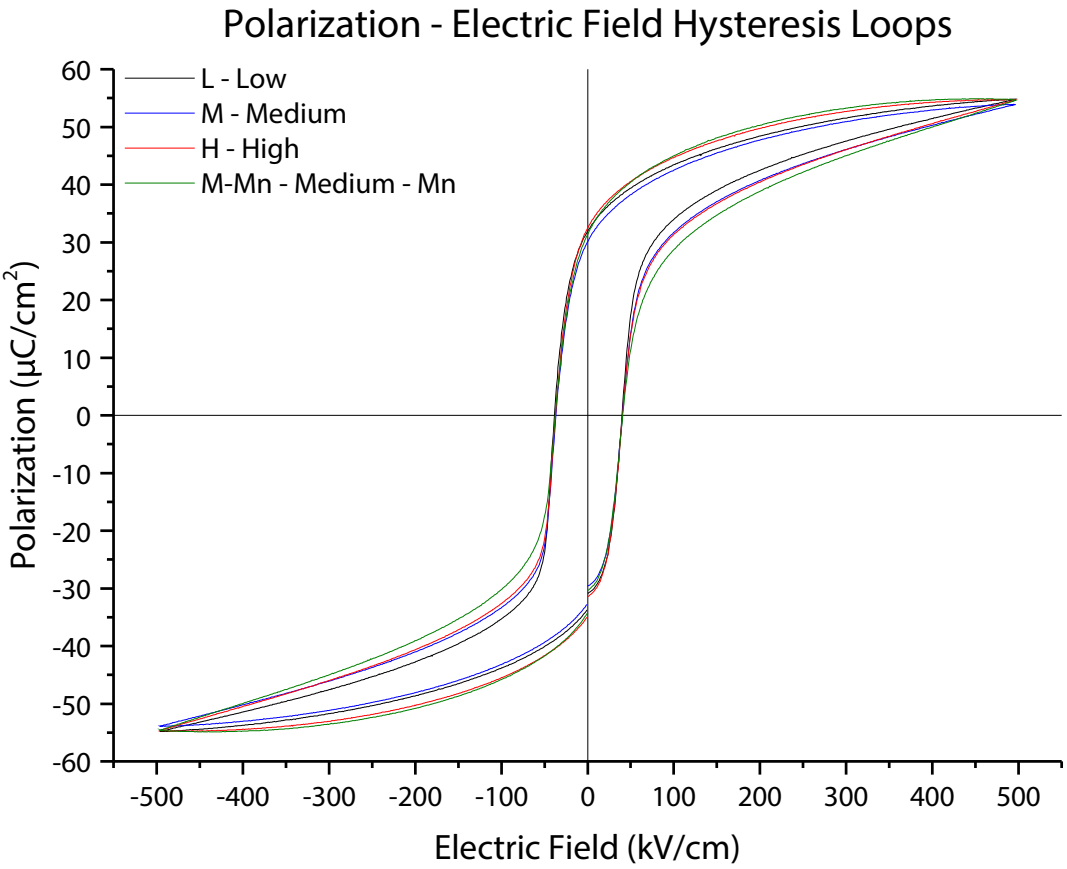

Figure 5.5: Polarization-electric field hysteresis loops measured at 500 kV/cm and 100 Hz. A prepolarization pulse was used, therefore the plotted loops are from the second pulse applied to each sample.

of H and M-Mn, this second polarization increase peaks at 375 kV/cm, while peaking at 400 kV/cm and 425 kV/cm for samples M and L respectively. This falls in order with the lead concentrations of the niobium doped PZT thick films. This sudden increase in the measured polarization could be a consequence of charge injection, field induced phase transformations,[157] or microcracking.[158] Of further note, sample L exhibits the highest polarization in the minor loop (25 kV/cm), in agreement with the report of Marincel *et al.*[144]

Microcracking of the PZT film during polarization - electric field measurements would lead to an irreversible declamping of the piezoelectric and ferroelectric responses of the film. As a consequence of microcracking, successive measurements of the same electrode may be anticipated to have higher polarizations than that which is observed in the first sweep. Two successive sweeps (from 25 – 600 kV/cm as in Figure 5.6) were measured on a single top electrode to determine if microcracking occurred. A significant increase ($\sim$20 $\mu C/cm^2$) in polarization was observed in the second sweep relative to the initial sweep for fields ranging from 50 – 400 kV/cm. The data point collected at 25 kV/cm is below the coercive field of the material (leaving polarization less susceptible to declamping) while the data above 400 kV/cm was collected during or after microcracking events in the first sweep. At high fields (circa 600 kV/cm) the data of the two sweeps converge, an indication that an insignificant amount of additional microcracking occurred during the second sweep.

Due to the variation in the breadth of hysteresis loop tips from sample to sample, Positive Up Negative Down (PUND) measurements were used as a means of separating the true remanent polarization of the material from other charge contributions to the measured polarization. PUND measurements consist of a negative pulse, two positive pulses, and two negative pulses. The PUND delay is defined as the time between each pair of consecutive pulses. The first negative pulse serves to set the material into a known state (negative remanent polarization). The charge associated with the first positive pulse is associated with the switching from the negative state to the positive saturation. After this pulse, charge flows back as a consequence of the ionic and electronic polarizability, space charge relaxation, and back switching of domains. The second positive pulse returns the system to the positive saturation state from the positive remanent state. The charge flow associated with this pulse includes the ionic and electronic polarizability, switching any backswitched domains, and leakage current or space charge contributions. The difference in the charge transfer during the first and second positive pulses is equivalent to twice the remanent polarization. The same methodology applies to the negative pair of consecutive pulses for the negative polarization of the material.[159]

PUND results in Figure 5.8 exhibit two clear regimes. The large changes in $2P_r^+$ observed in the first two to three data points can be attributed to microcracking of the samples. As the number of total pulses increases (and delay time, as single electrodes were measured from low to high delay times) the $2P_r^+$ saturates, an indication that microcracking is no longer occurring. At this point, the remanent polarization degrades roughly linearly with the log of time, as is the anticipated functional form for

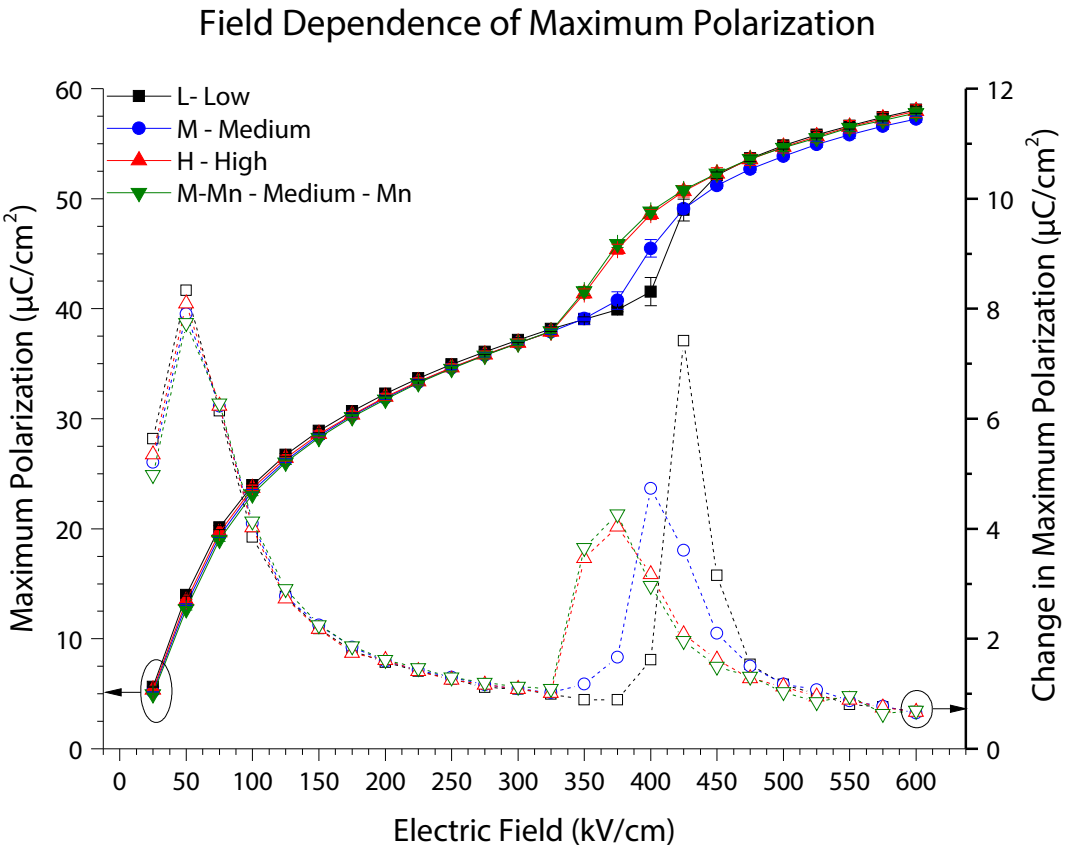

Figure 5.6: Maximum polarization and change in maximum polarization as a function of the measurement electric field at 100 Hz. All loops had a pre-pulse, of equivalent magnitude, prior to the measurement pulse (i.e. there were two pulses at each field level with the data from the second pulse plotted). The right axis is defined as the change in polarization between the current and prior data point (E and E-25 kV/cm). No difference was observed between the 2nd, 4th or 6th loops taken at a given field except those near the region of the rapid polarization increase (350 – 450 kV/cm). Error bars represent the standard deviation across multiple electrodes plus 0.5% error for electrode size uncertainty.

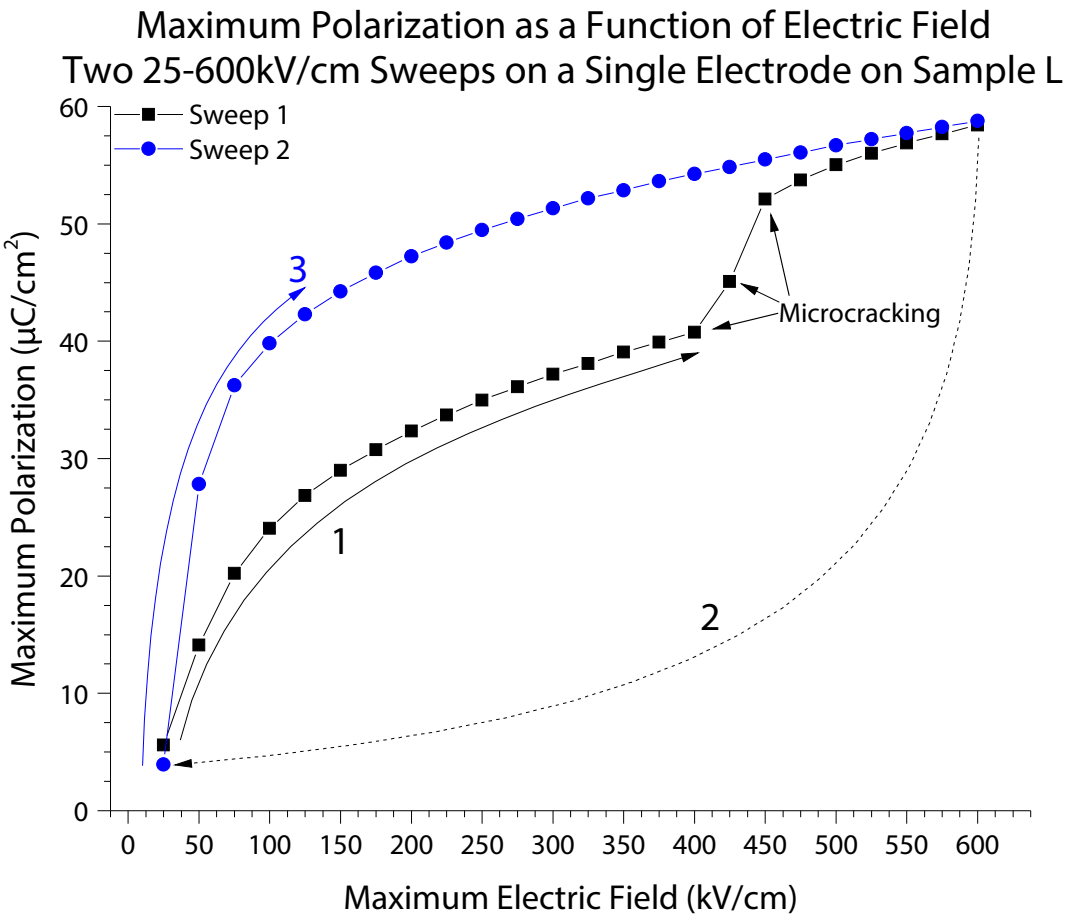

Figure 5.7: Maximum polarization plotted as a function of the measurement electric field and sweep number. PE hysteresis loops were measured on a single electrode from 25 – 600 kV/cm in 25 kV/cm increments (black). This sweep was repeated a second time, in the same direction on the same electrode (blue). The region of the most significant microcrack development is labeled, however microcracking events may extend beyond these points.

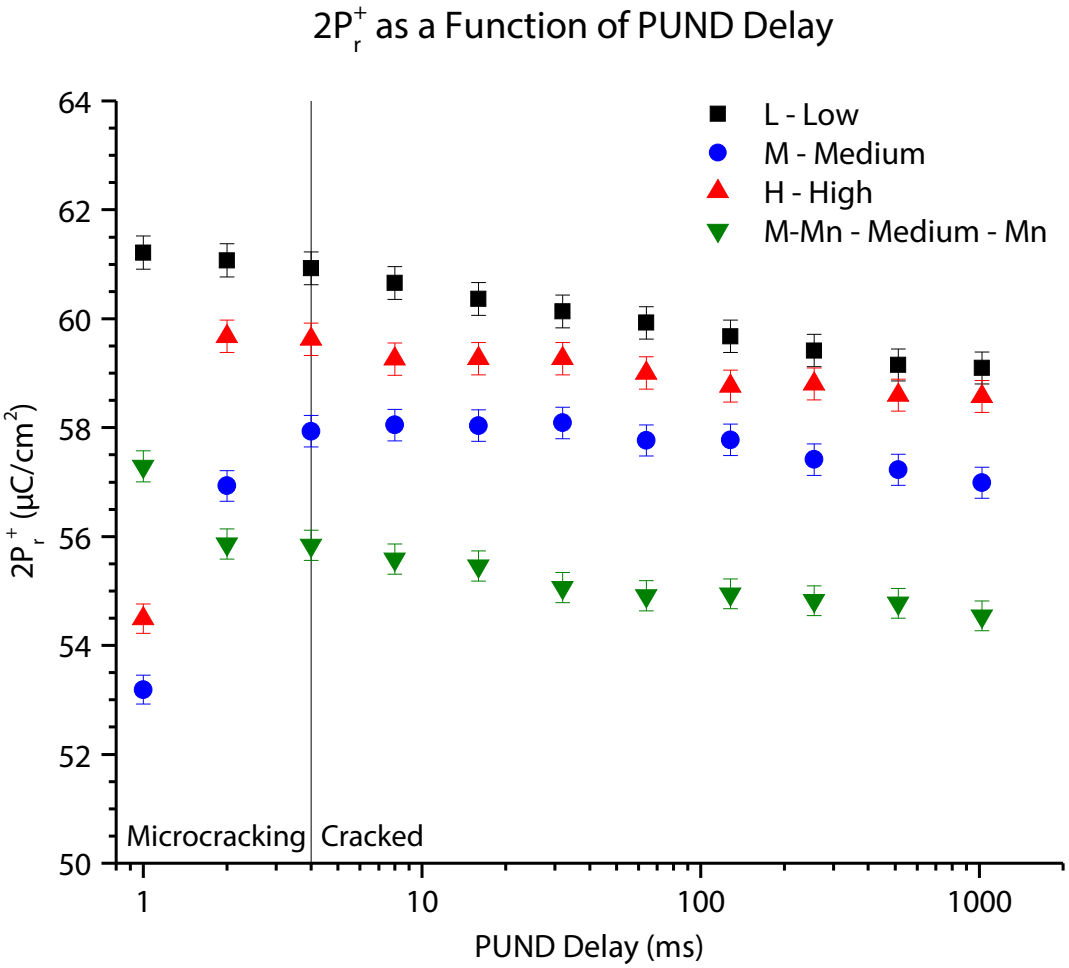

Figure 5.8: $2P_r^+$ measured via Positive Up Negative Down (PUND) polarization measurements. The PUND delay is defined as the time between the switching pulse and the non-switching pulse. All pulses had a square profile with a pulse width of 1 ms and a magnitude of 500 kV/cm. Error bars represent the 0.5% error for electrode size uncertainty.

Table 5.2: Remanent polarizations (P_r^+) as determined by standard PE hysteresis loops and PUND measurements.

Sample	P_r^+ from Hysteresis Loop (μC/cm²)	P_r^+ from PUND Measurement (8 ms delay) (μC/cm²)	Difference in P_r^+ Hysteresis – PUND (μC/cm²)
L - Low	30.1	30.3	-0.2
M - Medium	31.8	29.0	2.8
H - High	32.5	29.6	2.9
M-Mn - Medium - Mn	30.3	27.8	2.5

dielectric aging.[160] In the case of sample L, the sample may have cracked entirely on the first negative pulse, thus showing a linear degradation of polarization across the entire data range. Similarly sample M-Mn may have cracked fully during the first positive pulse, artificially enhancing the $2P_r^+$ for the first data point (the $2P_r^-$ does not show this anomaly). The remanent polarizations from standard hysteresis loops and PUND measurements at 500 kV/cm are listed in Table 5.2. As hypothesized in Figure 5.5, the measured polarization of M-Mn is higher than the true polarization; in fact it has the lowest polarization of any of the four films. Similarly, sample L was found to have the highest true polarization via PUND measurements; although any difference between PUND and hysteresis remanent polarizations for sample L is within statistical uncertainty. While it appears that leakage currents did contribute to the observed electrical polarization in sample H, it appeared to contribute a similar amount in sample M as well (as evidenced by the similar change in polarization between hysteresis and PUND measurements).

The high leakage current contribution to the polarization of M-Mn suggests that, while having gradient free layers with the same nominal composition as sample M, may have a higher lead stoichiometry in the film, closer to that of sample H. The M-Mn sample was made after samples L, M, and H chronologically. As such, the RTA would be expected to have the highest lead concentration during the processing of the Mn-doped sample. Furthermore, as discussed in Section 3.4, Nb doped PZT requires a higher solution lead concentration than undoped or doped PZT to maintain perovskite phase purity in the deposited film. Therefore, it is possible that the 13 at.% lead excess in the Mn film resulted in a higher lead concentration in the Mn doped layers of the film than in the 14 at.% lead excess would in the Nb doped layers. It is also apparent in Figures 5.6 and B.19 that the field at which microcracking occurs is dependent on the lead content of the niobium doped films. Sample M-Mn cracks at the same field as sample H, which may further indicate an increased lead content in M-Mn.

A Preisach distribution was fit to the poled First Order Reversal Curve response of electrodes on each sample. Plots for an electrode on M and M-Mn are presented in Figures 5.9 and 5.10 while those for L and

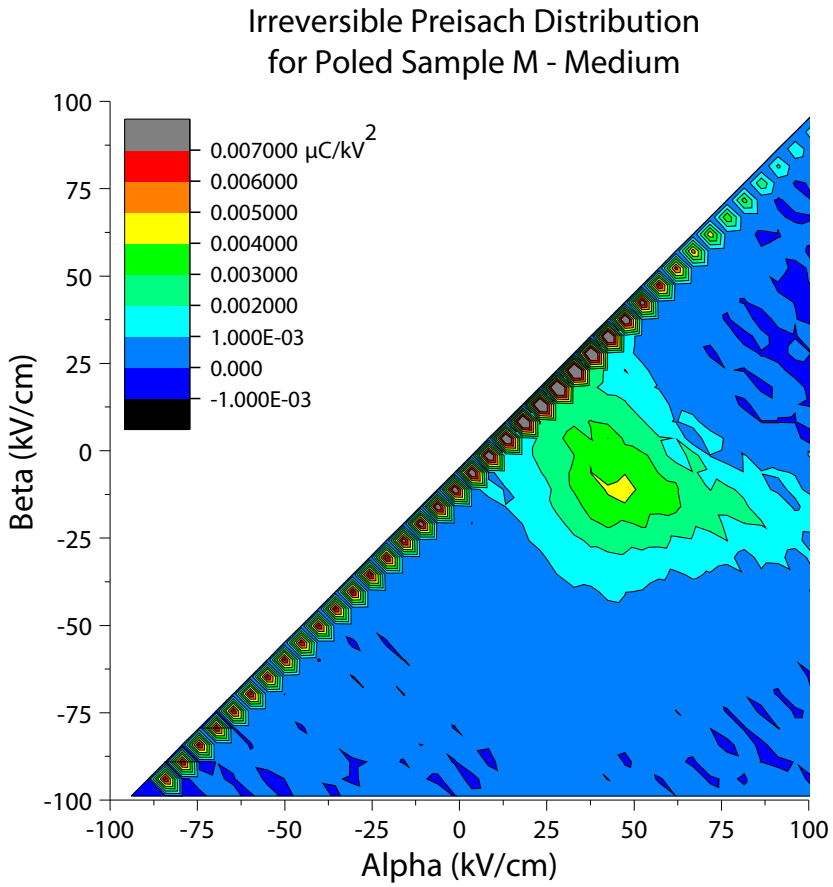

Figure 5.9: Irreversible Preisach distribution calculated from First Order Reversal Curves on Sample M. The electrode was poled at 100 kV/cm and 150 °C prior to measurement. The poling field and the starting state for the FORC measurement were in the same direction.

H as well as the irreversible distribution are presented in Figures B.20 to B.22. The distributions for films with low defect dipole concentrations (M and H) might be anticipated to form a sharper point (indicated by the yellow region). Conversely, those with a larger defect dipole population (containing lead vacancies in L, or Mn dopants and oxygen vacancies in M-Mn) have a more diffuse hysteron distribution. Local electric fields from the increased presence of defect dipoles, should, in principle, broaden the global electric field distribution necessary for switching of the material. No significant difference in the location of the hysteron distribution peak is observed (1 – 2 kV/cm shift of the peak in M-Mn relative to the ∼3 kV/cm spread of peak positions in uniformly Nb doped samples) as a consequence of defect dipole alignment unlike reports from Akkopru-Akgun for uniformly Mn doped films where shifts in excess of 50 kV/cm were observed.[54] This suggests that the local electric fields present in the Mn doped layers (from the alignment of defect dipoles upon poling) are not significant enough to alter the global electric fields necessary to switch the remainder of the film.

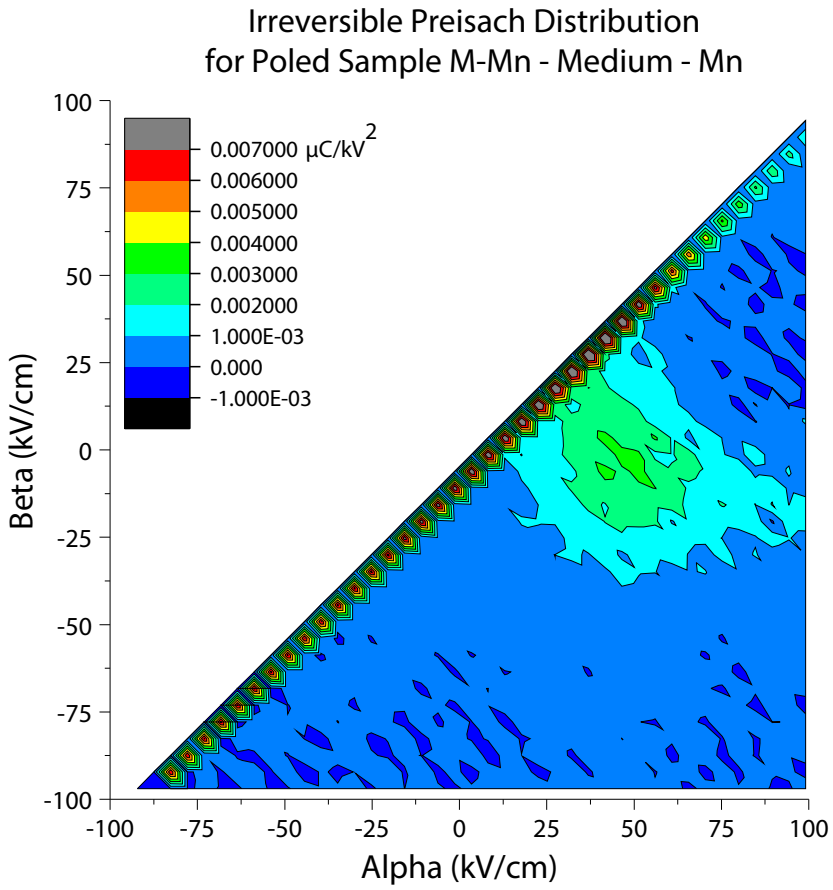

Figure 5.10: Irreversible Preisach distribution calculated from First Order Reversal Curves on Sample M-Mn. The electrode was poled at 100 kV/cm and 150 °C prior to measurement. The poling field and the starting state for the FORC measurement were in the same direction.

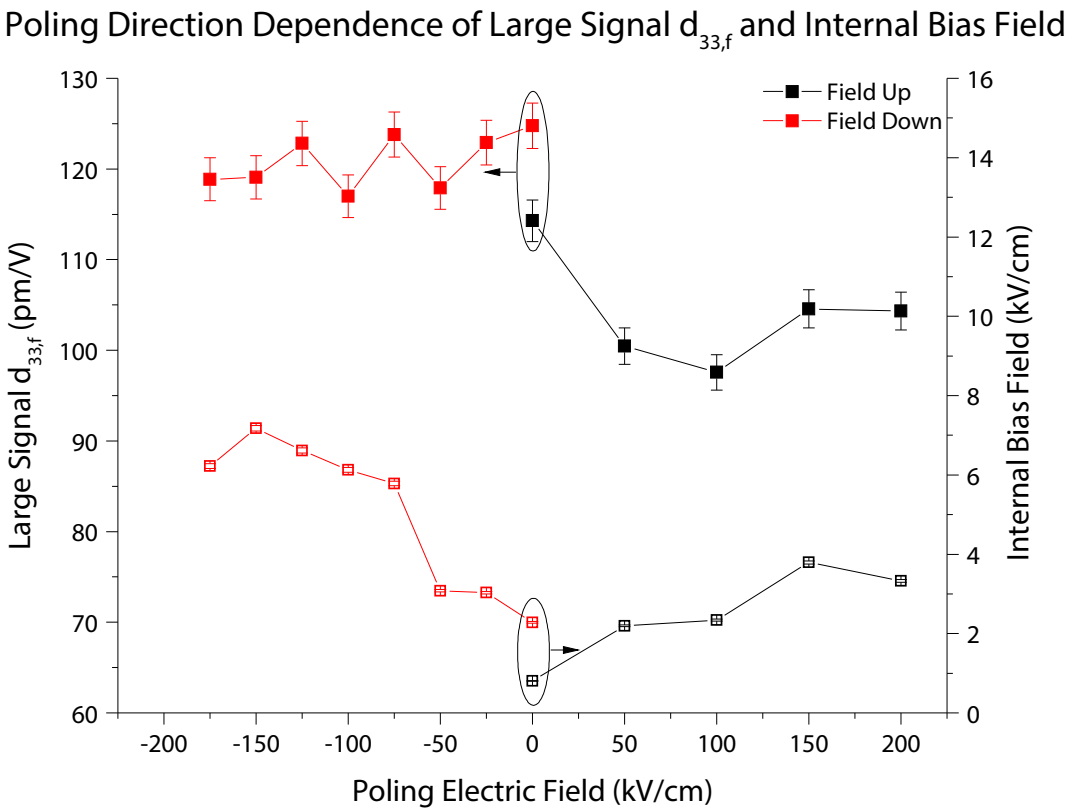

Figure 5.11: Dependence of the large signal $d_{33,f}$ and internal bias field of Sample M (medium lead content) as a function of poling field magnitude and direction. A preference towards poling in the field down direction (field pointing from the top to the bottom electrode) is observed. In the case of 0 kV/cm poling field, the drive direction for the unipolar $d_{33,f}$ measurement was varied. The error bars for $d_{33,f}$ data represents 1% uncertainty in thickness and 1% uncertainty in the noise of the $d_{33,f}$ measurement.

5.2 Poled Piezoelectric Response and Aging Rate

Electrodes on sample M were poled with the electric field pointing from the top to the bottom electrode (field down) or the opposite direction (field up) at 150 °C for 20 min. A significant reduction of the large signal $d_{33,f}$ (from saturation at ~120 pm/V to ~105 pm/V) and internal bias field (from a 7.2 kV/cm peak to a 3.8 kV/cm peak) was observed when poling in the field up condition relative to the field down condition (Figure 5.11). Thus there is a preference towards poling and driving the film in the field down condition. Imprint in PZT thin films can develop as a consequence of ionic vacancies, defect complexes, induced charges (e.g. from UV light exposure), or screening by a thin surface layer at the electrode interface.[161,162]

In principle, the asymmetry from the lead titanate seed layer, differing platinum densities and incorporated lead contents, or lead (vacancy) concentrations across the film thickness could result in

the observed imprint across the film thickness. Poling at 150 °C did not eliminate this preference for the field down driving direction; an indication that the imprint is not entirely a consequence of ionic defects or induced charges which are mobile at the temperature used for poling (150 °C). In essence, while imprint could be developed and changed with poling in either direction, part of the contribution to the total imprint appeared fixed in the field-down direction.[161] Niobium doping has been reported to reduce the magnitude of thermally induced imprint; this was attributed to a reduced concentration of oxygen vacancies.[54,163]

While imprint is detrimental to applications such as ferroelectric random access memory (which necessitate no bias towards one polarization state over the other), in actuator applications imprint is desired as it aids in poling retention and favors unipolar drive conditions.[54,164] Due to the strong preference for field down poling and driving, the remainder of the poling characterization were performed in the field down direction. The remanent and large signal $d_{33,f}$ coefficients were measured as a function of poling electric field on 500 μm electrodes (Figure 5.12). The $d_{33,f}$, as measured by double beam laser interferometry, is observed to vary as a function of electrode size. Sivaramakrishnan *et al.* demonstrated this to be a consequence of the Poisson effect in the substrate, finding that the measured $d_{33,f}$ has no contribution from the Poisson effect when the electrode diameter was the same as the substrate thickness under the assumption that the Poisson's ratio is an isotropic 0.3 in all directions.[165] However, when measuring films on a single crystal silicon wafer, the elastic properties are strongly anisotropic; Poisson's ratio varies from ∼0.06 – 0.27 in the plane of a (100) silicon wafer.[166] When considering the elastic anisotropy of the substrate, square and round contacts measure the true $d_{33,f}$ at electrode size (length of a side or diameter respectively) to substrate thickness ratios of 1.12 and 1.24 respectively.[167] In this work, electrodes 500 μm in diameter were used on a 400 μm substrate; a ratio of 1.25, close to the ideal value of 1.24 for circular electrodes. In all cases, samples were poled at a temperature of 150 °C for 20 min.(VIII)

All samples exhibit a relatively uniform large signal $d_{33,f}$ (open symbols of Figure 5.12) across the range of poling fields. With the exception of some data points (attributed to electrode variation), the large signal $d_{33,f}$ of all samples is $\sim(120 \pm 5)$ pm/V across the range of poling fields. While the sample with manganese doped layers (M-Mn) appears to have diminished properties relative to uniformly Nb doped samples at low poling field magnitudes <150 kV/cm, this difference disappears at higher poling fields >150 kV/cm. Remanent $d_{33,f}$ values rose sharply from unpoled samples up to poling fields near 100 kV/cm. At this field, the rate of increase of the remanent $d_{33,f}$ becomes more gradual for all films, increasing 12 pm/V with a tripling of poling field magnitude (75 – 225 kV/cm) for sample L. At a poling field of –175 kV/cm the remanent $d_{33,f}$ varies by 9 pm/V between samples M or H and L or M-Mn.

(VIII) 20 min is a measurement of the time under field at 150 °C, the field remained on during the cooling process ∼15 min.

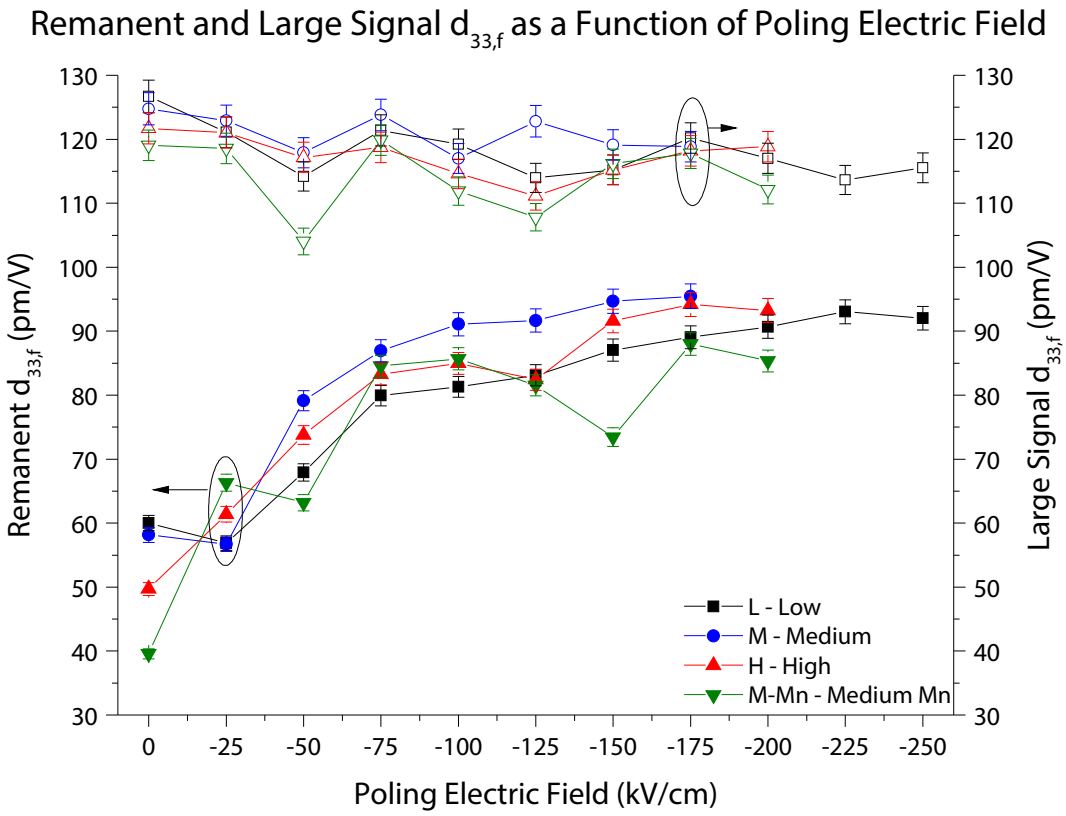

Figure 5.12: Remanent and large signal $d_{33,f}$ as a function of poling electric field. Note: electric field magnitude increases from left to right. The error bars for $d_{33,f}$ data represents 1% uncertainty in thickness and 1% uncertainty in the noise of the $d_{33,f}$ measurement.

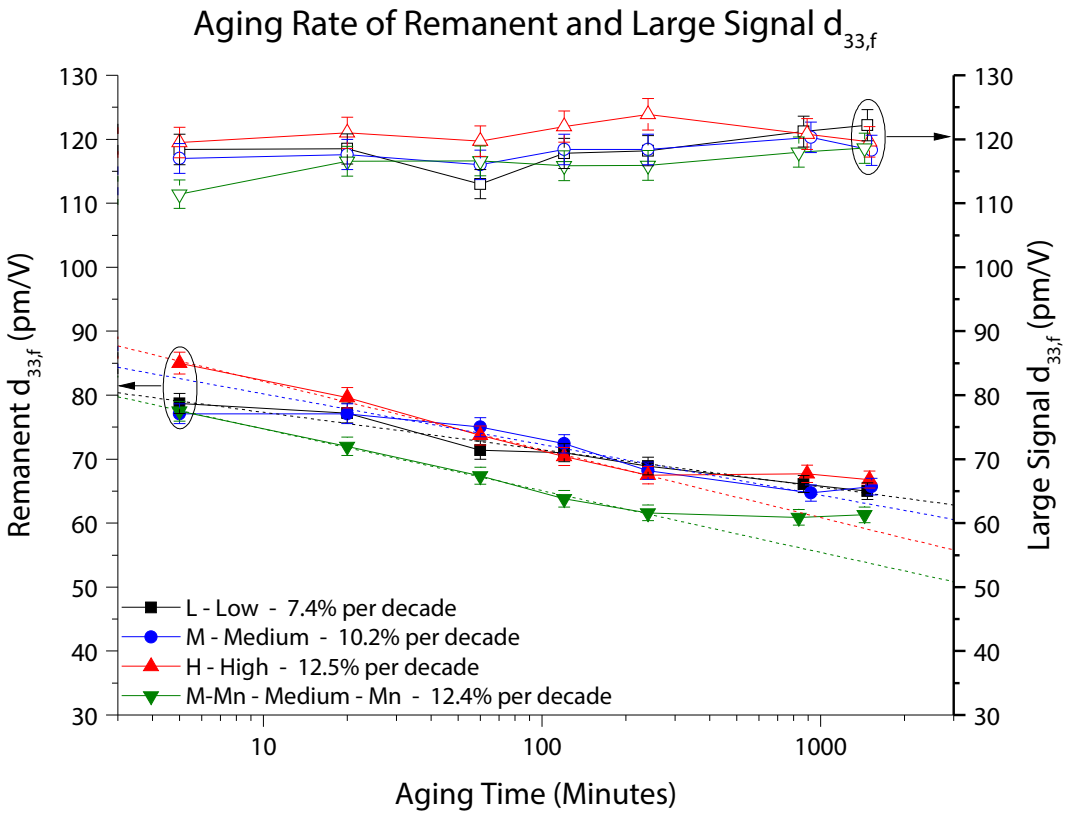

Figure 5.13: Aging rate of remanent and large signal $d_{33,f}$ at 150 °C as a function of time since poling at 100 kV/cm. The error bars for $d_{33,f}$ data represents 1% uncertainty in thickness and 1% uncertainty in the noise of the $d_{33,f}$ measurement.

An electrode on each sample was poled at 150 °C and 100 kV/cm in order to measure the aging rate of the large signal and remanent $d_{33,f}$ as a function of time. Aging took place at 150 °C in order to make the effects of aging measurable in a relatively short timeframe (Figure 5.13). The large signal $d_{33,f}$ remained stable (fluctuating ±3 pm/V from the average value ∼120 pm/V with no marked net decrease as a function of time) in all samples up to 1600 minutes after poling. Conversely, the small signal, remanent $d_{33,f}$ exhibited a linear degradation with log time, as expected.[160] It was observed that the aging rate increased with lead concentration in the film from 7.4% per decade in L to 10.2 and 12.5% per decade in M and H respectively. It is hypothesized that lower lead concentrations may lead to an increased quantity of lead vacancies and compensating oxygen vacancies. Resulting defect dipoles including $V''_{Pb}-V^{\bullet\bullet}_{O}$ or $V''_{Pb}-Nb^{\bullet}_{Zr/Ti}$ could, in principle, pin the poled domain structure in the film, reducing the aging rate in low lead films. Similarly, reports of imprint development and stabilization as a result of manganese doping have been attributed to the $Mn'_{Ti/Zr}-V^{\bullet\bullet}_{O}$ defect dipole reorienting (via migration of the oxygen vacancy) upon poling at elevated temperatures.[54] Under the presumption that sample M-Mn actually has a lead content closer to that of H (as indicated by breakdown and failure strengths), the addition of Mn doped layers does not appear to reduce the aging rate at elevated temperature (from 12.5 and 12.4% per decade for H and M-Mn respectively). It is noted that the oxygen vacancy should be mobile at the poling and aging temperature of 150 °C. As such, the impact of the small quantities of Mn doping in M-Mn on the aging rate may be limited at such temperatures.

The aging study was repeated under the same poling conditions, however samples were aged at ∼25 °C. It was observed that the aging rate was significantly slower at room temperature than 150 °C. This, combined with the noise in the small signal $d_{33,f}$ measurement results in greater uncertainty in the aging rate. Aging of the piezoelectric response on each sample is plotted across ∼3.3 decades of time in Figure 5.14. Electrodes aged at high temperature exhibited a relative change of ∼20 pm/V, a change twice that observed in those aged at room temperature while occurring in a shorter timeframe (2.5 decades). Curves of the small signal[(IX)] $d_{33,f}$ still exhibits fluctuations on the order of ±1 – 2 pm/V from a smooth curve of $d_{33,f}$ as a function of DC bias voltage. This fluctuation is on the order of 10-20% of the total change observed during the room temperature aging experiment. As a consequence of this measurement noise, no statistically significant difference in room temperature aging rate was observed between samples (Figure 5.14) as a function of lead content or presence of Mn doped layers. The room temperature aging rates observed in the $d_{33,f}$ of films in this work (∼2-4% per decade) are near the lower bound of other reported piezoelectric aging values for perovskite films: 3%[168] per decade in 45/55 {111} PZT films, 4-10%[169] per decade in 30/70 {001} PMN-PT films, and 4-8%[170] or 6-12%[171] per decade in 52/48 {111} PZT.

[(IX)] While this measurement took the typical functional form of small signal measurements (a range of DC bias voltages + a fixed, smaller amplitude AC electric field), the 500 mV excitation field is over an order of magnitude larger than that used to measure dielectric properties (30 mV) in order to reduce noise to acceptable levels

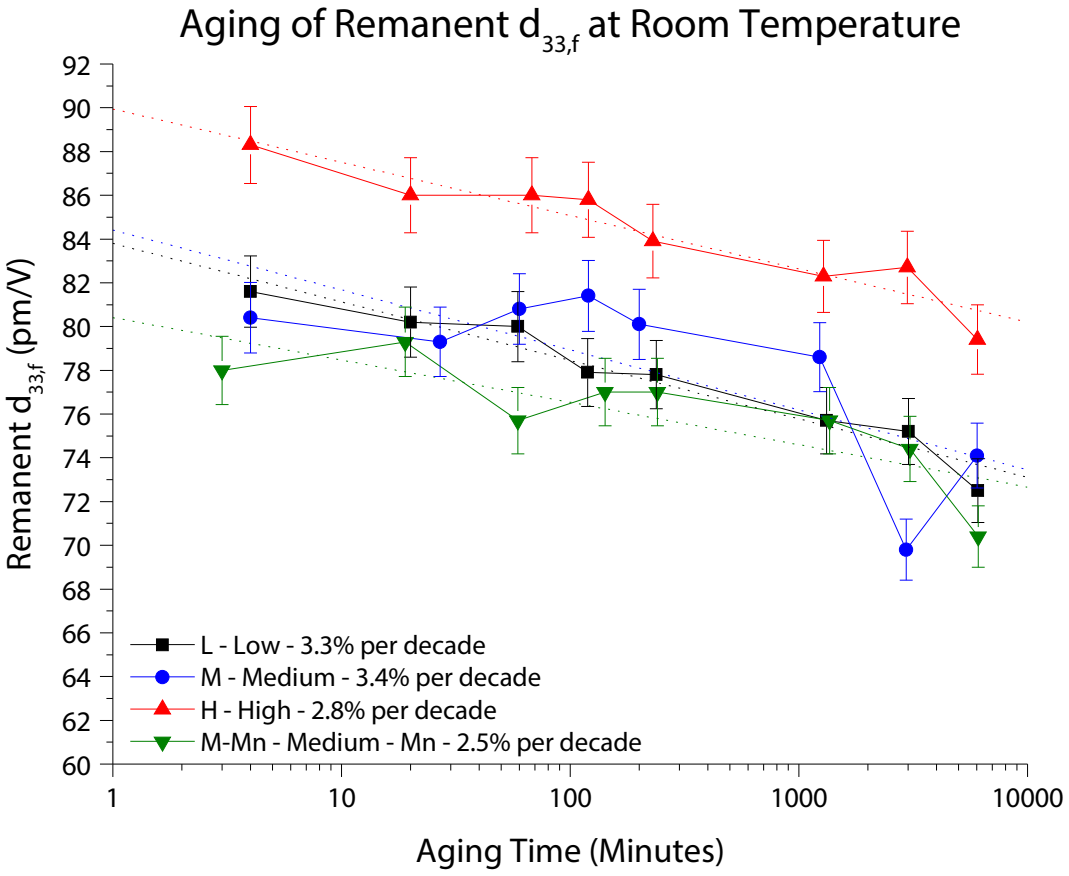

Figure 5.14: Aging rate of remanent and large signal $d_{33,f}$ at 25 °C as a function of time since poling at 100 kV/cm. The error bars for $d_{33,f}$ data represents 1% uncertainty in thickness and 1% uncertainty in the noise of the $d_{33,f}$ measurement.

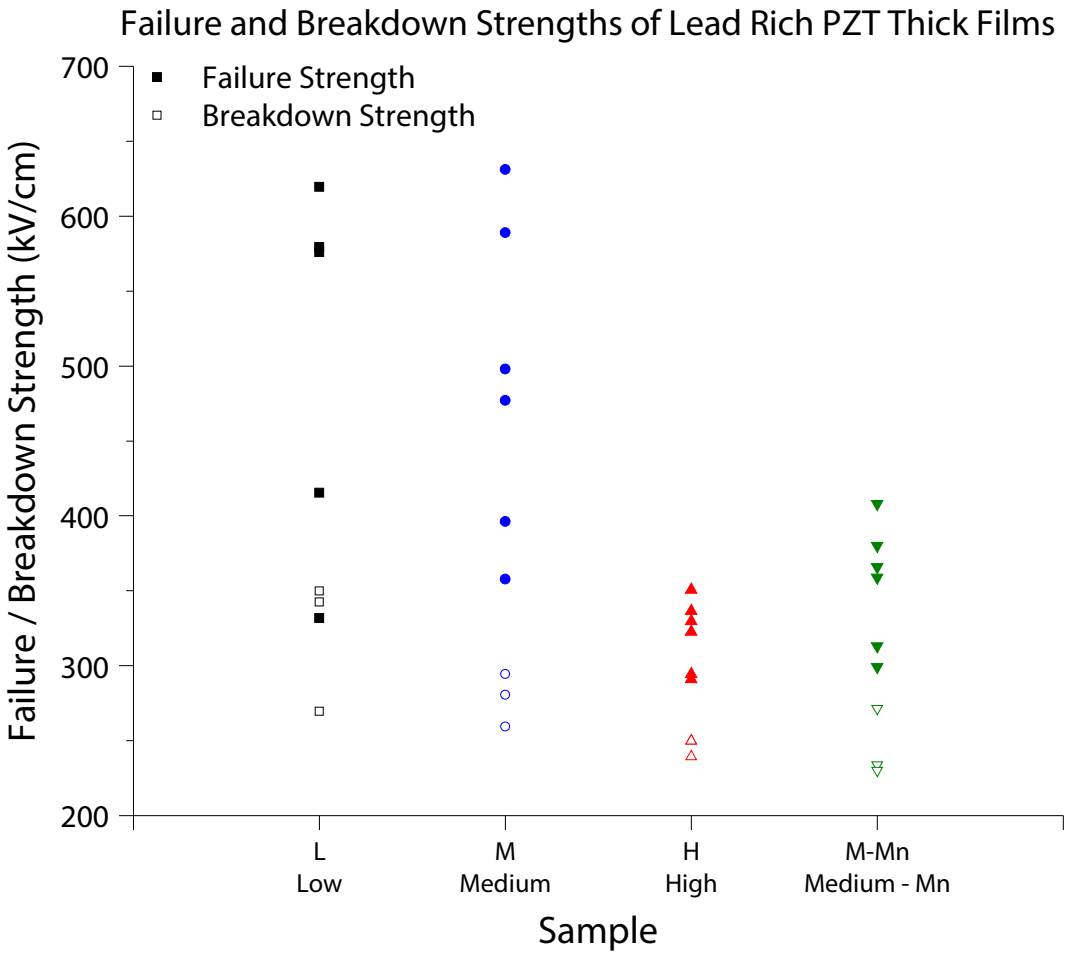

Figure 5.15: Failure (point of cracking or burning) and breakdown strengths (point at which leakage current increased 100 fold) of multiple top electrodes for all 4 thick film samples.

5.3 Lifetime and Failure

Several electrodes were tested on each sample in order to quantify the relative failure strengths as a consequence of lead content and Mn doping (Figure 5.15). As the (expected) lead content of the film increases, the average failure strength drops from ~500 – 550 kV/cm to ~325 – 350 kV/cm. Futhermore, the variability (standard deviation) in the failure strength decreases from ~40% of the breakdown strength to ~ 10% for films with a higher lead concentration.

Failure strength was defined as the point at which the film either cracked or burned, whichever occurred first. This may underestimate the acceptable fields somewhat, as some bulk actuators are still used following cracking. The tight distribution of failure strengths in the high lead samples (H, with M-Mn suspected to be high as well) suggest that the presence of excessive lead, which may segregate

along grain boundaries,[140] could be dominating the failure strength of the lead rich films. Garten reported that regions of ejected material (i.e. burned regions) likely originated from Joule heating caused by electric field concentrations at defects.[172] In the case of lead rich PZT films, low resistivity (comparatively) PbO clustered at grain boundaries could preferentially conduct, relative to the large PZT grains. This heating could lead to volatilization of the lead oxide and subsequent dielectric breakdown events, leading to ejection of vaporized material.[129,146]

Comparatively, samples with lower lead concentrations (L or M) have a wider spread of failure strengths. This indicates that there may be multiple mechanisms responsible for electrode failures resulting in increased variability from electrode to electrode on the low lead films. Films with high piezoelectric responses could favor cracking along grain boundaries as a consequence of the polycrystalline nature; adjacent grains may have slightly different orientations creating strain mismatches at grain boundaries.[173,174] Additionally, the presence of existing defects can further enhance crack growth, providing a field dependence on the growth rate.[174,175]

In order to further investigate the failure mechanisms of each film, videos of breakdown events were recorded using a digital camera mounted to the probe station microscope (MU853B – AmScope). A picoamp meter (4140B – Hewlett Packard) supplied a staircase wave which started at 20 V, stopped at 100 V and increased by 1 V every 3 s. The voltage source's current limiter was set to 10 mA (the maximum allowable) and the measurements were stopped when the current limit was reached. Review of the videos allowed for determination of whether cracking or material ejection occurred, the order in which the events occurred, and the delay between events. By syncing the video file to the voltage of the DC source, it was determined if both events occurred at the same voltage (time delay) or at different voltages.(X)

Multiple electrode failures were filmed on each film under the same conditions. Of these videos, one representative video was chosen for each sample. Six frames were extracted from each of these videos at different points along the failure process and are shown in Figures 5.16 to 5.19 All samples exhibited a combination of microcracking and vaporization / ejection of material throughout the process of failure. Microcracking started prior to vaporization / ejection of material in nearly all electrodes.

Some samples, such as L and H (Figures 5.16 and 5.18) went from completely intact to fully cracked within the span of $\sim$1 s under a fixed voltage. Cracks within the electrode region can be traced to the edge of the electrode and continue to propagate into the exposed PZT film regions. This indicates that the underlying PZT is cracking in conjunction with the top electrode; as opposed to the top electrode buckling or delaminating on an intact PZT film. The other samples, M and M-Mn (Figures 5.17 and 5.19) had a gradual cracking that took place across several seconds and at more than one voltage. The cracks

(X) The recording software for the camera (MU853B) is proprietary to the manufacturer (AmScope), providing no automated means of synchronizing the video and pA meter measurements. "Syncing" was achieved by signaling when the voltage switched to two predetermined levels (typically 25 and 30 V). Methods such as tapping the camera (vibration) or flashing the light source were used. With knowledge of the rate of voltage increase, and the voltage at two "sync" points, the voltage at any point in the video could be determined.

often originated near the probe tip and propagated across the electrode surface away from the probe tip as time and voltage progressed. A range of probe tip pressures (from the least contact possible that gave a valid capacitance measurement to heavy contact involving the probe tip sliding ∼50 µm across the surface) resulted in no noticeable difference in the origin of the cracking. Furthermore, it was observed that the cracks which propagated slowly appeared to have an overall lower density than those which formed simultaneously (limited by the camera framerate to Δt ∼33 ms). No apparent trend between cracking morphology (i.e. rapid and dense or gradual and sparse cracking) and lead content is observed. The low and high lead samples had rapid dense cracking while the medium and medium-Mn samples exhibited more gradual cracking with a lower crack density.

All samples exhibited black regions of vaporized / ejected material after microcracking of the film began. In the cases where cracks propagated rapidly (L and H), the entire top electrode and underlying film finished cracking prior to any black regions developing. Conversely, in samples with slower cracking (M and M-Mn), black regions began to appear prior to cracking across the entire sample. An example of this can be seen in Figure 5.19 where, in the frame from 41 V 2 s, black spots appear on the left side of the film (already cracked) while the rightmost edge of the film has yet to finish fully cracking. However, regions of ejected material tended to be localized to those areas which had already cracked.

It was observed in samples with higher lead content / lower failure strengths (H and M-Mn) that a large quantity of small material ejection events occurred across the surface of the top electrode. These may be associated with regions with locally higher conductivity (due, perhaps to lead oxide along grains boundaries) and Joule heating until material is vaporized.[129,146,172] Conversely, in samples with lower lead contents / higher failure strengths (L and M), the initial regions of material ejection tended to be fewer in quantity and larger in size. This indicates that decreased lead contents may decrease the number of regions favorable for breakdown events. The remaining regions may require higher fields in order to break down and subsequently be more violent, resulting in larger regions of ejected material.

Once a sufficiently high field was attained, all films had some electrodes which exhibited failure events on the scale of those depicted in the final frames of Figures 5.17 and 5.19. The extent and quantity of these large failure events is hypothesized to be related to the failures, if any, which occur near the probe tip applied to the top electrode. In cases, such as the final frame of Figure 5.16, the edge of failure event can be observed beneath the probe tip. If such a failure event produces either a short between the probe tip or top electrode and the bottom electrode, or electrically isolates the probe tip from the remainder of the top electrode, failure events may cease. However, if such an event does not occur, failure events may continue occurring in other regions of the film. As the voltage increases further and further, larger area breakdown events may be expected to occur.(XI)

(XI) It is coincidental that Figures 5.17 and 5.19 show large breakdown events while Figures 5.16 and 5.18 do not. Some electrodes across all films exhibited large area breakdown events while other electrodes did not. No correlation between the cracking morphology and the presence of high field large scale breakdown events was observed.

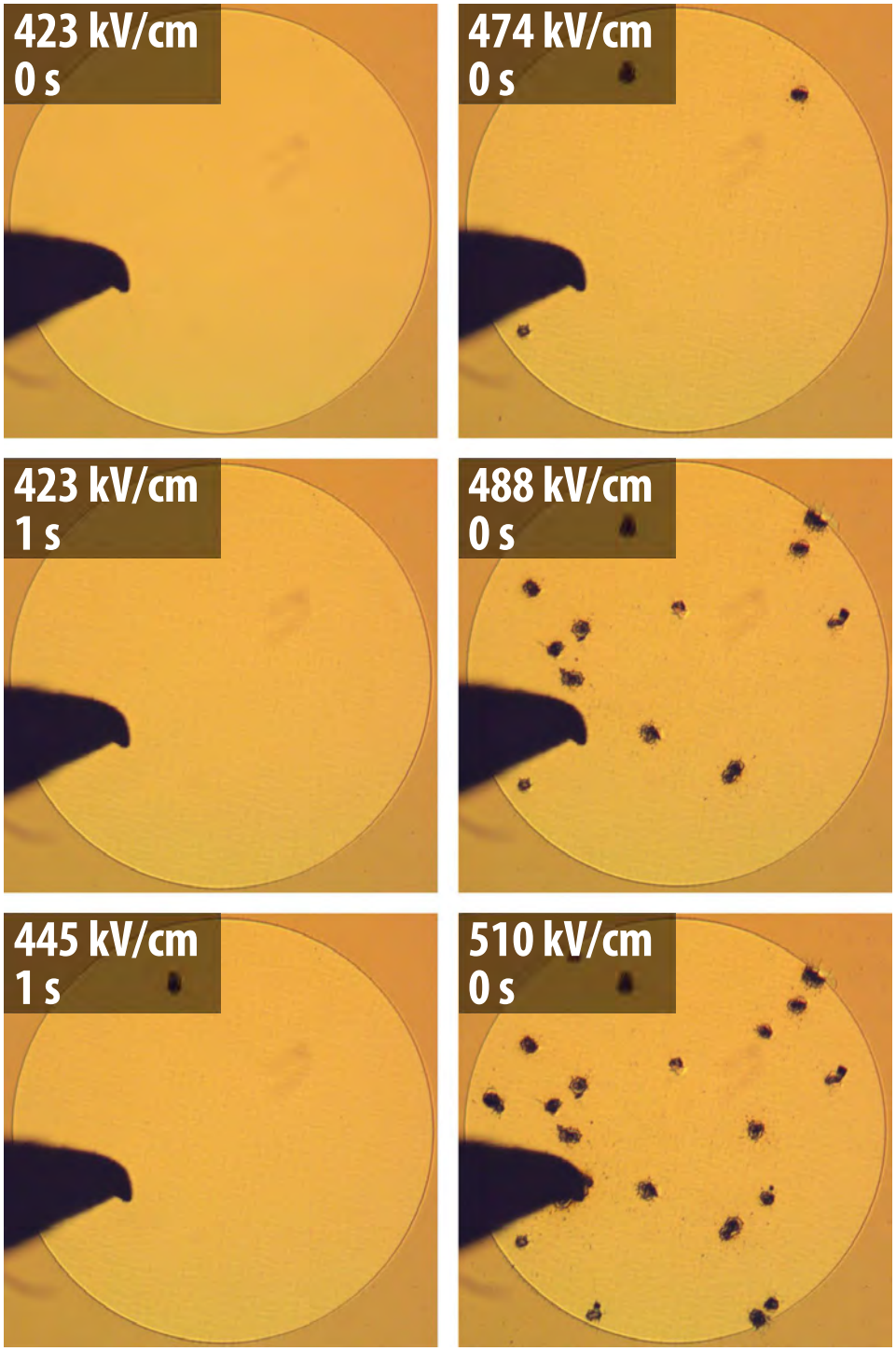

Figure 5.16: Failure of a 500 µm top electrode on the low lead sample (L). The labels represent the voltage and time at voltage that the frame was captured. The voltage increased by 1 V every 3 s.

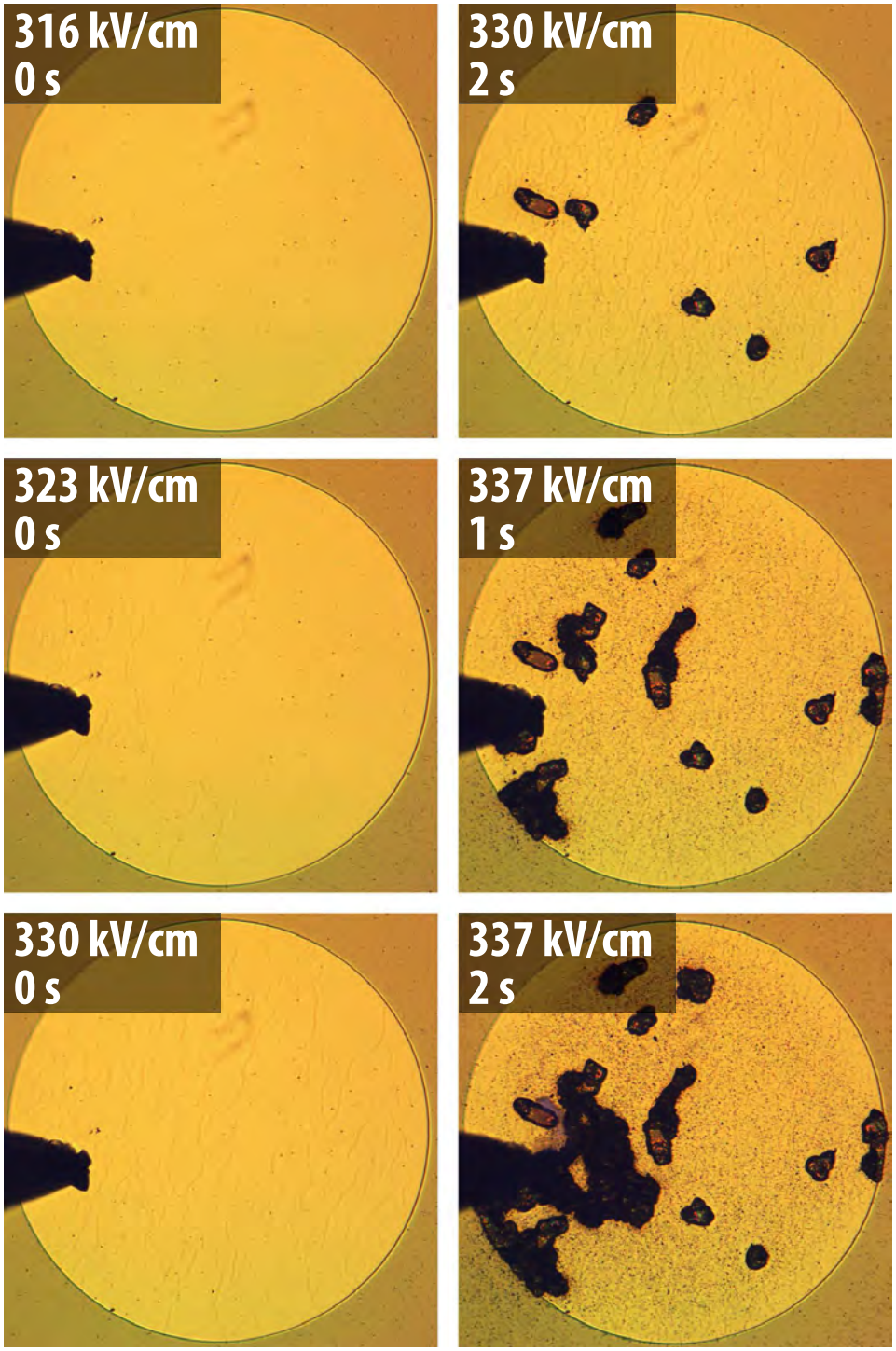

Figure 5.17: Failure of a 500 µm top electrode on the medium lead sample (M). The labels represent the voltage and time at voltage that the frame was captured. The voltage increased by 1 V every 3 s.

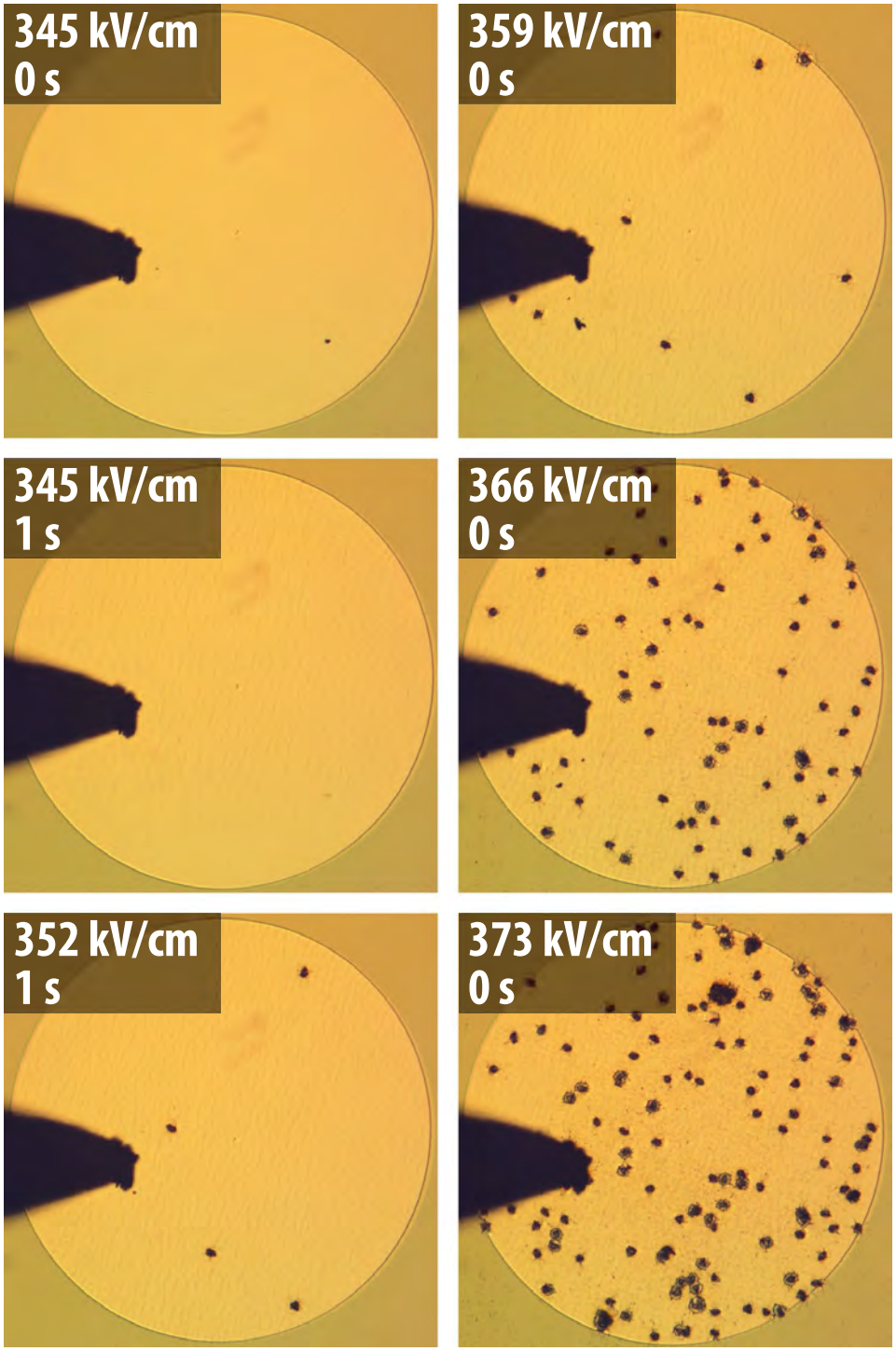

Figure 5.18: Failure of a 500 µm top electrode on the high lead sample (H). The labels represent the voltage and time at voltage that the frame was captured. The voltage increased by 1 V every 3 s.

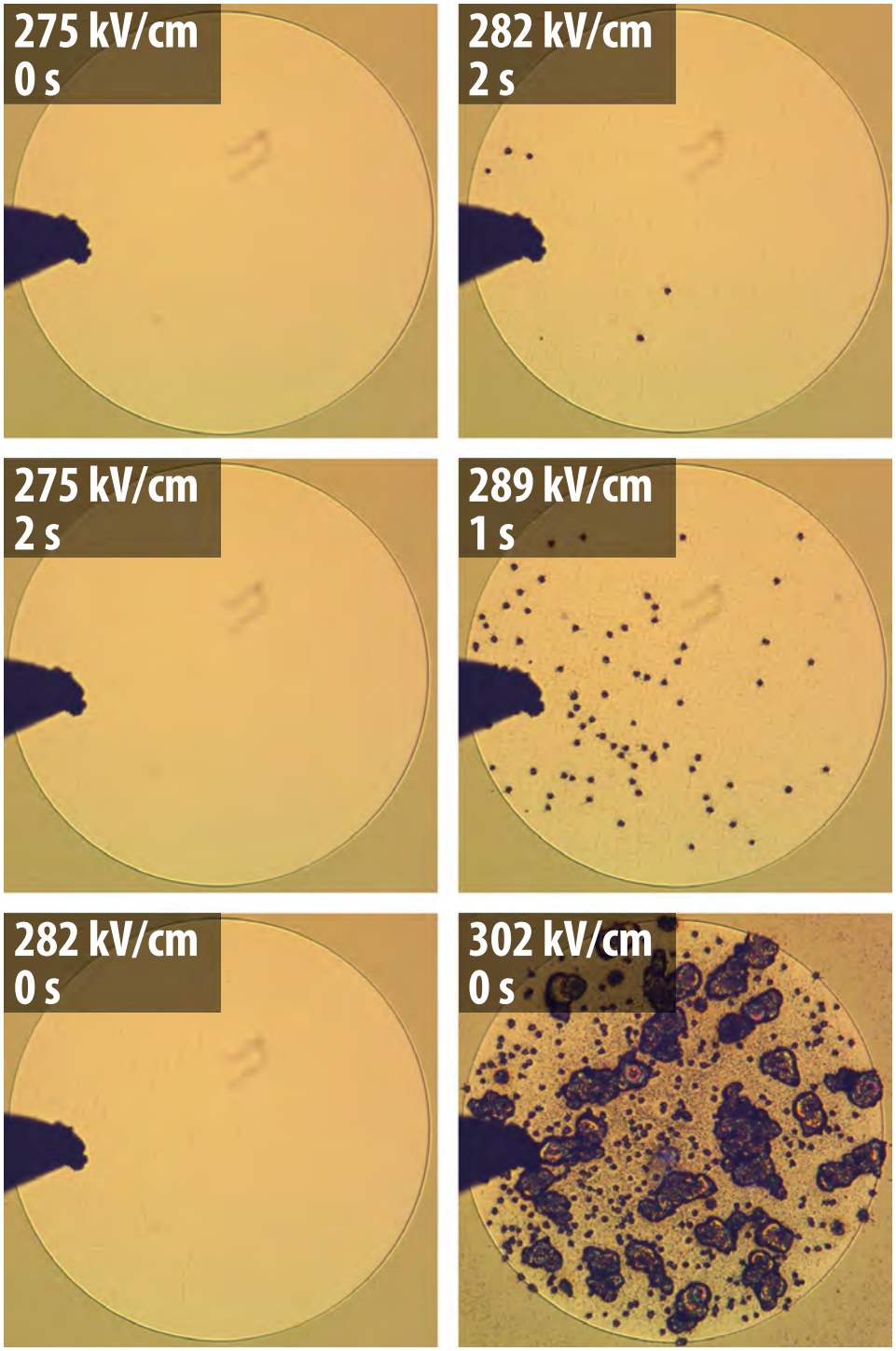

Figure 5.19: Failure of a 500 µm top electrode on the medium lead sample with Mn doped regions (M-Mn). The labels represent the voltage and time at voltage that the frame was captured. The voltage increased by 1 V every 3 s. The blue flash present just below the center of the bottom right frame is a dielectric breakdown event.

Cracked electrodes were further investigated with scanning electron microscopy and focused ion beam milling in order to determine the relation of the cracks to the film microstructure (Figure 5.20. Starting at low magnification (a), it is clear that the cracks propagate 10's of microns beyond the edge of the driven electrode. While clear deep cracks (black, indicating no secondary electron signal) and misalignment of the surface on either side of the crack can be observed in the PZT film, the same is not observed in the platinum top electrode. It appears that the platinum, rather than fully cracking with the underlying PZT film, plastically deforms(XII) and sinks into the crack in the PZT, giving the appearance of a crack in an optical microscope (as in later frames of Figures 5.16 to 5.19).

At a higher magnification (b), the relationship of the crack at the electrode edge can be seen relative to the PZT grain structure. The crack has a propensity to propagate in a predominately straight line. While the crack periodically propagates along the PZT grain boundaries, it frequently cracks directly through the center of PZT grains in order to maintain an approximately straight propagation path. Large obstacles may redirect the crack as seen in (a), but on short length scales the cracks propagate in a primarily straight direction through grains.

A region of a cracked top electrode was milled with a 30 kV Ga focused ion beam (FIB) (Quanta 200 3D – FEI Company) using 500 nm of Pt ("FIB Pt") as a protective layer to prevent milling of the film surface. Micrographs (Figure 5.20 (c)) of the resultant cross section were taken with an FESEM (Sigma – ZEISS Microscopy) for higher resolution than was available with the tungsten filament SEM source in the Quanta. Due to the FIB processing, the grain structure of the cross section is not easily visible; prior cross section micrgraphs obtained by cleaving (Figure 4.9) have predominately vertical grain boundaries. Similarly, seeing the cracks, or plastically deformed regions in the platinum electrode were more difficult after the FIB processing; crack paths have been highlighted with dashed white lines for clarity. It is unclear whether the cracks follow grain boundaries when propagating throughout the film thickness. Given the predominately columnar grain structure, and the angle of the cracks it is presumed that the cracks do not follow grain boundaries when propagating through the film thickness as well as across the surface. It is also noted that all cracks which were observed propagated throughout the entire film thickness.

Cracking of the PZT film at applied fields near 400 kV/cm is in close agreement with the work of Mazzalai *et al.* Films in the work of Mazzalai *et al.* were gradient free, 52/48 PZT films with {1 0 0} texture achieved via lead titanate seed layers,[176] very similar to the films of this work.(XIII) The critical stress for cracking was reported to be 550 MPa with 150 MPa originating from the crystallization process.

(XII) At least at the surface of the platinum. In Figure 5.20 (b) it is apparent that the thinner region at the end of the platinum electrode cracks with the PZT film. It is suspected that the platinum near the PZT interface may crack, but this crack does not propagate through the entire platinum layer thickness.

(XIII) The primary differences are the use of Mitsubishi Materials butanol based commercial solutions rather than 2-methoxyethanol solution chemistry, and the addition of Nb (and Mn) doping in this work. Films were also patterned into cantilevers in the work of Mazzalai *et al.*[176]

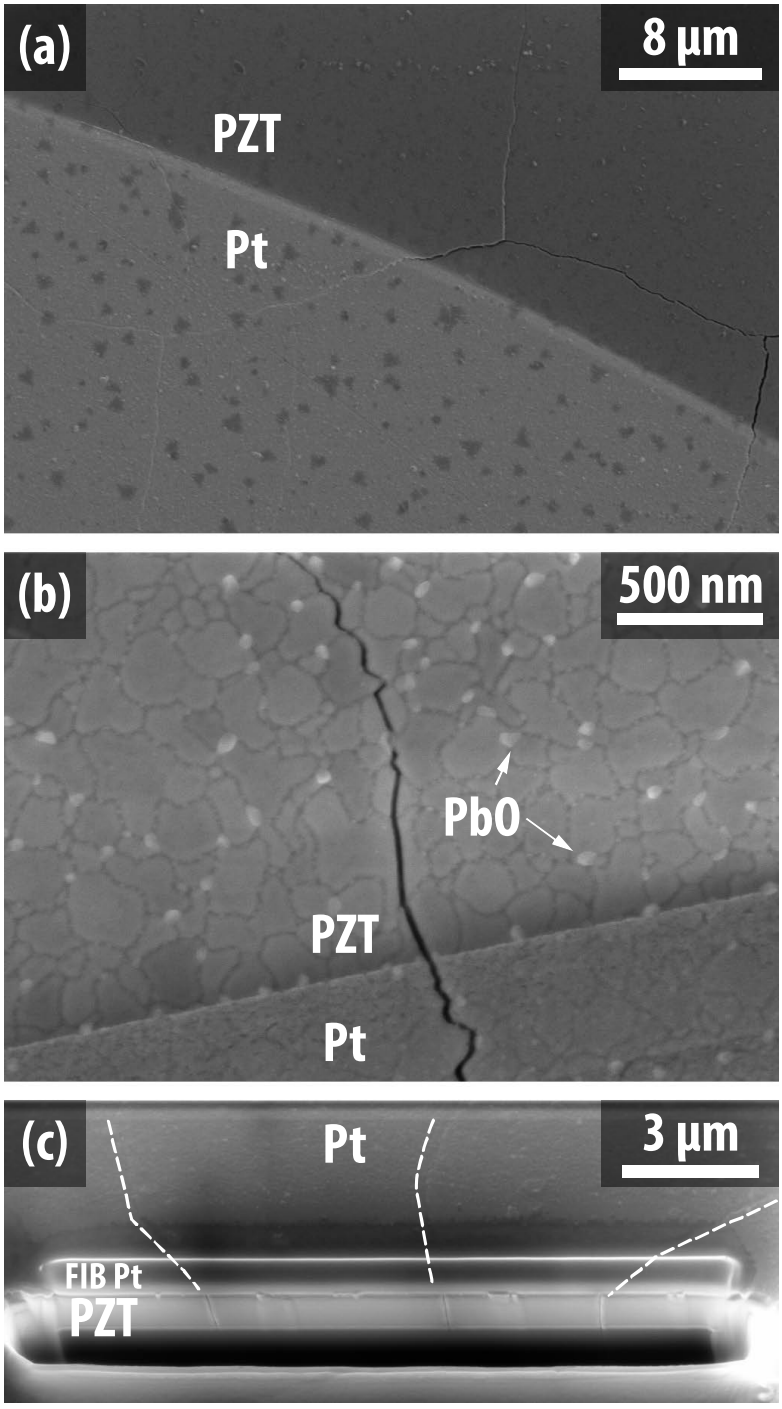

Figure 5.20: SEM micrographs of PZT films cracked via brief application of fields near 400 kV/cm. (a) a top electrode on sample M, showing cracks in the PZT film beyond the edge of the platinum electrode as well as in the electrode itself. (b) at the edge of a top electrode on sample H, showing the relationship of crack path to the grain structure of the underlying PZT film. (c) Cross section micrograph from focused ion beam milling perpendicularly across three cracks, showing the propagation of the cracks through the film thickness. Dashed lines indicate where the cracks are on the sample surface for clarity.

5.4 Conclusions on Dielectric and Piezoelectric Properties

Variations in the lead concentration (on the order of 2-3 at.%) of solutions used to deposit Nb doped, gradient-free, PZT thick films has a more limited effect on the dielectric and piezoelectric properties than the addition of approximately 10 vol.% of Mn doped PZT. Films without Mn doped regions exhibited dielectric constants near 1675 at 100 Hz while the film with Mn doping had a dielectric constant of 1550. A series model based on the layer sequence closely predicted the ratio of dielectric constants. Rayleigh coefficients were similar for samples without Mn doping while the Mn doped sample exhibited reduced reversible and irreversible contributions, attributed to domain wall pinning by defect dipoles. The niobium doped sample with a medium amount of lead was found to have a lower irreversible Rayleigh coefficient, the cause of which is unknown, but which is in agreement with the work of Marincel *et al.* The frequency dependence of the Rayleigh coefficients was found to be approximately constant across all films. This was attributed to the frequency regime measured, phenomena which may have changed upon Mn doping either occurred at time scales faster or slower than the measured range. No significantly enhanced threshold field was observed in films with Mn doping, indicating that 10 vol.% of Mn doped layers does not influence the threshold field for the entire film.

All films exhibited well-saturated hysteresis loops with an increasing space charge contribution in M-Mn, H, and M relative to L. All films exhibited cracking in the range of 350 – 450 kV/cm, an indication of high piezoelectric stresses. It was observed that films with higher lead contents cracked earlier than those with low lead contents, this suggests that lead oxide along grain boundaries lowers the stress necessary for cracking.

A preference for poling with the field pointing from the top to bottom electrode (field-down) was established. While the sign and magnitude of the imprint could be reversed upon poling in the field-up direction, the magnitude of the imprint was limited. While the source of this preference is unknown, it is clearly immobile at the poling temperature of 150 °C. All films exhibited large signal $d_{33,f}$ values near 120 pm/V across a broad range of poling fields. The small signal (remanent) $d_{33,f}$ value was found to saturate in most films by 100 kV/cm, yielding a remanent $d_{33,f}$ of 80 – 90 pm/V. Converse to dielectric and piezoelectric property measurements where sample L exhibited the highest response and M the lowest (of films L, M, and H), sample L exhibited a lower small signal response than sample M. Aging of the remanent $d_{33,f}$ was found to increase with lead content at elevated temperatures. No significant difference was found in the aging rates as a function of lead content or Mn doping at room temperature, however the rates (2-4% per decade) were in close agreement with the lower bounds reported in other works.

All films were found to fail at elevated electric fields by first cracking and then experiencing dielectric breakdown events with burning or ejection of material from the measured electrode. The average failure strength (defined by cracking or burning) was found to increase as lead content decreased, however the variability in the failure strength from electrode to electrode also became broader. Films with high lead

contents were found to exhibit small breakdown events at lower fields while films with low lead contents had large breakdown events at higher fields. Eventually, some electrodes on all samples would have large breakdown events at high fields. Cracks were observed to propagate throughout the entire PZT film thickness with little consideration for following grain boundaries.

The subtle differences in the dielectric properties of films with varying lead content could not be adequately explained on the basis of domain wall pinning by lead or oxygen vacancies, lead oxide at grain boundaries, or a combination of these factors. A more thorough investigation of the differences between films with variations in lead content is suggested in Section 6.2.4. While small additions of Mn had a strong impact on the low field dielectric properties of the PZT films, no appreciable improvement in poling retention was observed but may be achieved with further investigation (Section 6.2.3).

Chapter 6
Conclusions and Future Work

6.1 Conclusions

6.1.1 Platinized Silicon Substrates

Sputter deposition of platinum at elevated temperatures (500 – 600 °C) was investigated in conjunction with the use of {1 0 0} TiO_2 adhesion layers. {111} oriented platinum deposited at elevated temperatures on TiO_2 was found to have an enhanced grain size (by a factor of 3-7), reduced rocking curve FWHM (by a factor of 2-3) and with a similar roughness (for films deposited in the same production environment) to platinum deposited at room temperature on Ti adhesion layers. It was further established that the platinum microstructure is dependent on the platinum deposition conditions. Platinum simultaneously sputtered at PSU on 5 different TiO_2 adhesion layers exhibited the same microstructure and {111} FWHM. It is anticipated that time at temperature, ion bombardment levels, deposition rate or a combination of the three is responsible for the difference in grain size between ARL HT Pt and XP's or PSU's HT Pt; warranting further investigation (Section 6.2.1).

6.1.2 {0 0 1} Textured Seeding of PZT Directly on Platinized Silicon Substrates

Deposition of {0 0 1} textured PZT seed layers directly on platinized silicon (both RT and HT) can be achieved under the right processing conditions. Seed layers on HT Pt were found to have diminished surface pyrochlore coverage and larger grain sizes than counterparts on RT Pt. No significant changes were observed in seed layers deposited on HT platinum from different sources. Changes in solution lead excess stoichiometry reduced the pyrochlore coverage of seed layers on RT Pt by 25% and 10% in seed layers on HT Pt.[(I)] No statistically significant change in PZT grain size was noted as a function of solution lead stoichiometry. Manganese or niobium doped PZT seed layers crystallized similarly to undoped PZT on RT Pt, with a small increase in grain size observed for Nb doped seed layers. Similar behavior was observed in Nb doped seed layers on HT Pt. However, manganese doped seed layers crystallized poorly on HT Pt, exhibiting a rosette microstructure with large regions of pyrochlore. XRD signal intensity (for any PZT peak) was low relative to undoped or Nb doped films. It is also noted that Nb doped films had higher surface coverages of pyrochlore which may be attributed to enhanced pyrochlore phase stability.[51,52] Finally, highly {0 0 1} textured PZT seed layers could be deposited with thicknesses ranging from 30 – 70 nm thick. At higher spin speeds (thinner) a rosette microstructure or triangular grains (with a small {111} PZT peak) surrounded by pyrochlore were observed and a low XRD signal intensity while those at lower speeds (thicker) favored {111} orientation.

[(I)] Reductions are in terms of relative change, not absolute percent, of pyrochlore area coverage.

6.1.3 {0 0 1} Textured Growth of Doped Gradient Free PZT Thick Films

Preferential {0 0 1} orientation of PZT films was found to degrade as a function of film thickness. This was determined to be a result of the high surface pyrochlore concentrations observed in films deposited with low lead excess ($\sim$ 10 at.%) in lead depleted furnace conditions. Conversion of surface pyrochlore to the perovskite phase via lead oxide capping layers was investigated as a means of eliminating misorientation from pyrochlore. Lead oxide capping layers applied *prior to PZT crystallization* caused a new, misoriented grain structure to form with each crystallization. In contrast, applying lead oxide *after PZT crystallization* followed by recrystallizing was found to remove surface pyrochlore and, facilitate strong {0 0 1} texture. Using this methodology, films 1.5 – 1.8 μm thick were deposited with Lotgering factors as high as 0.97. However, the Lotgering factors were varied sample to sample, with some as low as 0.75 as a consequence of the surface pyrochlore concentration. In cases with low pyrochlore coverage, lead oxide capping layers were adequate to convert the pyrochlore to {0 0 1} oriented perovskite. Conversely, in the case with high pyrochlore coverage (i.e. few to no perovskite grains visible through several layers of pyrochlore grains), lead oxide capping layers had a limited ability to facilitate strong {0 0 1} texture. In all cases, the resultant films had high lead contents leading to low breakdown strengths and high leakage currents.

By utilizing solutions with high lead excess concentrations (averaging 14 - 17 at.% across the entire film thickness) strong {0 0 1} orientation was maintained (Lotgering factor of 0.99+) up to the final film thickness of 1.5 μm. For these films, Nb doped PZT seed layers did not reliably or reproducibly produce strong {0 0 1} orientation. Therefore, a $PbTiO_3$ seed layer was utilized under the PZT seed layer. Four thick films were made in order to test two compositional parameters. Three films had the same 2% niobium doped gradient free composition, with variations in the lead excess used between films. The low lead film used 10/14/20 at.% for the Zr-rich/MPB/Ti-rich layers while the medium and high lead films used 14/14/20 at.% and 14/17/20 at.% respectively. The fourth film replaced one of the 6 gradient free niobium doped layers in the medium lead film with a manganese doped PZT layer on either side of the 5 gradient free layer (15 PZT layers total) stack. With the set of four films, the influence of lead stoichiometry and the thin Mn doped PZT layers on the ferroelectric and piezoelectric properties of PZT thin films was investigated.

6.1.4 Ferroelectric and Piezoelectric Properties of {0 0 1} Textured PZT Thick Films

While subtle differences were observed in the dielectric properties as a function of lead content: i.e. low lead content had a higher dielectric constant, medium lead content had a lower dielectric constant and Rayleigh coefficients, it is unclear how these differences would arise on the basis of defects associated with lead concentration (lead and oxygen vacancy concentrations and PbO plating along grain boundaries). The film with Mn doped layers was found to have a diminished dielectric response attributed to domain wall pinning by defect dipoles. Some trends with lead content (decreased

Rayleigh coefficients with medium lead) aligned closely with the findings of Marincel *et al.*, however it is unclear if these are statistically significant. Films with increased lead were found to crack earlier in hysteresis measurements and have a larger space charge or leakage contribution to the apparent measured polarization.

All films exhibited large signal $d_{33,f}$ values near 120 pm/V across a range of poling fields, with remanent $d_{33,f}$ values near 90 pm/V at poling fields above 100 kV/cm. Elevated temperature (150 °C) aging rates of poled electrodes were found to increase with lead content. At room temperature, aging rates were 2 – 4% per decade; differences in aging rates were not found to be statistically significant. However, aging rates are in close agreement with the lower bounds reported by other authors.

When exposed to high fields, films were found to first crack from the piezoelectric stress, followed by dielectric breakdown as time and/or voltage progressed to higher values. Films with higher lead contents were found to fail at lower fields in a tighter distribution than those with lower lead contents. Furthermore, increased lead content lead to a greater population of small localized breakdown events at low fields while those with lower lead contents did not breakdown until high fields, at which breakdown events were much larger. Cracks were found to propagate in predominately straight lines throughout the film thickness, rather than following grain boundaries. The electric fields at which cracking occurred at (∼400 kV/cm) were similar to those reported by Mazzalai *et al.* for gradient free {1 0 0} PZT films.

6.2 Proposed Future Work

6.2.1 Factors Which Control the Grain Size of Platinum Sputtered at High Temperatures

In Section 2.5 it was established that the high temperature platinum deposition conditions were the dominating factor in the resultant grain size of the platinum microstructure. When comparing the deposition conditions (Table 2.8) there are multiple differences which could, in principle, lead to the observed grain size difference between ARL HT Pt, and XP or PSU HT Pt. Recrystallization and grain growth become significant circa $0.4 - 0.6T_{melt}$ on an absolute temperature scale, depending on the driving force.[177,178] In the case of Pt, with a melting temperature of 2042 K, deposition at 500 °C or 600 °C would represent 0.38 or $0.43T_{melt}$. Small grain sizes ($d < 100$ nm) would result in a large driving force for grain growth ($\propto d^{-1}$). For films which are slowly cooled (XP or PSU), a greater amount of time will be spent at temperatures within the threshold for grain growth.

Ionic bombardment during the sputtering process can provide energy to surface atoms, allowing for increased adatom mobility. As the sputtering pressure increases, the level of ionic bombardment at the surface of the film will decrease, decreasing surface adatom mobility.[179] Since the deposition temperatures are near the lower threshold for platinum grain growth,[179] supplementing thermal energy with energy from ionic bombardment may be necessary in order to allow for platinum grain growth at rates which are ample to double the grain size during the short deposition time period. The structure

zone model (Figure 6.1) shows that the boundaries between Zones 1 and T and Zones T and 2 are controlled by a combination of thermal energy (temperature) and bombardment energy (inversely related to pressure).[106,179] ARL uses the highest argon pressure during their sputtering process while XP uses the lowest. As such, ARL would be expected to have the least energetic growth process from an ionic bombardment standpoint.

Adatom mobilities will be higher at the surface of the film than in the bulk of the film.[106,180] Pt atoms will be sputtered onto the surface of the film with a finite amount of kinetic energy, as well as being bombarded by inert gas ions. Furthermore, the motion of surface atoms will be less restricted by surrounding Pt atoms than atoms within the bulk of the material, allowing for faster diffusion rates. In the case of a film sputtered at a low deposition rate, existing surface atoms will have a greater amount of time to rearrange and form a larger grain structure. If deposition rates are high, surface atoms will quickly become buried under the following layers of atoms, restricting the ability for further rearrangement and grain growth.[179]

When comparing the sputtering parameters of PSU, XP, and ARL (Table 2.8) it is not immediately clear which factor is controlling the final grain size. ARL has less bombardment than XP, the fastest deposition rate, and may be deposited at a lower temperature (500 °C is the setting, not necessarily the actual) so it is expected to have the smallest grain size, as it does. However, when comparing XP and PSU, both share approximately the same temperature. XP uses more bombardment during their deposition as well as a substantially faster deposition rate than PSU. The increased bombardment in XP's process may compensate for the reduced deposition temperature (500 °C vs. 525 – 550 °C) allowing both XP and PSU to maintain approximately the same grain size. PSU may have more or less bombardment than ARL, as PSU uses a substantially larger substrate target distance which approaches the mean free path of the gas at the sputtering pressure.[181,182]

It is of interest to deconvolute the roles of time at temperature, deposition rate, and ionic bombardment (as a function of pressure and target-substrate distance) in order to determine which factor(s) control(s) the resultant Pt grain size. Furthermore, it is of interest to study the densification and grain growth of thin film platinum grains after the deposition, as there are limited, if any, reports in the literature. In particular, it is suggested that a series of annealing experiments be conducted to induce grain growth without compromising the integrity of the film's adhesion, roughness, or crystallographic texturing. Annealing of films at temperatures in the range of 0.4-0.6$T_{melt,Pt}$ from minutes (i.e. time scale of the deposition) to hours to determine if and when Zone 3 structures can be developed in already deposited films. Roughness and crystallographic texture can be measured by AFM topography scans and XRD rocking curve measurements, as in this thesis. Adhesion can be measured qualitatively and/or quantitatively by scratch, tape, or "pulling" tests, as described by Hull *et al.*[183]

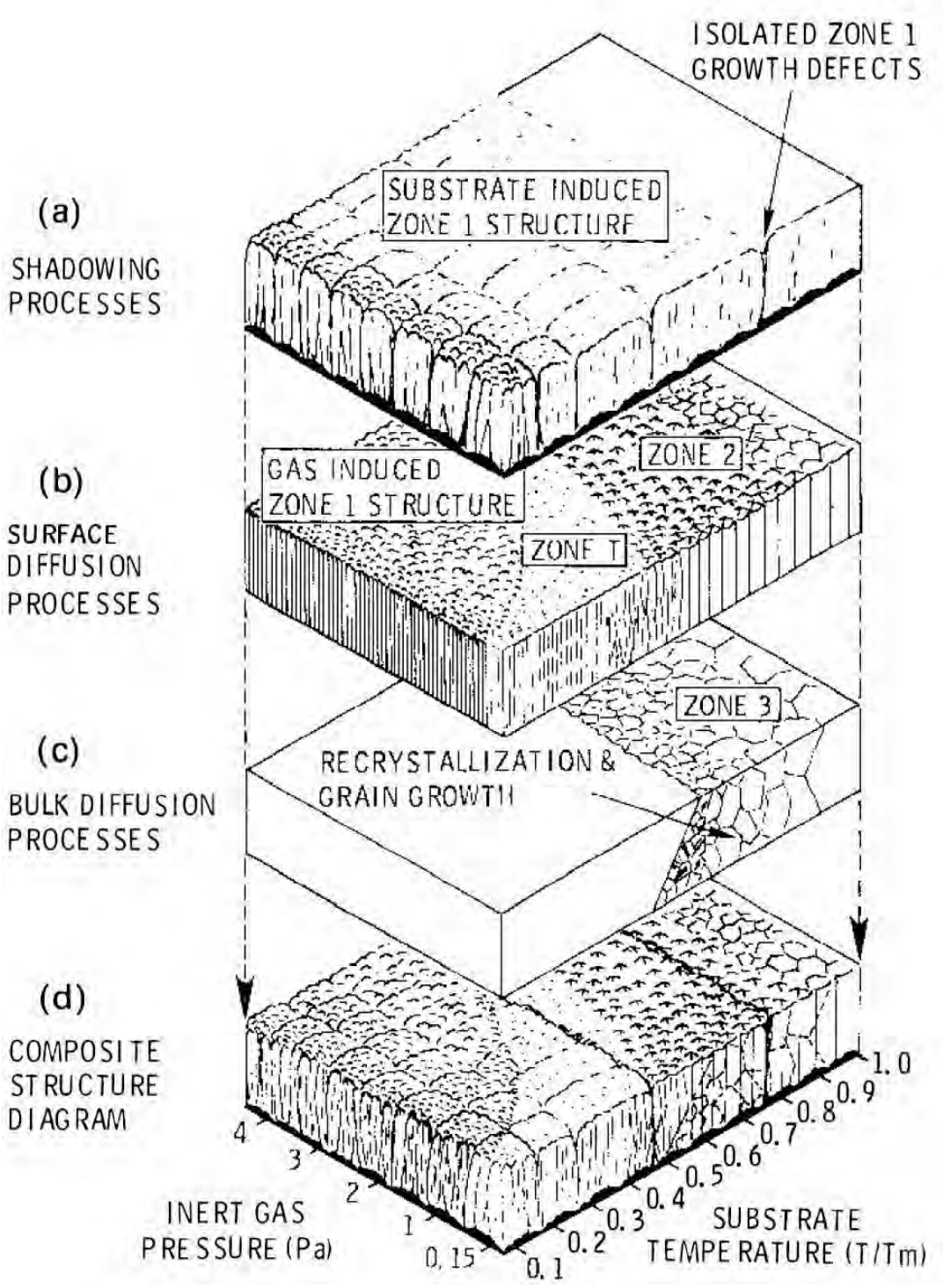

Figure 6.1: The structure zone model as described by Thornton.[179]

6.2.2 Chemical Homogeneity of Lead, Zirconium/Titanium Ratio, and Dopants

The presence of Zr/Ti ratio gradients in crystallized layers of PZT processed by CSD, as well as means to reduce these gradients have been thoroughly reported in the literature.[27,29,31,32,184] The formation of the Zr/Ti gradient, with Ti rich conditions at the bottom of the layer, has been ascribed to the more favorable nucleation characteristics of $PbTiO_3$ over $PbZrO_3$.[138] Building in an opposite and approximately equal gradient via solutions with varied composition serves as a means of reducing this gradient substantially.[27,31]

Lead rich conditions have also been found to favor nucleation. In particular $\{0\,0\,1\}$ textured PZT is reported to nucleate favorably on $(1\,0\,0)$ PbO seed layers produced by high lead fluxes at the $\{1\,1\,1\}$ Pt interface.[138] Films made in Chapter 4 had similar, artificially imposed lead concentration gradients in the amorphous layer sets as a consequence of the solution utilized. Similar to the logic employed by Ledermann *et al.*, high lead concentrations were utilized at the top surface to counter surface lead volatilization.[29] In some films (particularly samples H and L), the artificial concentration gradient was formed across the entire set of 3 layers, rather than just between the last two layers of a layer set as in Ledermann *et al.*[29]

The segregation of aliovalent dopant anion species has been established in bulk PZT. Manganese, particularly at higher doping levels, is reported to control grain size via preferential segregation towards grain boundaries, pinning them and limiting grain growth in Mn doped PZT.[131] Niobium likewise has been correlated, in conjunction with compensating lead vacancies, to increased stability of the pyrochlore phase relative to the perovskite phase.[51,52] Given the large $\pm$10% Zr/Ti concentration gradients which can form in PZT upon crystallization, it might be expected that Nb and Mn may also be able to diffuse easily.

While the Zr/Ti gradient has been thoroughly investigated, gradients (if any) which form in the lead or dopant concentrations leave many open questions. Lead may form spontaneous gradients (rich at the bottom for nucleation / less volatilization) upon the crystallization of a homogeneous amorphous film. Artificially induced lead concentration gradients in the amorphous film (such as those in Figure 4.6), may change during crystallization, altering the final lead gradient. It has been demonstrated that the Zr/Ti gradient can be reduced or enhanced by the sequence of deposited solution stoichiometries,[31] indicating that the driving force for Zr/Ti gradient formation can be easily overcome with solution stoichiometry. It is of interest to understand how the resultant lead gradient (if any) relates to the stoichiometry and sequence of the deposited solutions. For example, a significantly lead rich layer at the top surface may be necessary to counter volatilization; this might be the case where a naturally formed gradient is either lead rich at the bottom or does not form at all. Alternatively, a modest increase in excess lead in all solutions could give the same net result if there is a driving force for a gradient which is lead rich at the surface. Similarly, Mn, Nb or other dopants may form gradients within thick films.

Mn may favor interfaces[131] as is observed in bulk PZT while Nb may favor regions of pyrochlore[51,52] or those away from perovskite nucleation.

If gradients do develop in the lead or dopant concentrations, it may be of interest to make Zr/Ti, Pb, and dopant gradient free films. Due to the small concentration of dopants present, and the small magnitudes of the concentration gradients which may form, it is unknown whether dopant gradients (if present) would result in a significant impact on the properties of the resultant film, as was observed in gradient free (Zr/Ti) films. It is anticipated that the lead and dopant concentration gradients (if present) can be altered by artificially imposing gradients in the amorphous films, similar to the work on Zr/Ti films.

Concentration gradients in dopant species may be anticipated to be small, the B-site (or A-site) makes up 20% of the atomic species in the film. Doping on the level of 1-2 at.% on the B-site would yield a nominal doping level of 0.1-0.2 at.% total across all sites. The absolute magnitude of the Zr/Ti gradient has been demonstrated to be on the order of $\pm$10at.% (i.e. $\pm$20 relative percent to the nominal composition of 53% Zr, 47% Ti).[27,29] If dopant species segregated to a similar degree, a concentration gradient on the order of ±200 – 400 ppm may be expected. The small magnitude of the concentration gradients combined with the high necessary depth resolution (depth profiling of layers 80nm thick) in order to observe a gradient may require a technique such as Time of Flight - Secondary Ion Mass Spectroscopy (ToF-SIMS). Many alternative techniques such as Energy Dispersive Spectroscopy (EDS), X-ray Photoelectron Spectroscopy (XPS), Auger Electron Spectroscopy (AES), and Electron Energy Loss Spectroscopy (EELS) either have high detection limits, poor depth resolution, or a combination of both.

6.2.3 Dopant Concentration, Positioning, Thickness of Mn Doped Layers

Sample M-Mn (medium lead content with Mn doped layers) was fabricated in Chapter 4 as an initial study of introducing graded doping (predominately donor doped with small acceptor doped regions) in a PZT thin film. The layer sequence used in sample D was meant to maintain symmetry between the platinum electrodes while the low dopant concentration and volume fraction of manganese doping would limit property reductions. Therefore it is prudent to further study the dependence of imprint development, aging, and lifetime as a consequence of concentration, positioning and thickness of the Mn doped layers in a graded doped film.

For example, field-induced failure of many electroceramics has been attributed to the electromigration of oxygen vacancies through the bulk of the material.[66–68] Some reports suggest manganese doping can lead to a reduction in the oxygen vacancy concentration if manganese occupies the A-site (typically reported in doping levels below 0.5 at.%).[49,72] However, Mn dopant ions are reported to strongly bind to oxygen vacancies, preventing long-range electromigration.[54,63,65] If manganese doped layers do, in fact, bind oxygen vacancies, then the location, concentration of pinning Mn ions, and thickness of the pinning regions may strongly impact the lifetime of the film.

Similarly, a low volume fraction of Mn doped regions and a low concentration of Mn ions may limit the strength of the internal field which can be induced in the film upon poling.[54] The spatial extent of the electric field induced by imprint in the acceptor layers may also be limited. It may be necessary to use multiple, more closely spaced, acceptor doped layers in order to reduce the aging rate of the donor doped regions of the poled film.

A series of films (similar to M-Mn) could be studied with a variable number of donor doped layers (i.e. thickness) between the acceptor doped layers. A study of the aging rate as a function of film thickness could be used to qualitatively determine the spatial extent to which the acceptor doped layers influence the donor doped layers. Such a study is likely to convolute the effects of spatial influence with the varying volume fraction of Mn doped material. As such, it may be prudent to study pure acceptor and donor doped films and develop a series model. This could allow for subtraction of the property contributions from the acceptor doped regions allowing extraction of how the aging of donor doped regions varies with proximity to acceptor doped regions.

Similarly, a study of the dependence of the acceptor doped layer thickness and dopant concentration on the aging of donor doped regions could allow development of a model which relates the spatial influence of the acceptor doped layers to the dopant concentration and layer thickness. With this understanding, films where the negative influences of the acceptor doped layers (decreased piezoelectric and ferroelectric responses) are minimized while the influence of defect dipole alignment on the poling retention of surrounding donor doped regions is maximized could be developed.

6.2.4 Dependence of PZT Properties on Current and Prior Lead Stoichiometry

It was demonstrated in Section 3.3, as in the literature, that the level of lead excess in a solution can have a substantial impact on the phase purity of the resultant PZT seed layers.[30,71,140,185] In Chapter 4 high lead excess concentrations were necessary to retain strong {0 0 1} PZT texturing in thick films. However, it was established in Chapter 5, and within the literature, that there are consequences to fabrication of films with high lead excess concentrations; in particular low breakdown strengths and leakage under high fields.[71,140,185,186] The study of lead excess is further complicated as kinetic control is employed by most researchers; it is difficult to directly translate solution lead excess to the stoichiometry of resulting films.[144]

Marincel *et al.* developed a furnace where the lead oxide partial pressure can be controlled via the flow rate of tetraethyl lead precursor. They reported that, starting with portions of the same film, anneals at different PbO partial pressures could alter the dielectric and ferroelectric properties. Since all samples (of a given Zr/Ti ratio) were sourced from the same deposited film, they all had identical initial microstructure, properties, and stoichiometries.[144]

In this thesis, it was shown that high lead excess levels were beneficial to enhance the retention of {0 0 1} orientation, however low lead levels could lead to lower leakage currents and high breakdown

fields. It is presently unknown whether the properties of a film, after the lead oxide furnace anneal, will exhibit any dependence on the starting state of the film. That is, would a highly {0 0 1} textured film using high levels of lead excess (H), and one using low levels of lead excess (L) exhibit the same properties if annealed simultaneously in the PbO furnace under the same conditions? Or would some difference, related to structural changes (such as pores left behind by volatilized PbO) result in a difference in properties?

Brennecka *et al.* observed a reduction in polarization of a perovskite film which was converted to a mixed perovskite/pyrochlore film by lead volatilization followed by converting back to perovskite with the addition of excess lead.[187] However, it might be expected that a phase transformation may lead to larger changes in observed properties than adjusting the lead content within a single phase region without any perovskite to pyrochlore transformations.

If such a dependence isn't observed, it may be of interest to fabricate films with high lead contents (to ensure strong {0 0 1} orientation) and reduce the PbO content in the lead oxide furnace to levels near the perovskite/pyrochlore phase boundary to enhance the dielectric breakdown strength and leakage characteristics of the PZT film. If a dependence on the starting state is observed, then an understanding of what characteristics of the film do, or don't, change upon annealing in the lead oxide furnace is of interest. As a consequence, lead excess may be used as a means to control the factor(s) which depend on the starting state, while using equilibration in the PbO furnace to control parameters which are not strongly dependent on the starting state. An additional means of tailoring PZT properties could lead to enhanced overall film performance.

This thesis, as in the work of Marincel *et al.*, is unclear on whether the variations in the electrical properties of PZT films as a function of lead content (with the exception of breakdown strength) are statistically significant. If the variations are significant, it is unclear what mechanism is leading to the differences in properties. In a model in which vacancies serve as pinning sites for domain walls, samples with increased vacancy concentrations might be anticipated to have a lower dielectric response. Sample L would be expected to have the most lead vacancies while sample H would have the most oxygen vacancies. In either case, M might be expected to have a vacancy concentration between that of L and H, however M exhibits the lowest response which would imply the most domain pinning. This same behavior was observed by Marincel *et al.* in the reversible Rayleigh coefficient. The exact lead concentration in the films of this work is unknown as it is a consequence both of the batched lead content, and the lead concentration in the furnace at the time of processing. Quantification of the film stoichiometry and the defect populations in films processed under different conditions could help explain if the vacancy domain wall pinning model may be accurate, or if there is another mechanism responsible for the variations observed. Lead content could be quantified by ToF-SIMS while Deep-Level Transient Spectroscopy (DLTS) could measure relative defect populations between films. Finally, use of a greater set of films (a broader range of lead concentrations, and more films at each level) could

aid in determining if property variations are statistically significant as well as providing a stronger lead content trend than three data points can provide.

6.2.5 Role of Residual Stresses on Cracking via Application of Electric Field

Films of PZT deposited on Si wafers are subject to large residual stresses (∼150 MPa of tension) as a consequence of the large thermal expansion mismatch between the PZT film and the underlying silicon wafer.[96,108,176] (II) Upon application of an electric field in the out of plane direction, the piezoelectric $e_{31,f}$ coefficient will produce an additional in plane tensile stress which is additive with the residual stress. Mazzalai *et al.* reported cracking of gradient free $\{0\,0\,1\}$ textured PZT thick films at piezoelectric stresses ∼390 MPa, which, when added to ∼150 MPa of residual stresses, yielded a critical stress of ∼550 MPa.

If the formation of cracks occurs entirely from mechanical stress and fracture toughness (i.e. no thermally activated defect leading to crack formation or similar), then, in principle, the critical stress for cracking (and therefore critical applied field) should be altered via changes in the residual stress. That is, as the residual tensile stress is reduced (or a residual compressive stress is applied) the critical piezoelectric stress for cracking, and hence electric field for cracking, may increase.

This can be investigated via the use of substrates with different thermal expansion coefficients. As mentioned, silicon substrates produce stresses on the order of ∼150 MPa in tension as a consequence of the $\sim 3 - 5 \times 10^{-6}\,\mathrm{K}^{-1}$ thermal expansion coefficient mismatch. The use of metal foils as substrates, such as Ni with a thermal expansion coefficient of $\sim 13 - 16 \times 10^{-6}\,\mathrm{K}^{-1}$, will result in large compressive stresses on the PZT film although some of the stress may be relaxed by deformation of the metal foil.[190,191]

The means of achieving strong $\{0\,0\,1\}$ texturing of PZT thick films on silicon and metallic substrates does vary. The former uses a PZT or $PbTiO_3$ seed, while the latter uses a $LaNiO_3$ bottom electrode.[190,191] As a consequence of the different methods of achieving $\{0\,0\,1\}$ orientation, it is anticipated that the microstructure, particularly the grain size (or lack thereof) of the resultant films may be different.

Mazzalai *et al.* found the thickness of the film, i.e. a columnar grain boundary, to serve as the critical flaw in the K_{IC} expression for fracture toughness.[176] As such, a change in the number density of critical flaws (number density of grain boundaries) could also result in variations in the critical stresses. While the cracks in this work (Figure 5.20) were found to propagate both along grain boundaries and through grains, the origin point of these cracks is unknown. If the cracks do originate at grain boundaries, then controlling the grain size may be crucial to understand the role of residual stresses in the critical stress for cracking. Control of grain sizes could be achieved through a combination of electrode microstructure (particularly in the case of platinized Si as shown in this work), and crystallization conditions.[132] Variations in lead content which may accompany different crystallization conditions could be corrected

(II) Silicon has a thermal expansion coefficient of $2.6 \times 10^{-6}\,\mathrm{K}^{-1}$ at room temperature and $4.2 \times 10^{-6}\,\mathrm{K}^{-1}$ at 500 – 600 °C[105] while PZT has a thermal expansion coefficient of $6.5 - 8.5 \times 10^{-6}\,\mathrm{K}^{-1}$ above the Curie temperature.[188,189]

via extended anneals in the PbO atmosphere furnace constructed by Marincel[150] This may also serve as a means of further equilibrating the microstructures of the polycrystalline films.

Appendix A

Synthesis of 2-Methoxyethanol Based Lead Oxide CSD Solutions

Preparation of 2-methoxyethanol based PbO solutions was modeled after the process outlined by Wolf & Trolier-McKinstry with minor modifications.[96]

1. Dissolve lead (II) acetate trihydrate [$Pb(CH_3CO_2)_2 \cdot 3\,H_2O$] $\geq$ 99.99% trace metals basis (Sigma-Aldrich, Inc.) in 120 mL 2-methoxyethanol (2-MOE) [$CH_3OCH_2CH_2OH$] $\geq$ 99.0% (Sigma-Aldrich, Inc.) at 120 °C under flowing argon.
2. Vacuum distill lead acetate - 2-MOE solution at 120 °C until a dry precipitate is formed.
3. Add 120 mL of 2-MOE to dry precipitate. Stir and reflux at 120 °C under argon flow for 2 h.
4. Vacuum distill solution to 60 mL volume at 120 °C.
5. Add 4.5 vol % acetylacetone [$Ch_3COCH_2COCH_3$] $\geq$ 99% (Sigma-Aldrich, Inc.) to distilled solution, dilute solution with 2-MOE to desired solution molarity.
6. Stir while cooling for 30 minutes, bottle, and seal with parafin wax film. (Parafilm).

Note: 4.5 vol % is related to the molarity of the final solution (0.08 M in this case). If molarity is halved (0.04 M), acetylacetone should be halved as well (2.25 vol %)

Appendix B

Supplementary Figures

This appendix contains additional figures that the reader may find useful. These figures were not included in the main body of the text in order to preserve the flow of chapters. All figures will be grouped according to the sections that they correspond with.

General Supplementary Figures

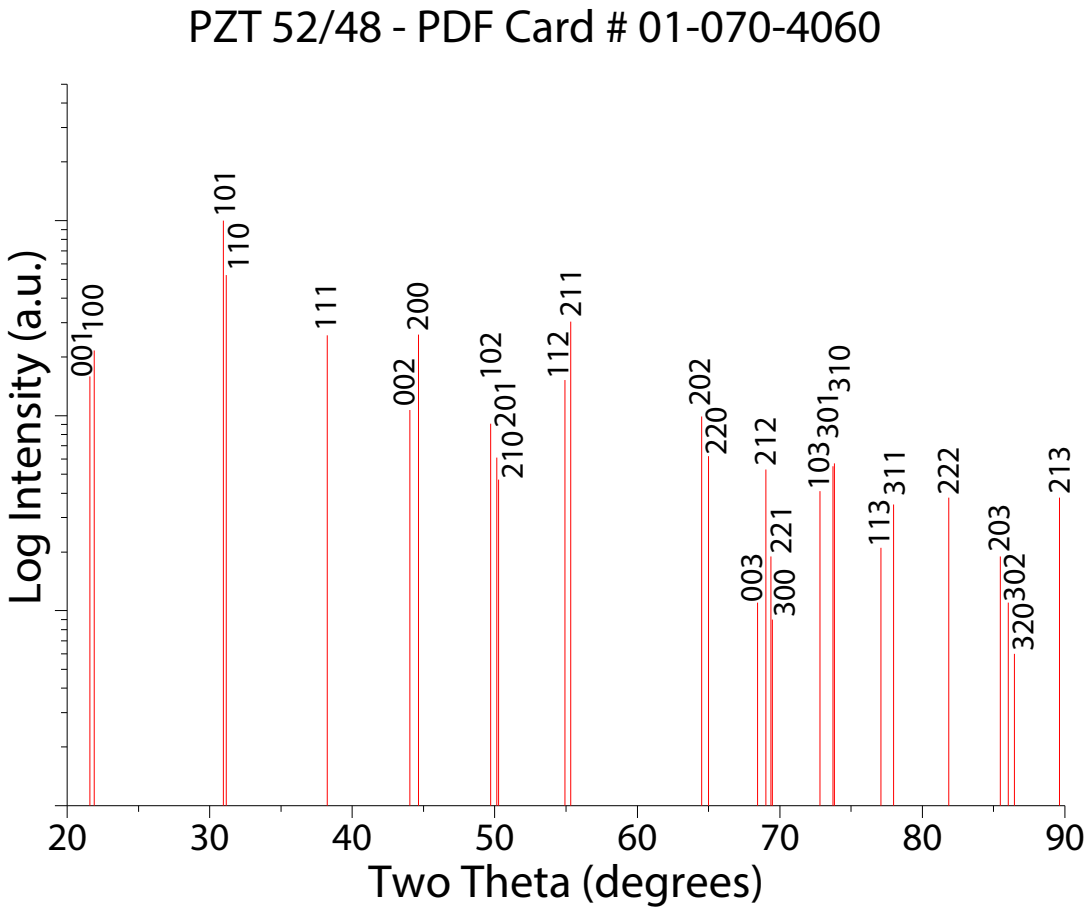

Figure B.1: PZT 52/48 X-ray diffraction pattern from ICDD PDF # 01-070-4060, truncated to 20 – 90° 2θ[99]

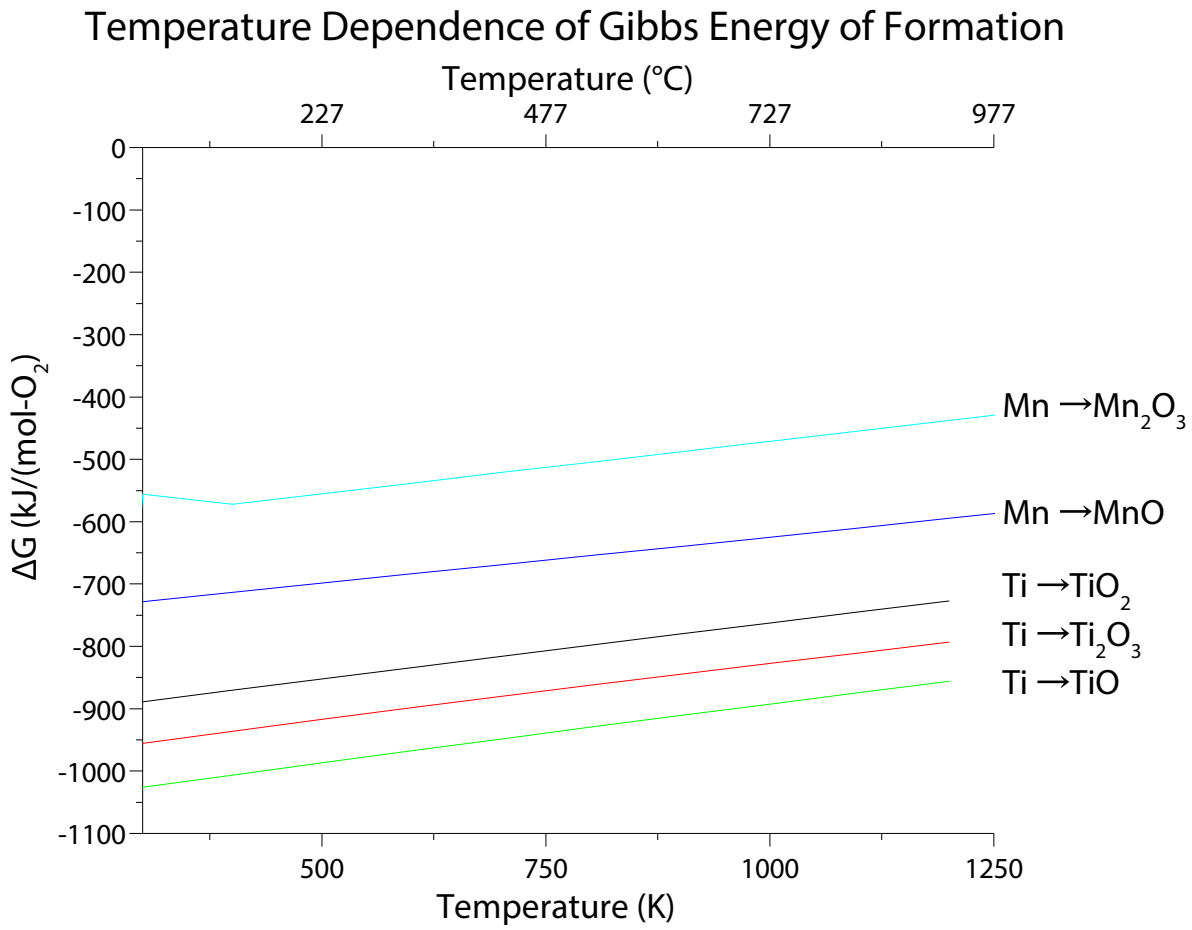

Figure B.2: Gibbs free energy of formation as a function of temperature for titanium and manganese oxides with differing oxidation states. Graph is a composite of data from [192–195].

Supplementary Figures for Section 2.4: Electrical Characterization

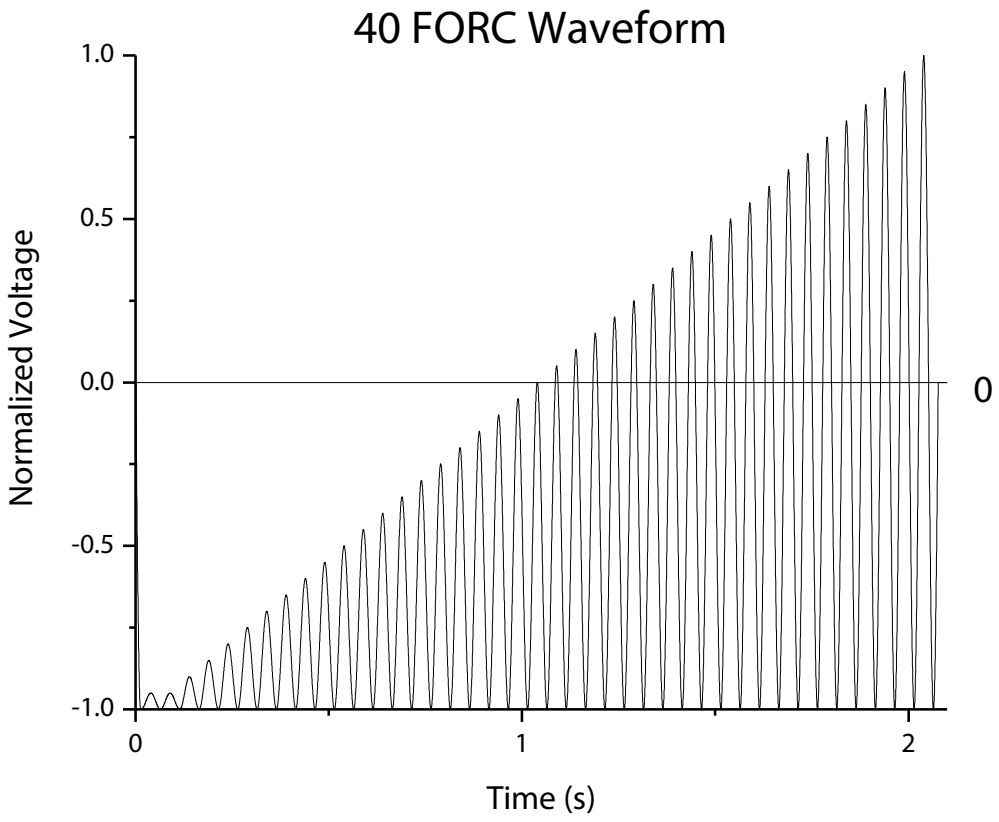

Figure B.3: Waveform used to generate 40 FORCs at 20 Hz, from Fujii.[78]

Supplementary Figures for Section 2.5: Platinized Silicon Substrates

As Sputtered Titanium

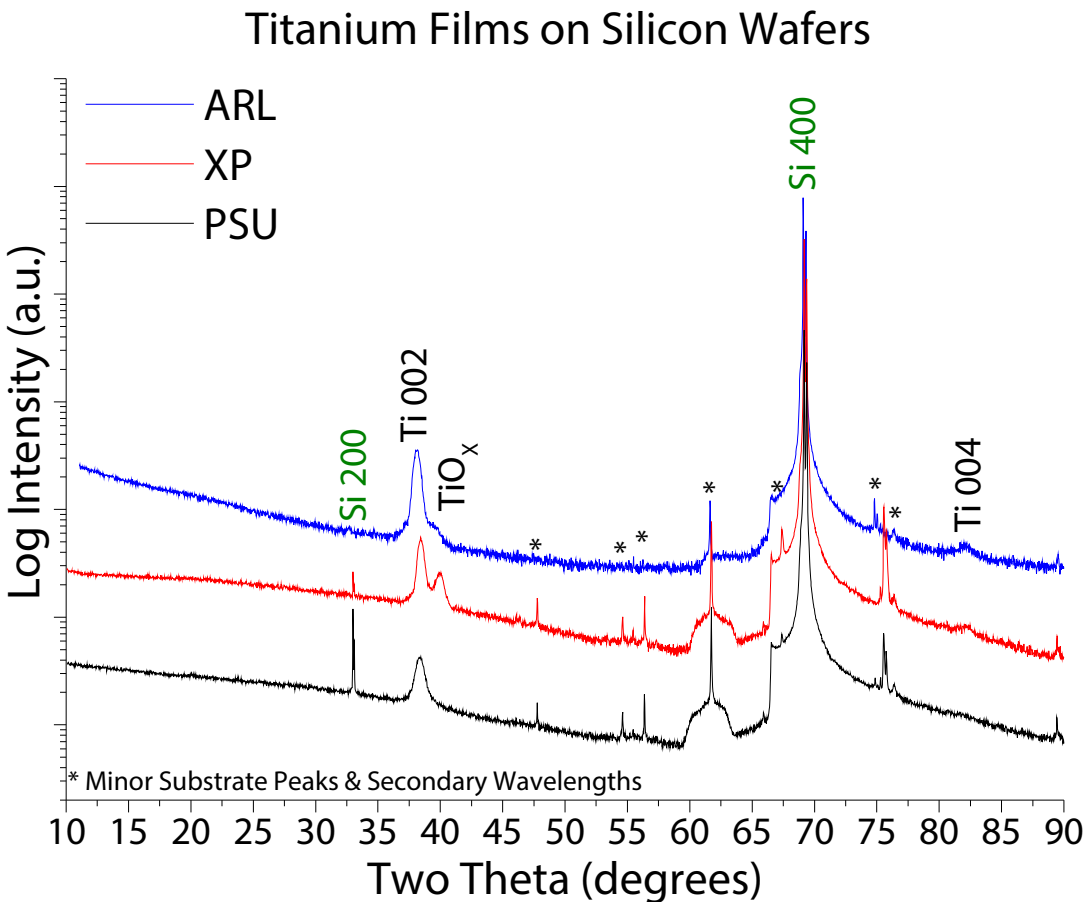

Figure B.4: Bragg-Brentano X-ray diffraction of as deposited / received titanium adhesion layers from PSU, ARL, and XP. The Ti film from XP had a small oxide peak indicating some oxidation during the deposition process or shipping to Penn State.

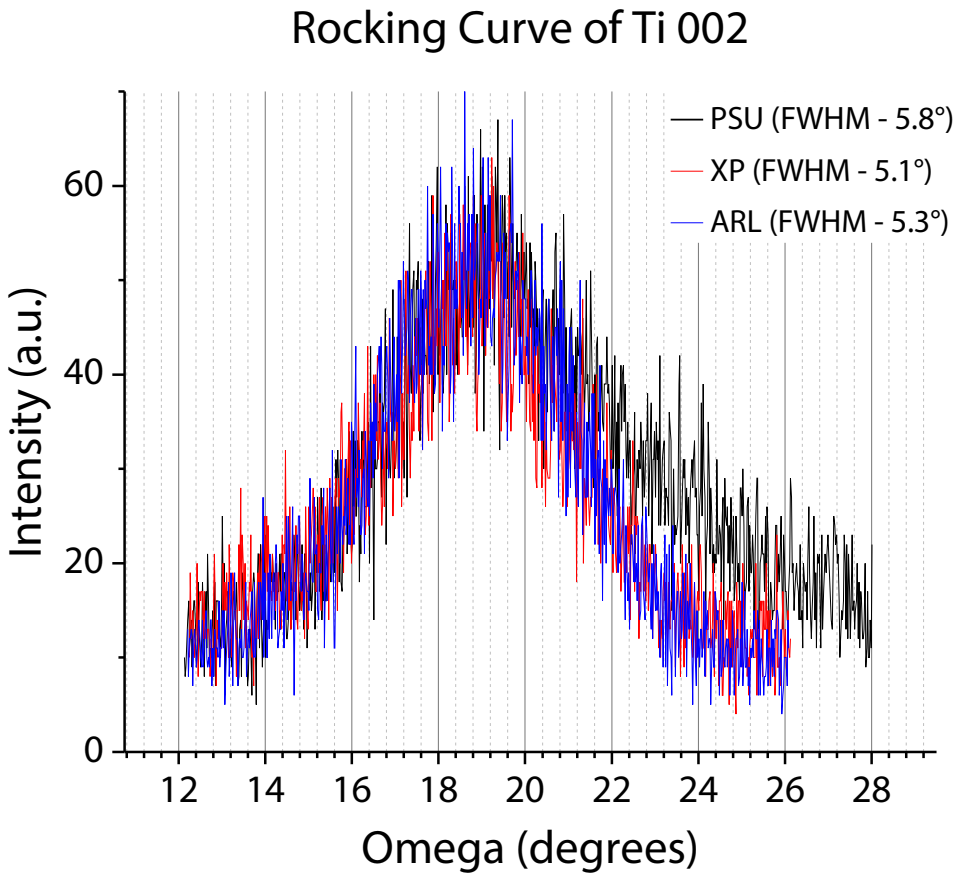

Figure B.5: Rocking curve X-ray diffraction of the Ti {0 0 2} peak from as deposited / received titanium adhesion layers from PSU, ARL, and XP. Peak FWHM were calculated from the raw data utilizing a Gaussian peak fitting function.

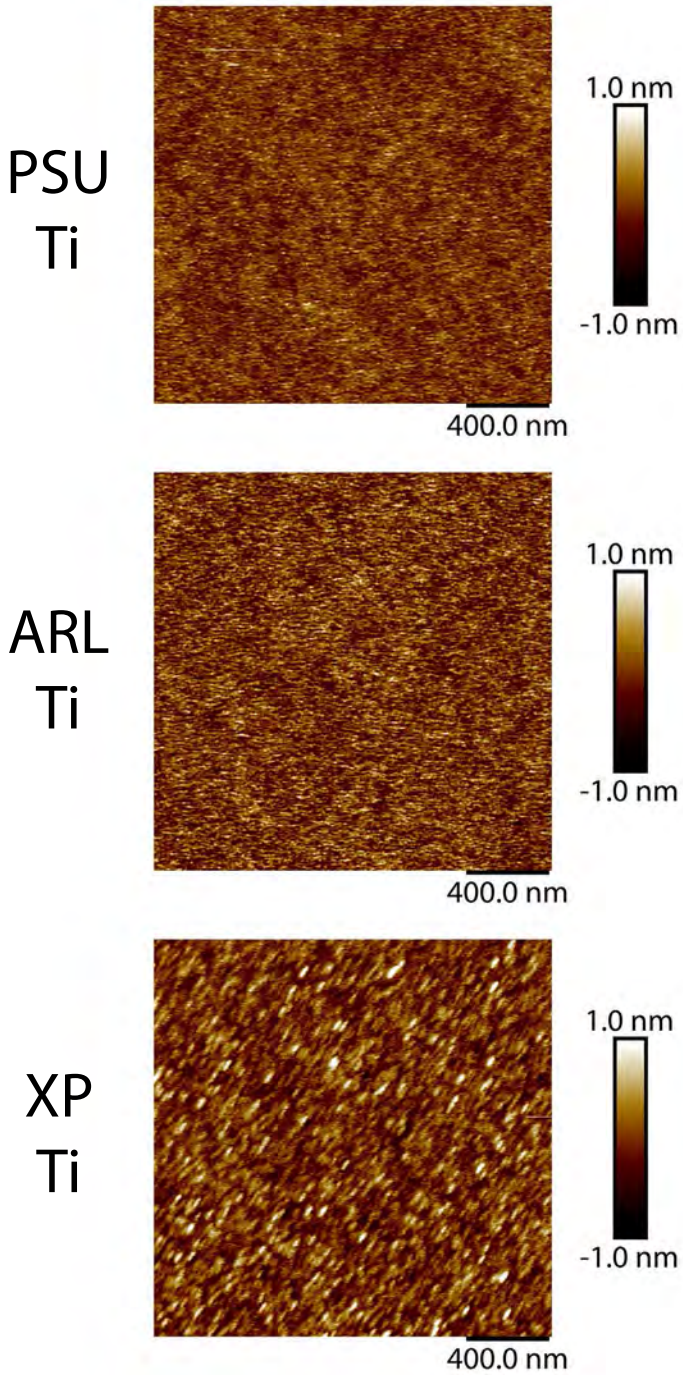

Figure B.6: 2 µm square AFM scans of as deposited / received titanium adhesion layers from PSU, ARL, and XP.

Oxidized Titanium TiO_2

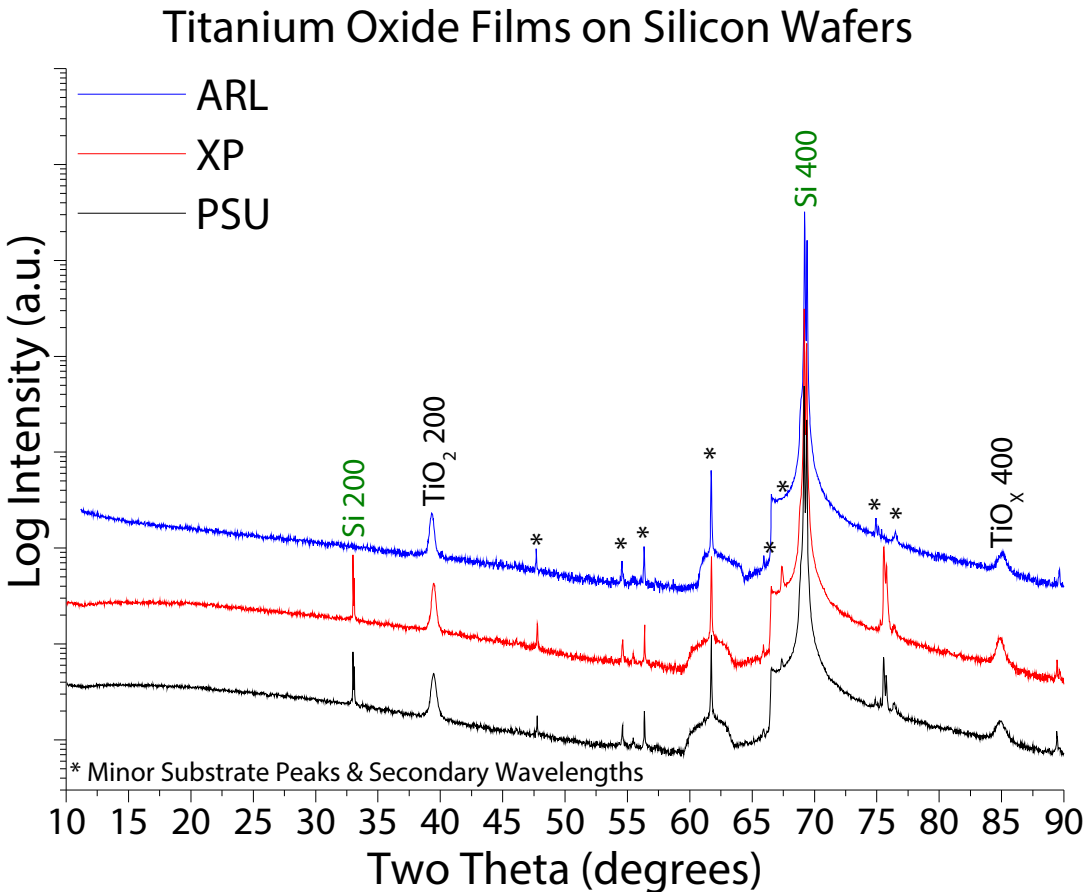

Figure B.7: Bragg-Brentano X-ray diffraction of as oxidized / received titanium oxide adhesion layers from PSU, ARL, and XP.

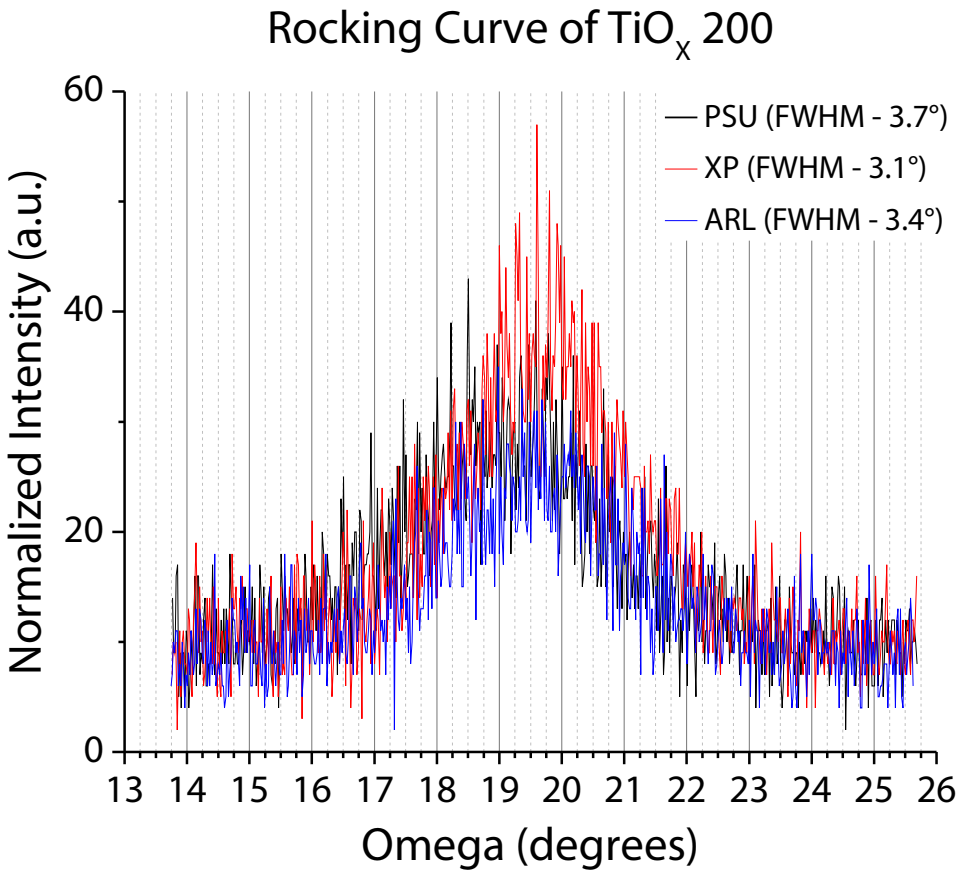

Figure B.8: Rocking curve X-ray diffraction of the TiO_2 {2 0 0} from as oxidized / received titanium oxide adhesion layers from PSU, ARL, and XP. Peak FWHM were calculated from the raw data utilizing a Gaussian peak fitting function.

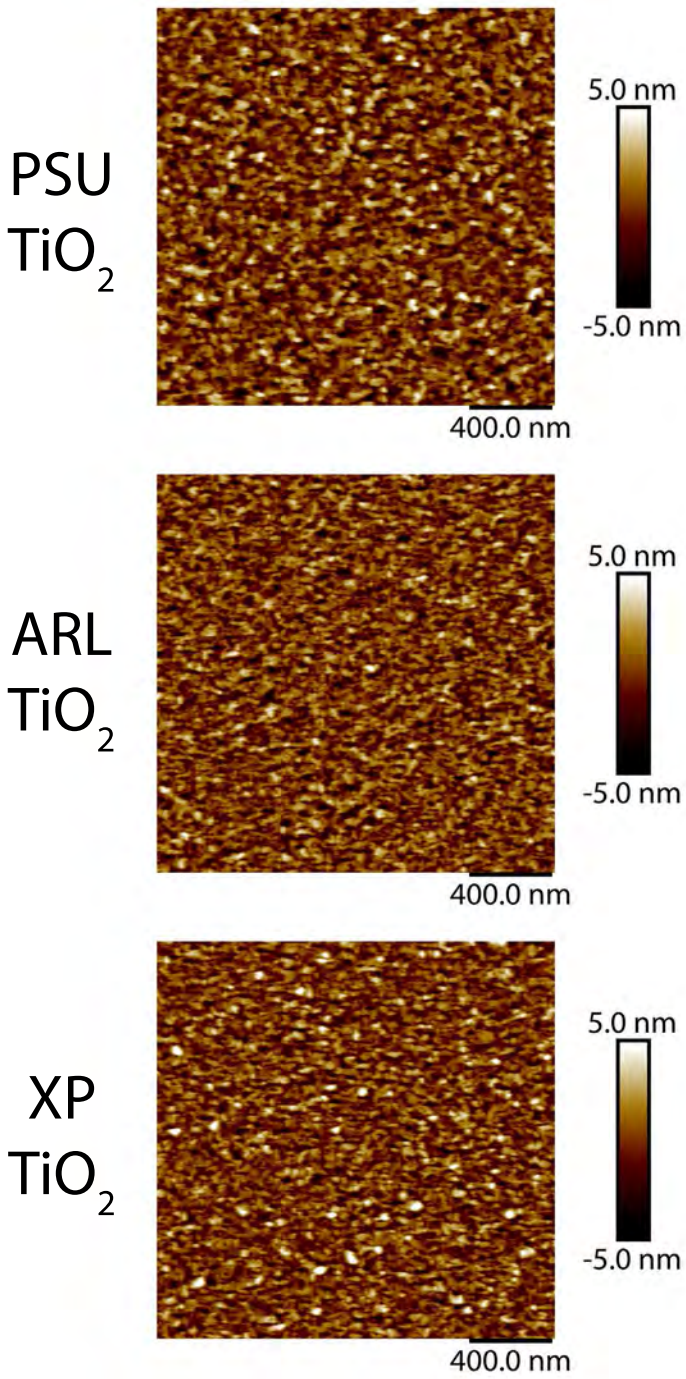

Figure B.9: 2 µm square AFM scans of as oxidized / received titanium oxide adhesion layers from PSU, ARL, and XP.

Platinum

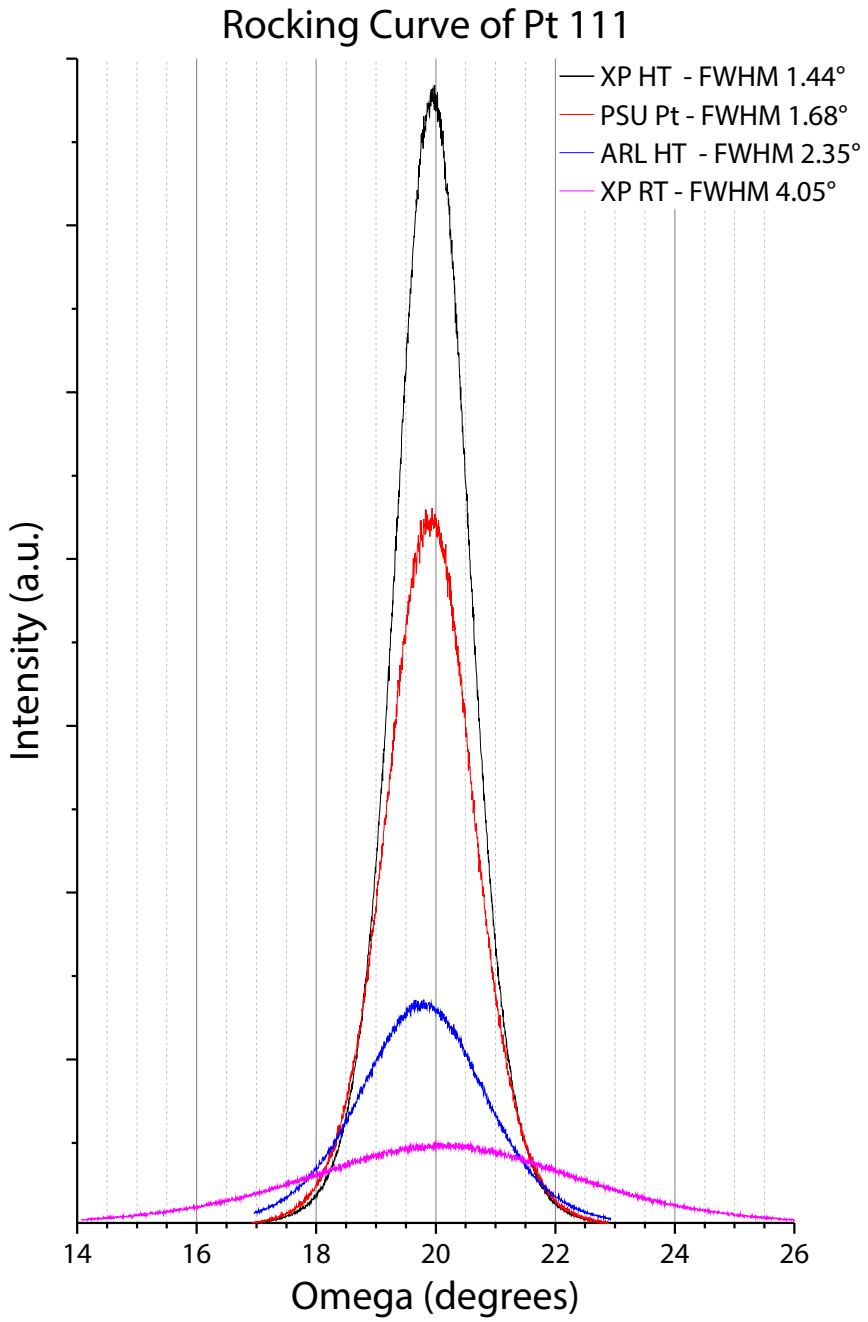

Figure B.10: Rocking curve scans of Pt {111} peak from as deposited / received Pt bottom electrodes, deposited at high temperature from PSU, ARL, and XP or room temperature from XP. FWHM's are for the specific peak which is presented. All scans were taken under the same scan conditions and beam intensity.

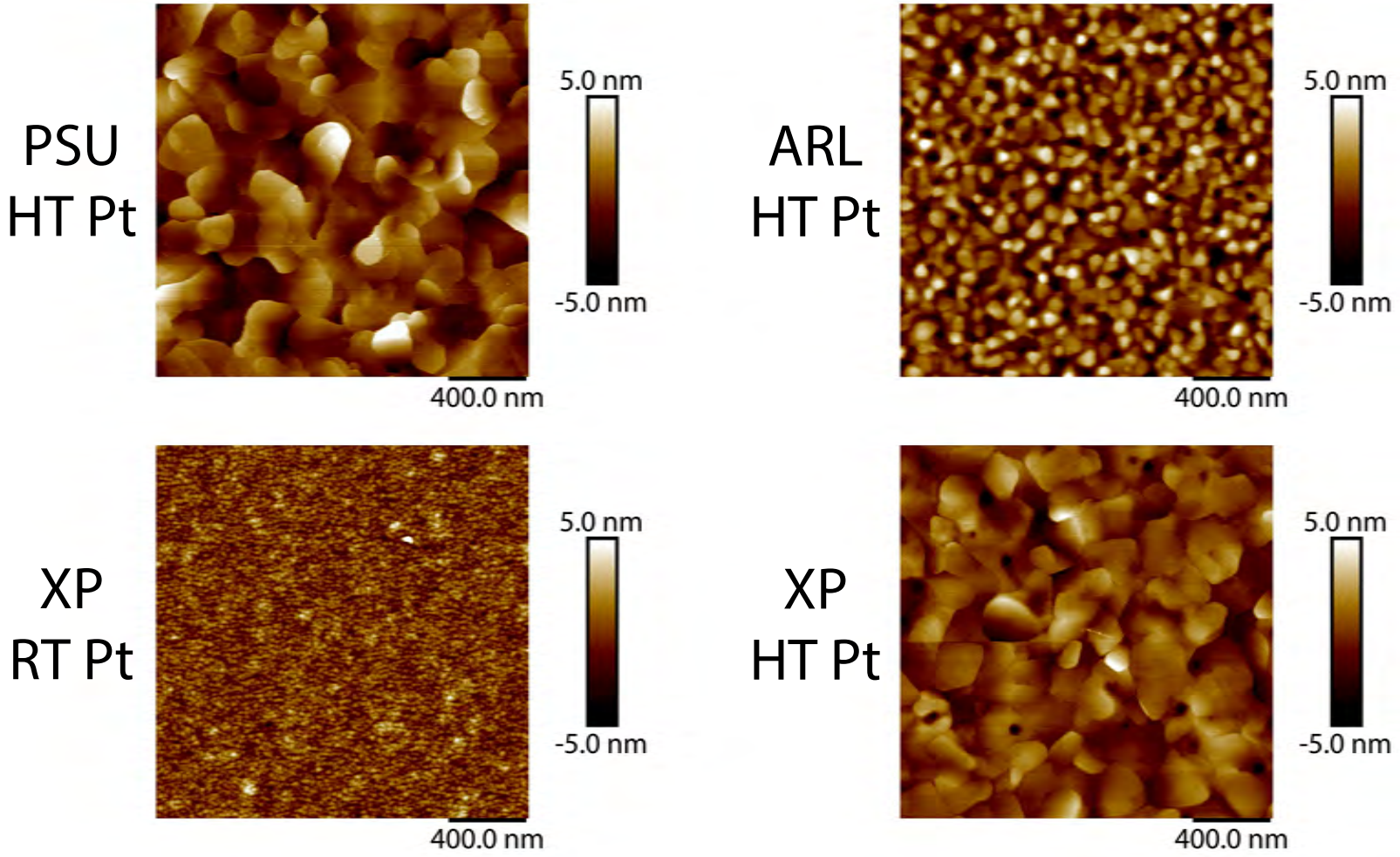

Figure B.11: 2 μm square AFM scans of as deposited / received platinum bottom electrodes deposited at high temperature PSU, ARL, and XP or room temperature by XP.

Supplementary Figures for Chapter 3: Textured Seeding of Doped Lead Zirconate Titanate Thin Films via Chemical Solution Deposition

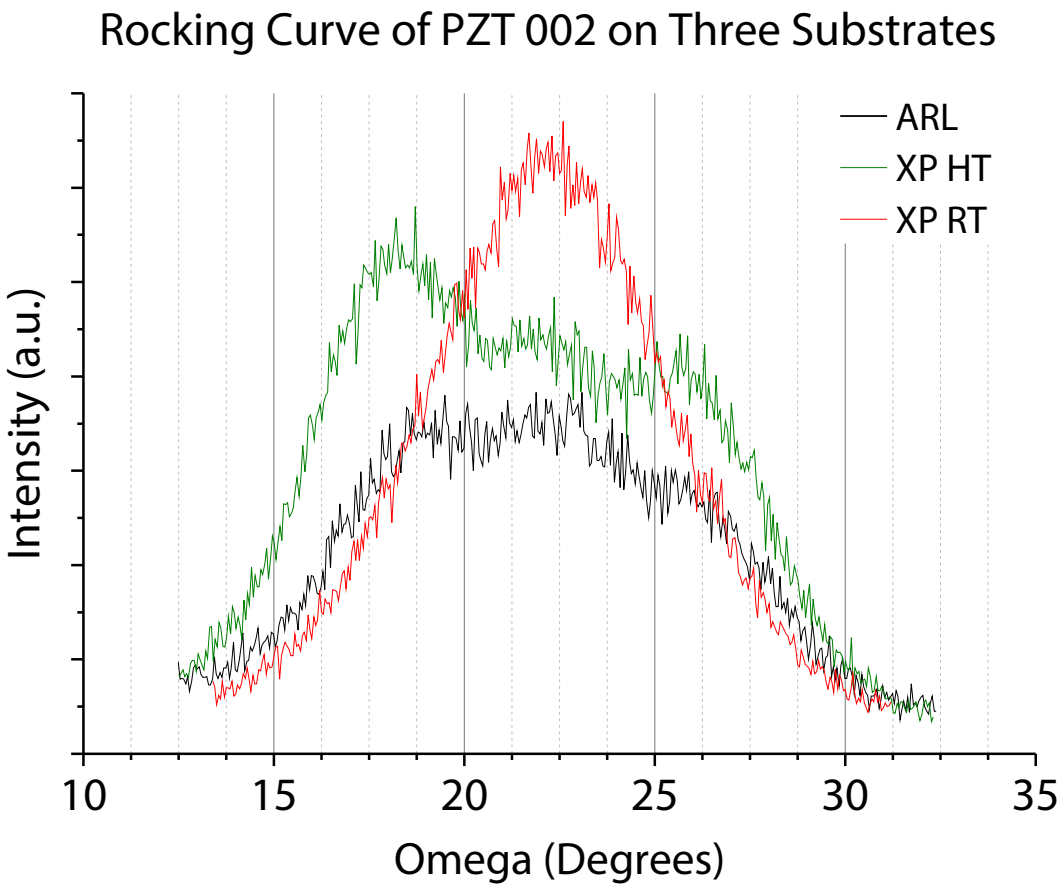

Figure B.12: Rocking curve of the PZT {0 0 2} peaks from the seed layers presented in Section 3.2. The PZT {0 0 2} peak on XP RT Pt exhibits the highest peak intensity as observed in the Bragg-Brentano scans (Figure 3.1). The origin of the three overlapping peaks present in films deposited on both HT Pt substrates is presently unknown. Though it is hypothesized that it may originate from {0 1 1} twin boundaries between a and c domains as reported by Theis & Schlom for epitaxial $PbTiO_3$ films on $SrTiO_3$ substrates.[196,197]

Supplementary Figures for Chapter 4: Deposition of Highly {001} Textured, Niobium Doped, Gradient-Free Lead Zirconate Titanate Thick Films Using Lead Zirconate Titanate Seed Layers

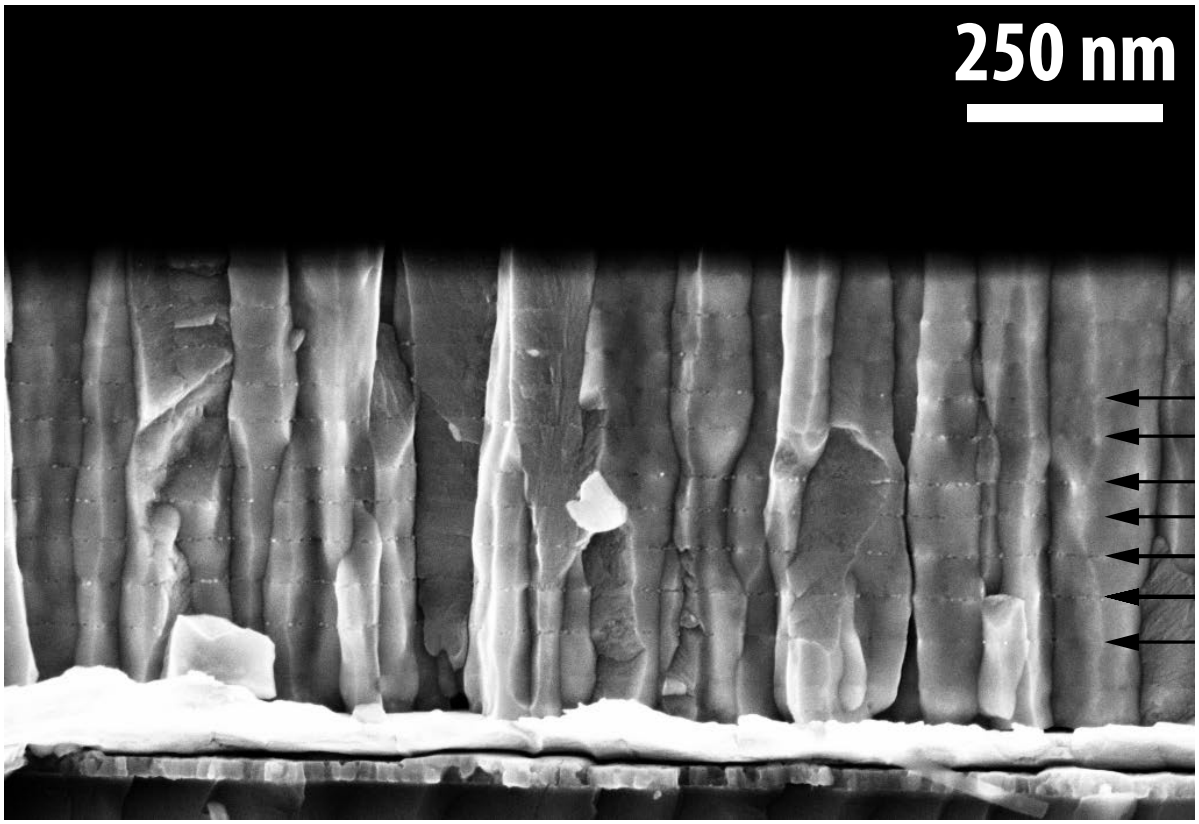

Figure B.13: Cross section micrograph of PZT thin film with a high pyrochlore concentration at many crystallization interfaces. Crystallization interfaces with high pyrochlore concentrations are indicated with arrows. The 20 nm particles at the interfaces are pyrochlore.

Supplementary Figures for Chapter 5: Electrical and Piezoelectric Characterization of Strongly {0 0 1} Oriented PZT Thick Films

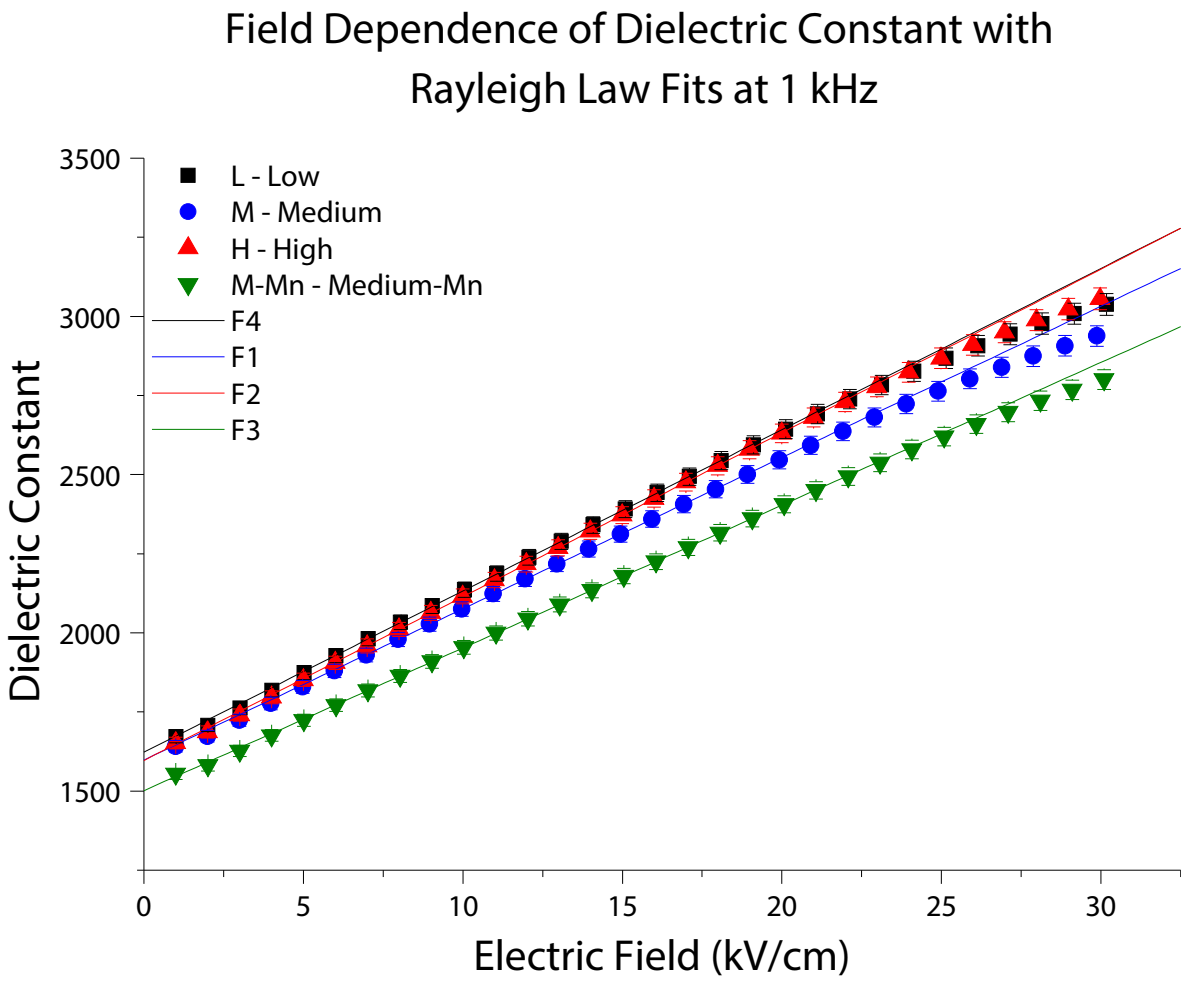

Figure B.14: Dielectric constant as a function of electric field and the accompanying linear fits for calculation of the Rayleigh coefficients at 1 kHz. Error bars represent the 1.5% error associated with film thickness and electrode area uncertainty.

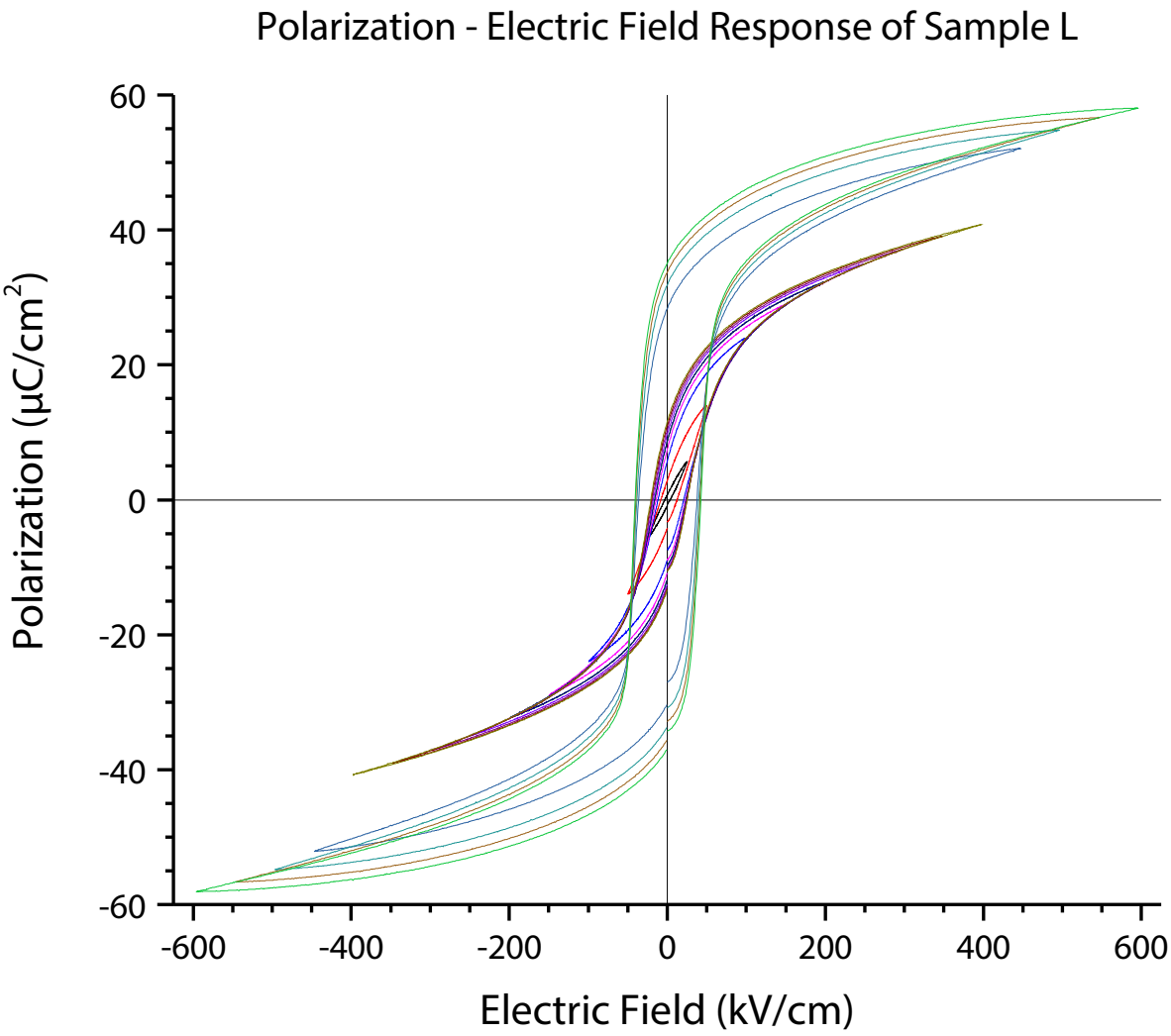

Figure B.15: Hysteresis loops for Sample L (low lead content) collected at 100 Hz and electric fields of 25 kV/cm and 50 – 600 kV/cm in 50 kV/cm increments.

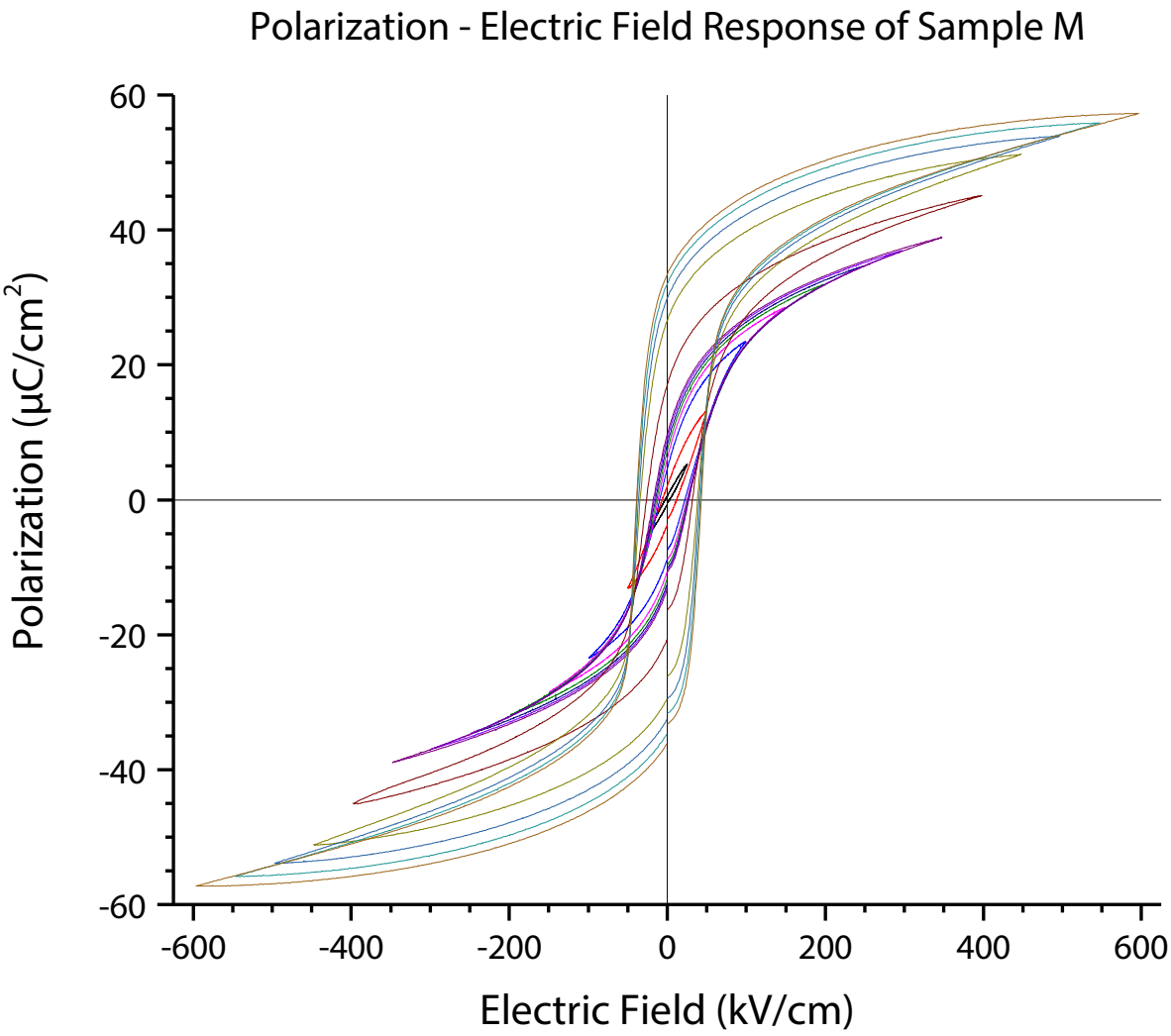

Figure B.16: Hysteresis loops for Sample M (medium lead content) collected at 100 Hz and electric fields of 25 kV/cm and 50 – 600 kV/cm in 50 kV/cm increments.

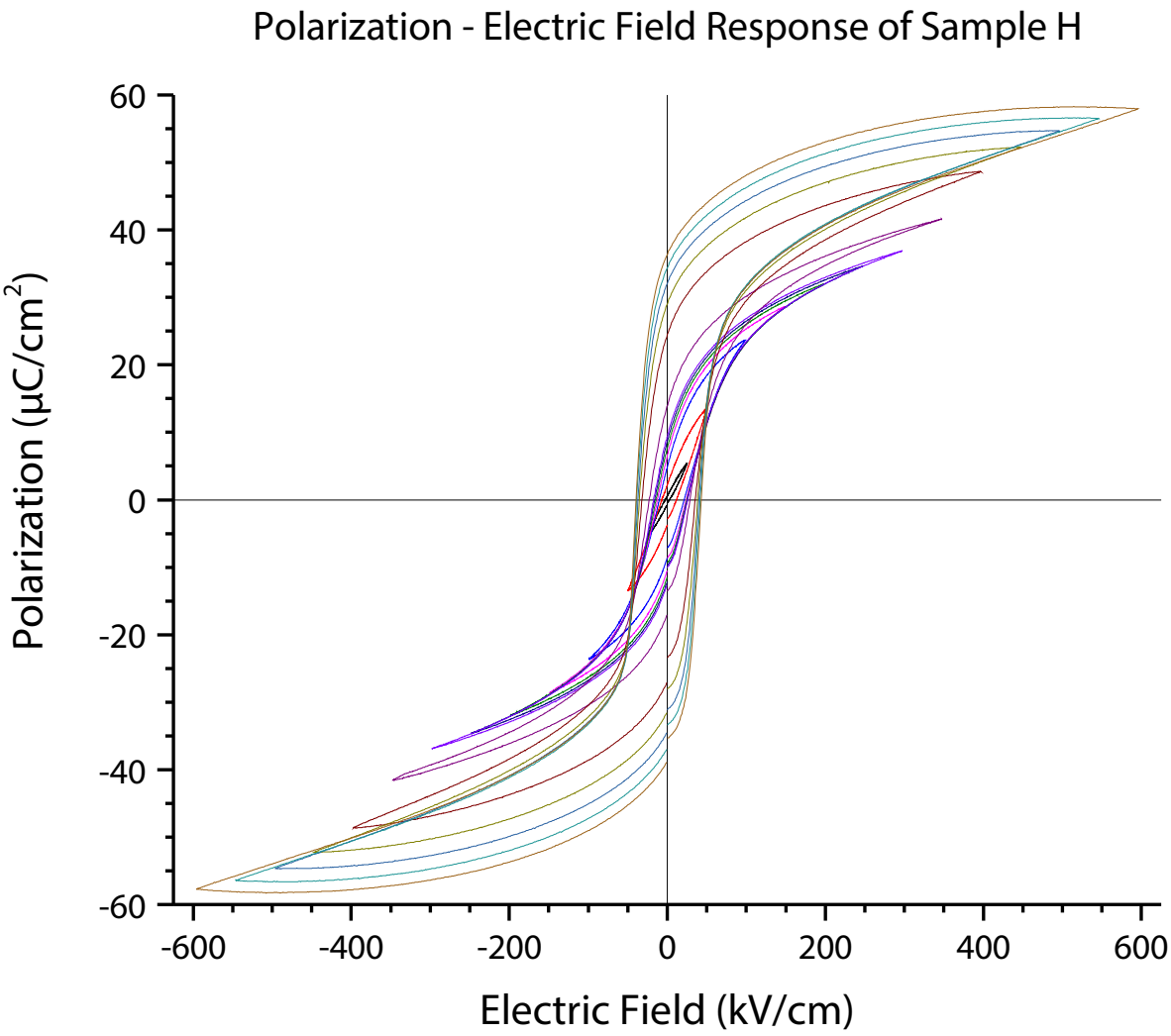

Figure B.17: Hysteresis loops for Sample H (high lead content) collected at 100 Hz and electric fields of 25 kV/cm and 50 – 600 kV/cm in 50 kV/cm increments.

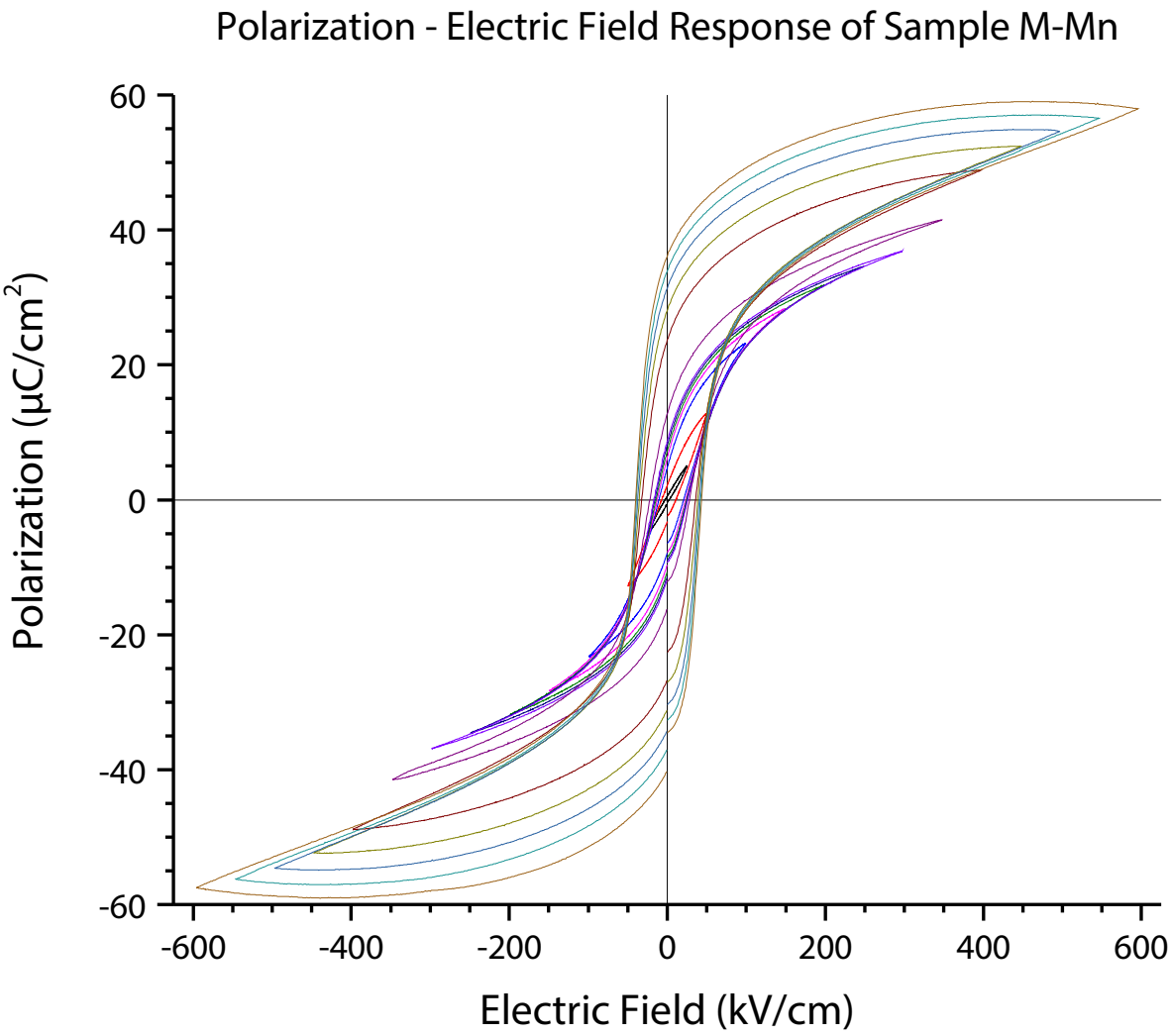

Figure B.18: Hysteresis loops for Sample M-Mn (medium lead content with Mn doping) collected at 100 Hz and electric fields of 25 kV/cm and 50 – 600 kV/cm in 50 kV/cm increments.

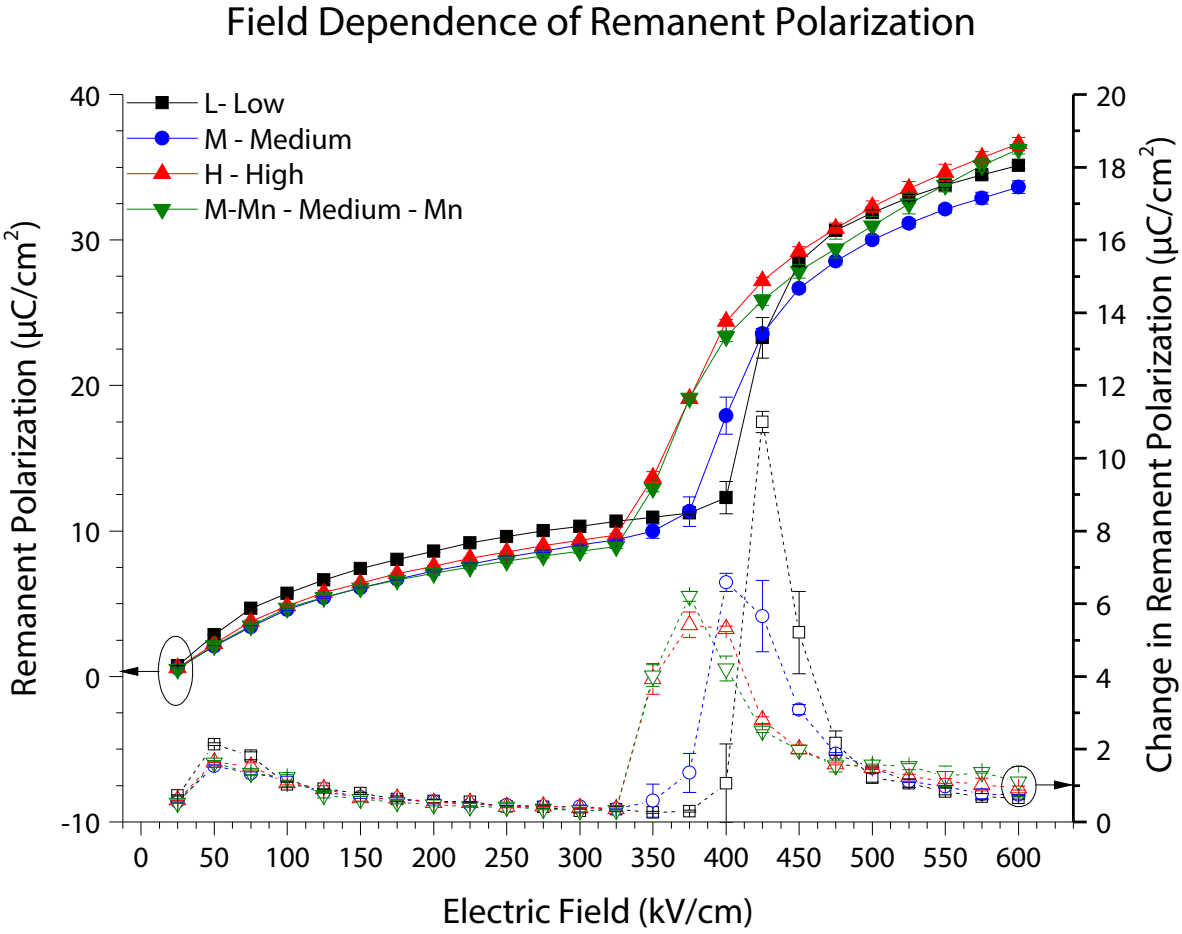

Figure B.19: Dependence of the positive remanent polarization as a function of measurement electric field at 100 Hz. Error bars represent the standard deviation across multiple electrodes plus 0.5% error for electrode area uncertainty.

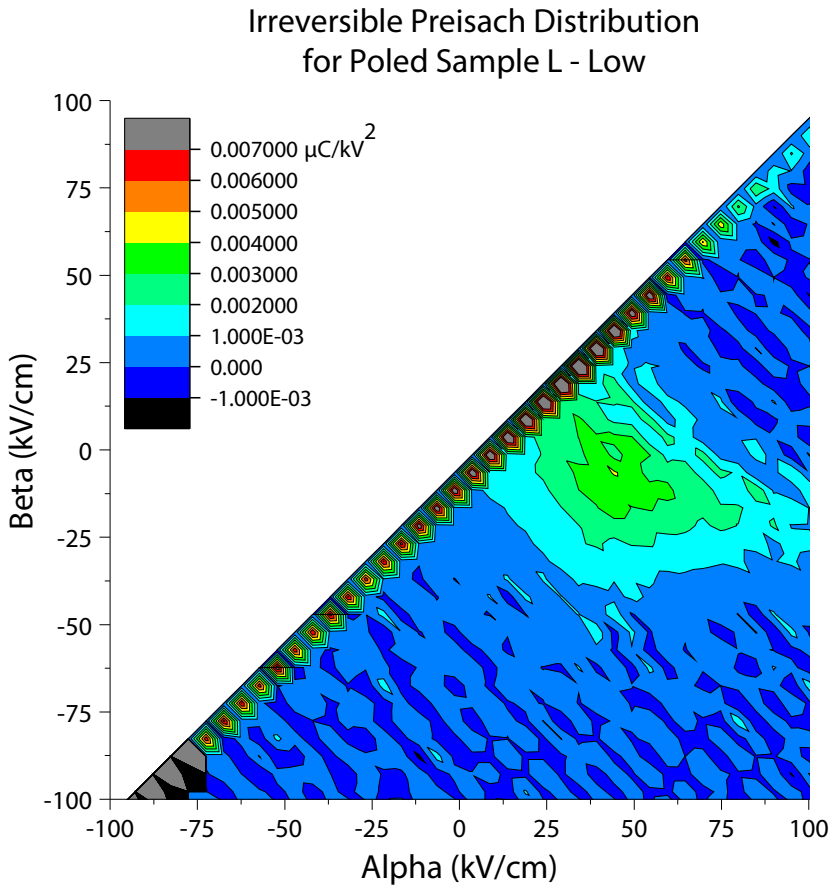

Figure B.20: Irreversible Preisach distribution calculated from First Order Reversal Curves on Sample L. The electrode was poled at 100 kV/cm and 150 °C prior to measurement. The poling field and the starting state for the FORC measurement were in the same direction.

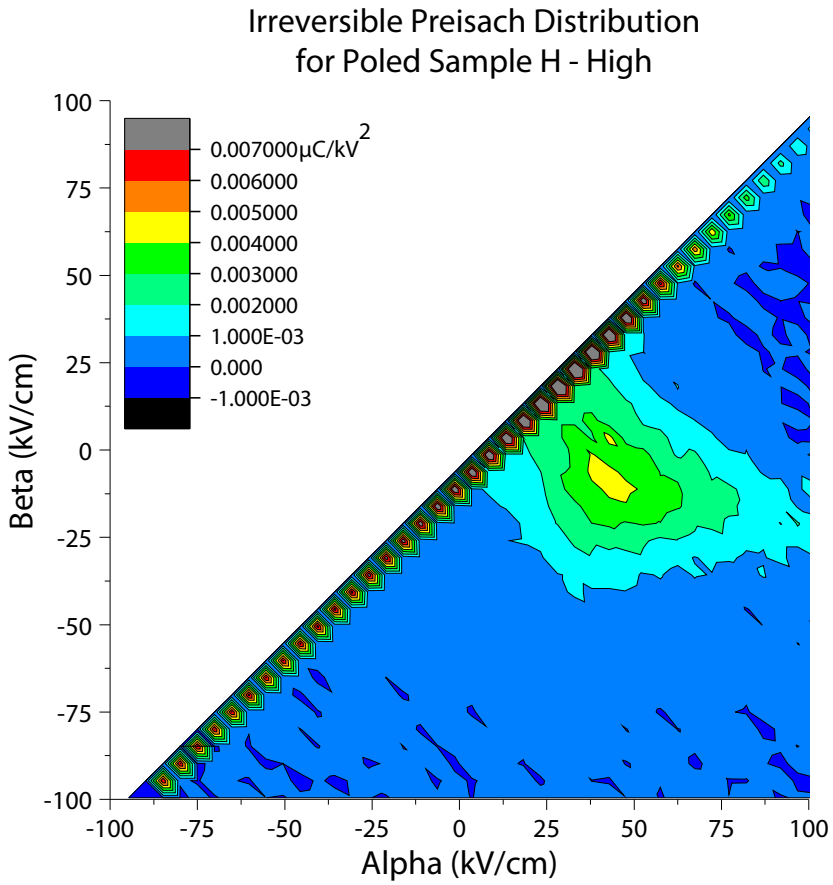

Figure B.21: Irreversible Preisach distribution calculated from First Order Reversal Curves on Sample H. The electrode was poled at 100 kV/cm and 150 °C prior to measurement. The poling field and the starting state for the FORC measurement were in the same direction.

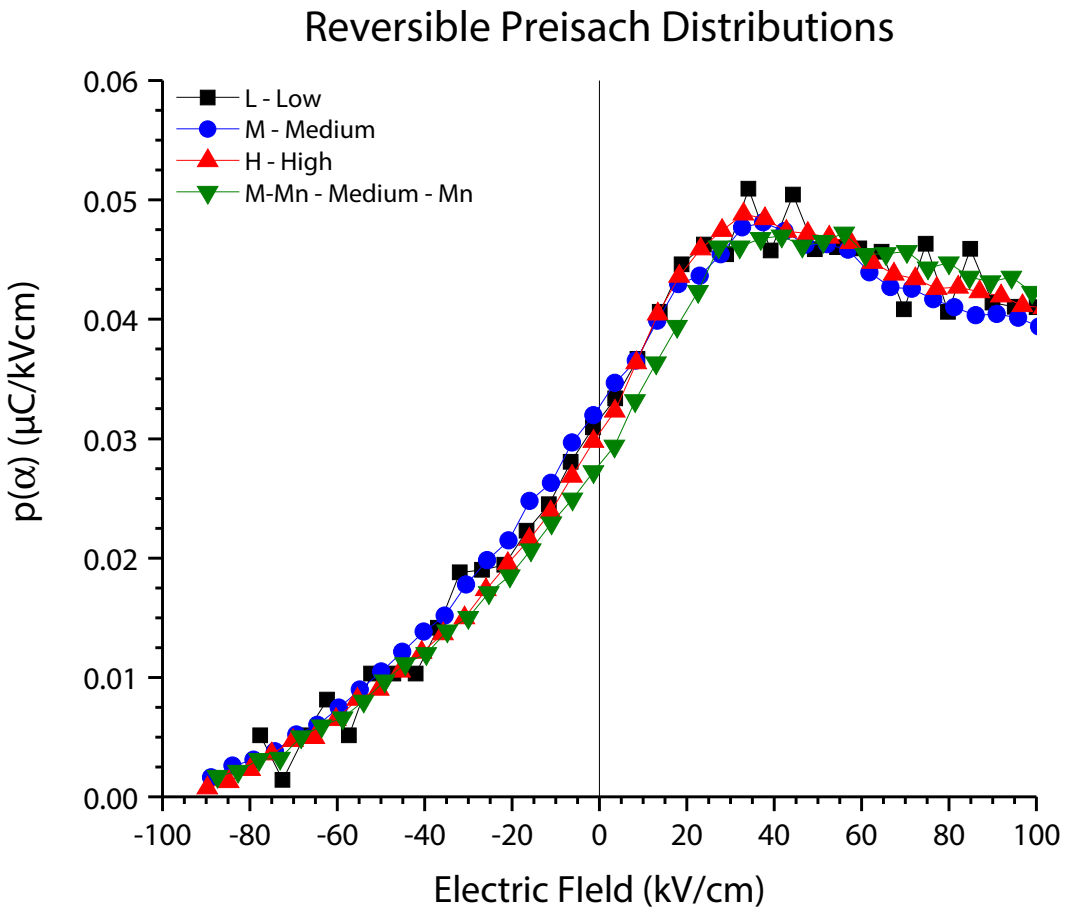

Figure B.22: Reversible Preisach distributions calculated from First Order Reversal Curves on all samples. The electrodes were poled at 100 kV/cm and 150 °C prior to measurement. The poling field and the starting state for the FORC measurement were in the same direction.

References

1. Jaffe, B., Cook, W. R. & Jaffe, H. *Piezoelectric Ceramics* (1971).
2. Newnham, R. E. *Properties of Materials: Anisotropy, Symmetry, Structure* (Oxford University Press, Oxford, 2005).
3. Lefki, K. & Dormans, G. J. M. Measurement of Piezoelectric Coefficients of Ferroelectric Thin Films. *Journal of Applied Physics* **76,** 1764–1767 (1994).
4. Muralt, P., Kholkin, A., Kohli, M. & Maeder, T. Piezoelectric Actuation of PZT Thin-Film Diaphragms at Static and Resonant Conditions. *Sensors and Actuators A: Physical* **53,** 398–404 (1996).
5. Zalachas, N., Laskewitz, B., Kamlah, M., Prume, K., Lapusta, Y. & Tiedke, S. Effective Piezoelectric Coefficients of Ferroelectric Thin Films on Elastic Substrates. *Journal of Intelligent Material Systems and Structures* **20,** 683–695 (2009).
6. Drougard, M. E., Landauer, R. & Young, D. R. Dielectric Behavior of Barium Titanate in the Paraelectric State. *Physical Review* **98,** 1010–1014 (1955).
7. Matsuda, T. & Abe, R. Nonlinear Dielectric Constants in Barium Titanate. *Journal of the Physical Society of Japan* **34,** 418–422 (1973).
8. Triebwasser, S. Space Charge Fields in $BaTiO_3$. *Physical Review* **118,** 100–105 (1960).
9. Von Hippel, A. Ferroelectricity, Domain Structure, and Phase Transitions of Barium Titanate. *Reviews of Modern Physics* **22,** 221–237 (1950).
10. Moulson, A. & Herbert, J. *Electroceramics: Materials, Properties, Applications* 2nd Ed. (John Wiley & Sons, West Sussex, 2003).
11. Frantti, J., Lappalainen, J., Eriksson, S., Lantto, V., Nishio, S., Kakihana, M., Ivanov, S. & Rundlöf, H. Neutron Diffraction Studies of Pb $(Zr_xTi_{1-x})O_3$ Ceramics. *Japanese Journal of Applied Physics* **39,** 5697–5703 (2000).
12. Momma, K. & Izumi, F. *VESTA3* for Three-Dimensional Visualization of Crystal, Volumetric and Morphology Data. *Journal of Applied Crystallography* **44,** 1272–1276 (Dec. 2011).
13. Randall, C. A., Rossetti, G. A. & Cao, W. Spatial Variations of Polarization in Ferroelectrics and Related Materials. *Ferroelectrics* **150,** 163–169 (1993).
14. Rossetti, G. A., Cao, W. & Randall, C. A. Microstructural Characteristics and Diffuse Phase Transition Behavior of Lanthanum-Modified Lead Titanate. *Ferroelectrics* **158,** 343–350 (1994).
15. Jaffe, B., Roth, R. S. & Marzullo, S. Piezoelectric Properties of Lead Zirconate-Lead Titanate Solid-Solution Ceramics. *Journal of Applied Physics* **25,** 809–810 (1954).
16. Noheda, B., Cox, D. E., Shirane, G., Guo, R., Jones, B. & Cross, L. E. Stability of the Monoclinic Phase in the Ferroelectric Perovskite $PbZr_{1-x}Ti_xO_3$. *Physical Review B* **63,** 014103 (2000).
17. Shirane, G. & Susuki, K. Crystal Structure of PZT. *Journal of the Physical Society of Japan* **7,** 333 (1952).
18. Sawaguchi, E. Ferroelectricity Versus Antiferroelectricity in the Solid Solutions of $PbZrO_3$ and $PbTiO_3$. *Journal of the Physical Society of Japan* **8,** 615–629 (1953).
19. Rohatgi, A. *WebPlotDigitizer* Austin, 2015.

20. Ragini, Ranjan, R., Mishra, S. K. & Pandey, D. Room Temperature Structure of Pb(Zr $_x$Ti$_{1-x}$O$_3$) Around the Morphotropic Phase Boundary Region: A Rietveld Study. *Journal of Applied Physics* **92,** 3266–3274 (2002).

21. Woodward, D. I., Knudsen, J. & Reaney, I. M. Review of Crystal and Domain Structures in the PbZr$_x$Ti$_{1-x}$O$_3$ Solid Solution. *Physical Review B - Condensed Matter and Materials Physics* **72,** 104110 (2005).

22. Zhang, N., Yokota, H., Glazer, M., Ren, Z., Keen, D., Keeble, D. S., Thomas, P. & Ye, Z.-G. The Missing Boundary in the Phase Diagram of PbZr$_{1-x}$Ti$_x$O$_3$. *Nature Communications* **5,** 5231 (2014).

23. Glazer, A. M., Thomas, P. A., Baba-Kishi, K. Z., Pang, G. K. H. & Tai, C. W. Influence of Short-Range and Long-Range Order on the Evolution of the Morphotropic Phase Boundary in Pb(Zr$_{1-x}$Ti$_x$)O$_3$. *Physical Review B* **70,** 184123 (2004).

24. Berlincourt, D. A., Cmolik, C. & Jaffe, H. Piezoelectric Properties of Polycrystalline Lead Titanate Zirconate Compositions. *Proceedings of the IRE* **48,** 220–229 (1960).

25. Hiboux, S., Muralt, P. & Maeder, T. Domain and Lattice Contributions to Dielectric and Piezoelectric Properties of Pb(Zr$_x$,Ti$_{1x}$)O$_3$ Thin Films as a Function of Composition. *Journal of Materials Research* **14,** 4307–4318 (1999).

26. Du, X.-H., Zheng, J., Belegundu, U. & Uchino, K. Crystal Orientation Dependence of Piezoelectric Properties of Lead Zirconate Titanate Near the Morphotropic Phase Boundary. *Applied Physics Letters* **72,** 2421–2423 (1998).

27. Calame, F. & Muralt, P. Growth and Properties of Gradient Free Sol-Gel Lead Zirconate Titanate Thin Films. *Applied Physics Letters* **90,** 062907 (2007).

28. Du, X.-H., Belegundu, U. & Uchino, K. Crystal Orientation Dependence of Piezoelectric Properties in Lead Zirconate Titanate: Theoretical Expectation for Thin Films. *Japanese Journal of Applied Physics* **36,** 5580–5587 (1997).

29. Ledermann, N., Muralt, P., Baborowski, J., Gentil, S., Mukati, K., Cantoni, M., Seifert, A. & Setter, N. {1 0 0}-Textured, Piezoelectric Pb(Zr$_x$,Ti$_{1-x}$)O$_3$ Thin Films for MEMS: Integration, Deposition and Properties. *Sensors and Actuators, A: Physical* **105,** 162–170 (2003).

30. Trolier-McKinstry, S. & Muralt, P. Thin Film Piezoelectrics for MEMS. *Journal of Electroceramics* **12,** 7–17 (2004).

31. Bastani, Y. & Bassiri-Gharb, N. Enhanced Dielectric and Piezoelectric Response in PZT Superlattice-Like Films by Leveraging Spontaneous Zr/Ti Gradient Formation. *Acta Materialia* **60,** 1346–1352 (2012).

32. Pelloquin, S., Le Rhun, G., Defaÿ, E., Renaux, P., Nolot, E., Abergel, J. & Sibuet, H. Improvement of Capacitive Behavior on Gradient-Free PZT Thin Films. *Integrated Ferroelectrics* **157,** 132–138 (2014).

33. Prisedsky, V. V., Shishkovsky, V. I. & Klimov, V. V. High-Temperature Electrical Conductivity and Point Defects in Lead Zirconate-Titanate. *Ferroelectrics* **17,** 465–468 (1977).

34. Damjanovic, D. Ferroelectric, Dielectric and Piezoelectric Properties of Ferroelectric Thin Films and Ceramics. *Reports on Progress in Physics* **61,** 1267–1324 (1999).

35. Cross, L. E. Relaxor Ferroelectrics. *Ferroelectrics* **76,** 241–267 (1987).

36. Zhang, Q. M., Zhao, J., Uchino, K. & Zheng, J. Change of the Weak-Field Properties of $Pb(ZrTi)O_3$ Piezoceramics with Compressive Uniaxial Stresses and its Links to the Effect of Dopants on the Stability of the Polarizations in the Materials. *Journal of Materials Research* **12,** 226–234 (1997).

37. Zhu, W., Fujii, I., Ren, W. & Trolier-McKinstry, S. Influence of Mn Doping on Domain Wall Motion in $Pb(Zr_{0.52}Ti_{0.48})O_3$ Films. *Journal of Applied Physics* **109,** 064105 (2011).

38. Zhu, W., Fujii, I., Ren, W. & Trolier-McKinstry, S. Domain Wall Motion in A and B Site Donor-Doped $Pb(Zr_{0.52}Ti_{0.48})O_3$ Films. *Journal of the American Ceramic Society* **95,** 2906–2913 (2012).

39. Waser, R., Baiatu, T. & Härdtl. Karl-Heinz. DC Electrical Degredation of Perovskite-Type Titanates: I, Ceramics. *Journal of the American Ceramic Society* **73,** 1645–1653 (1990).

40. Majumder, S. B., Roy, B., Katiyar, R. S. & Krupanidhi, S. B. Effect of Acceptor and Donor Dopants on Polarization Components of Lead Zirconate Titanate Thin Films. *Applied Physics Letters* **79,** 239–241 (2001).

41. Cross, J. S., Fujiki, M., Tsukada, M., Kotaka, Y. & Goto, Y. Microstructure and Electrical Properties of Chemical Solution Deposition $(Pb,La)(Zr,Ti)O_3$ Thin Films on Pt Electrodes. *Journal of Materials Research* **14,** 4366–4371 (2011).

42. Stolichnov, I., Tagantsev, A., Setter, N., Cross, J. S. & Tsukada, M. Top-Interface-Controlled Switching and Fatigue Endurance of $(Pb,La)(Zr,Ti)O_3$ Ferroelectric Capacitors. *Applied Physics Letters* **74,** 3552–3554 (1999).

43. Byun, J. M., Han, J. S., Park, J. H., Lee, S. E. & Lee, H. C. A Study on the Piezoelectric Properties of PZT and Doped PZT Thin Films by Sol-Gel Method. *Materials Science Forum* **663-665,** 650–653 (2011).

44. Haccart, T., Cattan, E., Remiens, D., Hiboux, S. & Muralt, P. Evaluation of Niobium Effects on the Longitudinal Piezoelectric Coefficients of $Pb(Zr, Ti)O_3$ Thin Films. *Applied Physics Letters* **76,** 3292–3294 (2000).

45. Kwok, K. W., Tsang, R. C. W., Chan, H. L. W. & Choy, C. L. Effects of Niobium Doping on the Piezoelectric Properties of Sol-Gel-Derived Lead-Zirconate-Titanate Films. *Journal of Applied Physics* **95,** 1372–1376 (2004).

46. Haccart, T., Remiens, D. & Cattan, E. Substitution of Nb Doping on the Structural, Microstructural and Electrical Properties in PZT Films. *Thin Solid Films* **423,** 235–242 (2003).

47. Zhang, Q. & Whatmore, R. W. Improved Ferroelectric and Pyroelectric Properties in Mn-Doped Lead Zirconate Titanate Thin Films. *Journal of Applied Physics* **94,** 5228–5233 (2003).

48. Victor, P., Krupanidhi, S. B., Majumder, S. B. & Katiyar, R. S. Effect of Manganese Doping on the Electrical Characteristics of Sol-Gel Derived Lead Zirconate Titanate Thin Films. *Integrated Ferroelectrics* **82,** 65–80 (2006).

49. Xin, H., Ren, W., Wu, X. & Shi, P. Effect of Mn Doping on Structures and Properties of Chemical Solution Deposited Lead Zirconate Titanate Thick Films with (100) Preferential Orientation. *Journal of Applied Physics* **114,** 027017 (2013).

50. Haccart, T., Cattan, E., Remiens, D., Hiboux, S. & Muralt, P. Ferroelectric and Piezoelectric Properties of Nb Doped PZT Films. *Integrated Ferroelectrics* **35,** 239–248 (2001).

51. Klissurska, R. D., Tagantsev, A. K., Brooks, K. G. & Setter, N. Use of Ferroelectric Hysteresis Parameters for Evaluation of Niobium Effects in Lead Zirconate Titanate Thin Films. *Journal of the American Ceramic Society* **80,** 336–342 (1997).

52. Klissurska, R. D., Brooks, K. G., Reaney, I. M., Pawlaczyk, C., Kosec, M. & Setter, N. Effect of Nb Doping on the Microstructure of Sol-Gel-Derived PZT Thin Films. *Journal of the American Ceramic Society* **78,** 1513–1520 (1995).

53. Al-Shareef, H., Dimos, D. & Dimes, D. Accelerated Life-Time Testing and Resistance Degradation of Thin-Film Decoupling Capacitors. English. *Proceedings of the Tenth IEEE International Symposium on Applications of Ferroelectrics* **1,** 421–425 (1996).

54. Akkopru-Akgun, B. Effects of Doping on Imprint, Aging and Reliability of PZT Thin Films. *Private Communications (pending publication)* (2016).

55. Ryder, D. F. & Raman, N. K. Sol-Gel Processing of Nb-Doped Pb(Zr,Ti)O_3 Thin Films for Ferroelectric Memory Applications. *Journal of Electronic Materials* **21,** 971–975 (1992).

56. Aoki, K. & Fukuda, Y. The Effects of La and Nb Modification on Fatigue and Retention Properties of Pb(Ti, Zr)O_3 Thin-Film Capacitors. *Japanese Journal of Applied Physics* **36,** 1195–1197 (1997).

57. Es-Souni, M., Piorra, A., Solterbeck, C. H., Iakovlev, S. & Abed, M. Microstructure and Properties of Solution Deposited, Nb-Doped PZT Thin Films. *Journal of Electroceramics* **9,** 125–135 (2002).

58. Pereira, M., Peixoto, A. G. & Gomes, M. J. M. Effect of Nb Doping on the Microstructural and Electrical Properties of the PZT Ceramics. *Journal of the European Ceramic Society* **21,** 1353–1356 (2001).

59. Hishinuma, Y., Fujii, T., Naono, T., Arakawa, T. & Li, Y. Recent Progress on Development of Sputtered PZT Film at FUJIFILM. *Joint IEEE International Symposium on the Applications of Ferroelectric (ISAF), International Symposium on Integrated Functionalities (ISIF), and Piezoelectric Force Microscopy Workshop (PFM),* 288–291 (2015).

60. Fujii, T., Hishinuma, Y., Mita, T. & Arakawa, T. Preparation of Nb Doped PZT Film by RF Sputtering. *Solid State Communications* **149,** 1799–1802 (2009).

61. Yokosuka, M., Ochiai, T. & Marutake, M. Search for a Material with Temperature-Independent Piezoelectric Constant d_{31} in Nb-Modified Pb(Zr,Ti)O_3 Ceramics. *Japanese Journal of Applied Physics* **30,** 2228–2231 (1991).

62. Randall, C., Kim, N., Kucera, J.-P., Cao, W. & Shrout, T. R. Intrinsic and Extrinsic Size Effects in Fine-Grained Morphotropic-Phase-Boundary Lead Zirconate Titanate Ceramics. *Journal of the American Ceramic Society* **81,** 677–688 (2005).

63. Zhang, Q. & Whatmore, R. R. Hysteretic Properties of Mn-Doped Pb(Zr,Ti)O_3 Thin Films. *Journal of the European Ceramic Society* **24,** 277–282 (2004).

64. Zhang, Q. & Whatmore, R. W. Sol-Gel PZT and Mn-Doped PZT Thin Films for Pyroelectric Applications. *Journal of Physics D: Applied Physics* **34,** 2296–2301 (2001).

65. Zhang, Q., Keeble, D. J., Coleman, P. G. & Mason, R. Fatigue Properties of Mn-Doped Lead Zirconate Tianate Thin Films Capacitors. *Integrated Ferroelectrics* **62,** 119–125 (2004).

66. Scott, J. F. & Dawber, M. Oxygen-Vacancy Ordering as a Fatigue Mechanism in Perovskite Ferroelectrics. *Applied Physics Letters* **76,** 3801–3803 (2000).

67. Dawber, M. & Scott, J. F. A Model for Fatigue in Ferroelectric Perovskite Thin Films. *Applied Physics Letters* **76,** 1060–1062 (2000).

68. Yoo, I. & Desu, S. Mechanism of Fatigue in Ferroelectric Thin Films. *Physica Status Solidi (a)* **133,** 565–573 (1992).

69. Kamiya, T. & Suzuki, T. Effects of Manganese Addition on Piezoelectric Properties of $Pb(Zr_{0.5}Ti_{0.5})\ O_3$. *Japanese Journal of Applied Physics* **31,** 3058–3060 (1992).

70. DeHoff, R. *Thermodynamics in Materials Science* 2nd Ed. (CRC Press - Taylor & Francis Group, Boca Raton, 2006).

71. Brennecka, G. L. & Tuttle, B. A. Fabrication of Ultrathin Film Capacitors by Chemical Solution Deposition. *Journal of Materials Research* **22,** 2868–2874 (2007).

72. He, L.-X. & Li, C.-E. Effects of Addition of MnO on Piezoelectric Properties of Lead Zirconate Titanate. *Journal of Materials Science* **35,** 2477–2480 (2000).

73. Hennings, D. & Pomplun, H. Evaluation of Lattice Site and Valence of Mn and Fe in Polycrystalline PbTiOs by Electron Spin Resonance and Thermogravimetry. *Journal of the American Ceramic Society* **57,** 527–530 (1974).

74. Liu, G., Zhang, S., Jiang, W. & Cao, W. Losses in Ferroelectric Materials. *Materials Science and Engineering R* **89,** 1–48 (2015).

75. Keech, R., Shetty, S., Kuroda, M. A., Hu Liu, X., Martyna, G. J., Newns, D. M. & Trolier-McKinstry, S. Lateral Scaling of $Pb(Mg_{1/3}Nb_{2/3})O_3$-$PbTiO_3$ Thin Films for Piezoelectric Logic Applications. *Journal of Applied Physics* **115,** 234106 (2014).

76. Rayleigh, L. XXV. Notes on Electricity and Magnetism.— III. On the Behaviour of Iron and Steel Under the Operation of Feeble Magnetic Forces. *Philosophical Magazine Series 5* **23,** 225–245 (1887).

77. Damjanovic, D. & Demartin, M. The Rayleigh Law in Piezoelectric Ceramics. *Journal of Physics D: Applied Physics* **29,** 2057–2060 (1996).

78. Fujii, I. *Dielectric Nonlinearity of Ferroelectrics* Doctoral Thesis (Penn State University, 2010).

79. Boser, O. Statistical Theory of Hysteresis in Ferroelectric Materials. *Journal of Applied Physics* **62,** 1344–1348 (1987).

80. Robels, U. & Arlt, G. Domain Wall Clamping in Ferroelectrics by Orientation of Defects. *Journal of Applied Physics* **73,** 3454–3460 (1993).

81. Morozov, M., Damjanovic, D. & Setter, N. The Nonlinearity and Subswitching Hysteresis in Hard and Soft PZT. *Journal of the European Ceramic Society* **25,** 2483–2486 (2005).

82. Preisach, F. Über Die Magnetische Nachwirkung. *Zeitschrift für Physik* **94,** 277–302 (1935).

83. Robert, G., Damjanovic, D., Setter, N. & Turik, A. V. Preisach Modeling of Piezoelectric Nonlinearity in Ferroelectric Ceramics. *Journal of Applied Physics* **89,** 5067–5074 (2001).

84. Wong, C. K., Tsang, C. H. & Shin, F. G. Modeling of Bias-Field-Dependent Dielectric Properties in Ferroelectric Thin Films. *Journal of Applied Physics* **98,** 074101 (2005).

85. Mayergoyz, I. D. *Mathematical Models of Hysteresis and Their Applications* Second Ed. (Elsevier Science, 2003).

86. Roberts, A., Pike, C. & Verosub, K. First-Order Reversal Curve Diagrams: a New Tool for Characterizing The Magnetic Properties of Natural Samples. *Journal of Geophysical Research* **105,** 28461–28475 (2000).

87. Muralt, P. Recent Progress in Materials Issues For Piezoelectric MEMS. *Journal of the American Ceramic Society* **91,** 1385–1396 (2008).

88. Bassiri-Gharb, N., Bastani, Y. & Bernal, A. Chemical Solution Growth of Ferroelectric Oxide Thin Films and Nanostructures. *Chemical Society Reviews* **43,** 2125–40 (2014).

89. Park, J.-H., Kim, B.-K., Song, K.-H. & Park, S. Piezoelectric Properties of Nb_2O_5 Doped and MnO_2-Nb_2O_5 Co-Doped $Pb(Zr_{0.53}Ti_{0.47})O_3$ Ceramics. *Journal of Materials Science: Materials in Electronics* **6,** 97–101 (1995).

90. Maki, K., Soyama, N., Mori, S. & Ogi, K. Evaluation of $Pb(Zr,Ti)O_3$ Films Derived from Propylene-Glycol-Based Sol-Gel Solutions. *Japanese Journal of Applied Physics* **39,** 5421–5425 (2000).

91. Léaustic, A., Babonneau, F. & Livage, J. Structural Investigation of the Hydrolysis-Condensation Process of Titanium Alkoxides $Ti(OR)_4$ (OR = OPr^i,OEt) Modified by Acetylacetone. 1. Study of Alkoxide Modification. *Chemistry of Materials* **1,** 240–247 (1989).

92. Mitsubishi Materials Corporation. PZT Sol-Gel Solution E-Series. *Safety Data Sheet* (2013).

93. Doi, T., Sakurai, H. & Soyama, N. Mn-Doped PZT-Based Piezoelectric Film Formation Composition and Mn-Doped PZT-Based Piezoelectric Film. *Patent Application WO2015147259 A1* (2015).

94. Doi, T., Sakurai, H. & Soyama, N. Method of Forming PNbZT Ferroelectric Thin Film. *Patent Application US20140295172 A1* (2014).

95. Noguchi, T., Doi, T., Sakurai, H., Watanabe, T. & Soyama, N. PZT-Based Ferroelectric Thin Film and Method of Manufacturing the Same. *Patent Application EP2645439 A2* (2013).

96. Wolf, R. A. & Trolier-McKinstry, S. Temperature Dependence of the Piezoelectric Response in Lead Zirconate Titanate Films. *Journal of Applied Physics* **95,** 1397–1406 (2004).

97. Doi, T., Noguchi, T., Fuji, J., Soyama, N. & Sakurai, H. The Orientation and Grain Texture Effect on Life Time Reliability of Sol–Gel Derived $PbZr_{0.52}Ti_{0.48}O_3$ Films. *Japanese Journal of Applied Physics* **51,** 09LA15 (2012).

98. Lotgering, F. Topotactical Reactions with Ferrimagnetic Oxides Having Hexagonal Crystal Structures—I. *Journal of Inorganic and Nuclear Chemistry* **9,** 113–123 (1959).

99. International Center for Diffraction Data. *PDF# 01-070-4060* 2014.

100. Wang, L.-P., Wolf, R., Zhou, Q., Trolier-McKinstry, S. & Davis, R. J. Wet-Etch Patterning of Lead Zirconate Titanate (PZT) Thick Films for Microelectromechanical Systems (MEMS) Applications. *MRS Proceedings* **657,** EE5.39 (2000).

101. Fox, A. J., Drawl, B., Fox, G. R., Gibbons, B. J. & Trolier-McKinstry, S. Control of Crystallographic Texture and Surface Morphology of Pt/TiO_2 Templates for Enhanced PZT Thin Film Texture. *IEEE Transactions on Ultrasonics, Ferroelectrics, and Frequency Control* **62,** 56–61 (2015).

102. Potrepka, D. M., Fox, G. R., Sanchez, L. M. & Polcawich, R. G. Pt/TiO_2 Growth Templates for Enhanced PZT films and MEMS Devices. *MRS Proceedings* **1299,** 67–72 (2011).

103. Maeder, T., Sagalowicz, L. & Muralt, P. Stabilized Platinum Electrodes for Ferroelectric Film Deposition Using Ti, Ta and Zr Adhesion Layers. *Japanese Journal of Applied Physics* **37,** 2007–2012 (1998).

104. Touloukian, Y. S., Kirby, R. K., Taylor, R. E. & Desai, P. D. *Thermal Expansion: Metallic Elements and Alloys* 254–255 (1970).

105. Touloukian, Y. S., Kirby, R. K., Taylor, R. E. & Desai, P. D. *Thermal Expansion: Nonmetallic Solids* 154–155 (1970).

106. Thornton, J. A. Influence of Apparatus Geometry and Deposition Conditions on the Structure and Topography of Thick Sputtered Coatings. *Journal of Vacuum Science and Technology* **11,** 666–670 (1974).

107. Swartz, S. L., Bright, S. J., Melling, P. J. & Shrout, T. R. Sol-Gel Processing of Composite $PbTiO_3$/PLZT Thin Films. *Ferroelectrics* **108,** 71–76 (1990).

108. Bintachitt, P. *Local Origin of Macroscopic Properties and Patterning in PZT Films* Doctoral Thesis (The Pennsylvania State University, 2009).

109. Bastani, Y. & Bassiri-Gharb, N. Processing Optimization of Lead Magnesium Niobate-Lead Titanate Thin Films for Piezoelectric MEMS Application. *Journal of the American Ceramic Society* **95,** 1269–1275 (2012).

110. Cattan, E., Roma, R., Velu, G., Jaber, B., Remiens, D. & Thierry, B. Influence of $PbTiO_3$ Buffer Layers on Microstructural Properties of $Pb(Zr,Ti)O_3$ Films Deposited by Sputtering. *MRS Proceedings* **433,** 291–296 (1996).

111. Hiboux, S. & Muralt, P. Mixed Titania-Lead Oxide Seed Layers for PZT Growth on Pt(111): A Study on Nucleation, Texture and Properties. *Journal of the European Ceramic Society* **24,** 1593–1596 (2004).

112. Sanchez, L., Potrepka, D., Fox, G., Takeuchi, I. & Polcawich, R. Improving PZT Thin Film Texture Through Pt Metallization and Seed Layers. *MRS Proceedings* **1299,** 53–58 (2011).

113. Chen, S.-Y. & Chen, I.-W. Temperature-Time Texture Transition of $Pb(Zr_{1-x}Ti_x)O_3$ Thin Films: I, Role of Pb-rich Intermediate Phases. *Journal of the American Ceramic Society* **77,** 2332–2336 (1994).

114. Kalpat, S. & Uchino, K. Highly Oriented Lead Zirconium Titanate Thin Films: Growth, Control of Texture, and its Effect on Dielectric Properties. *Journal of Applied Physics* **90,** 2703–2710 (2001).

115. Ea Kim, B., Varnière, F., Agius, B. & Bisaro, R. Pt Electrode Investigation and Electrical Properties of RF Magnetron Sputtered $Pb(Zr,Ti)O_3$. *Microelectronic Engineering* **29,** 231–234 (1995).

116. Lefevre, M. J., Speck, J. S., Schwartz, R. W., Dimos, D. & Lockwood, S. J. Microstructural Development in Sol-Gel Derived Lead Zirconate Titanate Thin Films: the Role of Precursor Stoichiometry and Processing Environment. *Journal of Materials Research* **11,** 2076–2084 (1996).

117. Subramanian, M. A., Aravamudan, G. & Subba Rao, G. V. Oxide Pyrochlores - A Review. *Progress in Solid State Chemistry* **15,** 55–143 (1983).

118. Jones, J. L., LeBeau, J. M., Nikkel, J., Oni, A. A., Dycus, J. H., Cozzan, C., Lin, F.-Y., Chernatynskiy, A., Nino, J. C., Sinnott, S. B., Mhin, S., Brennecka, G. L. & Ihlefeld, J. Combined Experimental and Computational Methods Reveal the Evolution of Buried Interfaces during Synthesis of Ferroelectric Thin Films. *Advanced Materials Interfaces,* 1500181 (2015).

119. Keech, R., Shetty, S., Wang, K. & Trolier-McKinstry, S. Management of Lead Content for Growth of {001}-Oriented Lead Magnesium Niobate-Lead Titanate Thin Films. *Journal of the American Ceramic Society* **99,** 1144–1146 (2016).

120. Nittala, K., Mhin, S., Dunnigan, K. M., Robinson, D. S., Ihlefeld, J. F., Kotula, P. G., Brennecka, G. L. & Jones, J. L. Phase and Texture Evolution in Solution Deposited Lead Zirconate Titanate Thin Films: Formation and Role of the Pt_3Pb Intermetallic Phase. *Journal of Applied Physics* **113,** 244101 (2013).

121. Fox, G. R. *Composition/Structure/Property Relations of Ferroelectric Lead-Lanthanum-Titanate Thin Films Deposited by Multi-Ion-Beam Reactive Sputtering* Doctoral Thesis (The Pennsylvania State University, 1992).

122. Li, J.-F., Zhu, Z.-X. & Lai, F.-P. Thickness-Dependent Phase Transition and Piezoelectric Response in Textured Nb-Doped $Pb(Zr_{0.52}Ti_{0.48})O_3$ Thin Films. *The Journal of Physical Chemistry C* **114,** 17796–17801 (2010).

123. Gong, W., Li, J.-F., Chu, X., Gui, Z. & Li, L. Combined Effect of Preferential Orientation and Zr/Ti Atomic Ratio on Electrical Properties of $Pb(Zr_xTi_{1-x})O_3$ Thin Films. *Journal of Applied Physics* **96,** 590–595 (2004).

124. Ihlefeld, J. F., Vodnick, A. M., Baker, S. P., Borland, W. J. & Maria, J. P. Extrinsic Scaling Effects on the Dielectric Response of Ferroelectric Thin Films. *Journal of Applied Physics* **103,** 074112 (2008).

125. Carim, A., Tuttle, B., Doughty, D. H. & Martinez, S. L. Microstructure of Solution-Processed Lead Zirconate Titanate (PZT) Thin Films. *Journal of the American Ceramic Society* **74,** 1455–1458 (1991).

126. Atkin, R. B. & Fulrath, R. M. Point Defects and Sintering of Lead Zirconate-Titanate. *Journal of the American Ceramic Society* **54,** 265–270 (1971).

127. Durruthy, M. D., Fuentes, L., Hernández, M. & Camacho, H. Influence of the Niobium Dopant Concentration on the $Pb(Zr_{0.54}Ti_{0.46})O_3$ Ceramics Sintering. *Journal of Materials Science* **34,** 2311–2317 (1999).

128. Sun, H., Zhang, Y., Liu, X., Guo, S., Liu, Y. & Chen, W. The Effect of Mn/Nb Doping on Dielectric and Ferroelectric Properties of PZT Thin Films Prepared by Sol–Gel Process. *Journal of Sol-Gel Science and Technology* **74,** 378–386 (2015).

129. Lou, X. J. & Wang, J. Effect of Manganese Doping on the Size Effect of Lead Zirconate Titanate Thin Films and the Extrinsic Nature of 'Dead Layers'. *Journal of Physics: Condensed Matter* **22,** 055901 (2010).

130. Ng, Y. S. & Alexander, S. M. Structural Studies of Manganese Stabilised Lead Zirconate-Titanate. *Ferroelectrics* **51,** 81–86 (1983).

131. Wersing, W. On the Stabilizing Field of Lead-Titanate-Zirconate Ceramics Doped with Transition Metal Ions. *Ferroelectrics* **12,** 143–145 (1976).

132. Kwok, C. K. & Desu, S. B. Low Temperature Perovskite Formation of Lead Zirconate Titanate Thin Films by a Seeding Process. *Journal of Materials Research* **8,** 339–344 (1993).

133. Myers, S. A. & Chapin, L. N. Microstructural Characterization of Ferroelectric Thin Films for Non-Volatile Memory Applications. *MRS Proceedings* **200** (eds Kingon, A. I. & Myers, E. R.) 231–236 (1990).

134. Spierings, G. A. C. M., Ulenaers, M. J. E., Kampschöer, G. L. M., Van Hal, H. A. M. & Larsen, P. K. Preparation and Ferroelectric Properties of $PbZr_{0.53}Ti_{0.47}O_3$ Thin Films by Spin Coating and Metalorganic Decomposition. *Journal of Applied Physics* **70,** 2290–2298 (1991).

135. Hammer, M. & Hoffmann, M. Sintering Model for Mixed-Oxide-Derived Lead Zirconate Titanate Ceramics. *Journal of the American Ceramic Society* **81,** 3277–3284 (1998).

136. Zhong, J., Batra, V., Han, H., Kotru, S. & Pandey, R. K. Effect of Pb Content and Solution Concentration of Pb_xTiO_3 Seed Layer on {100}-Texture and Ferroelectric/Dielectric Behavior of PZT (52/48) Thin Films. *Journal of Vacuum Science & Technology A: Vacuum, Surfaces, and Films* **33,** 05E119 (2015).

137. Sanchez, L. M., Potrepka, D. M., Fox, G. R., Takeuchi, I., Wang, K., Bendersky, L. A. & Polcawich, R. G. Optimization of $PbTiO_3$ Seed Layers and Pt Metallization for PZT-Based PiezoMEMS Actuators. *Journal of Materials Research* **28,** 1920–1931 (2013).

138. Muralt, P. Texture Control and Seeded Nucleation of Nanosize Structures of Ferroelectric Thin Films. *Journal of Applied Physics* **100,** 051605 (2006).

139. Voigt, J. A., Tuttle, B. A., Headley, T. J. & Lamppa, D. L. The Pyrochlore-to-Perovskite Transformation in Solution-Derived Lead Zirconate Titanate Thin Films. *MRS Proceedings* **361,** 395–402 (1994).

140. Aggarwal, S., Madhukar, S., Nagaraj, B., Jenkins, I. G., Ramesh, R., Boyer, L. & Evans, J. T. Can Lead Nonstoichiometry Influence Ferroelectric Properties of $Pb(Zr,Ti)O_3$ Thin Films? *Applied Physics Letters* **75,** 716–718 (1999).

141. Keezer, R. C., Bowman, D. L. & Becker, J. H. Electrical and Optical Properties of Lead Oxide Single Crystals. *Journal of Applied Physics* **39,** 2062–2066 (1968).

142. Lu, J., Zhang, Y., Ikehara, T., Mihara, T. & Maeda, R. Effects of Rapid Thermal Annealing on Nucleation, Growth, and Properties of Lead Zirconate Titanate Films. *IEEE Transactions on Ultrasonics, Ferroelectrics, and Frequency Control* **54,** 2548–2554 (Dec. 2007).

143. Roy, S. & Sarah, P. Dielectric Properties of Chemically Synthesized PLZT and PZT: Diffused Phase Transition and Effect of Lead Non-Stoichiometry. *Journal of Physics D: Applied Physics* **40,** 4668–4673 (2007).

144. Marincel, D. M., Jesse, S., Belianinov, A., Okatan, M. B., Kalinin, S. V., Jackson, T. N., Randall, C. A. & Trolier-McKinstry, S. A-Site Stoichiometry and Piezoelectric Response in Thin Film $PbZr_{1x}Ti_xO_3$. *Journal of Applied Physics* **117,** 204104 (2015).

145. Luo, H., Xu, G., Xu, H., Wang, P. & Yin, Z. Compositional Homogeneity and Electrical Properties of Lead Magnesium Niobate Titanate Single Crystals Grown by a Modified Bridgman Technique. *Japanese Journal of Applied Physics* **39,** 5581–5585 (2000).

146. Lou, X., Hu, X., Zhang, M., Morrison, F. D., Redfern, S. A. T. & Scott, J. F. Phase Separation in Lead Zirconate Titanate and Bismuth Titanate During Electrical Shorting and Fatigue. *Journal of Applied Physics* **99,** 044101 (2006).

147. Wilke, R. H. T., Johnson-Wilke, R. L., Cotroneo, V., Davis, W. N., Reid, P. B., Schwartz, D. & Trolier-McKinstry, S. Sputter Deposition of PZT Piezoelectric Films on Thin Glass Substrates for Adjustable X-Ray Optics. *Applied Optics* **52,** 3412–3419 (2013).

148. Chen, H. D., Udayakumar, K. R., Gaskey, C. J. & Cross, L. E. Electrical Properties' Maxima in Thin Films of the Lead Zirconate-Lead Titanate Solid Solution System. *Applied Physics Letters* **67,** 3411–3413 (1995).

149. Bassiri-Gharb, N. *Dielectric and Piezoelectric Nonlinearities in Oriented $Pb(Yb_{0.5}Nb_{0.5})O_3$-$PbTiO_3$ Thin Films* Doctoral Thesis (The Pennsylvania State University, 2005).

150. Marincel, D. M. *The Influence of Crystal Defects on Domain Wall Motion in Thin Film $Pb(Zr,Ti)O_3$* Doctoral Thesis (The Pennsylvania State University, 2014).

151. Bassiri-Gharb, N., Fujii, I., Hong, E., Trolier-Mckinstry, S., Taylor, D. V. & Damjanovic, D. Domain Wall Contributions to the Properties of Piezoelectric Thin Films. *Journal of Electroceramics* **19,** 47–65 (2007).

152. Bastani, Y., Schmitz-Kempen, T., Roelofs, A. & Bassiri-Gharb, N. Critical Thickness for Extrinsic Contributions to the Dielectric and Piezoelectric Response in Lead Zirconate Titanate Ultrathin Films. *Journal of Applied Physics* **109,** 014115 (2011).

153. Kim, D.-J., Maria, J.-P., Kingon, A. I. & Streiffer, S. K. Evaluation of Intrinsic and Extrinsic Contributions to the Piezoelectric Properties of $Pb(Zr_{1-x}Ti_x)O_3$ Thin Films as a Function of Composition. *Journal of Applied Physics* **93,** 5568–5575 (2003).

154. Hall, D. A. Nonlinearity in Piezoelectric Ceramics. *Journal of Materials Science* **36,** 4575–4601 (2001).

155. Damjanovic, D. Stress and Frequency Dependence of the Direct Piezoelectric Effect in Ferroelectric Ceramics. *Journal of Applied Physics* **82,** 1788–1797 (1997).

156. Ruangchalermwong, C., Li, J.-F., Zhu, Z.-X., Lai, F. & Muensit, S. Enhanced Ferro- and Piezoelectric Properties in (100)-Textured Nb-Doped $Pb(Zr_xTi_{1x})O_3$ Films With Compositions at Morphotropic Phase Boundary. *Thin Solid Films* **517,** 6599–6604 (Oct. 2009).

157. Menou, N., Muller, C., Baturin, I. S., Shur, V. Y. & Hodeau, J. L. Polarization Fatigue in $PbZr_{0.45}Ti_{0.55}O_3$ -Based Capacitors Studied from High Resolution Synchrotron X-Ray Diffraction. *Journal of Applied Physics* **97,** 064108 (2005).

158. Lou, X. J. Polarization Fatigue in Ferroelectric Thin Films and Related Materials. *Journal of Applied Physics* **105,** 024101 (2009).

159. Evans, J. T. Characterizing Ferroelectric Materials. *IEEE International Symposium on the Applications of Ferroelectrics and European Conference on the Applications of Polar Dielectrics* (2010).

160. Xu, Y. *Ferroelectric Materials and their Applications* (Elsevier Science Publishers, Amsterdam, 1991).

161. Pike, G. E., Warren, W. L., Dimos, D., Tuttle, B. A., Ramesh, R., Lee, J., Keramidas, V. G. & Evans, J. T. Voltage Offsets in $(Pb,La)(Zr,Ti)O_3$ Thin Films. *Applied Physics Letters* **484,** 484–486 (1995).

162. Grossmann, M., Lohse, O., Bolten, D., Boettger, U., Schneller, T. & Waser, R. The Interface Screening Model as Origin of Imprint in $PbZr_xTi_{1-x}O_3$ Thin Films. I. Dopant, Illumination, and Bias Dependence. *Journal of Applied Physics* **92,** 2680–2687 (2002).

163. Warren, W. L., Tuttle, B. A., Dimos, D., Pike, G. E., Al-Shareef, H. N., Ramesh, R. & Evans, J. T. Imprint in Ferroelectric Capacitors. *Japanese Journal of Applied Physics* **35,** 1521–1524 (1996).

164. Setter, N., Damjanovic, D., Eng, L., Fox, G., Gevorgian, S., Hong, S., Kingon, A., Kohlstedt, H., Park, N. Y., Stephenson, G. B., Stolitchnov, I., Taganstev, A. K., Taylor, D. V., Yamada, T. & Streiffer, S. Ferroelectric Thin Films: Review of Materials, Properties, and Applications. *J. Appl. Phys.* **100,** 51606 (2006).

165. Sivaramakrishnan, S., Mardilovich, P., Mason, A., Roelofs, A., Schmitz-Kempen, T. & Tiedke, S. Electrode Size Dependence of Piezoelectric Response of Lead Zirconate Titanate Thin Films Measured by Double Beam Laser Interferometry. *Applied Physics Letters* **103,** 132904 (2013).

166. Hopcroft, M. A., Nix, W. D. & Kenny, T. W. What is the Young's Modulus of Silicon? *Journal of Microelectromechanical Systems* **19,** 229–238 (2010).

167. Sivaramakrishnan, S. Measured $d_{33,f}$ as a Function of Elastically Anisotropic Substrate Thickness. *Private Communications (pending publication)* (2016).

168. Kholkin, A. L., Tagantsev, A. K., Colla, E. L., Taylor, D. V. & Setter, N. Piezoelectric and Dielectric Aging in Pb(Zr,Ti)O_3 Thin Films and Bulk Ceramics. *Integrated Ferroelectrics* **15,** 317–324 (1997).

169. Park, J. H., Xu, F. & Trolier-McKinstry, S. Dielectric and Piezoelectric Properties of Sol-Gel Derived Lead Magnesium Niobium Titanate Films with Different Textures. *Journal of Applied Physics* **89,** 568–574 (2001).

170. Shepard, J. F., Chu, F., Kanno, I. & Trolier-McKinstry, S. Characterization and Aging Response of the d_{31} Piezoelectric Coefficient of Lead Zirconate Titanate Thin Films. *Journal of Applied Physics* **85,** 6711–6716 (1999).

171. Polcawich, R. G. & Trolier-McKinstry, S. Piezoelectric and Dielectric Reliability of Lead Zirconate Titanate Thin Films. *Journal of Materials Research* **15,** 2505–2513 (2000).

172. Garten, L. M. *Residual Ferroelectricity, Piezoelectrictiy, and Flexoelectricity in Barium Strontium Titanate Tunable Dielectrics* Doctoral Thesis (The Pennsylvania State University, 2014).

173. Jiang, Q. Y. & Cross, L. E. Effects of Porosity on Electric Fatigue Behaviour in PLZT and PZT Ferroelectric Ceramics. *Journal of Materials Science* **28,** 4536–4543 (1993).

174. Tan, X. L. & Shang, J. K. In-Situ Transmission Electron Microscopy Study of Electric-Field-Induced Grain-Boundary Cracking in Lead Zirconate Titanate. *Philosophical Magazine A* **82,** 1463–1478 (2002).

175. Cao, H. & Evans, A. G. Electric-Field-Induced Fatigue Crack Growth in Piezoelectrics. *Journal of the American Ceramic Society* **77,** 1783–1786 (1994).

176. Mazzalai, A., Balma, D., Chidambaram, N., Muralt, P., Colombo, L. & Schmitz-Kempen, T. Dynamic and Long-Time Tests of the Transverse Piezoelectric Coefficient in PZT Thin Films. *IEEE International Symposium on the Applications of Ferroelectrics, International Workshop on Acoustic Transduction Materials and Devices & Workshop on Piezoresponse Force Microscopy* (2014).

177. Russell, A. M. & Lee, K. L. *Structure Property Relations in Nonferrous Metals* 1st Ed. (John Wiley & Sons, Hoboken, 2005).

178. Campbell, F. C. *Elements of Metallurgy and Engineering Alloys* 1st Ed. (ASM International, Materials Park, 2008).

179. Thornton, J. High Rate Thick Film Growth. *Annual Review of Materials Science* **7,** 239–260 (1977).

180. Brophy, J. H., Rose, R. M. & Wulff, J. *The Structure and Properties of Materials* 2nd Ed., 216 (Wiley, New York, 1964).

181. Musil, J. & Kadlec, S. Reactive Sputtering of TiN Films at Large Substrate to Target Distances. *Vacuum* **40,** 435–444 (1990).

182. Iriarte, G. F., Rodriguez, J. G. & Calle, F. Effect of Substrate-Target Distance and Sputtering Pressure in the Synthesis of AlN Thin Films. *Microsystem Technologies* **17,** 381–386 (2011).

183. Hull, T., Colligon, J. & Hill, A. Measurement of Thin Film Adhesion. *Vacuum* **37,** 327–330 (1987).

184. Abergel, J., Allain, M., Michaud, H., Cueff, M., Ricart, T., Dieppedale, C., Le Rhun, G., Faralli, D., Fanget, S., Defay, E. & Rhun, G. L. Optimized Gradient-Free PZT Thin Films for Micro-Actuators. *IEEE International Ultrasonics Symposium,* 972–974 (Oct. 2012).

185. Francis, L. F. & Payne, D. A. Thin-Layer Dielectrics in the $Pb[(Mg_{1/3}Nb_{2/3})_{1-x}Ti_x]O_3$ System. *Journal of the American Ceramic Society* **74,** 3000–3010 (1991).

186. Donnelly, N. J. & Randall, C. A. Refined Model of Electromigration of Ag/Pd Electrodes in Multilayer PZT Ceramics Under Extreme Humidity. *Journal of the American Ceramic Society* **92,** 405–410 (2009).

187. Brennecka, G. L., Parish, C. M., Tuttle, B. A., Brewer, L. N., Rodriguez, M. A. & Rye, M. J. Reversibility of the Perovskite-to-Fluorite Phase Transformation in Lead-Based Thin and Ultrathin Films. *Advanced Materials* **20,** 1407–1411 (2008).

188. Hooker, M. W. Properties of PZT-Based Piezoelectric Ceramics Between -150 and 250 °C. *NASA Report Number: NASA/CR-1998-208708* (1998).

189. Shirane, G., Suzuki, K. & Takeda, A. Phase Transitions in Solid Solutions of PbZrO 3 and PbTiO 3 (II) X-ray Study. *Journal of the Physical Society of Japan* **7,** 12–18 (1952).

190. Yeo, H. G. & Trolier-Mckinstry, S. {001} Oriented Piezoelectric Films Prepared by Chemical Solution Deposition on Ni Foils. *Journal of Applied Physics* **116,** 014105 (2014).

191. Yeo, H. G., Ma, X., Rahn, C. & Trolier-McKinstry, S. Efficient Piezoelectric Energy Harvesters Utilizing (001) Textured Bimorph PZT Films on Flexible Metal Foils. *Advanced Functional Materials* **26,** 5940–5946 (Aug. 2016).

192. Jacob, K. T., Kumar, A. & Waseda, Y. Gibbs Energy of Formation of MnO: Measurement and Sssessment. *Journal of Phase Equilibria and Diffusion* **29,** 222–230 (2008).

193. Jacob, K. T., Kumar, A., Rajitha, G. & Waseda, Y. Thermodynamic Data for Mn_3O_4, Mn_2O_3 and MnO_2. *High Temperature Materials and Processes* **30,** 459–472 (2011).

194. Fritsch, S. & Navrotsky, A. *Thermodynamic Properties of Manganese Oxides* 1996.

195. Chase Jr., M., Davies, C., Downey Jr., J., Frurip, D., McDonald, R. & Syverud, A. *NIST-JANAF Thermochemical Tables* Gaithersburg, 1986.

196. Theis, C. & Schlom, D. Epitaxy of $PbTiO_3$ on (100) $SrTiO_3$ and Vincial (100) $SrTiO_3$ by Pulsed Laser Deposition. *MRS Proceedings* **401,** 171–176 (1995).

197. Theis, C. *Adsorption-Controlled Growth of Titanates Containing Volatile Lead- or Bismuth-Based Components by Reactive MBE* Doctoral Thesis (The Pennsylvania State University, 1998).